

# DISSERTATION

submitted to the

Combined Faculty for the Natural Sciences and Mathematics

of

Heidelberg University, Germany

for the degree of

Doctor of Natural Science

put forward by

Dipl.-Math. Stephan Lenor

born

on January 30, 1986

in Dessau, Germany.

Day of oral examination: April 22, 2016



# Model-Based Estimation of Meteorological Visibility in the Context of Automotive Camera Systems

Advisor:

Prof. Dr. rer. nat. BERND JÄHNE



**Abstract.** Highly integrated and increasingly complex video-based driver assistance systems are rapidly developing nowadays. Following the trend towards autonomous driving, they have to operate not only under advantageous but also under adverse conditions. This includes sight impairments caused by atmospheric aerosols such as fog or smog. It is an important part of environmental understanding to thoroughly analyze the optical properties of these aerosols.

The aim of this thesis is to develop models and algorithms in order to estimate *meteorological visibility* in homogeneous daytime fog. The models for light transport through fog are carefully derived from the theory of radiative transfer. In addition to Koschmieder's well-established model for horizontal vision<sup>1</sup>, a recursively-defined sequence of higher-order models is introduced which yields arbitrarily good approximations to the solutions of the radiative boundary problem.

Based on the radiative transfer models, visibility estimation algorithms are proposed which are applicable to data captured by a driver assistance front camera. For any one of these algorithms, the recording of luminances from objects observed at distinct distances is required. This data can be acquired from moving objects being tracked as well as from depth-extended homogeneous objects such as the road. The resulting algorithms supplement each other with respect to different road traffic scenarios and environmental conditions. All given algorithms are extensively discussed and optimized regarding their run-time performance in order to make them applicable for real-time purposes. The analysis shows that the proposed algorithms are a useful addition to modern driver assistance cameras.

**Kurzfassung.** Video-basierte Fahrerassistenzsysteme erfahren derzeit eine rasante Entwicklung hin zu immer komplexeren und hoch-integrierten Produkten. Einhergehend mit dem Trend zum autonomen Fahren muss deren Einsatzfähigkeit nicht nur unter vorteilhaften sondern auch unter schwierigen Bedingungen sichergestellt werden. Dazu gehören auch Sichteinschränkungen, welche durch atmosphärische Aerosole wie Nebel oder Smog verursacht werden. Es ist ein wichtiger Teil eines ganzheitlichen Umgebungsverständnisses, diese Einschränkungen sowohl qualitativ als auch quantitativ zu erfassen.

Das Ziel dieser Arbeit ist die Entwicklung und Untersuchung von Modellen und Algorithmen zur Sichtweitschätzung in homogenem Tagnebel. Basierend auf der Strahlungstransporttheorie wird eine rekursiv definierte Folge von Modellen für Lichttransport durch Nebel hergeleitet. Während das Modell erster Ordnung Koschmieders etabliertem Modell für horizontale Sicht<sup>1</sup> entspricht, kann mit den Modellen höherer Ordnung die Lösung des Randwertproblems für Strahlungstransport beliebig genau approximiert werden.

Basierend auf den Strahlungstransport-Modellen werden Algorithmen zur Sichtweitschätzung auf Daten einer automobilen Frontkamera, welche die Leuchtdichte eines oder mehrerer Objekte erfasst, vorgestellt. Um eine modellbasierte Schätzung zu ermöglichen, müssen diese Objekte entweder, wie eine Straße, in der Tiefe ausgedehnt sein oder über mehrere Bilder hinweg auf verschiedenen Distanzen beobachtet werden. Die abgeleiteten Algorithmen unterscheiden sich vor allem in den zugrunde liegenden Daten, Modellen und Parameter-Schätzmethoden. Um den Einsatz in sicherheits- und laufzeitkritischen Systemen zu ermöglichen, wird hierbei großer Wert auf eine effiziente Parameter-Schätzung gelegt. Insgesamt zeigt sich, dass die vorgestellten Methoden für den Einsatz in heutigen Fahrerassistenzkameras gut geeignet sind.

---

<sup>1</sup>Harald Koschmieder. "Theorie der Horizontalen Sichtweite". In: *Physik der Freien Atmosphäre* 12 (1924), 33-55. DOI: 10.1007/978-3-663-04661-5\_2



---

# Acknowledgments

Allen, die mich bei der Entstehung dieser Arbeit unterstützt haben, danke ich von Herzen!

Mein erster Dank geht dabei an Prof. Bernd Jähne von der Universität Heidelberg und an Ulrich Stopper sowie Stefan Weber von der Robert Bosch GmbH. Sie haben mich über mehr als drei Jahre mit ihrem fachlichen Rat begleitet und mir dabei stets meine gewünschte Freiheit gelassen. Mit ihrer Hilfe konnte ich viele für mich neue Gebiete erschließen, ohne dabei den Blick für das Wesentliche zu verlieren.

Danken möchte ich auch allen anderen Personen, welche mir inhaltlich zur Seite gestanden haben, vor allem Prof. Pfeilsticker und Ugo Tricoli vom Institut für Umweltphysik für Diskussionen zum Strahlungstransport durch Nebel bzw. zu analytischen und numerischen Details der Mie-Theorie; Johannes Martini für das Vorantreiben der Tracking-basierten Sichtweitschätzung im Rahmen seiner Diplomarbeit; Florian Ohr für die Erlaubnis zur Nutzung seines Structure-from-Motion-Frameworks zur Tiefenrekonstruktion auf monokularen Kamerabildern; Björn Mayer für seine Unterstützung im Umgang mit der Kamerasoftware; und Mirjam Lenor für die vielen Stunden des Labelns.

Ganz allgemein geht mein Dank an die Robert Bosch GmbH, welche diese Promotion finanziell getragen hat. Durch das lebendige Doktorandenprogramm konnte ich nicht nur einen aufschlussreichen Einblick in das Unternehmen gewinnen, sondern auch viele wertvolle Bekanntschaften schließen. Ein besonderer Dank gilt dabei auch meinem Gruppenleiter Stefan und meinem Teamleiter Wolfgang, die mir auch nach Ende der Doktorandenzeit noch die nötige zeitliche Flexibilität eingeräumt haben um meine Dissertation zum Abschluss zu bringen.

Danken möchte ich auch den Benediktinerbrüdern des Klosters Huysburg, welche mich für zwei Wochen intensiven Schreibens herzlich aufgenommen haben. Noch oft vermisse ich den ruhigen Arbeitsplatz und den weitläufigen Ausblick über den Wald des Huys und die Hügel des Vorharzes.

Mein ganz besonderer Dank geht an all diejenigen, welche diese Arbeit liebevoll Korrektur gelesen haben: vor allem Uli für den unglaublichen Aufwand, den er über Monate hinweg in gründliche und sehr hilfreiche Korrekturen gesteckt hat; aber auch Michel für die vielen Stunden gemeinsamen Schwitzens über meiner Arbeit; Amanda für viele sprachliche Korrekturen; Johannes für die Diskussion meiner Notation beim gewohnt guten Grüntee; und Thomas für die hilfreichen Kommentare zum Prozess der Bildaufnahme.

Ein persönlicher Dank gilt meiner Familie und meinen Freunden für ihre uneingeschränkte Unterstützung über die gesamte Zeit der Promotion hinweg, vor allem Mirjam, die diese manchmal entbehrungsreiche Zeit mit mir durchgestanden hat.

“When I hear somebody sigh, ‘Life is hard,’  
I am always tempted to ask, ‘Compared to what?’”  
(Sydney J. Harris)



---

# Contents

<b>Abstract</b> . . . . .	<b>v</b>
<b>Kurzfassung</b> . . . . .	<b>v</b>
<b>Acknowledgments</b> . . . . .	<b>vii</b>
<b>Contents</b> . . . . .	<b>ix</b>
<b>Introduction</b> . . . . .	<b>I</b>
<hr/>	
<b>1. Motivation</b> . . . . .	<b>3</b>
1.1 Advanced Driver Assistance Systems . . . . .	3
1.2 Adverse Weather Conditions in Road Traffic . . . . .	4
<b>2. Contribution and Organization of this Thesis</b> . . . . .	<b>9</b>
<b>Light Transport through Fog</b> . . . . .	<b>II</b>
<hr/>	
<b>3. Meteorological Visibility</b> . . . . .	<b>15</b>
3.1 Definition . . . . .	15
3.2 Measuring Devices . . . . .	18
3.3 Applications of Image-Based Visibility Estimation . . . . .	19
<b>4. Light Scattering by Fog Droplets</b> . . . . .	<b>23</b>
4.1 Fog . . . . .	23

4.2	Light . . . . .	25
4.3	Scattering and Absorption . . . . .	26
4.3.1	Mie Theory: Scattering by Spherical Particles . . . . .	27
4.3.2	Volume Scattering . . . . .	32
<b>5.</b>	<b>Radiative Transfer Theory . . . . .</b>	<b>37</b>
5.1	Radiative Transfer Equation . . . . .	37
5.1.1	General Radiative Transfer Equation . . . . .	38
5.1.2	RTE for Light Transport through Fog . . . . .	38
5.2	Radiative Boundary Problem . . . . .	40
5.3	Integral Formulation . . . . .	42
5.3.1	RTE on the Line of Sight . . . . .	42
5.3.2	Equivalence of Classical and Integral Formulation . . . . .	44
5.4	Derived Models for Light Transport through Fog . . . . .	47
5.4.1	Koschmieder’s Model (for Horizontal Vision) . . . . .	48
5.4.2	Higher-Order Approximate Models . . . . .	49
5.5	Plane-Parallel Atmosphere . . . . .	55

**Model-Based Visibility Estimation III**

---

<b>6.</b>	<b>Preliminary Considerations . . . . .</b>	<b>63</b>
6.1	Literature Review . . . . .	63
6.1.1	Visibility Assessment at Daytime . . . . .	63
6.1.2	Visibility Assessment at Nighttime . . . . .	66
6.1.3	Visibility Assessment for Stationary Cameras . . . . .	67
6.2	Setting . . . . .	68
6.3	Measuring Principle . . . . .	70
6.4	Image Acquisition . . . . .	71
<b>7.</b>	<b>Tracking-Based Algorithm . . . . .</b>	<b>75</b>
7.1	Data Acquisition . . . . .	76
7.2	Model Selection . . . . .	79
7.3	Optimization Problem . . . . .	79

7.4	Fast Minimization Approach . . . . .	82
7.4.1	Analytical Discussion . . . . .	83
7.4.2	Derived Algorithms . . . . .	91
7.4.3	Open Questions and Conjectures . . . . .	95
7.5	$L_{\text{air}}$ Stabilization . . . . .	99
7.6	Further Evaluation . . . . .	106
<b>8.</b>	<b>Algorithm Based on Road Surface Luminance Curves . . . . .</b>	<b>115</b>
8.1	Data Acquisition . . . . .	116
8.2	First-Order: Koschmieder's Model . . . . .	120
8.3	Second-Order: Improved Fog Model . . . . .	121
8.3.1	In-Scattering Luminance Model . . . . .	123
8.3.2	Geometry . . . . .	124
8.3.3	Second-Order Model . . . . .	125
8.3.4	Notes on the Parameter Estimation . . . . .	125
8.4	Higher-Order Models . . . . .	130
8.5	Inflection Point Estimation from Observation Data . . . . .	135
8.6	Further Experiments and Evaluation . . . . .	136
8.6.1	Monte Carlo Simulation . . . . .	136
8.6.2	Further Numerical Experiments . . . . .	138
8.6.3	Real World Examples . . . . .	147
<b>9.</b>	<b>Algorithm Based on Partial Road Segments . . . . .</b>	<b>151</b>
9.1	Data Acquisition . . . . .	152
9.2	Model Selection . . . . .	153
9.3	Optimization Problem . . . . .	153
9.4	Experimental Results . . . . .	153
	<b>Conclusions and Outlook . . . . .</b>	<b>157</b>
	<b>Appendix A. Notation . . . . .</b>	<b>163</b>

<b>Appendix B. Selected Theorems . . . . .</b>	<b>171</b>
<b>Appendix C. Fast Noise Variance Estimation on Smooth Signals . . . . .</b>	<b>177</b>
<b>Appendix D. Proofs from the Analytical Discussion of <math>\mathcal{F}</math> . . . . .</b>	<b>187</b>
<b>Appendix E. Derivation of <math>L_{\text{air,min}}</math>'s Numerator and Denominator . . . . .</b>	<b>201</b>
<b>Bibliography . . . . .</b>	<b>205</b>
<b>Index . . . . .</b>	<b>217</b>

**I**

---

**Introduction**

---



# Chapter 1

---

## Motivation

### Contents

---

1.1	Advanced Driver Assistance Systems . . . . .	3
1.2	Adverse Weather Conditions in Road Traffic . . . . .	4

---

### 1.1 Advanced Driver Assistance Systems

Technologies assisting drivers during the driving process are experiencing a rapid development nowadays (*cf. e.g.* [Oku2014]). These so-called *advanced driver assistance systems* (ADAS) are designed to actively or passively increase the driver's and passenger's safety and comfort, and to improve the economical and ecological efficiency of a car. A prerequisite for the development of such systems is sensors that on the one hand monitor vehicle parameters (such as tire pressure, steering wheel angle, lateral acceleration, yaw rate, and individual road wheel speeds), and on the other hand allow for an increasingly precise perception of the vehicle's environment (such as the distance to preceding vehicles, and the relative positioning of the lanes).

This trend is further driven by the idea of fully autonomously driving vehicles which are able to operate even in uncontrolled and unknown environments. Several companies such as Daimler, Google and Bosch have already developed fully autonomously driving cars for various use cases and for more or less controlled environments for which detailed maps are available (*cf. e.g.* [Zie2014], [Mar2010] and [Bec2014] respectively). Some of the functionalities are almost ready for series production and can be expected to be found on the roads in a few years, such as a traffic jam assistant or highway assistant. Other domains of autonomous driving are still struggling with too complex and unpredictable environments, such as in urban or off-road settings, in which it is hard to replace a human driver's extensive wealth of experience. Further problems arise from safety aspects, social acceptance and high sensor costs.

Many successful driver assistance systems have already been established in the automotive market over the last decades, such as the *electronic stability control* (ESC) which enormously stabilizes the vehicle's behavior when turning and braking. These driver assistance systems are mature and have a high equipment rate even in the low-price car segment. While they are based on measurements of the vehicle's motion parameters only, many of the current and future assistance systems essentially rely on environmental information:

Parking assist systems use ultrasonic sensors to detect obstacles and measure their distance over a

range of a few meters around the car. In comparison, radar sensors allow for mid- and long-range applications, such as *adaptive cruise control* (ACC) or *autonomous emergency braking* (AEB).

Another class of active ranging sensors are lidar systems which, similar to radar, use electromagnetic radiation reflected by objects to localize them. In contrast to radar, they are not based on radio waves but on the infrared spectrum. In principle, the use of shorter wavelengths allows for an increased angular separability and the detection of smaller objects. This benefit is currently mainly exploited by laser scanners which are an interesting subform of lidars. They measure the distance for different directions through controlled steering of laser beams. This is most often realized by a rotating sensor head which scans its environment line-wisely. Especially for almost static environments, this allows for remarkably accurate and comprehensive depth acquisition. Therefore, laser scanners are often an essential part of the current working prototypes of autonomous vehicles. Since highly resolving lidar sensors are, however, still quite expensive and since infrared sensors in general suffer from absorption during rainfall, they are not well established for driver assistance. This might change with further decreasing sensor costs, increasing sensor performance and an increased need for data redundancy and ranging accuracy.

Besides the actively working ultrasonic, radar and lidar systems from above, cameras are a passively working and more common low-cost class of sensors. They can be used in various ways: as front cameras pointing along the road ahead, as interior cameras observing the driver's condition, or as surround-view cameras observing the maneuvering area around the car. As visual information is most relevant in road transport (*cf. e.g. [Siv1996]*), cameras cover the widest range of driver assistance applications. Current multi-purpose ADAS cameras provide various features, such as lane departure warning, lane keeping support, intelligent headlight control and road sign recognition. Furthermore, there are many enhancements of classical cameras, such as stereo sensors, fish-eye lenses as well as infra-red or polarization cameras. These extend the capabilities of classical cameras, adding further powerful features, such as more precise depth estimation, a larger field of view, night vision applications, and glare detection or removal.

While emphasizing the numerous capabilities of cameras, the benefits of other sensor technologies should not be neglected. They provide information a human driver cannot perceive with high precision on, for example, scene depth, vehicle parameters or relative speed and direction of other road entities. One could thus argue that they even have better synergy effects in cooperation with a human driver than cameras do. In any case, future driver assistance systems will have to operate more and more autonomously which requires a comprehensive and redundant sensing of the environment. To achieve this, many sensors have to work simultaneously and different sensor concepts have to be combined in order to guarantee a high level of safety. The strengths and weaknesses of the different sensor concepts have to be taken into account by implementing improved sensor data fusion. As a part of this future challenge it is important to assess the operability of each sensor, including the environmental conditions. In this context, fog detection and quantification, which is addressed in this work, is just one out of many challenges.

## 1.2 Adverse Weather Conditions in Road Traffic

Adverse weather in road traffic, such as rain, snow or fog, can lead to a problematic reduction of drivers' visual range and the controllability of vehicles. Water, snow or ice on the road surface cause diminished tire traction which, obviously, has a disadvantageous impact on the driving dynamics. This includes dangerous effects due to increased braking distances, understeering in



Figure 1.1: smog in Peking, January 2013 (by courtesy of AFP)

curves or even the absolute loss of braking or steering capabilities in the case of hydroplaning. Apart from that, adverse weather can strongly impair the visibility conditions, for instance in cases of dense fog, rain or sandstorms. Although humans are able to recognize these atmospheric sight impairments, they are basically unable to quantify their own visual range and the relative speed at which they are moving towards other road users or static objects. Even smog can turn into a risk for the driver's health and safety, not only by causing bronchial diseases, but also due to substantially decreased ranges of visibility (*cf.* Fig. 1.1).

Many studies show the connection between adverse weather conditions and increased crash and injury rates. A good summary can be found in the meta-analysis of Qiu and Nixon [Qiu2008] which not only includes the absolute number of accidents and injuries, but also the traffic volume reduction and the sample sizes and variances in order to correctly evaluate the statistical impact of adverse weather conditions. Studies focusing particularly on the influence mechanisms and statistics of fog regarding traffic safety can be found in [Cro2003], [Sit2011] and [Bab2011, 1]. Additionally, an interesting and comprehensive overview of weather impact on road accidents is provided by the U.S. Road Weather Management Program which can be found in [Tra2015].

The difficulties and dangers of adverse weather conditions are addressed by several assistance systems, such as the ESC which stabilizes vehicle dynamics close to the optimum, or the rain detector which automatically triggers the windshield wipers. Aside from that, driver assistance systems based on optical sensors can also be compromised by atmospheric sight impairments. The more autonomous the vehicles, the more important automated detection of and adaption to these adverse environmental conditions are. Therefore, fog detection and visibility estimation is an important challenge for video-based driver assistance systems, and additionally allows for several new driver assistance applications (*cf.* Sec. 3.3). This work constitutes one of the first steps of the investigations and developments required in this direction.

***Fog as Adverse Weather.*** Among other adverse weather conditions, fog is a particular challenge for humans as well as technical systems relying on visual perception. The term fog denotes an atmospheric aerosol which consists of numerous small water droplets dispersed in the air close to the Earth's surface (*cf.* Sec. 4.1). Light on its path from an object to an observer is scattered away and partially absorbed whenever it encounters one of these droplets; at the same time,

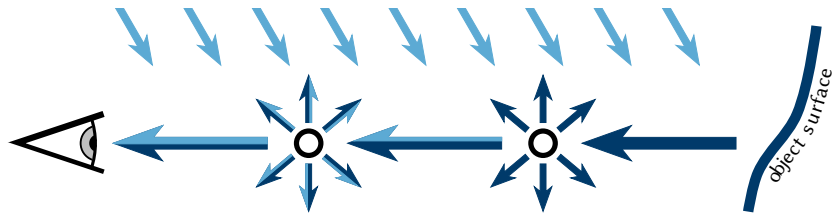


Figure 1.2: On its way from an object to an observer through fog, light is scattered away and simultaneously enriched with surrounding light.



Figure 1.3: daytime fog captured by a driver assistance front camera

surrounding light is scattered into the line of sight (*cf.* Fig. 1.2). Depending on the surrounding lighting conditions and the density and homogeneity of the fog, the resulting visual effects range from simple veils or halos to arbitrarily shaped ghost artifacts.

In the case of approximately homogeneous daytime fog, contrast reduction represents the most dominant visibility-reducing effect (*cf.* Fig. 1.3). This contrast reduction can be modeled as exponential attenuation over distance with a decay constant  $K$ :

$$C_v(d) = C_v(0)e^{-Kd},$$

where  $C_v(d)$  denotes the visual contrast at the distance  $d$  between an object and an observer (*cf.* Sec. 3.1). In practice, the so-called *extinction coefficient*  $K$  turns out to be the most relevant parameter for characterizing fog. As it is determined by the scattering and absorbing behavior of the atmosphere (*cf.* 4.3.2),  $K$  is related to the optical depth of the atmospheric aerosol and thus to the visual range of observers in foggy environments. This is further specified by the definition of the *meteorological visibility*  $d_{\text{met}}$  in Chap. 3.

A reliable estimation of  $K$  would allow for various applications in the context of driver assistance systems and (semi-)autonomous driving (*cf.* Sec. 3.3). This motivates a detailed discussion of

models for light transport through fog (*cf.* Part II) and the development of  $K$ -estimation methods (*cf.* Part III), which shall be the subject of this work.



## Chapter 2

---

### Contribution and Organization of this Thesis

Meteorological visibility as defined in Sec. 3.1 is an established quantity in the context of visibility assessment, with a history reaching back to the beginning of the 20<sup>th</sup> Century (*cf. e.g.* [Kos1924] or Table 3.1). In daytime fog, it is the distance at which the contrast between a dark object and the bright horizon falls below a certain perception threshold (*cf.* Sec. 3.1). Although several measuring devices for meteorological visibility are available (*cf.* Sec. 3.2), its estimation based on images is a comparatively new field of work which has emerged with the increased use of cameras for driver assistance and road traffic surveillance. This is mainly driven by a greater interest in achieving a holistic environmental understanding (*cf.* Chap. 1) and the search for further video-based driver assistance applications (*cf.* Sec. 3.3).

An overview of the literature on image-based visibility assessment is provided in Sec. 6.1. While most of the publications mentioned there aim to gradually assess fog's density, only a few of them are based on a well-defined physical quantity. The only rigorous method for image-based estimation of meteorological visibility is described in a series of works by Hautière *et al.* starting in 2006 (*cf. e.g.* [Hau2006c]). Based on Koschmieder's model for horizontal vision, they use the shape of the vertical luminance curve on the road and the sky to draw inference on the fog's density. This is done without taking into account the effects from non-horizontal vision; wherefore the resulting luminance curve model is not capable of describing the real luminance observations (*cf.* Chap. 8 and Fig. 8.5).

The measurement of physical quantities, however, relies on a good understanding of the related physics. This understanding is manifested in reliable models which can be used to infer underlying physical process parameters from statistical observations (*cf.* Sec. 6.3). Thus one aim of this thesis is to carefully derive and discuss models for light transport through fog. Based on these models, improved and novel approaches for image-based estimation of meteorological visibility are derived which are applicable to data captured by a driver assistance front camera. In this context, it is explicitly pointed out which assumptions have to be made for this derivation. As general feasibility of image-based visibility estimation has already been shown in the literature (*cf.* Sec. 6.1), the evaluation of algorithms focuses on the influence of models on the estimation accuracy. Furthermore, the resulting approaches are extensively discussed and optimized regarding their run-time performance in order to make them applicable for real-time purposes.

One should note that this work does not claim to answer all questions regarding visibility assessment. Instead, it should be considered as a first systematic and in-depth discussion on the theory of model-based visibility estimation from camera images, restricted to the case of homogeneous daytime fog. Nevertheless, several links and ideas are provided on how this work could be followed

up. Many of them can be found in one of the several remarks (provided in separate “Remark” environments) or in the outlook on page 157.

This thesis is organized in three parts: the introduction in Part I, which explains the motivation for using model-based visibility estimation in the context of video-based driver assistance systems; the theory and models for light transport through fog in Part II, in which the interaction of light and fog is discussed on the microscopic as well as on the macroscopic scale; and the model-based visibility estimation in Part III, in which the light transport models are used to introduce novel algorithms and improve existing algorithms for the estimation of meteorological visibility. Each part is organized in chapters, which consist of sections and subsections.

While chapters 3, 4 and 6 compile useful background information on the theory of light, fog, scattering, image-taking and other related topics, the main contribution made by this work can be found in chapters 5, 7, 8 and 9. In Chap. 5, the radiative transfer theory is used to explicitly derive arbitrarily accurate models for light transport through fog. The link between the classical and integral formulation of the radiative boundary problem is rigorously pointed out, and the models are derived from a fixed-point iteration for the integral operator. To the author’s knowledge, this work manifests these steps for the first time.

The last three chapters 7, 8 and 9 introduce the model-based algorithms. While Chap. 7 describes a completely novel approach for visibility estimation, Chap. 8 is based on the analysis of *road surface luminance curves* (RSLC), as described by Hautière *et al.* (*cf.* Sec. 6.1). It is shown that higher-order RSLC models can be applied to reduce the systematic model error in the visibility estimation. At the same time, the increased complexity of higher-order models can be broken down to precomputed look-up tables which can be used for real-time purposes. This is based on the insight that the fast parameter estimation method on the basis of the RSLC’s inflection point is valid not only for Koschmieder’s model as used by Hautière *et al.* but also for the novel higher-order models. Chap. 9 provides a sketch of an algorithm which could be a useful supplement to the algorithms presented in Chap. 7 and Chap. 8. It should be considered more as an outlook than as a fully evaluated algorithm.

A brief overview regarding motivation, contribution and linking of the chapters, sections and subsections can also be found in the introductions to Part II and Part III on pages 13 and 61, respectively.

After a conclusion and summary of the work, the parts are followed by several appendices which contain additional information provided at the end of the work mainly for reasons of readability. This includes a comprehensive overview of the notation in Appendix A. The bibliography and the index can be found at the very end of the document. The index also includes most of the abbreviations used in this work; further mathematical abbreviations and symbols are listed in Appendix A. In order to enrich the contents without decreasing the overall readability, several remarks are added to the end of the sections and subsections.

# II

---

## Light Transport through Fog

---



Light that propagates through a foggy atmosphere is scattered and absorbed whenever it interacts with fog droplets or other particles. As pointed out in Sec. 1.2, this leads to a substantial degradation of visibility. In order to quantitatively assess the reduced visual range caused by fog, the physical quantity *meteorological visibility*  $d_{\text{met}}$  is introduced in Chap. 3. It is shown how  $d_{\text{met}}$  can be derived from the combination of Duntley's law and the human's visual perception threshold, as a quantity inversely proportional to the extinction coefficient  $K$ . In addition, the definition of the meteorological visibility is discussed regarding its scope, limits and ambiguities (*cf.* Sec. 3.1). A rough overview is provided of the most common measuring devices (*cf.* Sec. 3.2). In addition, various applications for the camera-based estimation of meteorological visibility are pointed out (*cf.* Sec. 3.3).

To implement model-based approaches for visibility assessment, it is important to understand the microscopic and macroscopic processes of light transport through fog. Therefore, the theoretical foundations of fog, light, scattering and radiative transfer are discussed in chapters 4 and 5. Based on this, models can be derived which appropriately describe the overall process of light transport through fog. They are the basis for the visibility estimation methods introduced in Part III of this work.

Chap. 4 focuses on the microscopic process of scattering by fog droplets. In Sec. 4.1, fog is introduced as a dispersed medium that usually consists of numerous tiny water droplets. It is outlined how the macroscopic properties of fog can be described by the drop-size distribution without taking into account the exact positions or radii of individual particles. Besides, basic facts about light are compiled which include the particle and wave properties as well as radiometric and photometric terms such as *radiance* and *luminance* (*cf.* Sec. 4.2). In Sec. 4.3, the most important findings of the Mie theory are briefly but carefully brought together. This theory is used to describe the scattering and absorption of light by single particles as well as in fog volumes. From this, several useful assumptions can be made about light transport through fog, for instance, about wavelength independence and perfect scattering (no absorption).

In Chap. 5, the radiative transfer equation (RTE) is introduced and simplified with respect to fog and its use in the context of video-based driver assistance. Together with appropriate boundary conditions, the radiative boundary problem can be classically formulated (*cf.* Sec. 5.2). To remove the difficult-to-handle integro-differential formulation of the RTE, an integral formulation is derived and shown to be equivalent to the classical formulation under certain assumptions (*cf.* Sec. 5.3). Based on this, models for light transport through fog can be derived which are approximate solutions to the radiative transfer problem (*cf.* Sec. 5.4). These models make it possible to subsequently derive the visibility estimation algorithms. For the case of a plane-parallel atmosphere, the models are more extensively discussed in Sec. 5.5.

Although there is a lot of literature about the radiative transfer theory in general, one should note that it is hard to find explicit formulations or even proofs that rigorously describe the way solutions or approximate solutions of the radiative boundary problem are developed from the RTE. In fact, the author could not find any literature on the relation between the classical and integral formulation of the boundary problem in Sec. 5.3 or the higher-order approximate models provided in 5.4.2.



# Chapter 3

---

## Meteorological Visibility

### Contents

---

3.1	Definition . . . . .	15
3.2	Measuring Devices . . . . .	18
3.3	Applications of Image-Based Visibility Estimation . . . . .	19

---

Fog, smog and other optically dense atmospheric aerosols are a common cause for reduced visibility. Depending on the size and number of particles per unit volume, light is scattered and absorbed on its path from an object to an observer (*cf.* Part II of this work). As a result, object information carried by the light is more and more disturbed over distance and finally becomes imperceptible. As stated in Sec. 1.2, this effect can be measured by the loss of contrast. In this chapter, the *meteorological visibility* is introduced, the distance at which any contrast comes below the threshold of human perceptibility. This quantity is of substantial interest for visual environmental perception and can be used in various driver assistance applications (*cf.* Sec. 3.3).

### 3.1 Definition

Looking back at the history of visibility measurements, different terms and meanings have been introduced to turn visual range into a well-defined quantity. Basically all of them are designed to describe the maximum distance at which a sufficiently large object can be clearly discerned from its environment. In this work the current state-of-the-art definition is used, which follows the concept of the *visual contrast* and the related definition of *meteorological visibility*.

The *visual contrast*  $C_v$  (often referred to as *Weber contrast*) is defined in terms of an isolated object or feature of luminance  $L \in \mathbb{R}_{\geq 0}$  surrounded by a uniform and sufficiently extended background of luminance  $L_{bg} \in \mathbb{R}_{\geq 0}$  (*cf.* [Mid1952, 4.1]):

$$C_v := \frac{L - L_{bg}}{L_{bg}} \in [-1, \infty) \cup \{\infty\}, \quad (3.1)$$

where luminance denotes the photometric term for brightness (*cf.* Sec. 4.2), and  $0/0$  has to be interpreted as  $0$ . The human perception of this contrast has been shown to be approximately independent of the luminance level in the case of an unbalanced object-background setting, and thus constitutes a suitable basis for visibility measures (*cf.* [Pel1990]).

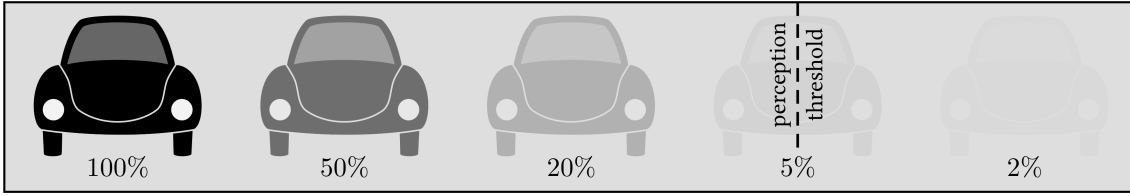


Figure 3.1: The definition of the meteorological visibility is based on the visual perception threshold of  $\tau_c = 5\%$ .

One should note that the concept of a signed contrast reflects the presumed asymmetry between the foreground and background. For objects brighter than the background the visual contrast ranges from 0 to  $\infty$ , while for objects darker than the background, it ranges from 0 to  $-1$ . Since the perceptibility of objects rises with increasing  $|C_v|$ , a contrast is said to be larger than another contrast (of the same sign) whenever this is true for the absolute values.

Caused by atmospheric attenuation, the apparent luminance  $L(d)$  of the object depends on the distance  $d$  between the object and observer. According to *Duntley's law* the distance-dependent visual contrast

$$C_v(d) = \frac{L(d) - L_{bg}}{L_{bg}}$$

decreases exponentially w.r.t.  $d$  (*cf.* [Mid1952, 4.5]). More precisely, it is

$$C_v(d) = C_v(0)e^{-Kd}, \quad (3.2)$$

where  $K \geq 0$  is an atmospheric parameter referred to as *extinction coefficient*. When the subtraction of  $L_{bg}$  is interpreted as a signal background correction, this equation is equivalent to the Beer-Lambert law, which is widely used in natural sciences. A comprehensive discussion on the relation between  $K$  and the fog's drop-size distribution can be found in 4.3.2.

With the help of Duntley's law (3.2), the *meteorological visibility* (in the daytime) can now be defined as the distance "at which it is just possible to distinguish a dark object against the horizon" (*cf.* [Mid1952, 1.1]). For a perfectly black object, *i.e.*  $L(0) = 0$ , this leads to

$$\tau_c = |C_v(d)| = e^{-Kd_{met}^{\tau_c}}, \quad (3.3)$$

where the meteorological visibility  $d_{met}^{\tau_c}$  is implicitly defined in terms of the extinction coefficient  $K$  and the *visual perception threshold*  $\tau_c \in [0, 1]$ :

$$d_{met}^{\tau_c} := -\frac{\log(\tau_c)}{K}. \quad (3.4)$$

There are two commonly used perception thresholds: 0.02 and 0.05. Some authors define the meteorological visibility based on the threshold  $\tau_c = 0.02$ , such as Middleton in [Mid1952, 6.2.1] (referred to as *meteorological range*) and the Verband Deutscher Ingenieure (VDI) in [VDI1983] (referred to as *standard visibility*). However, in this work  $\tau_c = 0.05$  is applied to define the meteorological visibility (illustrated in Fig. 3.1), following the definition of the International

Commission on Illumination CIE (*cf.* [CIE2012]):

$$d_{\text{met}} := d_{\text{met}}^{0.05} = -\frac{\log(0.05)}{K}. \quad (3.5)$$

This decision is further motivated by the increased safety demands in the automotive sector as well as by the clearly visible trend in the literature (*cf.* Table 3.1). Nevertheless, as the models and algorithms in this work are intended to estimate the atmospheric parameter  $K$ , the difference in the choice of  $\tau_c$  is only of marginal importance.

**Remark 1** (Other Definitions of Contrast). It is interesting to note that a suitable contrast definition essentially depends on the observation setting (*cf.* [Pel1990]). As stated above, the visual contrast  $C_v$  from (3.1), for example, is useful in scenarios where a small foreground object or feature is situated in front of a largely extended background. In comparison to this unbalanced foreground-background setting, the *Michelson contrast*  $C_M$  can be applied to more general patterns in which none of the luminances are preferred. It is given by

$$C_M := \frac{L_{\max} - L_{\min}}{L_{\max} + L_{\min}} \in [0, 1],$$

where  $L_{\min}$  and  $L_{\max}$  denote the minimum and maximum luminance of the pattern, respectively.

**Remark 2** (Scope of Meteorological Visibility). It is important to realize that meteorological visibility as defined in (3.5) does not cover non-atmospheric impairments of visibility, such as adverse illumination conditions (darkness, glare), geometrical blockages in the line of sight (due to curves, other traffic participants, dirt on the windshield, *etc.*), undersized objects or a low original contrast  $C_v(0)$ .

Nevertheless, it is still a meaningful visibility measure. For one thing, it is explicitly constructed to be focused on purely atmospheric impairments. For another thing, especially in the automotive context where almost all important information is (or should be) provided in a visually well observable way (concerning size, contrast, line of sight, illumination, *etc.*), atmospheric sight reductions form the most important aspects of visibility.

**Remark 3** (Wavelength Dependence). The meteorological visibility as defined in (3.5) is independent of the wavelength of the transmitted light. The actual relation between the extinction coefficient and the visibility of an atmosphere, however, slightly depends on the wavelength. Further discussions and a collection of empirical relations (with a focus on visible and infrared light) are provided in the highly informative work of Nebuloni [Neb2005].

**Remark 4** (Naming Convention). A consistent naming convention for meteorological visibility has not been established yet. Table 3.1 provides a compendium of the diverse conventions used in this context.

**Remark 5** (Limits of Meteorological Visibility). When working with a definition of meteorological visibility as provided in (3.5), it is important to know the limits of this term. The main practical restrictions can be found in the assumptions about the homogeneity of fog and the daytime.

In cases of highly non-homogeneous fog, for example, the extinction coefficient has to be understood as a spatially and temporally varying quantity. Therefore, it is neither useful nor possible to estimate  $d_{\text{met}}$  in those cases. In fact, the problem of visibility estimation can be interpreted as a

term	symbol	$\tau_c$	source example
visual range	$s_S$	$\approx 2\%$	[Kos1924, (33)]
visibility	$V$	2%	[Kam1952, (2a)]
meteorological range	$V_2$	$\approx 2\%$	[Mid1952, 6.2.1]
visibility range	$R_v$	$\approx 2\%$	[Bur1974, 7.3]
standard visual range	$V$	$\approx 2\%$	[Jiu1974, (1)]
standard visibility	$V_N$	$\approx 2\%$	[VDI1983, (2a)]
meteorological visibility distance	$V_{\text{met}}$	5%	[Hau2006c, (3)]
meteorological optical range	$P$	5%	[Org2008, (9.6)]
meteorological visibility	$V$	$\approx 5\%$	[Hau2011, (3)]
meteorological optical range	$v$	5%	[CIE2012, 17-772]
meteorological visibility	$v$	5%	[CIE2012, 17-773]
meteorological visibility	$d_{\text{met}}$	5%	[Len2013, (1)]

Table 3.1: examples for various conventions to define meteorological visibility

tomographical one, which is hardly accessible by only one camera. For this reason the models and algorithms proposed in this work are derived from the assumption of a spatially and temporally homogeneous atmospheric aerosol (*cf.* Remark 17 on page 69).

For observations of single light sources at night, the meteorological visibility represents a meaningful range quantity (*cf.* [Org2008, Chapter 9]). However, in road traffic, several light sources (in particular the own headlights) illuminate the scene, so visual impairment is dominated by glare and diffusion instead of by contrast reduction effects. Therefore, the definition of visibility at night has to be reconsidered. Although the atmospheric parameter  $K$  still plays a central role in this context, other parameters have also to be taken into account (*cf.* *e.g.* [Gal2010a]). Further literature on visibility assessment at nighttime can be found in 6.1.2.

### 3.2 Measuring Devices

At present, the most common measuring devices for the extinction coefficient (and in turn the meteorological visibility) can be divided into three classes. One class is the *transmissometers*. Based on the ratio between the emitted and received light, transmissometers measure the mean extinction coefficient between a transmitter and a photodetector over a defined distance. By using modulated light which can be separated from other light sources, such as the sun, this approach can be used for daytime as well as for nighttime measurements. Sub-types of transmissometers are single-ended and double-ended devices in which the light is attenuated over a path of single or double length compared to the transmissometer's extension, respectively.

The second common class of measuring devices is based on scattering analysis. These devices include *visibility lidars* which compute  $K$  from the time signal of the backscattered laser beam. More simple forward and backward *scatterometers* analyze the amount of light scattered into a certain angular range. To estimate the extinction coefficient from the scattered amount of light, the absorption in fog has to be neglected, which is a common assumption in natural fog (*cf.* Sec. 4.3 and (4.11)) but may lead to systematic errors in the case of smog.

A less commonly used class of measuring devices is *nephelometers*. Based on particle analy-

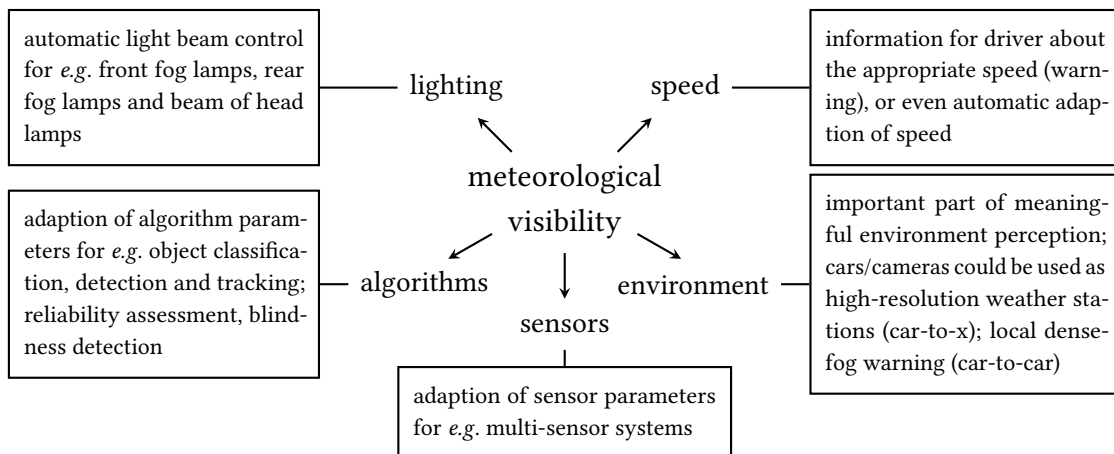


Figure 3.2: applications for image-based visibility estimation

sis within a small fog volume the drop-size distribution can be estimated. Based on this, all atmospheric parameters can be derived with the help of classical scattering theory (*cf.* Chap. 4).

A more comprehensive discussion on the different types of visibility-measuring devices can be found in [Org2008, Chapter 9] or, alternatively, in [Klo2008, 4.7.3]. One should note that these established measuring devices suffer from drawbacks in the automotive context (*cf.* [Pom1997, 1]). That is especially why image-based visibility estimation, which this work focuses on, has to be considered as a promising new class of visibility-measuring devices.

### 3.3 Applications of Image-Based Visibility Estimation

Visibility estimation usually is not the main objective of (automotive) camera systems. Nonetheless, there are diverse applications which justify a closer look at image-based measuring methods for meteorological visibility (*cf.* Fig. 3.2). This work will concentrate on the automotive context with focus on multi-purpose driver assistance cameras. It seems to be a promising option to extend existing embedded camera systems by adding the functionality of visibility measurement. Algorithms designed for this scenario should make use of as much available information as possible to reduce the additional hardware effort to a minimum.

**Light.** One of the classes of driver assistance functions that benefits most from a visibility estimation can be found in the automatic light control. For instance, according to the German road traffic regulations (namely StVO §17, Abs. 3) the headlamps have to be switched to dipped beam (or a comparable combination of two front fog lamps and marker lamps) in situations of low visibility due to dense fog (even in the daytime). Front fog lamps are only allowed to be turned on in these situations. Moreover, they explicitly state that rear fog lamps are only permitted to be turned on in cases of a meteorological visibility below 50 m. All these regulations could be automatically complied with based on  $d_{\text{met}}$  estimations provided by a driver assistance camera system.

**Speed.** Another category of driver assistance functions which can be enhanced by visibility information is speed-related warning or adaption systems. Based on a comparison of the speed-

dependent stopping distance and the current meteorological visibility, the driver could be informed about the appropriate speed. Moreover, it could be possible to introduce intelligent speed adaption (ISA) and intelligent inter-vehicle distance management systems based on the current visibility conditions (*cf.* [Hau2007a, 3.2.2]). This is supported by several regulations, such as the German road traffic regulations (namely StVO §3, Abs. 1) according to which the vehicle's speed has to be adapted to the environmental visibility conditions. For instance, in case of a meteorological visibility below 50 m, the speed has to be reduced to a maximum of 50 km h<sup>-1</sup>. Similar to the case of automatic light control, an automated fulfillment of these regulations requires a quantitative instead of a qualitative visibility assessment. Further information on the development of visibility-related speed warning and adaption systems can be found in [Gal2010b] and [Gal2013].

In addition, the measurement of the visibility conditions could also be interesting for static cameras, such as traffic surveillance cameras, in order to adjust the speed limit and inform drivers with variable-message signs.

**Computer Vision Algorithms.** The most diverse category of applications for visibility estimation is algorithmic enhancements within already existing functions for video-based driver assistance systems.

On the one hand, only the information about reduced visibility enables affected computer vision algorithms to adapt to the current visibility conditions. An example can be found in algorithms for generic or specific object detection. For instance, a meteorological visibility of  $d_{\text{met}} = 40$  m makes it implausible to find an object at 80 m and makes it an unreliable piece of information that no objects at  $> 100$  m have been found. Many algorithms should thus incorporate the visibility information to realize an appropriate degradation concept and implement checks for the plausibility and reliability of their results. In the worst case this could lead to a temporary shut-down of specific functions or the complete driver assistance system, which is supplemented by a warning to the driver.

In addition, some algorithms could even adapt their operation in order to optimize the performance in foggy scenarios. The tracking of road signs, for example, could be attuned to color and luminance changes with respect to the distance through multiple observation. The thresholds for edge detection could also be adapted to the distance-dependent loss of contrast, which in turn could lead to an enhanced lane marking or obstacle detection (*cf. e.g.* [Hau2007d] or [Hau2007a, 3]).

Moreover, the meteorological visibility can be the basis for novel algorithmic approaches to various computer vision tasks, such as free-space detection (*cf. e.g.* [Hau2009] and [Hau2014]) or model-based contrast restoration (*cf. e.g.* [Hau2007c], [Hau2008b], [Hau2010] and [Tar2010]). Even outside the driver assistance context, meteorological visibility can be applied for, *e.g.*, passive ranging of flying objects (*cf. e.g.* [Bar2012]).

**Sensor Data Fusion.** Whenever multiple different sensor systems are involved, visibility estimation can optimize the process of sensor data fusion. This is based on the observation that the attenuation of fog and other atmospheric aerosols substantially differs for the different bands of the electromagnetic spectrum. While fog significantly decreases the range of cameras, it has almost no impact on the operation of radar or ultrasonic sensors (*cf. e.g.* [Li2014]). As parts of the environment are perceived redundantly, one could thus temporarily reduce the confidence of environmental information provided by camera systems in fog.

In combination with other sensor systems, the estimation of  $d_{\text{met}}$  might even be extendable to

create a more comprehensive adverse weather detection (*cf.* [Fol2014]). Based on the observation of different atmospheric attenuation values for different sensor spectra, it could be possible to draw inference about the causative weather phenomenon.

**Environment.** Meteorological visibility in general is an important part of environmental modeling. The increasingly large number of stationary and mobile camera systems could be used as a network of low-cost sensors. As an application in the Internet of Things, this data in combination with data from weather stations could be used by the weather services to derive a more precise, dense and real-time visibility map. This so-called fog nowcasting can, for example, be useful for local fog warning with the help of broadcasting or variable-message signs. In addition, a dense fog map can be used for further research on fog formation and dissipation.



# Chapter 4

---

## Light Scattering by Fog Droplets

### Contents

---

4.1	Fog . . . . .	23
4.2	Light . . . . .	25
4.3	Scattering and Absorption . . . . .	26
4.3.1	Mie Theory: Scattering by Spherical Particles . . . . .	27
4.3.2	Volume Scattering . . . . .	32

---

To understand the visibility impairments caused by fog, it is helpful to take a look into the microscopic scattering and absorption processes first. In this chapter, the most relevant facts about fog, light and their interaction on the microscopic scale are brought together.

### 4.1 Fog

Fog is a visibility-reducing atmospheric aerosol that consists of numerous tiny water droplets or ice crystals dispersed and floating in the air close to the Earth's surface. In meteorology, fog requires a visibility below 1 km at an observation height of 1.8 m above ground (*cf. e.g.* [Klo2008, 4.4.2]). For visibilities above 1 km these aerosols are called *mist* or *haze*. Fog occurs in a wide variety of conditions. In 1928, Willett [Wil1928] started to categorize fog according to the various physical processes and environmental conditions causing its formation. This contributed to the establishment of a number of fog types which were modified and adapted to new findings over the years (*cf.* [Gul2007]).

In road transport, the most relevant types of fog are those that frequently occur over land. Two of them are the well-studied categories of radiation and advection fog. In both cases, fog occurs due to condensation where air of almost 100 % relative humidity is cooled down below its dew point leading to supersaturation. As a consequence, the surplus water starts to attach to condensation nuclei (usually  $< 1 \mu\text{m}$ , *cf. e.g.* [Kur1951]) resulting in tiny fog droplets reaching tens of micrometers in size (*cf.* [Gul2007, 3.1]).

Radiation fog is caused by nocturnal cooling of the ground and the saturated humid air close to it. Here, the dominant process of heat exchange is thermal radiation. The radiation fog slowly grows upwards which requires a low wind speed during its formation. Good conditions can often be found during autumn and early winter in valleys with high soil moisture. In contrast to the calm conditions required for radiation fog, advection fog forms when a body of warm and saturated

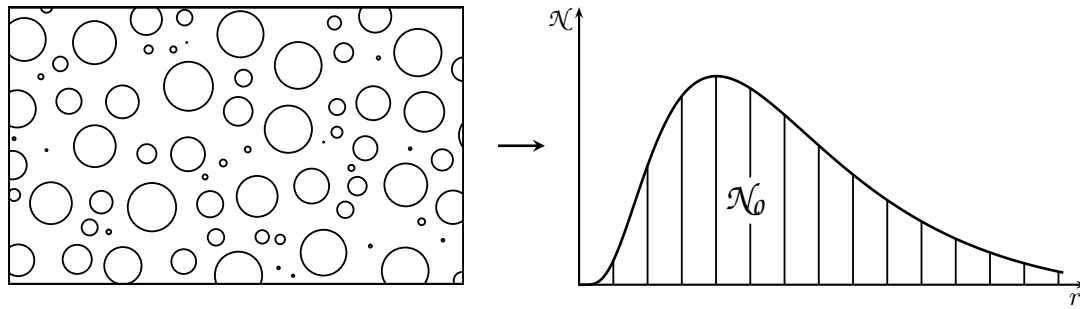


Figure 4.1: example for a drop-size distribution

humid air is pushed over a cold landmass such as a windward mountainside especially in coastal regions. The warm air is suddenly cooled down leading to condensation and a comparatively quick formation of fog. Besides these two, there are many different circumstances that can lead to various types of fog, most of which are also based on condensation. A more comprehensive review on them can be found in [Gul2007, Section 2].

In contrast to fog droplets emerging from condensation, aerosols composed of ice crystals occur due to sublimation of water vapor in extremely cold environments (usually at  $< -30^\circ\text{C}$ , *cf.* [Gul2007]). Since this so-called ice fog is a difficult-to-study and rare phenomenon, fog particles are assumed to consist of only liquid water droplets in this work. Nevertheless, since the exact knowledge about the microscopic scattering and absorption processes in fog is only of minor importance for visibility estimation, the algorithms proposed in this work can basically be applied to ice fog as well.

Due to their small size, the surface tension causes fog droplets to be almost perfectly spherically shaped. The sphere radii of typical droplets vary from 1 to  $50\ \mu\text{m}$  (*cf. e.g.* [Eld1961], [Klo2008, 4.4.2] or [Gul2007, 2]). In order to exactly describe an aerosol such as fog, actually all radii and positions of droplets would have to be taken into account. However, since one can expect fog to contain a sufficiently large number of particles per unit volume, it is reasonable to work with the distribution of particle radii instead of considering each particle individually. This so-called *drop-size distribution* is represented by a measurable and integrable function  $\mathcal{N} : \mathbb{R}_{\geq 0} \rightarrow \mathbb{R}_{\geq 0}$  (*cf.* Fig. 4.1), which has to be interpreted as the probability distribution of the radius scaled by the *total number of particles per unit volume*

$$\mathcal{N}_0 = \int_0^\infty \mathcal{N}(r) dr.$$

A typical magnitude of fog particles per  $\text{m}^3$  is  $10^9$  (*cf. e.g.* Remark 8 on page 35). The exact distribution of fog droplets in an aerosol significantly depends on the type of fog. Drop-size distributions have been studied many times and modeled in various ways (*cf. e.g.* [Gra2012] or [Dei1964]). One commonly used analytical model for  $\mathcal{N}$  is the log-normal density function, which is further discussed in Remark 8 on page 35.

## 4.2 Light

Light is one of the most fascinating aspects of physics. In this work, the term *light* denotes the visible part of the electromagnetic radiation which approximately covers a spectrum of 380 to 780 nm. Whenever light interacts with surfaces, particles or other objects it changes its properties by scattering (including reflection and refraction) and absorption. In this way light serves for humans as one of the most important sources of environmental information. It is the basis for any visual perception.

From the early optical experiments of Alhazen in the 11<sup>th</sup> Century to today's studies on quantum entanglement, metamaterials and ultrashort pulse lasers, scientists continue to improve the understanding of the nature of light and its interaction with matter. Only the most relevant facts regarding light are outlined in this section. The interested reader is referred to one of the more comprehensive overviews such as given in [Bey2012] or [Ber2004].

**Properties of Light.** In general, the properties of visible light do not differ from the rest of the electromagnetic spectrum with the exception of being perceivable by the human eye. Therefore, the physical properties discussed in the following are valid for all types of electromagnetic radiation.

Light is a wave in the electromagnetic field which can be described by Maxwell's equations. This wave always has a certain polarization, which describes the orientation of the underlying vector field oscillations with respect to the wave's direction of propagation. In vacuum the speed of light has the exact value of  $299\,792.458\text{ km s}^{-1}$  which is the maximum speed of information propagation in the universe.

According to quantum mechanics, the energy of the wave is quantized meaning that it is always an integral multiple of its energy quantum  $hf$ , which is the product of the Planck constant  $h$  and the wave's frequency  $f$ . The particle that represents an electromagnetic oscillation with the energy of  $hf$  is called *photon*. This particle is used to describe the interaction between matter and the electromagnetic field in terms of their energy: Photons are absorbed or emitted by matter.

Scattering can be regarded as the quasi-simultaneous absorption and emission of a photon with the traveling direction of the exiting particle randomly deviating from the incident particle's direction. The stochastic distribution of the angle between the exit and the incident direction is determined by the diffraction pattern that results from the light wave interfering with itself in the presence of the scattering object. Scattering of light at small spherical water droplets plays a fundamental role in this work, which is why Sec. 4.3 explains this phenomenon in more detail.

**Radiance and Luminance.** To make light measurable and in turn assessable for any investigation, meaningful physical quantities have to be defined. For the general electromagnetic spectrum the associated subject area is called *radiometry* and for visible light *photometry*. Each photometric quantity is derived from a corresponding radiometric quantity by a weighting with the *spectral luminous efficacy*  $\eta : \mathbb{R}_{>0} \rightarrow \mathbb{R}_{\geq 0}$  representing the sensitivity of a human eye w.r.t. to the wavelengths (*cf. e.g. (4.1)*).  $\eta$  has the unit  $\text{lm W}^{-1}$  and is integrable over  $\mathbb{R}_{>0}$ . Since usual cameras mainly capture the visible part of the electromagnetic spectrum, this work also uses the photometric quantities in the context of cameras.

In the center of considerations for the theory of radiative transfer and light transport through fog are the radiometric and photometric quantities *radiance* and *luminance*. The *spectral radiance* represents the radiation's power density function w.r.t. the solid angle, the projected area and the

wavelengths of emitted or received light. To compute, for example, the energy received from light one not only has to specify a certain time interval, but also the considered solid angle, the range of wavelengths, and the affected area and its positioning relative to the incident light. Its unit is given by  $\text{W sr}^{-1} \text{m}^{-2} \text{nm}^{-1}$ . In contrast to this, the term radiance (without “spectral”) describes the spectral radiance integrated over the wavelength. In this case the unit is  $\text{W sr}^{-1} \text{m}^{-2}$ .

The spectral radiance can be expressed as a locally integrable function

$$(\mathbb{R}^3, \mathbb{S}^2, \mathbb{R}, \mathbb{R}_{>0}) \ni (x, \sigma, t, \lambda) \mapsto L_e(x, \sigma, t, \lambda) \in \mathbb{R}_{\geq 0},$$

where  $x$  denotes the position,  $\sigma$  the direction,  $t$  the time and  $\lambda$  the wavelength. The luminance  $L_v$  can be derived from  $L_e$  as

$$L_v(x, \sigma, t) = \int_0^\infty L_e(x, \sigma, t, \lambda) \eta(\lambda) d\lambda, \quad (4.1)$$

with a unit  $\text{lm sr}^{-1} \text{m}^{-2} = \text{cd m}^{-2}$ . In the case of a non-scattering and non-absorbing atmosphere, the apparent luminance of an object does not depend on the observer’s distance towards the object. It corresponds to the non-quantitative term *brightness*, which describes the physiological sensation light causes in a human observer.

Another radiometric term relevant in the context of image taking, is given by the *spectral irradiance* which describes the overall power of light incident on a surface element. It can be derived from the spectral radiance as

$$E(x, t, \lambda) := \int_{\Omega(x)} L_e(x, \sigma, t, \lambda) \langle \sigma, \nu(x) \rangle d\sigma$$

where  $\nu(x)$  denotes the (inner) unit normal vector of the surface in  $x$ , and  $\Omega(x) \subset \mathbb{S}^2$  is the set of all incident light directions at  $x$ . Assuming sufficiently small pixels and a linearly operating sensor the intensity values in images can be considered as linear representation of the incident irradiance weighted by the camera’s spectral quantum efficacy (*cf.* (6.6)). Further assuming a pinhole camera model makes it plausible to consider  $E$  to be proportional to  $L_e$  (*cf.* (6.7)). This leads to an overall camera model where object luminances and image intensities are linearly related. This is discussed in more detail in Sec. 6.4.

Since furthermore the radiative transfer theory holds true for  $L_e$  as well as for  $L_v$ , it is reasonable to use only one symbol  $L$  in the following. A more comprehensive discussion on radiometry and photometry can be found in *e.g.* [Bey2012, 4].

### 4.3 Scattering and Absorption

The propagation of electromagnetic radiation is affected by any change of the medium’s optical density. In particular, in atmospheric aerosols each particle embodies an optical discontinuity which causes light to be scattered and absorbed. This process can be described by Maxwell’s equations, which for arbitrarily shaped particles leads to a not explicitly solvable problem. Based on a reformulation in spherical coordinates, Mie, at the beginning of the 20<sup>th</sup> Century, presented solutions to Maxwell’s equations in the special case of spherical particles (*cf.* [Mie1908]). These equations are applicable to the case of fog droplets, as they are approximately spherical due to

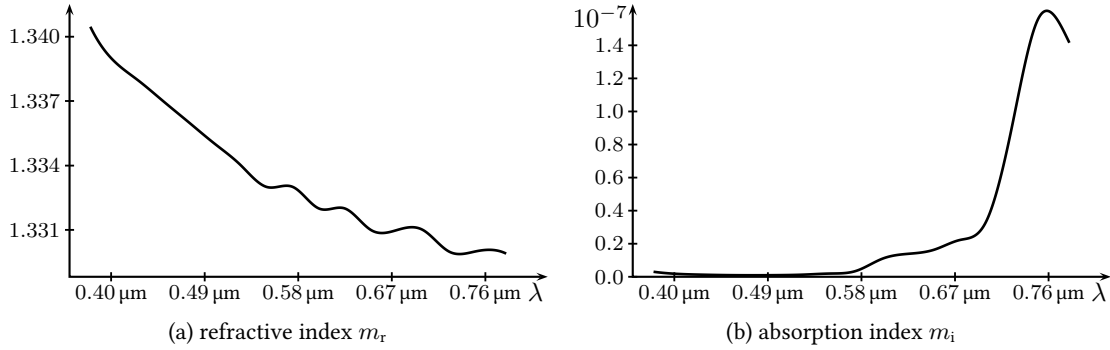


Figure 4.2: complex refractive index of water (for standard atmosphere and 25 °C) in the visible electromagnetic spectrum according to [Hal1973]

their surface tension and small size. This allows for a precise description of the scattering and absorption processes at single fog droplets (*cf.* 4.3.1). Combining this microscopic scattering behavior with drop-size distributions is a reliable way to model the macroscopic scattering behavior of fog volumes (*cf.* 4.3.2).

In this section, the terms and concepts of *Mie scattering* are addressed in a brief overview. More comprehensive works on Mie's theory can be found in *e.g.* [Str1941], [Hul1957], [Boh1998], [Mis2002b] and [Gra2004]. A discourse on non-spherical particles (such as ice crystals) can, for instance, be found in [Mis2002b, Chapter 10].

### 4.3.1 Mie Theory: Scattering by Spherical Particles

According to Mie, the scattering and absorption at a single spherical particle is determined by basically two parameters. One of them is the dimensionless *size parameter*

$$x = \frac{2\pi r}{\lambda}, \quad (4.2)$$

where  $r$  denotes the sphere's radius and  $\lambda$  the electromagnetic wavelength. The second dimensionless parameter is given by the *complex refractive index* of the particle

$$m = m_r + im_i \quad (\text{sometimes } m = m_r - im_i)$$

which is composed of the (lossless) refractive index  $m_r$ , describing the ratio of speed of light in vacuum to the speed of light in the particle's medium; and the *absorption index*  $m_i$ , indicating the amount of absorption loss of light that propagates through the particle. Since fog droplets almost completely consist of water, its optical properties play an important role for studies on scattering in fog. The complex refractive index data of water (for the standard atmosphere and 25 °C), which is used for Mie computations in this work, is taken from [Hal1973] (*cf.* Fig. 4.2).

Depending on the size parameter  $x$  and the complex refractive index  $m$  the complex-valued *Mie*

expansion coefficients  $(a_n)_{n \in \mathbb{N}}$  and  $(b_n)_{n \in \mathbb{N}}$  can be introduced as

$$a_n(x, m) = \frac{m\Psi_n(mx)\Psi'_n(x) - \Psi_n(x)\Psi'_n(mx)}{m\Psi_n(mx)\xi'_n(x) - \xi_n(x)\Psi'_n(mx)}$$

$$b_n(x, m) = \frac{\Psi_n(mx)\Psi'_n(x) - m\Psi_n(x)\Psi'_n(mx)}{\Psi_n(mx)\xi'_n(x) - m\xi_n(x)\Psi'_n(mx)},$$

where  $\Psi_n$  and  $\xi_n$ ,  $n \in \mathbb{N}$ , denote the so-called *Ricatti-Bessel functions* (cf. [Boh1998, (4.56), (4.57)]). The coefficients  $a_n$  and  $b_n$  are helpful in formulating the relation between the set of generating solutions of the scalar wave equation (given in terms of Bessel functions, Legendre polynomials and trigonometric functions, cf. [Boh1998, (4.15), (4.16)]) and the far-field boundary problem representing the scattering process. The boundary conditions are determined by  $x$  and  $m$ .

Some properties of this far field are of particular interest for this work. On the one hand, these are quantities that determine the amount of scattering, absorption and the overall extinction: the *extinction efficiency*

$$Q_{\text{ext}}(x, m) = \frac{2}{x^2} \sum_{n=1}^{\infty} (2n+1) \Re(a_n(x, m) + b_n(x, m)),$$

the *scattering efficiency*

$$Q_{\text{sca}}(x, m) = \frac{2}{x^2} \sum_{n=1}^{\infty} (2n+1) (|a_n(x, m)|^2 + |b_n(x, m)|^2)$$

and the *absorption efficiency*

$$Q_{\text{abs}}(x, m) = Q_{\text{ext}}(x, m) - Q_{\text{sca}}(x, m). \quad (4.3)$$

They describe the dimensionless ratio of the *effective cross section* to the *geometrical cross section* of the particle regarding extinction, scattering and absorption. Due to the very small absorption index  $m_i < 1.6 \cdot 10^{-7}$  of water for the spectrum of visible light (cf. Fig. 4.2), the absorption efficiency for fog droplets is also close to 0 (cf. Fig. 4.3).

On the other hand, the full far-field solution can be expressed in terms of two complex-valued scattering functions

$$[-1, 1] \ni \mu \mapsto S_1(\mu; x, m) = \sum_{n=1}^{\infty} \frac{2n+1}{n(n+1)} (a_n(x, m)\pi_n(\mu) + b_n(x, m)\tau_n(\mu)),$$

$$[-1, 1] \ni \mu \mapsto S_2(\mu; x, m) = \sum_{n=1}^{\infty} \frac{2n+1}{n(n+1)} (b_n(x, m)\pi_n(\mu) + a_n(x, m)\tau_n(\mu)),$$

where  $\mu$  denotes the cosine of the scattering angle, and  $\pi_n$  and  $\tau_n$  the angular eigenfunctions basically given by Legendre polynomials (cf. e.g. [Wis1980] or [Gra2004]). Based on  $S_1$  and  $S_2$ , the *scattering phase function* of a single particle scattering process in the case of unpolarized light

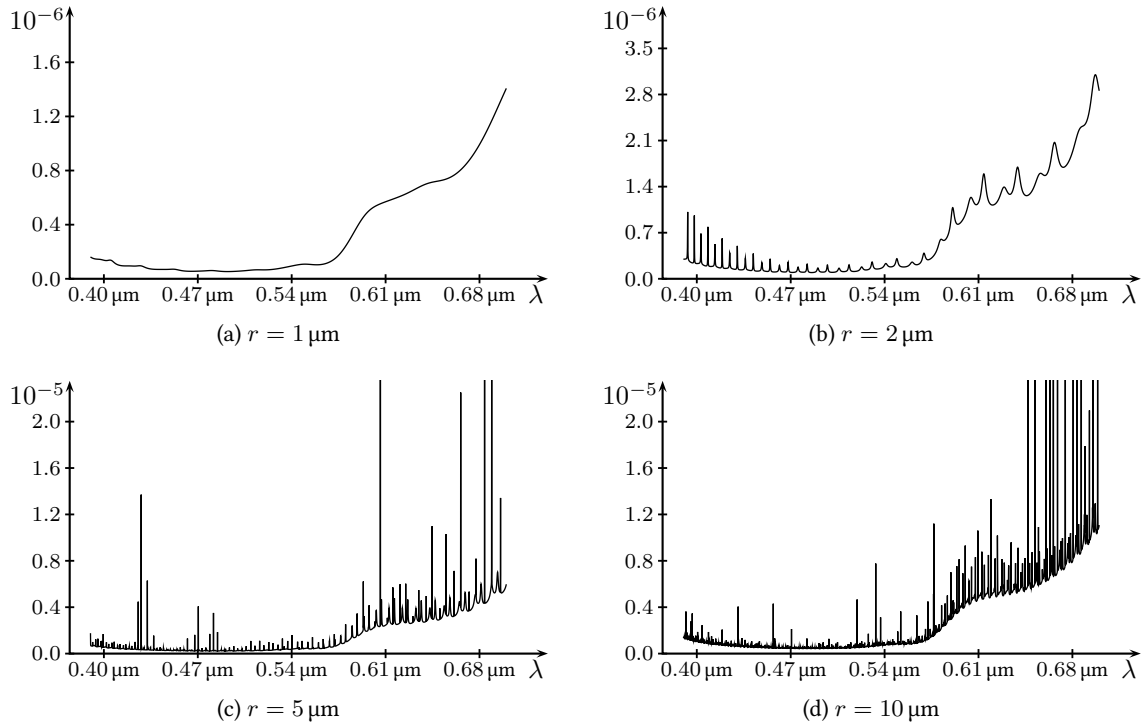


Figure 4.3: Absorption efficiency  $Q_{\text{abs}}$  w.r.t.  $\lambda \in [0.38 \mu\text{m}, 0.78 \mu\text{m}]$  (visible light), depicted for different drop radii  $r$ .



Figure 4.4: Scattering phase function  $\psi : \mathbb{S}^2 \times \mathbb{S}^2 \rightarrow \mathbb{R}_{\geq 0}$ . The directions in  $\mathbb{S}^2$  has always to be interpreted as pointing in the direction of propagation of the interacting light.

can be computed as

$$(\sigma, \omega) \mapsto \psi^{\text{Mie}}(\sigma, \omega; x, m) = \frac{1}{4\pi} \frac{2}{x^2 Q_{\text{sca}}(x, m)} \left( |S_1(\langle \sigma, \omega \rangle; x, m)|^2 + |S_2(\langle \sigma, \omega \rangle; x, m)|^2 \right).$$

$S_1$  and  $S_2$  can also be used to describe the full far-field scattering behavior including further effects such as polarization (*cf. e.g.* [Mis2002b] or [Boh1998, Chapter 13]). These effects will be ignored in this work.

In general, a scattering phase function  $\psi : \mathbb{S}^2 \times \mathbb{S}^2 \rightarrow \mathbb{R}_{\geq 0}$  describes the angular distribution of scattered luminances with exit direction  $\omega \in \mathbb{S}^2$  for light incident with a direction  $\sigma \in \mathbb{S}^2$  (*cf.* Fig. 4.4); the cosine of the scattering angle is given by  $\mu = \langle \sigma, \omega \rangle$ . Since any  $\psi$  represents a scattering

probability distribution on the sphere, it satisfies a normalization property

$$\forall \sigma \in \mathbb{S}^2 : \int_{\mathbb{S}^2} \psi(\sigma, \omega) dS(\omega) = 1. \quad (4.4)$$

All phase functions discussed in this work satisfy the assumption that no world direction is preferred, which apart from volumetric and stochastic arguments (randomly orientated particles) directly follows from the spherical shape of fog droplets. Hence, all phase functions can be written in terms of  $\langle \sigma, \omega \rangle$ , which is denoted by the hat notation

$$\hat{\psi} : [-1, 1] \rightarrow [0, \infty), \quad \hat{\psi}(\langle \sigma, \omega \rangle) = \psi(\sigma, \omega).$$

In particular, the symmetry of  $\langle \cdot, \cdot \rangle$  also applies to  $\psi(\cdot, \cdot)$ , i.e.  $\psi(\sigma, \omega) = \psi(\omega, \sigma)$ .

One characterizing parameter for scattering phase functions is given by the *asymmetry parameter*  $g$ . It is defined as the average of  $\psi$  weighted by the cosine of the scattering angle (cf. [Boh1998, Sections 4.3 and 4.5]), i.e. for any  $\sigma \in \mathbb{S}^2$  one has

$$g = \int_{\mathbb{S}^2} \psi(\sigma, \omega) \langle \sigma, \omega \rangle dS(\omega).$$

It describes the relation between forward and backward scattering and varies between  $g = -1$  (perfect backward scattering) and  $g = 1$  (perfect forward scattering). In the case of single spherical particles with phase function  $\psi^{\text{Mie}}(\cdot, \cdot; x, m)$  it can be computed as

$$g(x, m) = \frac{4}{x^2 Q_{\text{sca}}(x, m)} \left[ \sum_{n=1}^{\infty} \frac{n(n+2)}{n+1} \Re \left( a_n(x, m) \overline{a_{n+1}(x, m)} + b_n(x, m) \overline{b_{n+1}(x, m)} \right) + \sum_{n=1}^{\infty} \frac{n(n+2)}{n+1} \Re \left( a_n(x, m) \overline{b_n(x, m)} \right) \right].$$

For numerical simulations of Mie scattering, the implementation of [Mat2002] is used in this work. To illustrate the terms introduced in this section, some exemplary results are provided in Fig. 4.3, Fig. 4.5, Fig. 4.6 and Fig. 4.7. As expected, the absorption efficiency for typical fog droplets of radius  $r \in [1 \mu\text{m}, 50 \mu\text{m}]$  and visible light of wavelength  $\lambda \in [0.38 \mu\text{m}, 0.78 \mu\text{m}]$  turns out to be negligibly small compared to the scattering efficiency (cf. Fig. 4.3 and Fig. 4.5). Furthermore, Fig. 4.5 reveals why fog usually appears gray, which is because  $Q_{\text{sca}}$  has no systematic bias towards short or long wavelengths in the case of fog droplets and visible light. This justifies why in this work the scattering behavior in fog is assumed to be wavelength-independent in the context of visibility assessment (cf. 5.1.2). Similarly, Fig. 4.6 shows that the asymmetry parameter  $g$  can be assumed to be independent of  $\lambda$  and mainly lies in the interval  $[0.8, 0.9]$ .

**Remark 6** (Further Notes on the Size Parameter).

- (a) As the Mie theory is derived from Maxwell's equations, it covers all scales of scattering. For very small particles compared to the wavelength ( $x \ll 1$ ) it approaches to the theory of Rayleigh scattering, and for very large spheres ( $x \gg 10$ ) it agrees with classical ray optics (cf. [Mis2002b]). It represents an important tool for the studies of many scattering effects.

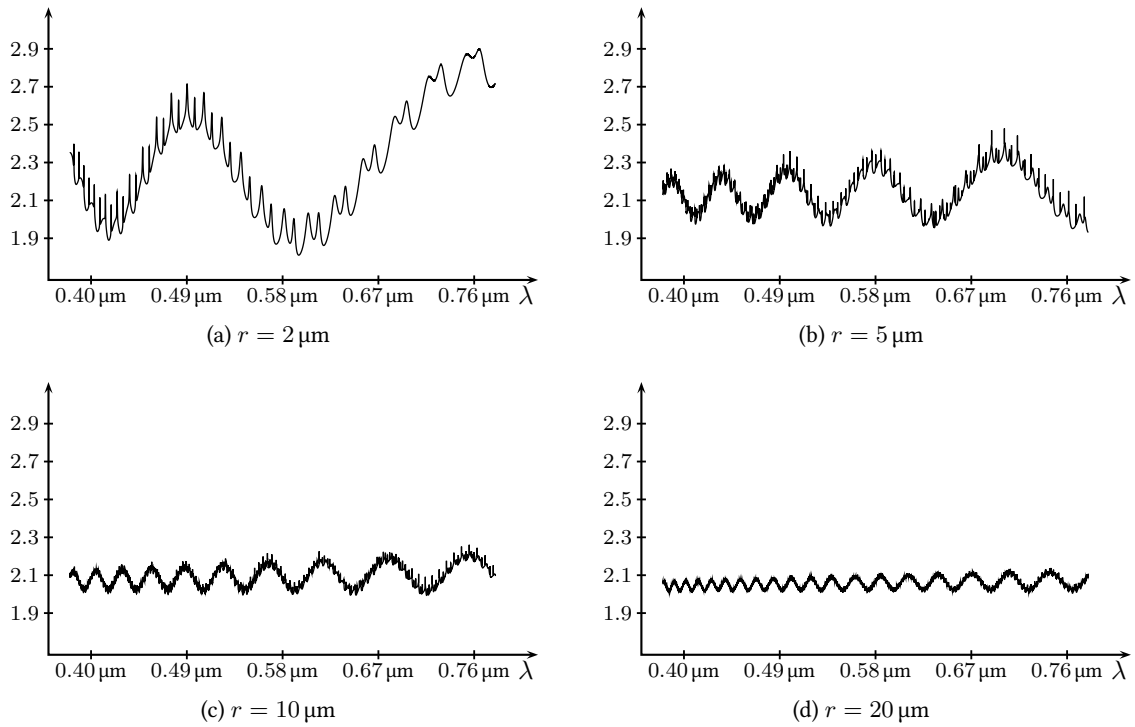


Figure 4.5: Scattering efficiency  $Q_{\text{sca}}$  w.r.t.  $\lambda \in [0.38 \mu\text{m}, 0.78 \mu\text{m}]$  (visible light), depicted for different drop radii  $r$ .

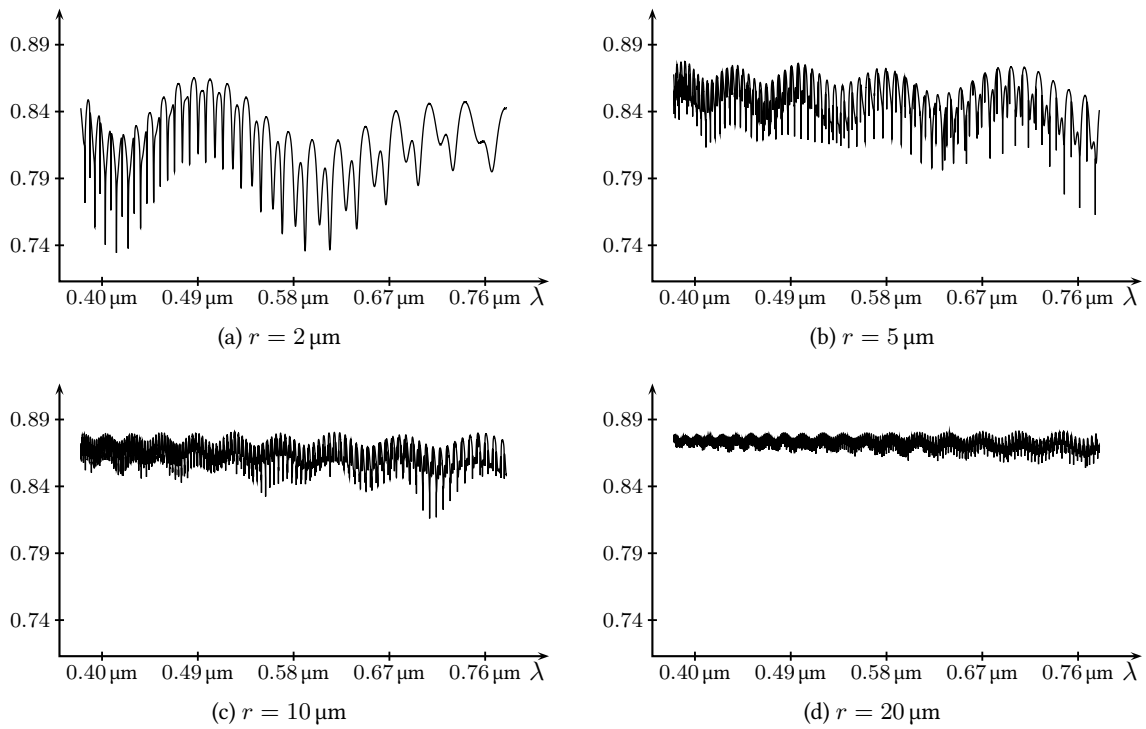


Figure 4.6: Asymmetry parameter  $g$  w.r.t.  $\lambda \in [0.38 \mu\text{m}, 0.78 \mu\text{m}]$  (visible light), depicted for different drop radii  $r$ .

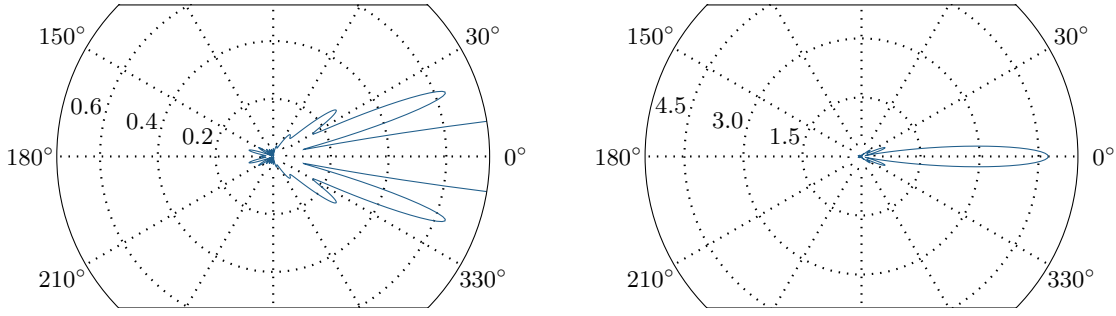


Figure 4.7: Example of a scattering phase function  $\psi^{\text{Mie}}$  of a single spherical particle of radius  $r = 1 \mu\text{m}$  and incident light of wavelength  $\lambda = 0.55 \mu\text{m}$ , i.e.  $x \approx 11.42$ .

- (b) Scattering depends on the size parameter  $x = 2\pi r/\lambda$ , where water droplets in fog range from  $1 \mu\text{m}$  to  $50 \mu\text{m}$  (cf. Sec. 4.1) and the visible spectrum ranges from  $0.38 \mu\text{m}$  to  $0.78 \mu\text{m}$  (cf. Sec. 4.2). Therefore, as a rule of thumb, the size parameter in fog lies in the range of

$$x \in \left[ \frac{2\pi \cdot 1 \mu\text{m}}{0.78 \mu\text{m}}, \frac{2\pi \cdot 50 \mu\text{m}}{0.38 \mu\text{m}} \right] \approx [8, 800].$$

### 4.3.2 Volume Scattering

The volume scattering behavior of fog can be described as the sum of individual droplet scattering processes (cf. Fig. 4.8). As introduced in Sec. 4.1, the radius dependent number of particles is represented by the drop-size distribution  $\mathcal{N} : \mathbb{R}_{\geq 0} \rightarrow \mathbb{R}_{\geq 0}$  and the total number of particles per unit volume  $\mathcal{N}_0$ . Basically all volumetric scattering properties can be derived from the combination of single particle scattering with a given drop-size distribution (cf. e.g. [Mid1952] or [Gra2012]).

Among them, the most relevant quantities in the study of visibility conditions are the extinction, scattering and absorption coefficients as introduced in Sec. 1.2 and Chap. 3. They can be derived as integral over the effective cross sections  $\pi r^2 Q_{\{\text{ext}, \text{sca}, \text{abs}\}}$  weighted by the present drop-size distribution

$$\begin{aligned} K(\lambda) &= \int_0^\infty \pi r^2 Q_{\text{ext}}(x(r, \lambda), m(\lambda)) \mathcal{N}(r) dr, \\ K_s(\lambda) &= \int_0^\infty \pi r^2 Q_{\text{sca}}(x(r, \lambda), m(\lambda)) \mathcal{N}(r) dr, \\ K_a(\lambda) &= \int_0^\infty \pi r^2 Q_{\text{abs}}(x(r, \lambda), m(\lambda)) \mathcal{N}(r) dr, \end{aligned} \quad (4.5)$$

where  $x(r, \lambda)$  denotes the Mie size parameter as defined in (4.2). The average scattering phase function can be obtained from

$$\psi(\sigma, \omega; \lambda) = \frac{1}{K_s(\lambda)} \int_0^\infty \pi r^2 Q_{\text{sca}}(x(r, \lambda), m(\lambda)) \psi^{\text{Mie}}(\sigma, \omega; x(r, \lambda), m(\lambda)) \mathcal{N}(r) dr, \quad (4.6)$$

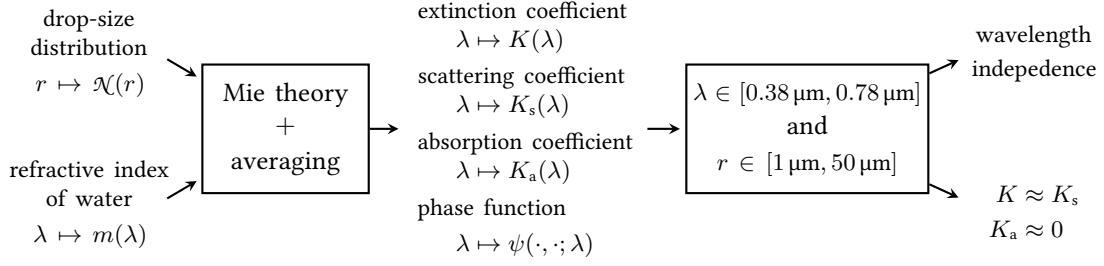


Figure 4.8: From combining a fog's drop-size distribution with the scattering behavior of single spherical water droplets (described by Mie theory), one obtains the relevant volumetric scattering properties of fog, such as the extinction coefficient  $K$  and the scattering phase function  $\psi$ .

and the corresponding average asymmetry parameter can be computed as

$$g(\lambda) = \frac{1}{K_s(\lambda)} \int_0^\infty \pi r^2 Q_{\text{sca}}(x(r, \lambda), m(\lambda)) g(x(r, \lambda), m(\lambda)) \mathcal{N}(r) dr. \quad (4.7)$$

From (4.3), (4.5) and the linearity of integration it directly follows that

$$K = K_s + K_a. \quad (4.8)$$

Furthermore, assuming  $\mathcal{N}$  to be a fog drop-size distribution one can expect the droplets to be mainly distributed in the interval  $[1 \mu\text{m}, 50 \mu\text{m}]$  (cf. Sec. 4.1), *i.e.*

$$\int_{1 \mu\text{m}}^{50 \mu\text{m}} \mathcal{N}(r) dr \approx \mathcal{N}_0. \quad (4.9)$$

Combining (4.9) with (4.5), (4.7) and the numerical results for single spherical droplets (cf. Fig. 4.3, Fig. 4.5, and Fig. 4.6) leads to the reasonable assumptions of wavelength independence for  $K$ ,  $K_s$ ,  $K_a$  and  $g$ , namely

$$\lambda \mapsto (K(\lambda), K_s(\lambda), K_a(\lambda), g(\lambda)) \approx \text{const.}, \quad (4.10)$$

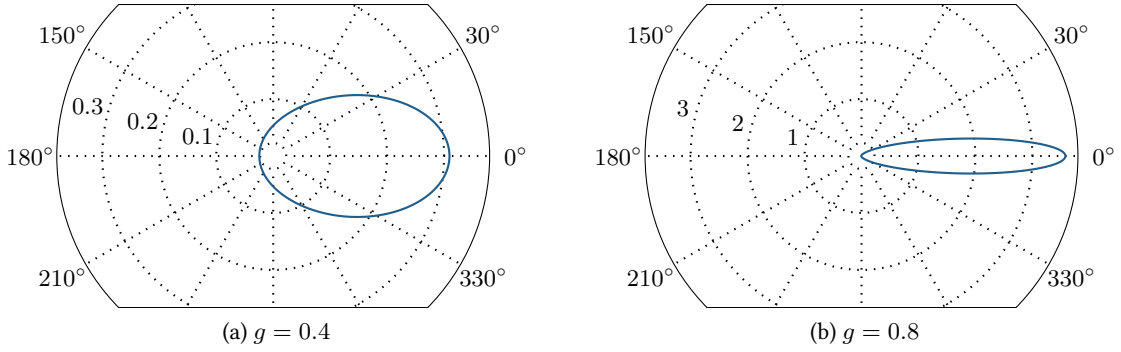
and the negligibility of absorption compared to scattering

$$K_a/K_s \approx 0 \quad (4.11)$$

as long as  $\lambda \in [0.38 \mu\text{m}, 0.78 \mu\text{m}]$ .

In contrast, the average scattering phase function requires a more careful consideration. Without further assumptions it a-priori can neither be treated as wavelength independent nor as being of a simple shape. Fortunately, the high complexity and the large number of lobes as well as the wavelength dependency of the single particle scattering (cf. Fig. 4.7) is reduced a lot by the radius-related averaging in (4.6). In order to efficiently model volumetric scattering processes, analytical approximations for the average phase functions have to be found.

One of the oldest and most popular examples is given by the so-called *Henry-Greenstein phase*

Figure 4.9: Henyey-Greenstein phase functions for different asymmetry parameters  $g$ 

function (cf. [Hen1941] and Fig. 4.9) which reduces the whole complexity to just the asymmetry parameter  $g$ . It is given as

$$\psi^{\text{HG}}(\sigma, \mu; g) = \frac{1}{4\pi} \frac{1 - g^2}{(1 - 2g\langle\sigma, \mu\rangle + g^2)^{3/2}}. \quad (4.12)$$

Although it is a quite simplifying model it provides many beneficial analytical properties and performs well for many practical applications (cf. e.g. [Ish1978], [Dav2006, 2.3], or [Jar2008, 63–66]). The discussion on more realistic phase functions can be found in e.g. [Liu1994] or [Shi2006]. However these models are often not only more complex or equipped with additional parameters, but also suffer from a limited applicability and thus require additional a-priori knowledge on the actual drop-size distribution. In order to develop highly performant, stable and generally applicable parameter estimation algorithms, these are important arguments for the use of the simple Henyey-Greenstein phase function. This is why phase functions are mostly modeled by (4.12) in this work.

In context of the Henyey-Greenstein phase function, the asymmetry parameter is also often restricted to the interval  $[0, 1]$  and referred to as *forward scattering parameter* (cf. e.g. [Met2007], [Len2013]). Moreover, in the context of parameter estimation it is helpful to see that for scattering of visible light in fog the average asymmetry parameter lies in  $[0.8, 0.9]$  (cf. e.g. [Met2007]); this agrees with the results for single fog droplets (cf. Fig. 4.6).

**Remark 7** (Normalization of Average Phase Function). As one would expect, the averaging in (4.5), (4.6) and (4.7) is well normalized, i.e. the normalization is preserved by the volumetric averaging. As an example, this is shown for the average phase function in this remark. For reasons of clarity the wavelength  $\lambda$  is hidden in this calculation. Without further explanation the Fubini-Tonelli theorem is applied for a change of the integration order:

$$\begin{aligned} \int_{\mathbb{S}^2} \psi(\sigma, \omega) dS(\omega) &= \int_{\mathbb{S}^2} \left[ \frac{1}{K_s} \int_0^\infty \pi r^2 Q_{\text{sca}}(x(r), m) \psi^{\text{Mie}}(\sigma, \omega; x(r), m) \mathcal{N}(r) dr \right] dS(\omega) \\ &= \frac{1}{K_s} \int_0^\infty \pi r^2 Q_{\text{sca}}(x(r), m) \underbrace{\int_{\mathbb{S}^2} \psi^{\text{Mie}}(\sigma, \omega; x(r), m) dS(\omega) \mathcal{N}(r) dr}_{=1} \end{aligned}$$

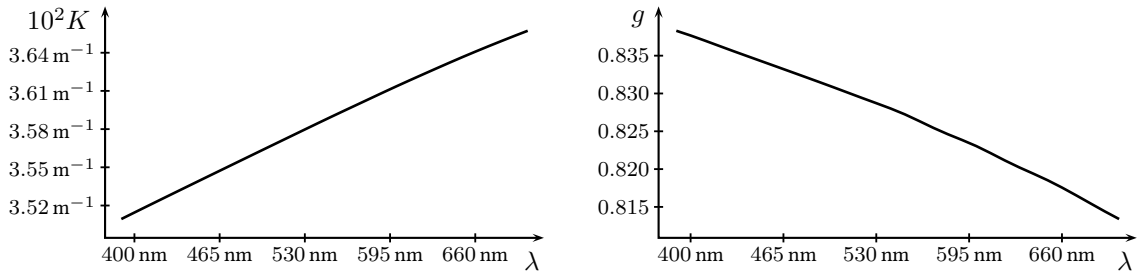


Figure 4.10: average extinction coefficient and asymmetry parameters according to Mie theory and a log-normal drop-size distribution with parameters given in (4.14)

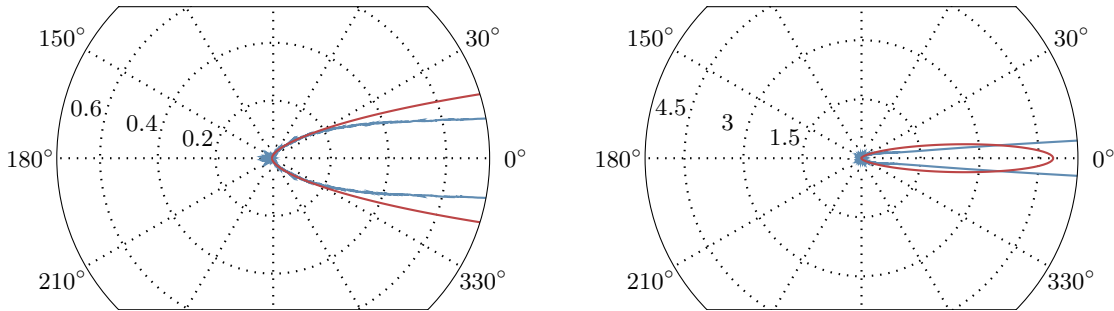


Figure 4.11: Henyey-Greenstein phase function (red) compared to the log-normal average Mie phase function (light blue). Setting:  $\lambda = 0.55 \mu\text{m}$ ,  $g = 0.8272$ , log-normal drop-size distribution parameters given in (4.14).

$$= \frac{1}{K_s} \int_0^\infty \pi r^2 Q_{\text{sca}}(x(r), m) \mathcal{N}(r) dr = 1.$$

**Remark 8** (Volume Scattering for a Log-Normal Drop-Size Distribution). The most common model for drop-size distributions in fog is given by a log-normal density function (*cf. e.g.* [Gra2004], [Tai2008, 2.2] or [Gra2012, 1.3, 1.4]). It can be written as

$$\mathcal{N}^{\text{ln}}(r; r_m, S) = \frac{\mathcal{N}_0}{\sqrt{2\pi r \log(S)}} \exp\left(-\frac{1}{2} \left(\frac{\log(r/r_m)}{\log(S)}\right)^2\right), \quad (4.13)$$

where  $r_m$  and  $S$  denote the model parameters. Based on this drop-size distribution and the single particle scattering theory of Mie, it is possible to compute  $K$  and  $g$ . Moreover, compared to the Henyey-Greenstein phase function from (4.12), it is possible to derive a more realistic but also more complex average phase function from the combination of (4.6) and (4.13).

As an illustration, the resulting  $K$ ,  $g$  and  $\psi$  are plotted in Fig. 4.10 and Fig. 4.11 based on the log-normal parameters

$$\mathcal{N}_0 = 10^9 \text{ m}^{-3}, \quad S = 1.4241, \quad r_m = 2 \mu\text{m}. \quad (4.14)$$

These parameters are motivated by log-normal fits to real drop-size distributions in fog (*cf.* [Tai2008, 2.2]).

As one can see, Fig. 4.10 supports the assumption of the wavelength independence of  $K$  and  $g$  (cf. (4.10)). The reached range of  $K \in [0.0351 \text{ m}^{-1}, 0.0366 \text{ m}^{-1}]$  corresponds to just a small variation in  $d_{\text{met}}$  between 81.91 m and 85.36 m. However, this figure also reveals a slightly increased extinction for longer wavelengths. This explains why objects through fog appear not only brighter and blurrier, but also slightly blue tinted.

Fig. 4.11 reveals that the Henyey-Greenstein phase function only coarsely represents a realistic phase function, which especially becomes clear at the maximum peak at  $0^\circ$ . The differences in the backscattering behavior can be expected to be compensated by an averaging over different wavelengths. In Sec. 8.6, an experiment is provided which addresses the impact of the deviation depicted in Fig. 4.11 on one of the visibility estimation algorithms from this work.

**Remark 9** (Liquid Water Content). Another property of fog volumes which is sometimes used in the context of visibility assessment is the *liquid water content*

$$\text{LWC} = \rho_{\text{W}} \frac{4\pi}{3} \int_0^\infty r^3 \mathcal{N}(r) dr, \quad (4.15)$$

where  $\rho_{\text{W}}$  denotes the density of water (cf. e.g. [Tra1901], [Tom1976] or [Kha2012]). As one might expect, the meteorological visibility and the the liquid water content are not independent of each other. However, this relation essentially depends on many other conditions such as the specific  $\mathcal{N}$  (cf. e.g. [Kam1952]). In contrast to the extinction coefficient, the liquid water content is not directly motivated by visual considerations and thus the worse choice as visibility parameter in fog.

# Chapter 5

---

## Radiative Transfer Theory

### Contents

---

5.1	Radiative Transfer Equation . . . . .	37
5.1.1	General Radiative Transfer Equation . . . . .	38
5.1.2	RTE for Light Transport through Fog . . . . .	38
5.2	Radiative Boundary Problem . . . . .	40
5.3	Integral Formulation . . . . .	42
5.3.1	RTE on the Line of Sight . . . . .	42
5.3.2	Equivalence of Classical and Integral Formulation . . . . .	44
5.4	Derived Models for Light Transport through Fog . . . . .	47
5.4.1	Koschmieder's Model (for Horizontal Vision) . . . . .	48
5.4.2	Higher-Order Approximate Models . . . . .	49
5.5	Plane-Parallel Atmosphere . . . . .	55

---

The propagation of radiation through participating media is described by the *radiative transfer theory* (RTT). In contrast to the microscopic view of the scattering theory in Chap. 4, it addresses the interaction of light and fog on a macroscopic scale.

The core of the RTT is the *radiative transfer equation* (RTE), which is formulated in terms of spatially and directionally varying radiances (*cf.* 5.1.2). Equipped with proper boundary conditions this integro-differential equation yields a global problem description, called the *radiative boundary problem* (*cf.* Sec. 5.2). Finding approximate solutions to the integral formulation of the radiative boundary problems (*cf.* Sec. 5.3) allows for the derivation of fog models (*cf.* Sec. 5.4). They are the foundation for the visibility estimation algorithms proposed in Part III of this work.

### 5.1 Radiative Transfer Equation

The radiative transfer equation (RTE) is the fundamental equation which governs the propagation of radiation in scattering, absorbing and emitting media. It can be applied to various domains such as astrophysics, for the description of radiation received from celestial bodies and nebulae (*cf.* *e.g.* [Ryb1979]); climatology, to model scattering processes in different layers of the atmosphere (*cf.* *e.g.* [Kos2014]); and tomography-based imaging, which can be applied in medicine (*cf.* *e.g.* [Web2002]), material science (*cf.* *e.g.* [Mid2009]), geophysics (*cf.* *e.g.* [Nol1987]), oceanography

(*cf. e.g.* [Mun1988]) or industry (*cf. e.g.* [Fli1999]). Among many other applications, it is also applied in computer graphics in form of the rendering equation (*cf. e.g.* [Kaj1986]); in analytical chemistry in form of the Beer-Lambert law (*cf. e.g.* [Har2000, Chap. 10]); in geoscience for remote sensing (*cf. e.g.* [Hal1995]); and in the investigation of many high-temperature and plasma-physical processes, such as the combustion of organic fuels (*cf. e.g.* [Vis1987]) or in nuclear science to describe explosion or fusion processes (*cf.* [Alb2002]).

Motivated by these various applications many publications address the radiative transfer equation. One of the most important contributions was published by Chandrasekhar in 1960 (*cf.* [Cha1960]). Modern overviews can be found in *e.g.* [Mih1984], [Per2001] or [Shaz2003, Chap. 9].

### 5.1.1 General Radiative Transfer Equation

The RTE is most commonly derived by applying the law of conservation of energy to elementary volumes on a beam's propagation path (*cf. e.g.* [Cha1960] or [Shaz2003, Chap. 9]). Alternatively, the time-independent form of the RTE can also be derived from statistical electromagnetics and Maxwell's equations (*cf. e.g.* [Mis2002a]).

The *general radiative transfer equations* is an integro-differential equation which considers scattering, absorbing and emitting media. The (spectral) radiance function  $L$  depends on the position  $x \in \mathbb{R}^3$ , the direction  $\sigma \in \mathbb{S}^2$ , the time  $t \in \mathbb{R}$  and the wavelength  $\lambda \in \mathbb{R}_{>0}$ :

$$\begin{aligned} \frac{1}{c} \frac{\partial L}{\partial t}(x, \sigma, t, \lambda) + \langle \nabla_x L(x, \sigma, t, \lambda), \sigma \rangle = & -K(x, t, \lambda)L(x, \sigma, t, \lambda) + S(x, \sigma, t, \lambda) \\ & + K_s(x, t, \lambda) \int_{\mathbb{S}^2} L(x, \omega, t, \lambda) \psi(\sigma, \omega, t, \lambda) dS(\omega), \end{aligned} \quad (5.1)$$

where  $K$ ,  $K_s$  and  $\psi$  denote the extinction coefficient, the scattering coefficient and the scattering phase function as introduced in Chap. 4. Additionally,  $c$  denotes the speed of light, and  $S$  the emission source term.

The radiative transfer equation states that a beam of radiation loses energy in time and location through out-scattering and absorption, and gains energy from emitting sources in the medium and scattered radiation which is directed towards the beam. The out-scattering and absorption are proportional to the strength of the beam and the medium's extinction coefficient  $K$  (sum of absorption and scattering coefficient, *cf.* (4.8)). The in-scattering is proportional to the scattering coefficient  $K_s$  and the amount of ambient radiation weighted with the medium's phase function  $\psi$ .

Although it is of no importance for this work, it is interesting to note that other light properties such as polarization can also be covered by the RTE. In this case it becomes a vector equation, where  $L$  is replaced by the stokes vector and  $\psi$  by the so-called phase matrix (*cf. e.g.* [Cha1960, 36] or [Zha2012]).

### 5.1.2 RTE for Light Transport through Fog

The radiative transfer equation as it is provided in (5.1) is a rather general description of macroscopic interactions of radiation and media. In the case of light transport through fog, many reasonable assumptions help to simplify the equation in order to make it applicable for practical

purposes.

The first assumption is that of an equilibrium scenario, *i.e.* observations are assumed to be locally stationary in time. Furthermore, according to Sec. 4.3 and (4.10), the scattering and absorption process is assumed to be independent of the wavelength (*cf.* Fig. 4.5). Another assumption is that of an emission-free atmosphere, which is obviously (approximately) true for visible light.

This leads to the stationary, monochromatic and emission-free version of the RTE:

$$\langle \nabla_x L(x, \sigma), \sigma \rangle = -K(x)L(x, \sigma) + K_s(x) \int_{\mathbb{S}^2} L(x, \omega) \psi(\sigma, \omega) dS(\omega). \quad (5.2)$$

One should note that, in the literature, the in-scattered light is often referred to as “emission” and the in-scattering integral as “source integral”, even in the emission-free case (*cf.* *e.g.* [Cha1960, I.4]).

The version of the RTE that is primarily used to derive fog models in this work is obtained from additionally assuming a homogeneous ( $K \equiv \text{const.}$  and  $K_s \equiv \text{const.}$ ) and absorption-free ( $K = K_s$ ) atmosphere. This leads to the homogeneous, absorption-free, emission-free, monochromatic and stationary version of the RTE:

$$\langle \nabla_x L(x, \sigma), \sigma \rangle = -KL(x, \sigma) + K \int_{\mathbb{S}^2} L(x, \omega) \psi(\sigma, \omega) dS(\omega). \quad (5.3)$$

According to 4.3.1, in particular Fig. 4.2 and (4.11), the assumption  $K = K_s$  is approximately true for small fog droplets which mainly consist of water. One should note that emission-free and absorption-free atmospheres are often referred to as “perfect scattering atmospheres”, while emission-free atmospheres are referred to simply as “scattering atmospheres” (*cf.* [Cha1960, I.4]).

The assumption of a homogeneous atmosphere is the only serious restriction in the derivation of (5.3). Unfortunately, without homogeneity the estimation of fog density becomes a full 3-dimensional tomography problem which is very difficult to solve. Moreover, in many cases of dense fog atmospheric homogeneity is a reasonable assumption.

**Remark 10** (On the Surface Integral). To explicitly evaluate the surface integral on  $\mathbb{S}^2$ , one has to apply a parametrization of the sphere. In this work, the sphere’s standard parametrization  $\Phi$  is primarily used (*cf.* Fig. 5.1), which is well-known and combines some advantageous properties:

$$\Phi : [0, 2\pi) \times [0, \pi] \rightarrow \mathbb{S}^2, \quad (\varphi, \theta) \mapsto \begin{pmatrix} \sin(\theta) \cos(\varphi) \\ \sin(\theta) \sin(\varphi) \\ \cos(\theta) \end{pmatrix}. \quad (5.4)$$

Here, the north pole is given by  $\Phi(0, 0) = (0, 0, 1)^T$ , and the size of the surface element is determined by

$$\begin{aligned} \left| \frac{\partial \Phi}{\partial \varphi} \times \frac{\partial \Phi}{\partial \theta} \right| &= \left| \begin{pmatrix} -\sin(\theta) \sin(\varphi) \\ \sin(\theta) \cos(\varphi) \\ 0 \end{pmatrix} \times \begin{pmatrix} \cos(\theta) \cos(\varphi) \\ \cos(\theta) \sin(\varphi) \\ -\sin(\theta) \end{pmatrix} \right| = \left| \begin{pmatrix} -\sin^2(\theta) \cos(\varphi) \\ -\sin^2(\theta) \sin(\varphi) \\ -\sin(\theta) \cos(\theta) \end{pmatrix} \right| \\ &= \sqrt{\sin^4(\theta) + \sin^2(\theta) \cos^2(\theta)} \stackrel{\theta \in [0, \pi]}{=} \sin(\theta). \end{aligned}$$

This allows for the rewriting of the surface integral from (5.3) as

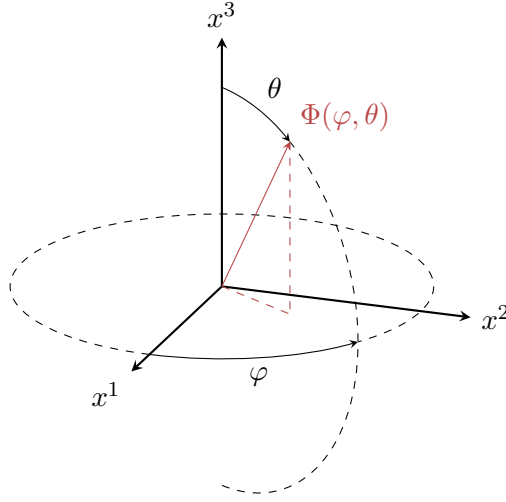


Figure 5.1: Standard parametrization of the sphere.

$$\int_{\mathbb{S}^2} L(x, \omega) \psi(\sigma, \omega) dS(\omega) = \int_0^{2\pi} \int_0^\pi L(x, \Phi(\varphi, \theta)) \psi(\sigma, \Phi(\varphi, \theta)) \sin(\theta) d\varphi d\theta. \quad (5.5)$$

## 5.2 Radiative Boundary Problem

To derive models for the light distribution in foggy environments one not only has to describe the light transport through the atmosphere, but also to specify what happens at the boundaries of the system. Considering both allows for a well stated problem and proper discussions regarding existence, uniqueness, regularity, constructability and other properties of the problem's solutions (cf. Theorem 2 on page 50). From this, approximate fog models can be constructed as well as evaluated.

One can think of different ways to describe the boundary behavior in foggy environments (cf. e.g. [Shaz2003, 9.6] or [Has1994]). Very common are Dirichlet-like boundary conditions, where the radiances at all boundary points and all inward pointing directions are explicitly prescribed.

To rigorously formulate the boundary conditions, let  $\Omega \subset \mathbb{R}^3$  be a domain (open and connected) which represents the environment. For each boundary position  $x \in \partial\Omega$  one can define the *set of boundary directions in  $x$  w.r.t.  $\Omega$* :

$$\mathbb{S}_{x,\Omega}^2 := \{ \omega \in \mathbb{S}^2 : \exists \varepsilon > 0, \text{ s.t. } x + \varepsilon\omega \in \Omega, \forall 0 < \hat{\varepsilon} < \varepsilon \}, \quad (5.6)$$

which represents the set of inward pointing directions at  $x$  (cf. Fig. 5.2). Additionally, the following abbreviatory notation shall denote the *directional boundary of  $\Omega \times \mathbb{S}^2$* :

$$\partial\Omega \times \mathbb{S}_{x,\Omega}^2 := \{ (x, \omega) \in \partial\Omega \times \mathbb{S}^2 : \omega \in \mathbb{S}_{x,\Omega}^2 \}. \quad (5.7)$$

Finally, given a boundary function  $L_b : \partial\Omega \times \mathbb{S}_{x,\Omega}^2 \rightarrow \mathbb{R}_{\geq 0}$ , the Dirichlet-like boundary condition

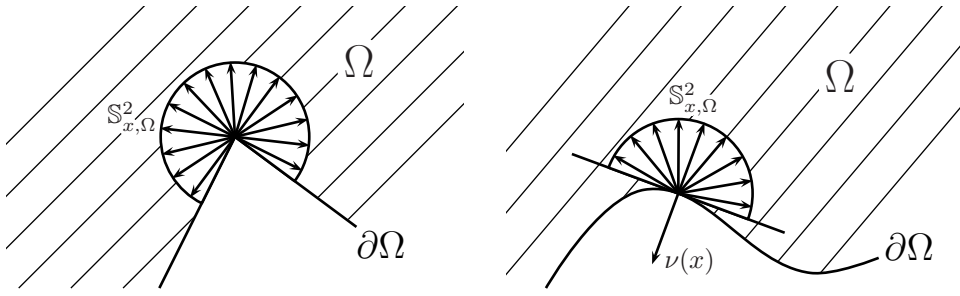


Figure 5.2: Boundary directions in a non-smooth and in a locally  $C^1$ -smooth case.

can be defined for each boundary position and each boundary direction:

$$\forall x \in \partial\Omega, \forall \sigma \in \mathbb{S}_{x,\Omega}^2 : L(x, \sigma) = L_b(x, \sigma). \quad (5.8)$$

Combining (5.3) and (5.8) yields the radiative boundary problem:

**Definition 1** (Classical Formulation of the Radiative Boundary Problem). Let  $\Omega \subset \mathbb{R}^3$  be a domain and  $L_b : \partial\Omega \times \mathbb{S}_{x,\Omega}^2 \rightarrow \mathbb{R}_{\geq 0}$  be a boundary function. Then, the radiative boundary problem can be written as:

Find an  $L \in C^1(\Omega \times \mathbb{S}^2; \mathbb{R}_{\geq 0})$ , s.t. it solves the radiative transfer equation and the Dirichlet-like boundary condition:

$$\begin{aligned} \langle \nabla_x L(x, \sigma), \sigma \rangle &= -KL(x, \sigma) + K \int_{\mathbb{S}^2} L(x, \omega) \psi(\sigma, \omega) dS(\omega), & \text{in } \Omega \times \mathbb{S}^2, \\ L(x, \sigma) &= L_b(x, \sigma), & \text{on } \partial\Omega \times \mathbb{S}_{x,\Omega}^2. \end{aligned} \quad (5.9)$$

**Remark 11** (Drawback of the Classical Formulation Regarding Smoothness). The classical formulation of the radiative boundary problem unfortunately excludes very natural situations like depth edges and non-smooth boundary values, which could cause the solution to be non-smooth or not even continuous. This is one motivation to reformulate the classical boundary problem (5.9) to an integral equation (cf. Definition 2 on page 45). This integral formulation allows for a more general boundary setting and turns out to be equivalent to the classical formulation under uniform boundedness and sufficiently smooth data (cf. Theorem 1 on page 47).

**Remark 12** (Boundary Directions for  $C^1$ -Smooth Boundaries). If  $\partial\Omega$  is  $C^1$ -smooth in some local environment of  $x \in \partial\Omega$ , the set of boundary directions in  $x$  equals an inner hemisphere bordered by the affine tangent plane in  $x$ , i.e.

$$\mathbb{S}_{x,\Omega}^2 = \{ \omega \in \mathbb{S}^2 : \langle \omega, \nu(x) \rangle < 0 \},$$

where  $\nu(x)$  denotes the exterior normal of the boundary in  $x$  (cf. Fig. 5.2).

In the case of a globally  $C^1$ -smooth boundary, one could come up with an idea to avoid the confusing notation  $\partial\Omega \times \mathbb{S}_{x,\Omega}^2$ . To achieve this, one could define  $L_b : \partial\Omega \times \mathbb{S}_{\geq 0}^2$  and combine it with  $L$  with the help of a rotation mapping  $R_{-\nu(x)}$  that rotates the upper hemisphere to the inner hemisphere at each  $x \in \partial\Omega$ . As shown in Sec. B.3 in the Appendix it is possible to find such rotations for each  $x$ . However, in cases where  $\Omega$  is topologically equivalent to a sphere, it is impossible to construct a mapping  $x \mapsto R_{-\nu(x)}$  which is additionally smooth. This would be a desirable property, since it would allow for the regularity in  $L_b$  to directly transfer to the boundary

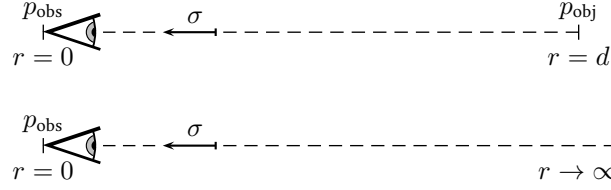


Figure 5.3: Line of sight. Top: between object point  $p_{\text{obj}} \in \mathbb{R}^3$  and observer at  $p_{\text{obs}} \in \mathbb{R}^3$  ( $d < \infty$ ). Bottom: ray not hitting any objects ( $d = \infty$ ).

regularity of  $L$ . Taking a closer look reveals the problem that all approaches collapse at least at one direction. This can be explained by the hairy ball theorem [Eis1979], which is famously stated as “you can’t comb a hairy ball flat without creating a cowlick”. The existence of a continuous mapping  $\mathbb{S}^2 \ni x \mapsto R_{-\nu(x)}$  would imply the sphere’s tangent vector field  $x \mapsto R_{-\nu(x)}(0, 1, 0)^T$  to be continuous and never vanishing, a contradiction to the hairy ball theorem.

### 5.3 Integral Formulation

For visibility estimation based on camera systems, it is essential to understand radiance values which are measured at given pixel positions. Each pixel position on the image plane corresponds to a 3-dimensional world direction (determined by the camera parameters and the camera’s position in the world). Therefore, it is quite natural to interpret the light arriving at one pixel as the sum of scattering and emitting events on the corresponding line of sight.

At the beginning of this section, the 3-dimensional radiative boundary problem is restricted to a specific line of sight. Assuming the in-scattered light to be given, this leads to an ordinary differential equation which can be solved but still depends on the in-scattering function. Applying this to all observation points and all observation directions leads to an overall integral formulation of the radiative boundary problem. It turns out that the classical and the integral formulation are equivalent (*cf.* 5.3.2).

The integral formulation plays an important role in this work. It is not only possible to derive all necessary models for the visibility estimation algorithms presented in Chapters 7, 8 and 9 from this formulation, but also to answer interesting analytical questions on *e.g.* the existence, uniqueness or regularity of solutions of (5.9). It is even possible to provide a method for the iterative construction of solutions, which is of particular practical interest.

#### 5.3.1 RTE on the Line of Sight

An observer’s *line of sight*

$$\mathbb{R} \ni r \mapsto p(r) := p_{\text{obs}} - r\sigma \in \mathbb{R}^3,$$

is determined by an observer position  $p_{\text{obs}} \in \mathbb{R}^3$  and a direction  $\sigma = (\sigma^1, \sigma^2, \sigma^3)^T \in \mathbb{S}^2$  pointing towards the observer (*cf.* Fig. 5.3). In the finite case, the ray of observation hits an object surface of intrinsic radiance  $L_0$  at a distance  $d$ . Assuming the in-scattered radiance to be given as  $L_{\text{in}}$ , the radiative transfer equation (5.2) transforms along the line of sight to an ordinary differential

equation in  $r$  (cf. Remark 13(a)). Together, one obtains an initial value problem:

$$\frac{d\tilde{L}}{dr}(r) = K(r)\tilde{L}(r) - K_s(r) \int_{\mathbb{S}^2} L_{\text{in}}(p(r), \omega) \psi(\sigma, \omega) dS(\omega), \quad (5.10)$$

$$\tilde{L}(d) = L_0, \quad (5.11)$$

with an abbreviatory notation  $\tilde{L}(\cdot) := L(p(\cdot), \sigma)$ ,  $K(\cdot) := K(p(\cdot))$  and  $K_s(\cdot) := K_s(p(\cdot))$ . Since (5.10) is a first-order linear ODE, standard techniques (variation of constants, cf. Sec. B.2 in the Appendix) can be applied to obtain a solution to (5.10, 5.11):

$$\tilde{L}(r) = L_0 e^{-\int_r^d K(\tau) d\tau} + \int_r^d K_s(s) e^{-\int_r^s K(\tau) d\tau} \int_{\mathbb{S}^2} L_{\text{in}}(p(s), \omega) \psi(\sigma, \omega) dS(\omega) ds.$$

In particular, the radiance reaching the observer from direction  $\sigma$  is given by

$$L(p_{\text{obs}}, \sigma) = L_0 e^{-\int_0^d K(\tau) d\tau} + \int_0^d K_s(s) e^{-\int_0^s K(\tau) d\tau} \int_{\mathbb{S}^2} L_{\text{in}}(p(s), \omega) \psi(\sigma, \omega) dS(\omega) ds. \quad (5.12)$$

In the infinite case, the observation ray never hits an object and the boundary distance is given by  $d = \infty$ . For any  $\hat{d} \in \mathbb{R}$  and  $L_0 = \tilde{L}(\hat{d}) = L_{\text{in}}(p(\hat{d}), \sigma)$  one can formulate (5.10, 5.11) analogous to the finite case which leads to

$$L(p_{\text{obs}}, \sigma) = \underbrace{\tilde{L}(\hat{d}) e^{-\int_0^{\hat{d}} K(\tau) d\tau}}_{=: T_1(\hat{d})} + \underbrace{\int_0^{\hat{d}} K_s(s) e^{-\int_0^s K(\tau) d\tau} \int_{\mathbb{S}^2} L_{\text{in}}(p(s), \omega) \psi(\sigma, \omega) dS(\omega) ds}_{=: T_2(\hat{d})},$$

where  $T_1$  and  $T_2$  denote abbreviatory notations for the first and the second term of this statement, respectively. Since  $T_1 \geq 0$  and  $T_2$  is monotonously increasing in  $\hat{d}$  while  $T_1 + T_2$  remains constant, the limits  $\lim_{\hat{d} \rightarrow \infty} T_1(\hat{d})$  and  $\lim_{\hat{d} \rightarrow \infty} T_2(\hat{d})$  exist. Hence, it is

$$L(p_{\text{obs}}, \sigma) = \lim_{\hat{d} \rightarrow \infty} T_1(\hat{d}) + \int_0^{\infty} K_s(s) e^{-\int_0^s K(\tau) d\tau} \int_{\mathbb{S}^2} L_{\text{in}}(p(s), \omega) \psi(\sigma, \omega) dS(\omega) ds.$$

In the case  $K \equiv 0$  it is

$$\lim_{\hat{d} \rightarrow \infty} T_1(\hat{d}) = \lim_{\hat{d} \rightarrow \infty} L_{\text{in}}(p(\hat{d}), \sigma)$$

which can be treated as 0 from a physical point of view. Assuming  $K$  to be constant and  $> 0$  and  $L_{\text{in}}$  to be uniformly bounded on the line of sight, *i.e.*

$$\exists C > 0, \forall s > 0 : \quad L_{\text{in}}(p(s), \sigma) \leq C,$$

the first term becomes 0 as well

$$\lim_{\hat{d} \rightarrow \infty} T_1(\hat{d}) = \lim_{\hat{d} \rightarrow \infty} \tilde{L}(\hat{d}) e^{-\int_0^{\hat{d}} K(\tau) d\tau} = \lim_{\hat{d} \rightarrow \infty} \underbrace{\tilde{L}(\hat{d})}_{\leq C} \underbrace{e^{-K\hat{d}}}_{\rightarrow 0} = 0.$$

Therefore, in the infinite, homogeneous and bounded case the observed radiance is given by

$$L(p_{\text{obs}}, \sigma) = \int_0^\infty K_s(s) e^{-\int_0^s K(\tau) d\tau} \int_{\mathbb{S}^2} L_{\text{in}}(p(s), \omega) \psi(\sigma, \omega) dS(\omega) ds. \quad (5.13)$$

**Remark 13** (On the Derivation of the Line-of-Sight Formulation).

- (a) The line of sight  $p$  is parametrized by the arc length (due to  $|\sigma| = 1$ ). This is why the directional derivative in the PDE (5.2) transforms to the  $r$ -derivative in the ODE (5.10) without any scaling factors:

$$\frac{d\tilde{L}}{dr}(r) = \frac{d}{dr} [L(p(r), \sigma)] = \langle \nabla_x L(p(r), \sigma), \dot{p}(r) \rangle = -\langle \nabla_x L(p(r), \sigma), \sigma \rangle$$

- (b) Given an object point  $p_{\text{obj}}$  and an observer point  $p_{\text{obs}}$  one can obtain  $\sigma$  and  $d$  from

$$d = |p_{\text{obs}} - p_{\text{obj}}|, \quad \sigma = \frac{p_{\text{obs}} - p_{\text{obj}}}{d}.$$

- (c) In order to derive (5.13), assumptions on  $L_{\text{in}}$  and  $K$  are introduced. While the requirement on  $K$  to be constant can easily be softened, the uniform boundedness of  $L_{\text{in}}$  seems to be unavoidable. From a theoretical point of view there might exist classical solutions which increase with an exponential rate to infinity. These solutions are of no importance for practical considerations. Therefore, the uniform boundedness requirement for the integral formulation in 5.3.2 is a very natural one, it does not exclude any relevant solutions of the radiative boundary problem.
- (d) The statement (5.12) is a well-known formulation to describe the transmission of light over a distance  $d$  ([Cha1960, Sec. I.7, I.8]). In some cases the complex radiative boundary problem can be explicitly solved based on (5.12) and further assumptions on  $L_{\text{in}}$ , e.g. for scattering-free, absorbing and emitting media, for transparent media, or for a constant in-scattering function (cf. e.g. [Sha2003, Chap. 9] or 5.4.1).

### 5.3.2 Equivalence of Classical and Integral Formulation

The classical formulation of the radiative boundary problem (5.9) is given by an integro-differential PDE and a Dirichlet-like boundary condition. In this section an integral formulation of (5.9) is introduced which is derived from the line-of-sight formulation in 5.3.1 applied to each  $(x, \sigma) \in \Omega \times \mathbb{S}^2$ . In contrast to (5.9) it does not require  $C^1$ -smoothness of the boundary or solutions and can be written as one compact and pure integral equation. It turns out that under certain assumptions the classical and the integral formulation of the radiative boundary problem are equivalent. Based on this equivalence, in the following light transport through fog can legitimately be discussed with the help of the more natural integral instead of the classical formulation.

To derive the integral formulation, the boundary condition has to be taken into account. This can be done by introducing functions  $L_0 : \Omega \times \mathbb{S}^2 \rightarrow \mathbb{R}_{\geq 0}$  and  $d : \Omega \times \mathbb{S}^2 \rightarrow \mathbb{R}_{\geq 0} \cup \{\infty\}$  which denote the intrinsic luminance of the border and the distance to the border for each observer position and direction in  $\Omega \times \mathbb{S}^2$  respectively. These functions encode the boundary condition of the radiative boundary problem, which can be incorporated to the integral formulation in this way. To clarify the difference between  $L_b$  and  $L_0$ , one can think of  $L_0$  as radiance function

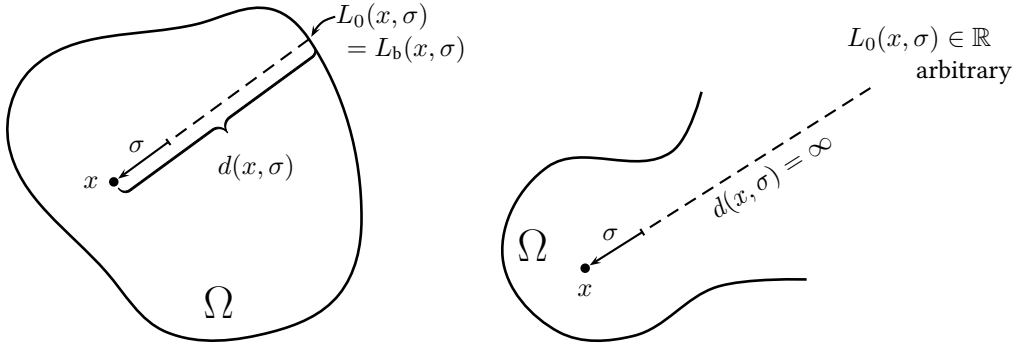


Figure 5.4: Setting of  $d$  and  $L_0$  in  $(x, \sigma) \in \Omega \times \mathbb{S}^2$ .

on  $\Omega \times \mathbb{S}^2$  in the scattering and absorption free situation, while  $L_b$  only specifies the boundary values on  $\partial\Omega \times \mathbb{S}_{x,\Omega}^2$ .

**Definition 2** (Integral Formulation of the Radiative Boundary Problem). Let  $\Omega \subset \mathbb{R}^3$  be a domain and  $d : \Omega \times \mathbb{S}^2 \rightarrow \mathbb{R}_{\geq 0} \cup \{\infty\}$  be the *boundary distance function* on  $\Omega$ , i.e. for any  $(x, \sigma) \in \Omega \times \mathbb{S}^2$  it is

$$d(x, \sigma) = \sup \{s \in \mathbb{R}_{\geq 0} : x - \hat{s}\sigma \in \Omega, \forall \hat{s} \in [0, s]\}. \quad (5.14)$$

The boundary condition shall be encoded by  $L_0 : \Omega \times \mathbb{S}^2 \rightarrow \mathbb{R}_{\geq 0}$  which, due to the context, has to be constant on each line of sight, i.e.  $\forall (x, \sigma) \in \Omega \times \mathbb{S}^2$

$$(0, d(x, \sigma)) \ni s \mapsto L_0(x - s\sigma, \sigma) \equiv \text{const.} \quad (\text{cf. Fig. 5.4}). \quad (5.15)$$

Then, the *integral formulation of the radiative boundary problem* on the set of bounded and measurable functions  $\mathfrak{B}(\Omega \times \mathbb{S}^2)$  is to find an  $L \in \mathfrak{B}(\Omega \times \mathbb{S}^2)$ , s.t.  $\forall (x, \sigma) \in \Omega \times \mathbb{S}^2$

$$L(x, \sigma) = L_0(x, \sigma)e^{-Kd(x, \sigma)} + \int_0^{d(x, \sigma)} Ke^{-Ks} \int_{\mathbb{S}^2} L(x - s\sigma, \omega)\psi(\sigma, \omega)dS(\omega)ds. \quad (5.16)$$

**Lemma 1** (Integral Solutions in the Classical Context). Let  $\Omega \subset \mathbb{R}^3$  be a domain with  $C^1$ -smooth boundary  $\partial\Omega$  and exterior normal  $\nu : \partial\Omega \rightarrow \mathbb{S}^2$  (which is well-defined due to  $\partial\Omega \in C^1$ ). Let  $L \in C^1(\Omega \times \mathbb{S}^2)$  and  $d$  and  $L_0$  be given as described in (5.14) and (5.15), s.t.  $L$  solves the corresponding integral formulation of the radiative boundary problem (5.16).

Then,  $L$  solves the classical formulation of the radiative boundary problem (5.9)

$$\begin{aligned} \langle \nabla_x L(x, \sigma), \sigma \rangle &= -KL(x, \sigma) + K \int_{\mathbb{S}^2} L(x, \omega)\psi(\sigma, \omega)dS(\omega), & \text{in } \Omega \times \mathbb{S}^2, \\ L(x, \sigma) &= L_b(x, \sigma), & \text{on } \partial\Omega \times \mathbb{S}_{x,\Omega}^2, \end{aligned}$$

where  $L_b$  is given by  $L_0$  on  $\partial\Omega \times \mathbb{S}_{x,\Omega}^2$ :

$$\forall x \in \partial\Omega, \forall \sigma \in \mathbb{S}_{x,\Omega}^2 : \quad L_b(x, \sigma) := L_0(x, \sigma).$$

*Proof.* One firstly has to realize two facts about the derivations of  $d$  and  $L_0$  along any line of

sight: Let  $(x, \sigma) \in \Omega$  and select an arbitrary  $\varepsilon > 0$  s.t.  $B_\varepsilon(x) \subset \Omega$ , which is possible due to  $\Omega$ 's openness. Furthermore, let  $d(x, \sigma) < \infty$ . Then, it directly follows from (5.14) and (5.15) that  $d$  and  $L_0$  are differentiable on each line of sight, where

$$\begin{aligned} \frac{d}{d\tau}d(x + \tau\sigma, \sigma) &= \lim_{h \rightarrow 0, h < \varepsilon} \frac{d(x + (\tau + h)\sigma, \sigma) - d(x + \tau\sigma, \sigma)}{h} = \lim_{h \rightarrow 0} \frac{h}{h} = 1, \\ \frac{d}{d\tau}L_0(x + \tau\sigma, \sigma) &= \lim_{h \rightarrow 0, h < \varepsilon} \frac{L_0(x + (\tau + h)\sigma, \sigma) - L_0(x + \tau\sigma, \sigma)}{h} = \lim_{h \rightarrow 0} \frac{0}{h} = 0. \end{aligned} \quad (5.17)$$

For the following, one also has to realize that

$$\left. \frac{d}{d\tau}L(x + (\tau - s)\sigma, \omega) \right|_{\tau=0} = -\left. \frac{d}{ds}L(x + (\tau - s)\sigma, \omega) \right|_{\tau=0} = -\frac{d}{ds}L(x - s\sigma, \omega). \quad (5.18)$$

Combining Leibniz's integral rule, basics facts about directional derivatives, Lebesgue's dominated convergence theorem (for interchanging differentiation and integration), (5.17) and (5.18) yields

$$\begin{aligned} \langle \nabla_x L(x, \sigma), \sigma \rangle &= \left. \frac{d}{d\tau}L(x + \tau\sigma, \sigma) \right|_{\tau=0} \\ &= \left. \frac{d}{d\tau} \left[ L_0(x + \tau\sigma, \sigma) e^{-Kd(x + \tau\sigma, \sigma)} \right] \right|_{\tau=0} \\ &\quad + \left. \frac{d}{d\tau} \int_0^{d(x + \tau\sigma, \sigma)} K e^{-Ks} \int_{\mathbb{S}^2} L(x + (\tau - s)\sigma, \omega) \psi(\sigma, \omega) dS(\omega) ds \right|_{\tau=0} \\ &= 0 \cdot e^{-Kd(x, \sigma)} - KL_0(x, \sigma) e^{-Kd(x, \sigma)} \\ &\quad + \int_0^{d(x, \sigma)} K e^{-Ks} \int_{\mathbb{S}^2} \left. \frac{d}{d\tau} [L(x + (\tau - s)\sigma, \omega)] \right|_{\tau=0} \psi(\sigma, \omega) dS(\omega) ds \\ &\quad + 1 \cdot K e^{-Kd(x, \sigma)} \int_{\mathbb{S}^2} L(x - d(x, \sigma)\sigma, \omega) \psi(\sigma, \omega) dS(\omega) \\ &= -KL(x, \sigma) + K \int_0^{d(x, \sigma)} K e^{-Ks} \int_{\mathbb{S}^2} L(x - s\sigma, \omega) \psi(\sigma, \omega) dS(\omega) ds \\ &\quad - \int_0^{d(x, \sigma)} K e^{-Ks} \int_{\mathbb{S}^2} \frac{d}{ds} L(x - s\sigma, \omega) \psi(\sigma, \omega) dS(\omega) ds \\ &\quad + K e^{-Kd(x, \sigma)} \int_{\mathbb{S}^2} L(x - d(x, \sigma)\sigma, \omega) \psi(\sigma, \omega) dS(\omega), \end{aligned}$$

where partial integration applied to the third term allows to proceed

$$\begin{aligned} &\int_0^{d(x, \sigma)} K e^{-Ks} \int_{\mathbb{S}^2} \frac{d}{ds} L(x - s\sigma, \omega) \psi(\sigma, \omega) dS(\omega) ds \\ &= - \int_0^{d(x, \sigma)} \frac{d}{ds} [K e^{-Ks}] \int_{\mathbb{S}^2} L(x - s\sigma, \omega) \psi(\sigma, \omega) dS(\omega) ds \\ &\quad + \left[ K e^{-Ks} \int_{\mathbb{S}^2} L(x - s\sigma, \omega) \psi(\sigma, \omega) dS(\omega) \right]_0^{d(x, \sigma)} \end{aligned}$$

$$\begin{aligned}
 &= K \int_0^{d(x,\sigma)} K e^{-Ks} \int_{\mathbb{S}^2} L(x - s\sigma, \omega) \psi(\sigma, \omega) dS(\omega) ds \\
 &\quad + \left[ K e^{-Kd(x,\sigma)} \int_{\mathbb{S}^2} L(x - d(x,\sigma)\sigma, \omega) \psi(\sigma, \omega) dS(\omega) \right. \\
 &\quad \left. - K \int_{\mathbb{S}^2} L(x\sigma, \omega) \psi(\sigma, \omega) dS(\omega) \right],
 \end{aligned}$$

and thus together

$$\langle \nabla_x L(x, \sigma), \sigma \rangle = -KL(x, \sigma) + K \int_{\mathbb{S}^2} L(x, \omega) \psi(\sigma, \omega) dS(\omega).$$

Carefully checking each equation reveals that this remains correct for  $d(x, \sigma) = \infty$ .

On the other hand,  $L$  fulfills the boundary condition, since for any  $x \in \partial\Omega$  and  $\sigma \in \mathbb{S}_{x,\Omega}^2$

$$\begin{aligned}
 L(x, \sigma) &= L_0(x, \sigma) e^{-K \cdot 0} + \int_0^0 K e^{-Ks} \int_{\mathbb{S}^2} L(x - s\sigma, \omega) \psi(\sigma, \omega) dS(\omega) ds \\
 &= L_0(x, \sigma) = L_b(x, \sigma).
 \end{aligned}$$

□

**Theorem 1** (Equivalence Between Classical and Integral Formulation). *Let  $\Omega$  be a domain with  $C^1$ -smooth boundary  $\partial\Omega$  and exterior normal  $\nu : \partial\Omega \rightarrow \mathbb{S}^2$ . Let  $L \in C^1(\Omega \times \mathbb{S}^2) \cap \mathfrak{B}(\Omega \times \mathbb{S}^2)$  and  $d$  and  $L_0$  be given as described in (5.14) and (5.15), and  $L_b$  related to  $L_0$  by*

$$\forall x \in \partial\Omega, \forall \sigma \in \mathbb{S}_{x,\Omega}^2 : \quad L_b(x, \sigma) := L_0(x, \sigma).$$

*Then,  $L$  solves the integral formulation of the radiative boundary problem (5.16) if and only if it solves the classical formulation of the radiative boundary problem (5.9).*

*Proof.* The forward implication is given by Lemma 1; the backward implication is proven in 5.3.1 by applying the line-of-sight formulation to each  $(x, \sigma) \in \Omega \times \mathbb{S}^2$ . The uniform boundedness of  $L$  required for the backward direction is assured by  $L \in \mathfrak{B}(\Omega \times \mathbb{S}^2)$ . □

**Remark 14** (Note on  $(\mathfrak{B}, \|\cdot\|_{C^0})$ ). One should note that  $\mathfrak{B}$  with maximum norm  $\|\cdot\|_{C^0}$  is up to the discussion on null sets (sets of Lebesgue measure 0) the same as the function space of essentially bounded and measurable functions  $\mathbb{L}^\infty$  with a.e. maximum norm  $\|\cdot\|_{\mathbb{L}^\infty}$ . For  $f \in \mathbb{L}^\infty$  this norm is given by

$$\|f\|_{\mathbb{L}^\infty} = \text{ess sup } |f| = \inf_{\mathcal{N} \text{ is null set}} \sup_{x \notin \mathcal{N}} |f(x)|.$$

## 5.4 Derived Models for Light Transport through Fog

Without further assumptions, the radiative boundary problem is complicated and without an explicit solution. Therefore, the prediction of a radiative transfer observation (*forward problem*) is a difficult task which most often can only be realized by numerical methods. Unfortunately, in order to estimate the atmospheric extinction coefficient  $K$  based on a given observation, one

even has to solve the *inverse problem* (cf. Sec. 6.3). Typically, the inverse problem is much more complex than the forward problem, since multiple forward problems have to be solved to find a parameter setting which explains the observation satisfactorily.

To nonetheless allow for parameter estimation, less complex approximate models for solutions of the radiative boundary problem with a manageable number of parameters have to be found.

At the beginning of this section, Koschmieder's model for horizontal vision is introduced, which for more than 90 years has been the most popular model for light transport through fog (cf. [Kos1924]). Furthermore, a generic class of models is derived from a fixed-point iteration based on the integral formulation of the radiative boundary problem (5.16). In this way, approximate models of arbitrary accuracy are proposed, which can be used for parameter estimation on the one hand and evaluation on the other hand.

#### 5.4.1 Koschmieder's Model (for Horizontal Vision)

Koschmieder's model, originally published in 1924 (cf. [Kos1924]), is, given the complexity of the radiative transfer equation, a remarkably simple and successful model. The two assumptions required to derive Koschmieder's model from the full radiative line-of-sight formulation (5.12) are a spatially constant in-scattering function

$$\forall \omega \in \mathbb{S}^2 : \quad s \mapsto L_{\text{in}}(p(s), \omega) \equiv \text{const.}$$

and a homogeneous atmosphere

$$K \equiv \text{const.}, \quad K_s \equiv \text{const.},$$

where  $K$  and  $K_s$  are not necessarily the same. With these assumptions (5.12) becomes

$$\begin{aligned} L(p_{\text{obs}}, \sigma) &= L_0 e^{-Kd} + \int_0^d K_s e^{-Ks} \int_{\mathbb{S}^2} L_{\text{in}}(p(0), \omega) \psi(\sigma, \omega) dS(\omega) ds \\ &= L_0 e^{-Kd} + \left[ \frac{K_s}{K} \int_{\mathbb{S}^2} L_{\text{in}}(p(0), \omega) \psi(\sigma, \omega) dS(\omega) \right] \int_0^d K e^{-Ks} ds \\ &= L_0 e^{-Kd} + \left[ \frac{K_s}{K} \int_{\mathbb{S}^2} L_{\text{in}}(p(0), \omega) \psi(\sigma, \omega) dS(\omega) \right] (1 - e^{-Kd}). \end{aligned}$$

This can be summarized to Koschmieder's model

$$L(d) = L_0 e^{-Kd} + L_{\text{air}} (1 - e^{-Kd}), \quad (5.19)$$

where  $L(d)$  is the radiance received from an object with intrinsic luminance  $L_0$  at distance  $d$ . The second summand represents in-scattered ambient light, referred to as *air light*.  $L_{\text{air}}$  denotes the so-called *air light parameter*

$$L_{\text{air}} := \frac{K_s}{K} \int_{\mathbb{S}^2} L_{\text{in}}(p(0), \omega) \psi(\sigma, \omega) dS(\omega). \quad (5.20)$$

One should note that in a plane-parallel atmosphere the assumptions required to derive Koschmieder's model are true for horizontal vision, since  $K$ ,  $K_s$  and  $L_{\text{in}}(\cdot, \omega)$  are assumed to be constant

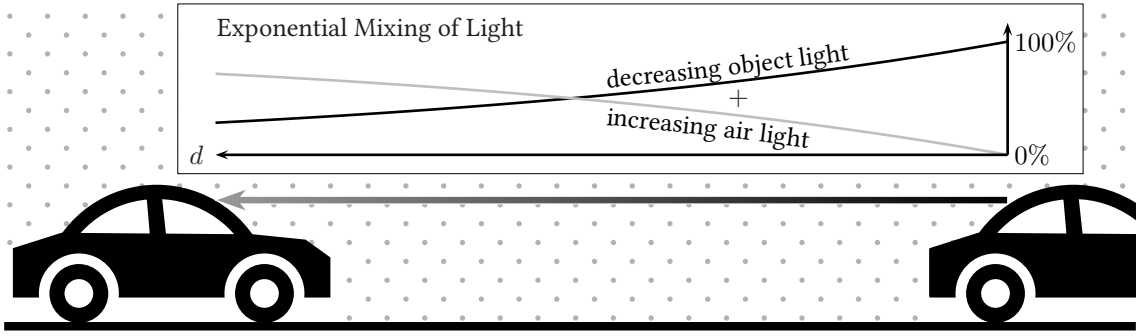


Figure 5.5: Koschmieder's model (5.19) can reliably be applied to scenarios of horizontal vision.

on a plane parallel to the ground (*cf.* Sec. 5.5, (5.23)). For this reason, (5.19) is often referred to as *Koschmieder's model for horizontal vision* in the context of atmospheric physics. In many not too complex settings horizontal vision is a reasonable assumption (*cf.* *e.g.* Fig. 5.5).

#### 5.4.2 Higher-Order Approximate Models

Thanks to the assumption on the in-scattered light  $L_{\text{in}}$ , Koschmieder's model has been derived in 5.4.1 without taking the surrounding light distribution into account. Aside from this restriction to the line of sight, models for a full light distribution in  $\Omega \times \mathbb{S}^2$  are desirable in order to more appropriately cover cases of, for instance, non-horizontal vision. These models can be derived from the integral formulation of the radiative boundary problem (5.16) as this formulation describes the light distribution according to the RTT (*cf.* Sec. 5.2).

One way to derive an approximate light distribution model  $(x, \sigma) \mapsto L(x, \sigma)$  is to assume the in-scattered light in (5.16) to be of a constant value  $L_{\text{air}}$ , which leads to Koschmieder's model applied to the entire  $\Omega \times \mathbb{S}^2$ :

$$\begin{aligned}
 L(x, \sigma) &= L_0(x, \sigma)e^{-Kd(x, \sigma)} + \int_0^{d(x, \sigma)} Ke^{-Ks} \int_{\mathbb{S}^2} L_{\text{air}} \psi(\sigma, \omega) dS(\omega) ds \\
 &= L_0(x, \sigma)e^{-Kd(x, \sigma)} + L_{\text{air}} \int_0^{d(x, \sigma)} Ke^{-Ks} ds \underbrace{\int_{\mathbb{S}^2} \psi(\sigma, \omega) dS(\omega)}_{=1 \text{ (cf. (4.4))}} \\
 &= L_0(x, \sigma)e^{-Kd(x, \sigma)} + L_{\text{air}} \left(1 - e^{-Kd(x, \sigma)}\right). \tag{5.21}
 \end{aligned}$$

This motivates the idea to derive more appropriate models by replacing the constant in-scattered light  $L_{\text{air}}$  by more sophisticated in-scattered light distributions. As a first step of improvement, it seems to be a natural approach to use (5.21) as an advanced in-scattered light model. This idea can be iterated to successively derive higher-order models  $(L^n)_{n \in \mathbb{N}_0}$ :

$$\begin{aligned}
 L^0(x, \sigma) &:= L_{\text{air}} \\
 L^n(x, \sigma) &:= L_0(x, \sigma)e^{-Kd(x, \sigma)} + \int_0^{d(x, \sigma)} Ke^{-Ks} \int_{\mathbb{S}^2} L^{n-1}(x - s\sigma, \omega) \psi(\sigma, \omega) dS(\omega) ds,
 \end{aligned}$$

where  $L^1$  represents Koschmieder's model as shown above.

The following theorem addresses the convergence and further properties of the sequence of higher-order models. It turns out that  $(L^n)_{n \in \mathbb{N}_0}$  converges to a solution of the radiative boundary problem (5.16).

**Theorem 2** (Properties of Higher-Order Approximate Models). *Let  $\Omega \subset \mathbb{R}^3$  be a domain and  $d$  and  $L_0$  be given as described in (5.14) and (5.15), where  $L_0$  and  $d$  are supposed to be Lebesgue-measurable. Let furthermore*

$$0 \leq L_0^{\text{low}} \leq L_0(x, \sigma) \leq L_{\text{air}}, \quad \forall (x, \sigma) \in \Omega \times \mathbb{S}^2,$$

be bounds on  $L_0$ . The right-hand side operator  $\mathcal{T} : \mathfrak{B}(\Omega \times \mathbb{S}^2) \rightarrow \mathfrak{B}(\Omega \times \mathbb{S}^2)$  is defined on the space of bounded, measurable functions as

$$[\mathcal{T}(f)](x, \sigma) := L_0(x, \sigma)e^{-Kd(x, \sigma)} + \int_0^{d(x, \sigma)} Ke^{-Ks} \int_{\mathbb{S}^2} f(x - s\sigma, \omega) \psi(\sigma, \omega) dS(\omega) ds.$$

Let finally the sequence of higher-order models be recursively defined as

$$L^0 := L_{\text{air}}, \quad L^n := \mathcal{T}(L^{n-1}), \quad n \in \mathbb{N}. \quad (5.22)$$

Then, the following holds:

- (a) **Well-definedness.**  $\mathcal{T}$  is well-defined.
- (b) **Uniform Boundedness.** For all  $n \in \mathbb{N}_0$  it holds that

$$L_0^{\text{low}} \leq L^n(x, \sigma) \leq L_{\text{air}}, \quad \forall (x, \sigma) \in \Omega \times \mathbb{S}^2.$$

- (c) **Monotonicity.** For all  $n \in \mathbb{N}$  it holds that

$$L^{n+1}(x, \sigma) \leq L^n(x, \sigma), \quad \forall (x, \sigma) \in \Omega \times \mathbb{S}^2.$$

- (d) **Pointwise Convergence.** There exists a measurable function  $L^\infty : \Omega \times \mathbb{S}^2 \rightarrow \mathbb{R}$ , s.t. for each  $(x, \sigma) \in \Omega \times \mathbb{S}^2$

$$L^n(x, \sigma) \rightarrow L^\infty(x, \sigma), \quad n \rightarrow \infty.$$

- (e) **Bounds on  $L^\infty$ .**  $L^\infty$  from (d) is uniformly bounded by

$$L_0^{\text{low}} \leq L^\infty(x, \sigma) \leq L^n(x, \sigma) \leq L_{\text{air}}, \quad \forall (x, \sigma) \in \Omega \times \mathbb{S}^2, \forall n \in \mathbb{N}_0.$$

- (f) **Existence.**  $L^\infty$  from (d) is a fixed point of  $\mathcal{T}$ . In particular, it solves the radiative boundary problem (5.16):

$$L^\infty(x, \sigma) = L_0(x, \sigma)e^{-Kd(x, \sigma)} + \int_0^{d(x, \sigma)} Ke^{-Ks} \int_{\mathbb{S}^2} L^\infty(x - s\sigma, \omega) \psi(\sigma, \omega) dS(\omega) ds.$$

- (g) **Linearity in  $L_0$  and  $L_{\text{air}}$ .** For each  $n \in \mathbb{N}_0 \cup \{\infty\}$  the function  $L^n$  changes linearly with respect to (uniform changes on) the boundary parameters  $L_0 : \Omega \times \mathbb{S}^2 \rightarrow \mathbb{R}_{\geq 0}$  and  $L_{\text{air}} > 0$ , more precisely

$$L_{\alpha L_0 + \beta, \alpha L_{\text{air}} + \beta}^n = \alpha L_{L_0, L_{\text{air}}}^n + \beta, \quad \forall \alpha, \beta > 0,$$

where an abbreviatory notation for  $L^n$  definitions based on different boundary parameters is used.

- (h) **Uniform Convergence on Compacta.** The sequence  $(L^n)_{n \in \mathbb{N}}$  converges uniformly to  $L^\infty$  on any compact subset  $\Omega_C \subset \Omega$ , i.e.

$$\|L^n - L^\infty\|_{C^0(\Omega_C \times \mathbb{S}^2)} \rightarrow 0, \quad n \rightarrow \infty.$$

- (i) **Uniform Convergence with Guaranteed Rate of Convergence on Bounded Domains.** Let further  $\Omega \subset \mathbb{R}^3$  be bounded with  $\text{diam}(\Omega) < \infty$ . Then,  $(L^n)_{n \in \mathbb{N}}$  converges uniformly on  $C^0(\Omega \times \mathbb{S}^2)$  with guaranteed rate of convergence:

$$\|L^n - L^\infty\|_{C^0(\Omega \times \mathbb{S}^2)} \leq \frac{(1 - e^{-K \text{diam}(\Omega)})^n}{e^{-K \text{diam}(\Omega)}} (L_{\text{air}} - L_0^{\text{low}}) \rightarrow 0, \quad n \in \mathbb{N}.$$

Furthermore, the limit function  $L^\infty$  is the only fixed point of  $\mathcal{T}$  on  $\mathfrak{B}(\Omega \times \mathbb{S}^2)$ . In particular, the radiative boundary problem (5.16) has only one solution.

*Proof.* In the following, standard notation and basic results from measure theory are applied. Regarding this topic, the interested reader may wish to consult standard literature such as [Els2011].

- (a) Proof sketch: Let  $f \in \mathfrak{B}(\Omega \times \mathbb{S}^2)$  be arbitrary with  $C > 0$ , s.t.  $|f| \leq C$  on  $\Omega \times \mathbb{S}^2$ . For any  $(x, \sigma) \in \Omega \times \mathbb{S}^2$  it obviously holds that

$$|Ke^{-Ks}f(x - s\sigma, \omega)\psi(\sigma, \omega)| \leq CKe^{-Ks}\psi(\sigma, \omega), \quad \forall \omega \in \mathbb{S}^2, s \in (0, d(x, \sigma)),$$

where  $x - s\sigma \in \Omega$  for all  $s \in (0, d(x, \sigma))$  due to the definition of  $d$ . Additionally, all related functions are measurable, with

$$\begin{aligned} C \int_0^{d(x, \sigma)} Ke^{-Ks} \underbrace{\int_{\mathbb{S}^2} \psi(\sigma, \omega) dS(\omega)}_{=1} ds &= C \int_0^{d(x, \sigma)} Ke^{-Ks} ds \\ &= C(1 - e^{-Kd(x, \sigma)}) \leq C. \end{aligned}$$

Therefore,  $(s, \omega) \mapsto CKe^{-Ks}\psi(\sigma, \omega)$  is an integrable dominating function for  $(s, \omega) \mapsto Ke^{-Ks}f(x - s\sigma, \omega)\psi(\sigma, \omega)$ , and thus

$$\left| \int_0^{d(x, \sigma)} \int_{\mathbb{S}^2} Ke^{-Ks}f(x - s\sigma, \omega)\psi(\sigma, \omega) dS(\omega) ds \right| \leq C.$$

Finally, the Fubini-Tonelli theorem allows for any change of integration order, and thus makes  $\mathcal{T}(f)$  a well-defined uniformly bounded and measurable function:

$$\begin{aligned} |[\mathcal{T}(f)](x, \sigma)| &\leq \left| L_0(x, \sigma)e^{-Kd(x, \sigma)} \right| \\ &\quad + \left| \int_0^{d(x, \sigma)} Ke^{-Ks} \int_{\mathbb{S}^2} f(x - s\sigma, \omega)\psi(\sigma, \omega) dS(\omega) ds \right| \\ &\leq L_{\text{air}} + C. \end{aligned}$$

(b) Proof by induction: The base case ( $n = 0$ ) obviously follows from the lemma's assumptions:

$$\forall (x, \sigma) \in \Omega \times \mathbb{S}^2 : \quad L_0^{\text{low}} \leq L_{\text{air}} = L^0(x, \sigma) = L_{\text{air}} \leq L_{\text{air}}.$$

For the inductive step, it is assumed that for a given  $n \in \mathbb{N}_0$  it holds that

$$\forall (x, \sigma) \in \Omega \times \mathbb{S}^2 : \quad L_0^{\text{low}} \leq L^n(x, \sigma) = L_{\text{air}}.$$

From the properties of  $\psi$ ,  $L_0$  and the integral discussed in (a), the assumption can be proven to be true for  $n + 1$  as well:

$$\begin{aligned} L^{n+1}(x, \sigma) &= L_0(x, \sigma)e^{-Kd(x, \sigma)} + \int_0^{d(x, \sigma)} K e^{-Ks} \int_{\mathbb{S}^2} \underbrace{L^n(x - s\sigma, \omega)}_{\leq L_{\text{air}}} \psi(\sigma, \omega) dS(\omega) ds \\ &\leq L_0(x, \sigma)e^{-Kd(x, \sigma)} + L_{\text{air}} \int_0^{d(x, \sigma)} K e^{-Ks} \underbrace{\int_{\mathbb{S}^2} \psi(\sigma, \omega) dS(\omega)}_{=1} ds \\ &= \underbrace{L_0(x, \sigma)}_{\leq L_{\text{air}}} e^{-Kd(x, \sigma)} + L_{\text{air}} \underbrace{\int_0^{d(x, \sigma)} K e^{-Ks} ds}_{=1 - e^{-Kd(x, \sigma)}} \\ &\leq L_{\text{air}} e^{-Kd(x, \sigma)} + L_{\text{air}} (1 - e^{-Kd(x, \sigma)}) = L_{\text{air}}, \\ L^{n+1}(x, \sigma) &= L_0(x, \sigma)e^{-Kd(x, \sigma)} + \int_0^{d(x, \sigma)} K e^{-Ks} \int_{\mathbb{S}^2} \underbrace{L^n(x - s\sigma, \omega)}_{\geq L_0^{\text{low}}} \psi(\sigma, \omega) dS(\omega) ds \\ &\geq \underbrace{L_0(x, \sigma)e^{-Kd(x, \sigma)}}_{\geq L_0^{\text{low}}} + L_0^{\text{low}} (1 - e^{-Kd(x, \sigma)}) \geq L_0^{\text{low}}. \end{aligned}$$

(c) Proof by induction: The base case ( $n = 1$ ) obviously follows from (b):

$$L^1(x, \sigma) \leq L_{\text{air}} = L^0(x, \sigma).$$

For the inductive step, it is assumed that for a given  $n \in \mathbb{N}$  it holds that

$$L^n(x, \sigma) \leq L^{n-1}(x, \sigma).$$

Then, taking into account the non-negativity of  $\psi$  and the linearity of integration, the assumption remains true for  $n + 1$ :

$$\begin{aligned} L^n(x, \sigma) - L^{n+1}(x, \sigma) &= [\mathcal{T}(L^{n-1})](x, \sigma) - [\mathcal{T}(L^n)](x, \sigma) \\ &= \int_0^{d(x, \sigma)} K e^{-Ks} \int_{\mathbb{S}^2} \underbrace{(L^{n-1}(x - s\sigma, \omega) - L^n(x - s\sigma, \omega))}_{\geq 0} \psi(\sigma, \omega) dS(\omega) ds \geq 0 \end{aligned}$$

(d) Due to (b) and (c)  $(L^n(x, \sigma))_{n \in \mathbb{N}_0}$  is a monotone and bounded sequence, for each  $(x, \sigma) \in \Omega \times \mathbb{S}^2$ . As a consequence it is converging (cf. e.g. [Wal2004, 4.7]), and  $L^\infty$  can be defined

pointwise as

$$L^\infty(x, \sigma) := \lim_{n \rightarrow \infty} L^n(x, \sigma).$$

Since  $L^\infty$  is the pointwise limit of measurable functions, it is measurable itself.

(e) This is a direct consequence of (b), (c) and (d).

(f) First, for each  $n \in \mathbb{N}_0 \cup \{\infty\}$  and  $(x, \sigma) \in \Omega \times \mathbb{S}^2$  an abbreviatory notation is introduced:

$$A_{x,\sigma}^n : (0, d(x, \sigma)) \times \mathbb{S}^2 \rightarrow \mathbb{R}_{\geq 0}, \quad A_{x,\sigma}^n(s, \omega) := K e^{-Ks} L^n(x - s\sigma, \omega) \psi(\sigma, \omega).$$

As shown in (a),  $A_{x,\sigma}^n$  is integrable for each  $n \in \mathbb{N}_0$ . Due to (b), for all  $n \in \mathbb{N}_0$  the functions  $A_{x,\sigma}^n$  are dominated by the following integrable function:

$$A_{x,\sigma}^n(s, \omega) \leq L_{\text{air}} K e^{-Ks} \psi(\sigma, \omega).$$

On the other hand,  $(A_{x,\sigma}^n)_{n \in \mathbb{N}}$  converges pointwise to  $A_{x,\sigma}^\infty$ , due to (d). Therefore, from Lebesgue's dominated convergence theorem it follows that  $A_{x,\sigma}^\infty$  is integrable and

$$\begin{aligned} L^\infty(x, \sigma) &= \lim_{n \rightarrow \infty} L^n(x, \sigma) = \lim_{n \rightarrow \infty} [\mathcal{T}(L^{n-1})](x, \sigma) = \lim_{n \rightarrow \infty} [\mathcal{T}(L^n)](x, \sigma) \\ &= L_0(x, \sigma) e^{-Kd(x, \sigma)} + \lim_{n \rightarrow \infty} \int_0^{d(x, \sigma)} \int_{\mathbb{S}^2} A_{x,\sigma}^n(s, \omega) dS(\omega) ds \\ &= L_0(x, \sigma) e^{-Kd(x, \sigma)} + \int_0^{d(x, \sigma)} \int_{\mathbb{S}^2} A_{x,\sigma}^\infty(s, \omega) dS(\omega) ds \\ &= L_0(x, \sigma) e^{-Kd(x, \sigma)} + \int_0^{d(x, \sigma)} K e^{-Ks} \int_{\mathbb{S}^2} L^\infty(x - s\sigma, \omega) \psi(\sigma, \omega) dS(\omega) ds. \end{aligned}$$

Due to (d) and (e), the limit function  $L^\infty$  is also measurable and bounded, and thus a fixed point of  $\mathcal{T}$ .

(g) Proof by induction: The base case ( $n = 0$ ) directly follows from the definition of  $L^0$ :

$$L_{\alpha L_0 + \beta, \alpha L_{\text{air}} + \beta}^0 = \alpha L_{\text{air}} + \beta = \alpha L_{L_0, L_{\text{air}}}^0 + \beta.$$

For the inductive step, it is assumed that for a given  $n \in \mathbb{N}_0$  it holds that

$$L_{\alpha L_0 + \beta, \alpha L_{\text{air}} + \beta}^n = \alpha L_{L_0, L_{\text{air}}}^n + \beta.$$

The linearity of integration yields the same property for  $n + 1$ :

$$\begin{aligned} L_{\alpha L_0 + \beta, \alpha L_{\text{air}} + \beta}^{n+1}(x, \sigma) &= (\alpha L_0(x, \sigma) + \beta) e^{-Kd(x, \sigma)} \\ &\quad + \int_0^{d(x, \sigma)} K e^{-Ks} \int_{\mathbb{S}^2} L_{\alpha L_0 + \beta, \alpha L_{\text{air}} + \beta}^n(x - s\sigma, \omega) \psi(\sigma, \omega) dS(\omega) ds \\ &= (\alpha L_0(x, \sigma) + \beta) e^{-Kd(x, \sigma)} \\ &\quad + \int_0^{d(x, \sigma)} K e^{-Ks} \int_{\mathbb{S}^2} (\alpha L_{L_0, L_{\text{air}}}^n(x - s\sigma, \omega) + \beta) \psi(\sigma, \omega) dS(\omega) ds \end{aligned}$$

$$\begin{aligned}
&= \alpha \left[ L_0(x, \sigma) e^{-Kd(x, \sigma)} + \int_0^{d(x, \sigma)} K e^{-Ks} \int_{\mathbb{S}^2} L_{L_0, L_{\text{air}}}^n(x - s\sigma, \omega) \psi(\sigma, \omega) dS(\omega) ds \right] \\
&\quad + \beta \left[ e^{-Kd(x, \sigma)} + \int_0^{d(x, \sigma)} K e^{-Ks} \int_{\mathbb{S}^2} \psi(\sigma, \omega) dS(\omega) ds \right] \\
&= \alpha L_{L_0, L_{\text{air}}}^{n+1}(x, \sigma) + \beta \left[ e^{-Kd(x, \sigma)} + \left(1 - e^{-Kd(x, \sigma)}\right) \right] \\
&= \alpha L_{L_0, L_{\text{air}}}^{n+1}(x, \sigma) + \beta.
\end{aligned}$$

For  $n = \infty$  this directly follows from the linearity of limits.

- (h) Since  $\Omega_C \times \mathbb{S}^2$  is a compact subset of  $\Omega \times \mathbb{S}^2$ , the pointwise convergence yields the claimed uniform convergence.
- (i) One can prove this with the help of a standard fixed-point argument. First of all one has to realize that the vector space  $\mathfrak{B}(\Omega \times \mathbb{S}^2)$  equipped with its canonical maximum norm  $C^0$  becomes a Banach space, since any Cauchy sequence in  $\mathfrak{B}(\Omega \times \mathbb{S}^2)$  has a pointwise limit which is, due to the compactness of  $\bar{\Omega} \times \mathbb{S}^2$ , an element of  $\mathfrak{B}(\Omega \times \mathbb{S}^2)$  itself. On the other hand,  $\mathcal{T}$  is a contraction mapping, *i.e.* it is Lipschitz continuous with constant  $< 1$ :

$$\begin{aligned}
&\|\mathcal{T}(L_1) - \mathcal{T}(L_2)\|_{C^0(\Omega \times \mathbb{S}^2)} \\
&= \max_{(x, \sigma) \in \Omega \times \mathbb{S}^2} \left| \int_0^{d(x, \sigma)} K e^{-Ks} \int_{\mathbb{S}^2} [L_1 - L_2](x - s\sigma, \omega) \psi(\sigma, \omega) dS(\omega) ds \right| \\
&\leq \|L_1 - L_2\|_{C^0(\Omega \times \mathbb{S}^2)} \max_{(x, \sigma) \in \Omega \times \mathbb{S}^2} \left| \int_0^{d(x, \sigma)} K e^{-Ks} \int_{\mathbb{S}^2} \psi(\sigma, \omega) dS(\omega) ds \right| \\
&\leq \|L_1 - L_2\|_{C^0(\Omega \times \mathbb{S}^2)} \max_{(x, \sigma) \in \Omega \times \mathbb{S}^2} \left| \int_0^{d(x, \sigma)} K e^{-Ks} ds \right| \\
&= \|L_1 - L_2\|_{C^0(\Omega \times \mathbb{S}^2)} \max_{(x, \sigma) \in \Omega \times \mathbb{S}^2} \left(1 - e^{-Kd(x, \sigma)}\right) \\
&\leq \underbrace{\left(1 - e^{-K \text{diam}(\Omega)}\right)}_{< 1, \text{ since } \text{diam}(\Omega) < \infty} \|L_1 - L_2\|_{C^0(\Omega \times \mathbb{S}^2)}.
\end{aligned}$$

One can apply Banach's fixed-point theorem (*cf.* *e.g.* [Wer2007, IV.7]) which proves that  $\mathcal{T}$  has a unique fixed point in  $\mathfrak{B}(\Omega \times \mathbb{S}^2)$  given by the  $C^0$ -limit  $\lim_{n \rightarrow \infty} \mathcal{T}^n(L^0) = L^\infty$ . Furthermore, Banach's fixed-point theorem guarantees a rate of convergence depending on the Lipschitz constant

$$\begin{aligned}
\|L^n - L^\infty\|_{C^0(\Omega \times \mathbb{S}^2)} &= \|\mathcal{T}^n(L^0) - L^\infty\|_{C^0(\Omega \times \mathbb{S}^2)} \\
&\leq \frac{(1 - e^{-K \text{diam}(\Omega)})^n}{e^{-K \text{diam}(\Omega)}} \|L^1 - L^0\|_{C^0(\Omega \times \mathbb{S}^2)} \\
&\leq \frac{(1 - e^{-K \text{diam}(\Omega)})^n}{e^{-K \text{diam}(\Omega)}} (L_{\text{air}} - L_0^{\text{low}}).
\end{aligned}$$

□

## 5.5 Plane-Parallel Atmosphere

One way to reduce the complexity of the radiative boundary problem is to assume the atmosphere to consist of planar horizontal layers with similar atmospheric properties. This applies to flat-world scenarios, in which the domain  $\Omega$  is arranged above the ground level  $\{x \in \mathbb{R}^3 : x^3 = 0\}$  with an atmospheric height  $H_{\text{atm}} \in \mathbb{R}_{>0} \cup \{\infty\}$ , i.e.  $\Omega = \mathbb{R} \times \mathbb{R} \times (0, H_{\text{atm}})$ .  $K$ ,  $K_s$  and  $L$  are assumed to be constant on planes parallel to the ground, i.e. for all  $H \in [0, H_{\text{atm}})$  and  $\sigma \in \mathbb{S}^2$  it is

$$\begin{aligned} \mathbb{R}^2 \ni (x^1, x^2) &\mapsto K((x^1, x^2, H)^T) = \text{const.}, \\ \mathbb{R}^2 \ni (x^1, x^2) &\mapsto K_s((x^1, x^2, H)^T) = \text{const.}, \\ \mathbb{R}^2 \ni (x^1, x^2) &\mapsto L((x^1, x^2, H)^T, \sigma) = \text{const.} \end{aligned} \quad (5.23)$$

This type of atmosphere is an important and well-known special case, commonly referred to as *plane-parallel atmosphere* (cf. e.g. [Shaz003, 9.5], [Cha1960]). In this section, only the case of  $K = K_s$  is considered.

The following transformation reduces the general spatial and directional information to the relevant part for the case of a plane-parallel atmosphere:

$$\begin{aligned} H : \mathbb{R}^3 \times \mathbb{S}^2 &\rightarrow \mathbb{R}, & (x, \sigma) &\mapsto x^3 \\ \mu : \mathbb{R}^3 \times \mathbb{S}^2 &\rightarrow [-1, 1], & (x, \sigma) &\mapsto \sigma^3 \end{aligned} \quad (5.24)$$

where  $H$  denotes the height above ground and  $\mu$  the cosine of the angle between the plane normal  $(0, 0, 1)^T$  and direction  $\sigma$  (Fig. 5.6).

Furthermore, let  $\bar{L} : \mathbb{R} \times [-1, 1] \rightarrow [0, H_{\text{atm}})$  be the plane-parallel representation of  $L$  according to (5.24), i.e.

$$L(x, \sigma) = \bar{L}(H(x, \sigma), \mu(x, \sigma)).$$

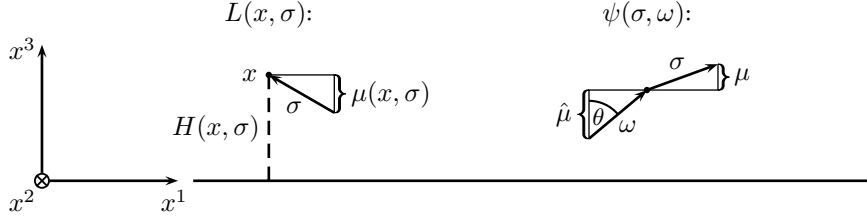
Then, the directional derivative  $\langle \nabla_x L(x, \sigma), \sigma \rangle$  transforms to

$$\begin{aligned} \langle \nabla_x L(x, \sigma), \sigma \rangle &= \langle \nabla_x \bar{L}(H(x, \sigma), \mu(x, \sigma)), \sigma \rangle \\ &= \left\langle \frac{\partial}{\partial H} \bar{L}(H(x, \sigma), \mu(x, \sigma)) \nabla_x H(x, \sigma), \sigma \right\rangle \\ &\quad + \left\langle \frac{\partial}{\partial \mu} \bar{L}(H(x, \sigma), \mu(x, \sigma)) \nabla_x \mu(x, \sigma), \sigma \right\rangle \\ &= \sigma^3 \frac{\partial}{\partial H} \bar{L}(H(x, \sigma), \mu(x, \sigma)) = \mu(x, \sigma) \frac{\partial}{\partial H} \bar{L}(H(x, \sigma), \mu(x, \sigma)). \end{aligned}$$

Considering w.l.o.g.  $\sigma$  to have the form

$$\sigma = \begin{pmatrix} \sqrt{1 - \mu^2} \\ 0 \\ \mu \end{pmatrix} \quad (\text{cf. Remark 15}), \quad (5.25)$$

applying the standard parametrization of the sphere (cf. Remark 10 on page 39) and substituting

Figure 5.6: Directional convention for  $L$  and  $\psi$  with reference to the plane-parallel case.

$\hat{\mu} = \cos(\theta)$  allows for a reinterpretation of the RTE (5.3) in plane-parallel coordinates

$$\begin{aligned}
& \mu \frac{\partial}{\partial H} \bar{L}(H, \mu) \\
&= \langle \nabla_x L(x, \sigma), \sigma \rangle = -KL(x, \sigma) + K \int_{\mathbb{S}^2} L(x, \omega) \psi(\sigma, \omega) dS(\omega) \\
&= -KL(x, \sigma) + K \int_0^\pi \int_0^{2\pi} L(x, \Phi(\varphi, \theta)) \psi(\sigma, \Phi(\varphi, \theta)) \sin(\theta) d\varphi d\theta \\
&= -K\bar{L}(H, \mu) + K \int_0^\pi \int_0^{2\pi} \bar{L}(H, \cos(\theta)) \psi \left( \begin{pmatrix} \sqrt{1-\mu^2} \\ 0 \\ \mu \end{pmatrix}, \Phi(\varphi, \theta) \right) \sin(\theta) d\varphi d\theta \\
&= -K\bar{L}(H, \mu) + K \int_{-1}^1 \bar{L}(H, \hat{\mu}) \bar{\psi}(\mu, \hat{\mu}) d\hat{\mu},
\end{aligned}$$

where

$$\begin{aligned}
\bar{\psi}(\mu, \hat{\mu}) &:= \int_0^{2\pi} \psi \left( \begin{pmatrix} \sqrt{1-\mu^2} \\ 0 \\ \mu \end{pmatrix}, \begin{pmatrix} \sqrt{1-\hat{\mu}^2} \cos(\varphi) \\ \sqrt{1-\hat{\mu}^2} \sin(\varphi) \\ \hat{\mu} \end{pmatrix} \right) d\varphi \\
&= \int_0^{2\pi} \hat{\psi}(\mu \hat{\mu} + \sqrt{1-\mu^2} \sqrt{1-\hat{\mu}^2} \cos(\varphi)) d\varphi,
\end{aligned} \tag{5.26}$$

where the phase notation  $\psi(\cdot, \cdot) = \hat{\psi}(\langle \cdot, \cdot \rangle)$  is used.

The integral formulation of the plane-parallel radiative boundary problem corresponding to Definition 2 on page 45 is given by

$$\bar{L}(H, \mu) = \bar{L}_0(\mu) e^{-Kd} + \int_0^d K e^{-Ks} \int_{-1}^1 \bar{L}(H - s\mu, \hat{\mu}) \bar{\psi}(\mu, \hat{\mu}) d\hat{\mu} ds, \tag{5.27}$$

where  $L_0(x, \sigma) = \bar{L}_0(H(x, \sigma), \mu(x, \sigma))$ .

**Remark 15** (Selection of  $\sigma$ ). Due to symmetry,  $\sigma$ 's first and second coordinate are of no importance in the plane-parallel scenario. This is why  $\sigma$  can be chosen w.l.o.g. as done in (5.25). This can be formally checked considering an arbitrary  $\sigma$ . It can be written as

$$\sigma = \begin{pmatrix} \sqrt{1-\mu^2} \cos(\hat{\varphi}) \\ \sqrt{1-\mu^2} \sin(\hat{\varphi}) \\ \mu \end{pmatrix},$$

which leads to a general formulation of  $\bar{\psi}$ :

$$\bar{\psi}(\mu, \hat{\mu}) = \int_0^{2\pi} \hat{\psi} \left( \mu \hat{\mu} + \sqrt{1 - \mu^2} \sqrt{1 - \hat{\mu}^2} [\cos(\hat{\varphi}) \cos(\varphi) + \sin(\hat{\varphi}) \sin(\varphi)] \right) d\varphi.$$

It is easy to check that  $\bar{\psi}$  is independent of  $\hat{\varphi}$  and thus consistent to (5.26).

**Remark 16** (Alternative Formulations). Depending on the sphere parametrization used for the transformation of the RTE from the arbitrary  $(x, \sigma)$ - to the plane-parallel  $(H, \mu)$ -coordinates, the plane-parallel RTE looks differently. For instance, another convenient choice could be the use of a  $\sigma$ -dependent sphere parametrization  $\Phi_\sigma$  according to Sec. B.3 in the Appendix which leads to the following plane-parallel formulation

$$\begin{aligned} & \mu \frac{\partial}{\partial H} \bar{L}(H, \mu) \\ &= -KL(x, \sigma) + K \int_0^\pi \int_0^{2\pi} L(x, \Phi_\sigma(\varphi, \theta)) \psi(\sigma, \Phi_\sigma(\varphi, \theta)) \sin(\theta) d\varphi d\theta \\ &= -K\bar{L}(H, \mu) + K \int_0^\pi \int_0^{2\pi} \bar{L}(H, \Phi_\sigma^3(\varphi, \theta)) \hat{\psi}(\cos(\theta)) \sin(\theta) d\varphi d\theta \\ &= -K\bar{L}(H, \mu) + K \int_{-1}^1 \int_0^{2\pi} \bar{L}\left(H, \sigma^3 \hat{\mu} - \sqrt{1 - \hat{\mu}^2} (\sigma^1 \cos(\varphi) + \sigma^2 \sin(\varphi))\right) d\varphi \hat{\psi}(\hat{\mu}) d\hat{\mu} \\ &= -K\bar{L}(H, \mu) + K \int_{-1}^1 \hat{\psi}(\hat{\mu}) \int_0^{2\pi} \bar{L}\left(H, \mu \hat{\mu} - \sqrt{1 - \mu^2} \sqrt{1 - \hat{\mu}^2} \cos(\varphi)\right) d\varphi d\hat{\mu}, \end{aligned}$$

where once again the  $\sigma$ -representation  $(\sqrt{1 - \mu^2}, 0, \mu)^T$  is used (cf. Remark 15). The difference to the standard formulation mainly lies in a shifted complexity from the  $\hat{\psi}$  argument to the  $\bar{L}$  argument. This allows to either remove  $\hat{\psi}$  or  $\bar{L}$  from the inner integral. Depending on the requirements, either one of both formulations can be used.



# III

---

## Model-Based Visibility Estimation

---



The investigation and measurement of meteorological aspects of visibility has a long history, reaching back to the beginning of the 20<sup>th</sup> Century (see Chap. 3). The central element is the atmosphere's extinction coefficient  $K$  which represents the optical density of the atmospheric aerosol; the reduced range of visibility due to this extinction is called meteorological visibility  $d_{\text{met}}$  (*cf.* Sec. 3.1). Today, all reliable measuring devices estimate  $K$  from either scattering or transmission methods (*cf.* Sec. 3.2). Only a few works can be found that consider a camera to be the proper device for meteorological visibility measurements. Remarkably, only one rigorous method has been published so far, namely [Hau2006c] (and some subsequent works containing minor extensions), that estimates the extinction coefficient from road and sky luminances with the help of a driver assistance camera. Further details can be found in Sec. 6.1. However, this approach is just a first view of the field of model-based visibility estimation from camera images and will be substantially deepened in this work.

In this part different novel methods for camera-based visibility measurement are presented. Although all approaches are discussed in the context of driver assistance cameras, most of the algorithms can be used in more general applications as well. All of these algorithms rely on luminances  $L$  observed from objects of comparable intrinsic luminance at different distances  $d$  and models that describe the relation between  $L$  and  $d$  according to the radiative transfer theory (*cf.* Sec. 5.4). Then, the model parameter can be estimated from the observation data by solving inverse problems (*cf.* Sec. 6.3) or, in other words, fitting the model to the data. With the objective of developing real-time applications, a fast parameter estimation is established for each of the approaches.

Before the novel methods are proposed, Chap. 6 provides a broader literature review on visibility issues, a specification of the video-based driver assistance setting and a remark on the underlying measurement principle which is applied for all estimation processes presented here.

Chapters 7 and 8 introduce the two main estimation methods that make use of different data from the camera image. While the tracking-based approach in Chap. 7 requires objects to be moved relative to the camera or multiple cameras observing the same objects, the road surface luminance curve (RSLC) based approach relies on a rather homogeneous road surface as one depth-extended object. It turns out that not only the type of data but also the model used to explain the observations has to be chosen differently in both cases. While Koschmieder's model for horizontal vision applies well to tracking-based observations, effects of non-horizontal vision should be taken into account in the case of road surface luminance curves (*cf.* Fig. 8.5). This leads to complex RSLC models (derived from 5.4.2) which only become applicable by utilizing the relation given in Theorem 2(g) on page 50. It reveals that the idea of linking the RSLC's inflection point to the underlying extinction coefficient  $K$  (originally stated in [Hau2006c]) can be extended to higher-order approximate fog models, and even to the exact solution of the plane-parallel radiative boundary problem (*cf.* Sec. 5.5). In the case of tracking-based visibility estimation, a maximum likelihood parameter estimation is applied (*cf.* Sec. 7.3). Here, a dimensional reduction leads to drastically reduced costs for the related optimization problem.

In Chap. 9 both approaches are combined in a third estimation method. If the RSLC cannot be extracted to the whole, the remaining part can be used for a fall-back fitting of Koschmieder's model. This algorithm is more of practical interest than of scientific interest.

The reader should note that part of the content presented here is subject of the publications [Len2013], [Len2014], the patents [Web2014], [Len2015], [Web2015], and the diploma thesis [Mar2013].



# Chapter 6

---

## Preliminary Considerations

### Contents

---

6.1	Literature Review . . . . .	63
6.1.1	Visibility Assessment at Daytime . . . . .	63
6.1.2	Visibility Assessment at Nighttime . . . . .	66
6.1.3	Visibility Assessment for Stationary Cameras . . . . .	67
6.2	Setting . . . . .	68
6.3	Measuring Principle . . . . .	70
6.4	Image Acquisition . . . . .	71

---

## 6.1 Literature Review

### 6.1.1 Visibility Assessment at Daytime

During the last century a number of reliable instruments have been developed in order to measure atmospheric visibility conditions (see Sec. 3.2). However, estimation methods based on ordinary cameras have been disregarded for a long time. This is changing nowadays, driven by the rapid development of multi-purpose driver assistance cameras. These systems have to operate autonomously under the influence of various visibility conditions, such as limitations caused by adverse weather. Despite these urgent needs still only a few visibility assessment approaches are available.

By far the first framework for camera-based visibility assessment was provided in 1997 by Pomerleau [Pom1997], called the “Rapidly Adapting Lateral Position Handler” (RALPH). He estimates a visibility value between 0 (no visibility at all) and 1 (clear daytime visibility) using the attenuation of the contrast along similar road features such as road markings, extracted from a camera pointing along a road. Due to its construction this approach allows for a general qualitative evaluation of visibility. However, it neither provides a well-defined quantitative assessment of visibility nor does it distinguish between different cause categories of visibility reduction.

Several years later Hautière, Boussard *et al.* started to develop more convenient measurement procedures. They introduced their own visibility measures  $V_{\text{mob}}$  and  $V_{\text{max}}$  (*cf. e.g.* [Hau2005; Hau2007b]). The “mobilized visibility distance”  $V_{\text{mob}}$  denotes the distance to the farthest distinguishable feature at the road plane with contrast above the human’s visual perception threshold



Figure 6.1: The road surface luminance curve (RSLC) is extracted line by line from the segmented region in the middle of the camera frame.

of 5% (e.g. lane features).  $V_{\max}$  is called the “mobilizable visibility distance” and approximately equal to the meteorological visibility  $d_{\text{met}}$  (which they call  $V_{\text{met}}$ ). In the most reasonable scenarios the following relation holds:

$$V_{\text{mob}} \leq V_{\max} \approx V_{\text{met}} = d_{\text{met}}.$$

Based on these visibility terms the numerous works of Hautière *et al.* can be categorized into essentially two approaches for visibility estimation.

One category of procedures combines depth and contrast information of the road with the objective of estimating the mobilized visibility  $V_{\text{mob}}$ . In the first works describing this method [Hau2005; Hau2006a; Hau2006b; Cha2008] the road depth map is obtained from a stereo camera system and an algorithm called “v-disparity” (cf. [Lab2002]). Boussard, Hautière *et al.* extended this idea to monocular cameras in [Bou2007; Bou2008; Bou2010]. Here, the road’s depth map is estimated by a flat-world assumption and successive image alignment, namely a homography-based structure from motion approach. Besides the depth, the contrast computation is also discussed carefully, since camera noise seriously interfere with the measurement of contrast values at the required level of around 5%. However, while estimating the term  $V_{\text{mob}}$  seems to be a natural approach towards visibility assessment, the value of  $V_{\text{mob}}$  is scene dependent and not well motivated by atmospheric physics. One can easily think of scenarios where  $V_{\text{mob}}$  and  $V_{\text{met}}$  strongly differ, e.g. in uphill or off-road scenarios. Once again a fogged-up windshield, or glare from the sun cannot be distinguished from atmospheric causes of reduced visibility.

The first rigorous method to estimate meteorological visibility is that described in the second category of Hautière *et al.*’s works (cf. e.g. [Hau2006c]). They segment parts of the road and the sky and extract line-wise median intensities (linearly related to the observed luminances) from it. The resulting mapping

$$v \mapsto L(v) := \text{median intensity at (segmented part of) line } v$$

is called *road surface luminance curve* (RSLC) in this work (cf. Fig. 6.1 and Sec. 8.1). Under the assumption of a flat and homogeneously dark road surface, Hautière *et al.* apply Koschmieder’s

model (*cf.* 5.4.1) to describe the resulting RSLCs by

$$v \mapsto L(v) = \begin{cases} L_{\text{air}} + (L_0 - L_{\text{air}})e^{-K \frac{H_{\text{cam}} f}{\cos(\xi)} \frac{1}{v - v_h}} & , \quad v > v_h \\ L_{\text{air}} & , \quad v \leq v_h \end{cases} \quad (6.1)$$

where  $H_{\text{cam}}$  and  $\xi$  describe the geometry (height and angle) of a slightly pitched camera installed above the ground;  $f$  denotes the focal length of the camera,  $v_h$  the horizontal line in the image (flat-world horizon) and  $L_0$  the intrinsic luminance of the road surface.

To utilize the RSLC model for parameter estimation Hautière *et al.* introduce a remarkable idea. Instead of classically fitting the model to the data by regression (*e.g.* by least-square minimization), they find a relation between the curve's inflection point  $v_i$  and the extinction coefficient  $K$  implied by their model (6.1):

$$0 = L''(v_i) = (L_0 - L_{\text{air}})K \frac{H_{\text{cam}} f}{\cos(\xi)} \frac{1}{(v_i - v_h)^3} e^{-K \frac{H_{\text{cam}} f}{\cos(\xi)} \frac{1}{v_i - v_h}} \left[ -2 + K \frac{H_{\text{cam}} f}{\cos(\xi)} \frac{1}{v_i - v_h} \right]$$

which is, for  $L_0 \neq L_{\text{air}}$ ,  $K > 0$  and  $H_{\text{cam}} > 0$ , equivalent to

$$K = 2(v_i - v_h) \frac{\cos(\xi)}{H_{\text{cam}} f}, \quad \text{or} \quad d_{\text{met}} = -\frac{\log(0.05)}{2(v_i - v_h)} \frac{H_{\text{cam}} f}{\cos(\xi)}.$$

This relation allows for an easy estimation of  $d_{\text{met}}$  just from estimating  $v_i$  from an RSLC. Although the drawback of Koschmieder's model is the tough assumption of horizontal vision, it can be developed further without loosing the  $K$ - $v_i$  correspondence (*cf.* Chap. 8 and [Len2013]). Other recently published optimized implementation of Hautière's RSLC algorithm can be found in [Neg2013] and [Neg2014].

All RSLC-based approaches work on just a single frame. However, they require an inflection point model and depend strongly on a specific road scenario that does not allow for objects blocking the view to the horizon.

In addition, both visibility assessment approaches proposed by Hautière *et al.* can be combined. This is done in *e.g.* [Hau2007a; Hau2008b], where not only both algorithms are reviewed in detail but also further discussions such as a sensitivity analysis, confidence measures and derived applications are provided. In [Hau2008a] one can find some experimental validation for the new visibility measures and procedures.

Apart from the attempts of Hautière *et al.* to quantitatively measure visibility, a couple of qualitative fog detection and classification algorithms can be found in literature by now:

Mori *et al.* [Mor2006; Mor2007] use cooperating radar and video sensors. With the help of the radar sensor they detect preceding vehicles (incl. distance) in order to extract visibility features from the corresponding region in the camera image. Combining the information they detect fog and classify it in three categories of density ("dense", "normal", "light"). It is interesting to note that the visibility feature is derived from Koschmieder's model applied on the luminance variance of the vehicle in front.

In 2009, Bronte *et al.* [Bro2009] presented another framework for robust fog detection. Similar to RSLC approaches, they segment parts of the road and the sky in order to investigate the transition at the horizon. From the vertical positions of the sky, the road and the vanishing point, they compute a heuristic visibility measure. Combined with a preceding "Sobel based sunny-foggy

detector” the framework outputs a qualitative fog rating (“low fog and sunny”, “medium fog”, “high fog”).

Finally, a pure classification approach has been published by Pavlić *et al.* [Pav2012; Pav2013]. Based on spectral features both daytime and nighttime fog are detected, distinguishing four categories of fog:

$$\begin{aligned}
 \text{“no fog”}: & \quad 1000 \text{ m} < d_{\text{met}}, \\
 \text{“low fog”}: & \quad 300 \text{ m} < d_{\text{met}} \leq 1000 \text{ m}, \\
 \text{“fog”}: & \quad 100 \text{ m} < d_{\text{met}} \leq 300 \text{ m}, \\
 \text{“dense fog”}: & \quad d_{\text{met}} \leq 100 \text{ m}.
 \end{aligned} \tag{6.2}$$

This is done with a remarkably high accuracy; they out-perform wavelet and Roser features (originally used for weather classification in [Ros2008]).

Fog detection and classification have become quite sophisticated nowadays. Approaches for physical visibility estimation (as proposed in this work) and classification approaches are very well supplementing each other as they suffer from different weaknesses and allow for different levels of visibility assessment.

### 6.1.2 Visibility Assessment at Nighttime

Visibility-reducing effects of fog at nighttime somewhat differ from effects in the daytime. Without daylight, blurred light-sources and glare caused by the own headlights are the dominating sight issues. Daytime algorithms which assume objects to be indirectly illuminated and diffusely reflecting are not applicable in these scenarios. Only a few works on nighttime visibility assessment for driver assistance cameras exist in literature.

One among them is a classification approach based on frequency features [Pav2013], which has already been mentioned in 6.1.1. In order to adapt to different scenarios, variable sets of features are proposed. At night they distinguish between low beam and high beam, applying sets of 32 and 7 frequency features respectively. Four classes of fog are discerned (see (6.2)).

The most comprehensive investigations of nighttime visibility assessment during fog come from Gallen, Dumont, Hautière *et al.* They carefully discuss fog effects at night and introduce a new nighttime visibility index [Gal2014]. With an intelligent headlamp control in mind (automatic high-beam/low-beam switching), they specify three classes of fog which have to be distinguished at night:

$$\begin{aligned}
 \text{“light fog”}: & \quad 300 \text{ m} < d_{\text{met}}, \\
 \text{“fog”}: & \quad 100 \text{ m} < d_{\text{met}} \leq 300 \text{ m}, \\
 \text{“dense fog”}: & \quad d_{\text{met}} \leq 100 \text{ m}.
 \end{aligned} \tag{6.3}$$

Besides further discussions on nighttime visibility measures, improved scattering models and light adaption strategies [Dum2004; Tai2008; Dum2008; Dum2010; Gal2011b; Gal2011c], they introduce an elaborate framework for fog detection and characterization in [Gal2011a; Gal2014]. Gallen *et al.* distinguish between two road scenarios which lead to different detection algorithms (*cf.* Fig. 6.2). In the presence of external light sources, the main measurable effects of fog appear as luminous regions around the light sources, so-called halos. In order to distinguish between presence and absence of fog, intensity profiles of these halos are extracted and analyzed regarding their smoothness. According to Gallen *et al.*, a further graduation of fog density is an ill-posed

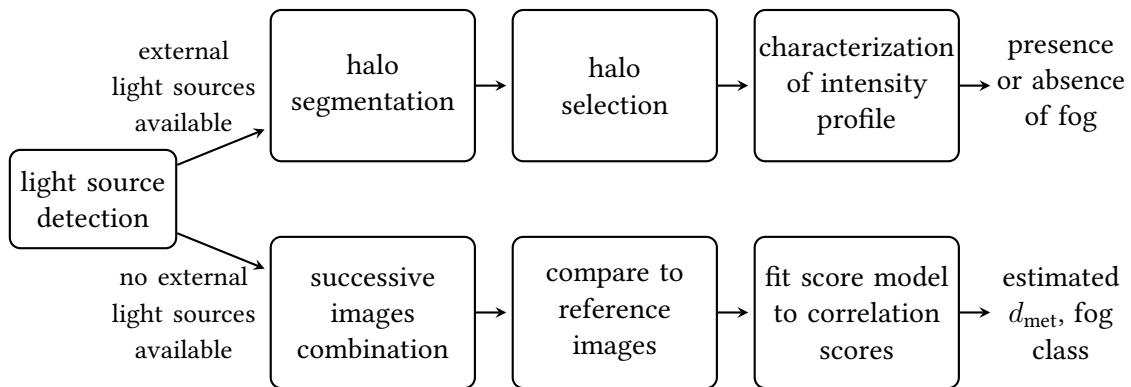


Figure 6.2: Summarizing flowchart for the nighttime visibility framework from [Gal2014].

problem in this case.

If no external light sources are present in the scene, fog manifests in a backscattered veil caused by the own headlights. Based on a correlation index, several reference images are compared to the averaged appearance of the veil. These reference images represent six different densities of fog (namely 12.6 m, 51.4 m, 91.8 m, 167.8 m, 415.6 m, 2000 m); they are either captured in a fog chamber or obtained from Monte Carlo simulations considering the full geometrical and photometrical calibration of the camera and the lighting system. In contrast to [Gal2011a], a supplementary fog characterization step is added in [Gal2014] and [Gal2015] which allows for a more precise visibility measurement in this scenario. To achieve this, a correlation score model is fitted onto the measured correlation scores. In particular, no hard threshold has to be applied to the correlation results anymore and the resulting fog classes directly follow from (6.3). A drawback of this correlation method is that for every beam position a separate set of reference images is needed, which for instance becomes problematic in the application of bending lights or matrix headlights.

### 6.1.3 Visibility Assessment for Stationary Cameras

Today, stationary cameras, such as for traffic surveillance, are already installed densely close to the highways. These cameras could serve as cheap visibility meters, which results in interesting applications for road safety or meteorology (*cf.* Sec. 3.3). However, the setting for visibility estimation by stationary cameras substantially differs from that of mobile driver assistance cameras. This involves disadvantages and advantages, such as being less flexible or having the possibility to compare the same static scene over time. Therefore, the estimation approaches from both settings can only partially be applied to each other. Only a few examples of stationary approaches for visibility estimation are introduced here.

Various visibility estimation methods for stationary cameras are based on contrast computation combined with a known depth-map of the road or the whole catchment area. In 1998, Busch *et al.* were one of the first proposing such an algorithm. In order to overcome the difficult choice of a mask-size for the direct local contrast computation (which suffers from either too much noise, or bad localization) they introduce a technique for wavelet-based contrast computation. From this, edges with a local Michelson contrast (*cf.* Remark 1 on page 17) above 5 % are identified. Another

contrast-based approach is presented in [Zha2009], where multiple virtual targets at different distances are defined at the road surface. Assuming a constant intrinsic contrast of road features, the visibility is permanently estimated from fits of Duntley’s law on the apparent contrast values.

More recent algorithms working with contrast observations are usually also taking the temporal variation of contrast into account. In [Min2010], for example, the approach of [Zha2009] is further combined with a temporal stabilization. In [Bab2011] and [Hau2011], another model-driven approach for stationary outdoor cameras is presented. Assuming a scene where targets are distributed continuously w.r.t. the distance from the camera, a model for the contrast distance histogram can be derived. The distribution of targets is estimated from observations in different weather conditions. From this, the visibility can be estimated from a fit of the resulting model onto the current contrast-depth histogram.

Since approaches based on road surface luminance curves only rely on one image (*cf.* 6.1.1 or Chap. 8), they can be applied to stationary cameras as well. In [Son2012], an RSLC-based fog detection method is introduced which is specialized to traffic surveillance cameras. The road and the sky are segmented with the help of texture analysis and the RSLC is extracted over multiple frames to mask out non-static traffic participants. If the resulting luminance curve has an exponential characteristic, the atmosphere is judged as fog without a detailed estimation of  $K$  or  $d_{\text{met}}$ .

Other works dealing with visibility assessment by stationary cameras are based on machine learning approaches. One of them can be found in [Lag2008], where Gaussian mixture models are used to detect changes in the spatial and the temporal frequency domain that are caused by meteorological events. Other features that turn out to be useful in this context can be found in [Liu2014], where color histograms are applied for fog detection.

Visibility assessment for stationary cameras at nighttime is extensively discussed in [Kwo1998], [Met2007], and [Gal2010a]. It is mainly based on the temporal comparison of multiple known light sources at defined distances and appropriate scattering and extinction models.

## 6.2 Setting

**Driver Assistance Context.** The algorithms presented in Chap. 7, Chap. 8 and Chap. 9 are mainly discussed in the context of advanced driver assistance systems (ADAS) (*cf.* Sec. 1.1). They are designed for and tested on a commercial multi-purpose camera (MPC, *cf.* Fig. 6.3) mounted behind the windshield at a height above ground of about 1.25 m and observing the road and traffic ahead.

However, most of the models and algorithms presented in this work are not restricted to ADAS front camera systems. They could also be applied to various other settings, such as static traffic or airfield surveillance cameras (algorithms based on (partial) road surface luminance curves, *cf.* Chap. 8, Chap. 9), or mobile cameras in drones or other airborne vehicles (tracking-based algorithms, *cf.* Chap. 7).

**Monocular Gray-Scale Camera.** Bosch’s MPC uses a monocular camera with a high dynamic range CMOS sensor, a field of view of about  $45.6^\circ \times 23.7^\circ$ , a frame rate of about 30 frames/s and a resolution of  $1024 \text{ px} \times 512 \text{ px}$  (source: personal communication). Although it provides one non-standard “red pixel” per  $2 \text{ px} \times 2 \text{ px}$  pattern, no color information (only intensities) are

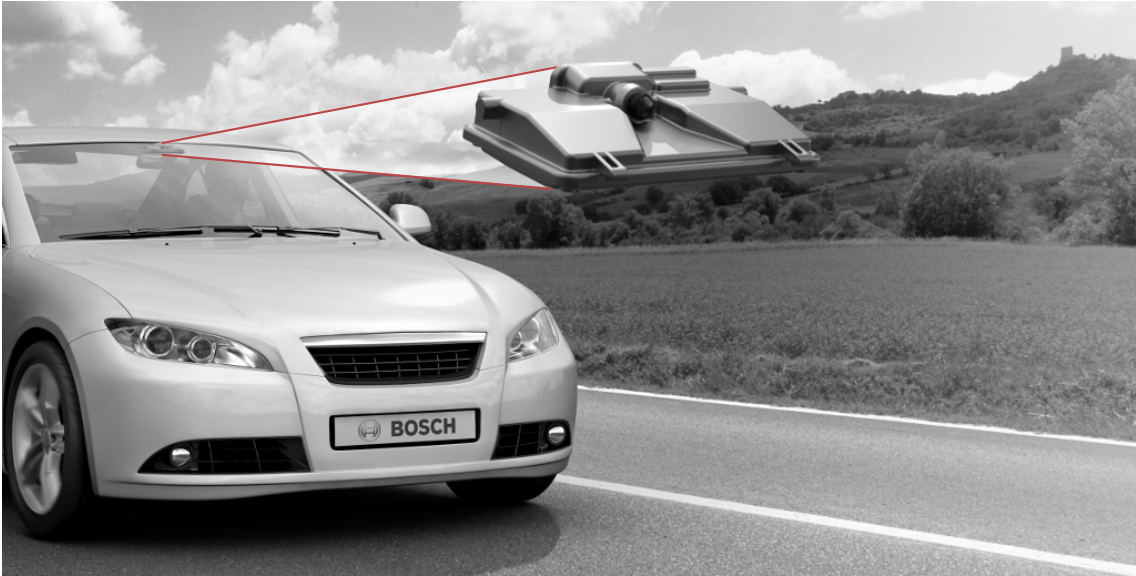


Figure 6.3: MPC installed behind the windshield (source: media database “Mediaspace” of the Bosch business sector Mobility Solutions)

involved in the discussions of this work.

**Homogeneous Daytime Fog.** Motivated by the pioneering work of Hautière *et al.* [Hau2006c] (*cf.* 6.1.1), this thesis focuses on model-based visibility measurement in homogeneous daytime fog. Compared to nighttime, daytime scenarios have the benefit that the atmospheric extinction coefficient  $K$  is a useful measure for visibility reduction. It can directly be expressed by the meteorological visibility  $d_{\text{met}} = -\log(0.05)/K$  (*cf.* Chap. 3 and 4.3.2). All visibility estimation methods are exclusively constructed to measure the impact of the foggy atmosphere on the visibility range. In the context of daytime fog, “visibility” and “meteorological visibility” are therefore often used as interchangeable terms in this work.

One should note that many of the concepts and algorithms presented in this work can actually also be applied to other atmospheric phenomena such as sandstorms, rain, smog or snow. In some of these cases, such as rain, snow or sandstorms, one also has to consider effects from water or dirt on the windshield.

**Remark 17** (Homogeneity Assumption). Usually, the density of fog and thus  $K$  spatially varies within a scene. By taking this into account, visibility estimation becomes a tomography-like problem. This task seems to be impossible to solve for driver-assistance cameras, which can only take few pictures from a very limited range of viewing angles. Fortunately, only large changes in the fog’s density, such as fog banks, are a problem for the concept of meteorological visibility. Smaller inhomogeneities are compensated by the large scale averaging effects of light transport. In these cases, the extinction coefficient  $K$  represents an average density of the atmosphere. This is similar to the step from single particle scattering to volume scattering in Sec. 4.3.

**Lambertian Surfaces.** As previously mentioned, visibility estimating algorithms rely on object observations at different distances, either from widely extended objects or from multiple observations. In both cases it is very likely that an object is observed from different viewing angles. Therefore, if not stated otherwise, object surfaces are assumed to be approximately Lambertian,

so that the light radiated from the objects in the direction of the observer (intrinsic luminance) is approximately constant for a set of observations from different viewing angles.

**Linear Camera Model.** In order to apply atmospheric radiance models to measured image intensities a linear camera model is assumed, *i.e.*  $\exists \alpha_I, \beta_I \in \mathbb{R}$  s.t. an object of luminance  $L$  is represented by the image intensity

$$I = \alpha_I L + \beta_I, \quad (6.4)$$

apart from discretization, saturation and spectral effects (*cf.* Sec. 6.4, in particular (6.9)). Here, the luminance has to be interpreted as the object's spectral radiance weighted with the spectral luminous efficacy of the camera. In the following, the luminance and the image intensity are usually treated as interchangeable quantities; this is valid since all models applied for visibility estimation turn out to be invariant under non-trivial linear intensity transformations. The scale invariance of these models also justifies that, in the context of visibility estimation, luminance values and parameters such as  $L_{\text{air}}$  and  $L_0$  are often treated as dimensionless quantities (*cf.* *e.g.* Chap. 8).

Of course, the assumption (6.4) is only valid in the theoretical case of an ideal linear sensor. However, transferring the considerations of this work to real CCD or CMOS cameras is a trivial step as long as the non-linear sensor characteristics (*e.g.* due to high dynamic range exposures or other tone mappings) are known.

**Tooling.** Almost all algorithms and experiments in this work have been implemented in the prototyping language MATLAB from MathWorks [Mat2012].

### 6.3 Measuring Principle

Methods to estimate physical quantities always rely on observations. These observations are almost always the outcome of a stochastic (or sufficiently chaotic) process. In order to establish an estimation method, a model for the stochastic process is required that depends on the physical quantity as a model parameter. The problem and process of drawing conclusions from the observation data with the help of the model is called *inverse problem*. To guarantee a meaningful result, one has to care about all three aspects of this principle: the data, the model and the parameter estimation (*cf.* Fig. 6.4). This is one of the most important tasks in many branches of science, such as computer vision, astronomy, machine learning, medical imaging and geophysics. Much work can be found on this topic (*e.g.* [Tar2005; Cas2002]).

In this work all algorithms are based on this measuring principle. To estimate the extinction coefficient one has to find meaningful types of observations in the camera image. These observations always consist of luminances and distances of objects and surfaces which somehow allow for an assumption on constant intrinsic luminances. The models are derived from the radiative transfer theory discussed in Sec. 5.4. Some of the observed phenomena lead to complex models and lots of data. This complicates the inverse problem and makes parameter estimation with standard methods too expensive for real-time purposes. Therefore, efficient alternative approaches have to be found for driver assistance cameras which have to combine several complex real-time functions in a small and economic embedded system.

The focus of this work is to establish models for observations and to optimize the corresponding

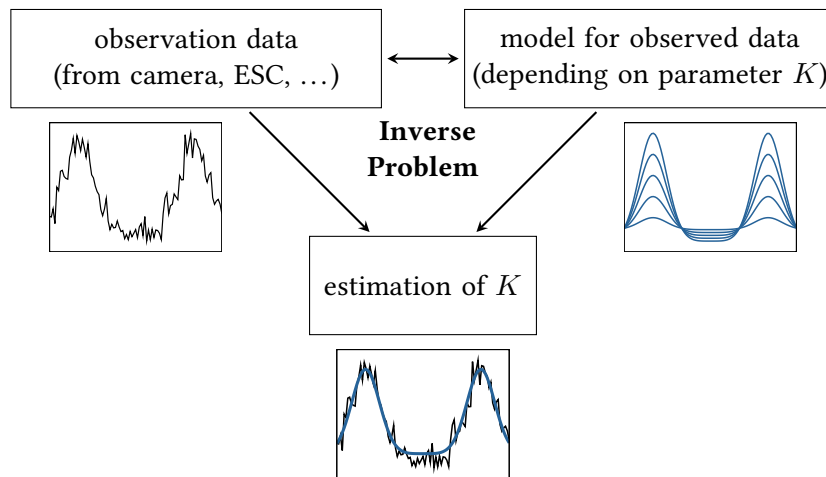


Figure 6.4: Measuring Principle.

parameter estimation. In contrast, the data acquisition from the camera images mainly consists of standard computer vision problems such as segmentation, tracking and 3D reconstruction. This is a wide field where much work has been done in the past and will be done in the future. It only plays a minor role in the following.

## 6.4 Image Acquisition

Before models which describe radiation can be applied to camera images it is important to understand how the camera images and the real-world radiation are related. Light entering the camera passes through a number of lenses and is finally captured and digitized by an image sensor (*imager*). This is a complex process where, among others, geometrical, radiometric, stochastic and discretization aspects have to be taken into account (*cf. e.g.* [Jah2012]). In this work, the impact of the camera's lens system on the image-taking process is, up to the lens transmittance in (6.7), neglected by assuming an ideal pinhole camera (*cf. e.g.* [Jah2012, 7.3.1]). The process of image acquisition can thus be described in terms of the imager which for the camera used in this work is a CMOS sensor (*cf.* Sec. 6.2). The EMVA Standard 1288 [Eur2010] describes how image taking by CMOS sensors can be characterized. In this section, only the most relevant facts about digital image acquisition based on CMOS sensors are compiled to a brief overview.

Light radiated from objects and scattered by the atmosphere can be understood as light quanta (photons), each of which has a certain frequency (*cf.* Sec. 4.2). Photons reaching the camera lens are partially projected to a 2D image sensor that consists of multiple distinct photosensitive areas each corresponding to a later picture element (*pixel*). Exploiting the inner or outer photoelectric effect, these photons induce voltage which can be accumulated and collected periodically. After digitization this results in a sequence of images, where each image represents the collected image intensities for all pixel positions. Since an image intensity represents the digitized form of the accumulated voltage in one pixel, it is also referred to as *digital gray value* given in DN (*digital number*).

Depending on the amount of arriving photons and the sensor's quantum efficiency, the number of counted photons  $N$  of a certain frequency within a certain time interval can be considered as a

Poisson distributed random variable. Therefore, to achieve a given relative measurement accuracy  $\varepsilon > 0$ , the expected number of photons (per unit time interval)  $\mu_p$  has to be sufficiently large:

$$\varepsilon \geq \frac{\sqrt{\text{Var}(N)}}{E(N)} = \frac{\sqrt{\mu_p}}{\mu_p} = \sqrt{\frac{1}{\mu_p}} \Rightarrow \mu_p \geq \frac{1}{\varepsilon^2}.$$

The stochastic deviation of  $N$  to its expected value  $\mu_p$  represents the so-called *shot noise*. Other sources of *temporal noise* are specific to the construction of the image sensor. Even if no photons are entering the camera, for instance, the imager generates a temperature dependent noise level. In this work, the camera noise model is based on the very common assumption of Gaussian noise, which is motivated by the central limit theorem and the dominating parts of the noise being Poisson distributed. Due to shot noise and other multiplicative effects, the noise's variance has to depend on the image intensity. For the camera system described in Sec. 6.2, this variance can be reliably modeled by a third-order polynomial term

$$\sigma^2(L) := \text{Var}(L) = c_3 L^3 + c_2 L^2 + c_1 L + c_0, \quad (6.5)$$

where  $L$  denotes the image intensity (or luminance, see below).

Other forms of image degeneration arise from spatial (but not temporal) inhomogeneities of the image sensor (*dark signal non-uniformity* and *photo response non-uniformity*) and from the signal's digitization rounding error (*quantization noise*). In this work these effects are disregarded since the camera used is equipped with an automatic non-uniformity correction, and the quantization is assumed to be negligible. Therefore, in the following the full camera noise model is given by (6.5).

Apart from noise disturbing the image acquisition, the photon current at a sensor element is not one-to-one assigned to a pixel's image intensity  $I$ . According to the EMVA Standard 1288 [Eur2010] there is a linear relation between the irradiance  $E$  received by the sensor element and the resulting image intensity  $I$ : The expected number  $\mu_p$  of photons with frequency  $f$  (or wavelength  $\lambda = c/f$ ) arriving on a given sensor area  $A$  during an exposure time  $t_{\text{exp}}$  is proportional to the incident irradiance  $E$

$$\mu_p = \frac{A t_{\text{exp}}}{h f} E = \frac{A t_{\text{exp}} \lambda}{h c} E,$$

where  $h$  denotes the well-known Planck constant and  $c$  the speed of light in vacuum. The total quantum efficiency  $\eta(\lambda)$  describes the rate between the (expected number of) photons  $\mu_p$  and the (expected number of) induced electrons  $\mu_e$ , namely  $\eta(\lambda) = \mu_e / \mu_p$ . The light induced electrons add up with thermally generated electrons with expected value  $\mu_d$  (*dark signal*). The resulting voltage is converted into a digital signal  $I$  with expected value  $\mu_I$  (image intensity). The conversion is assumed to be a linear process with a *system gain*  $\kappa$  which leads to

$$\mu_I = \kappa(\mu_e + \mu_d) = \kappa(\eta(\lambda)\mu_p + \mu_d) = \kappa\eta(\lambda) \frac{A t_{\text{exp}}}{h f} E + \kappa\mu_d.$$

This is a monochromatic formulation which in the general case has to be interpreted as

$$\mu_I = \kappa \frac{A t_{\text{exp}}}{h c} \int_0^\infty \lambda \eta(\lambda) E(\lambda) d\lambda + \kappa \mu_d. \quad (6.6)$$

For all models used in this work the incident irradiance has to be related to the radiances of object surfaces observed by the camera. Assuming a pinhole camera model and an object of radiance  $L$  that covers a full pixel area, the relation between  $E(\lambda)$  and  $L(\lambda)$  is given by

$$E(\lambda) = \tau(\lambda)\pi \frac{\cos^4(\theta)}{4k^2(1+m_l)^2} L(\lambda), \quad (6.7)$$

where  $\tau(\lambda)$  is the transmittance of the lens,  $\theta$  describes the observation angle,  $k$  is the focal ratio, and  $m_l$  is the magnification factor (*cf.* e.g. [Jah2012, 7.5]).

Combining (6.6) and (6.7) yields

$$\mu_I = \kappa \frac{At_{\text{exp}}}{hc} \pi \frac{\cos^4(\theta)}{4k^2(1+m_l)^2} \int_0^\infty \lambda \eta(\lambda) \tau(\lambda) L(\lambda) d\lambda + \kappa \mu_d. \quad (6.8)$$

That means the expected image intensity is linearly related to the radiance. Since the overall efficiency of the camera is more or less similar to the human spectral luminous efficacy the term  $\int_0^\infty \lambda \eta(\lambda) \tau(\lambda) L(\lambda) d\lambda$  is called *luminance*  $L$  in the following, s.t.

$$I \sim \alpha_I L + \beta_I + \mathcal{N}(0, \sigma^2(L)), \quad (6.9)$$

where  $\alpha_I, \beta_I \in \mathbb{R}$  describe the linear relation given in (6.8). As expounded in Sec. 6.2, in most parts of the work there is no need to differentiate between the image intensity  $I$  and the luminance  $L$ . Assuming a radiometrically calibrated camera, the relation between  $I$  and  $L$  can be given explicitly.

According to (6.8), the factor  $\beta_I$  and in turn the image intensities depend on the angle of observation  $\theta$ . In order to provide comparable image intensities over the whole image, this effect can be compensated by a pixel dependent correction factor. In theory, this factor can be easily computed for intrinsically calibrated cameras. However, since the factor  $\cos^4(\theta)$  is derived from the simplifying pinhole model it is useful to determine the correction factors by experiment (*cf.* e.g. [Jah2012, 7.5]). This could in addition allow for a full radiometric calibration.



# Chapter 7

---

## Tracking-Based Algorithm

### Contents

---

7.1	Data Acquisition . . . . .	76
7.2	Model Selection . . . . .	79
7.3	Optimization Problem . . . . .	79
7.4	Fast Minimization Approach . . . . .	82
7.4.1	Analytical Discussion . . . . .	83
7.4.2	Derived Algorithms . . . . .	91
7.4.3	Open Questions and Conjectures . . . . .	95
7.5	$L_{\text{air}}$ Stabilization . . . . .	99
7.6	Further Evaluation . . . . .	106

---

Light traveling from an object to an observer is heavily influenced by fog. The object light is absorbed and scattered away by each droplet where at the same time surrounding light is scattered into the line of sight (*cf.* Fig. 1.2). This mixing of light leads to a distance dependence of the perceived brightness for observed objects. Everybody having taken a walk through daytime fog should have experienced approaching objects to appear whiter at larger than at closer distances.

Based on this observation a novel algorithm for visibility estimation can be introduced which analyzes object tracks in camera images. With the help of Koschmieder's model for horizontal vision (*cf.* 5.4.1), the luminance values of tracked objects can be described w.r.t. the varying distances (*cf.* Fig. 7.1). In order to estimate the extinction coefficient  $K$  from the distance-luminance data the inverse problem (*cf.* Sec. 6.3) is tackled by a maximum likelihood approach. To make this algorithm applicable for real-time purposes, an easy-to-implement and remarkably fast minimization method for the log-likelihood functional is proposed which exploits the semi-linear structure of Koschmieder's model. It is shown that additional information on the air light parameter  $L_{\text{air}}$  can be used to heavily stabilize the tracking-based visibility estimation. Finally, the approach is tested on real-world sequences as well as on artificial images generated by Monte Carlo simulations.

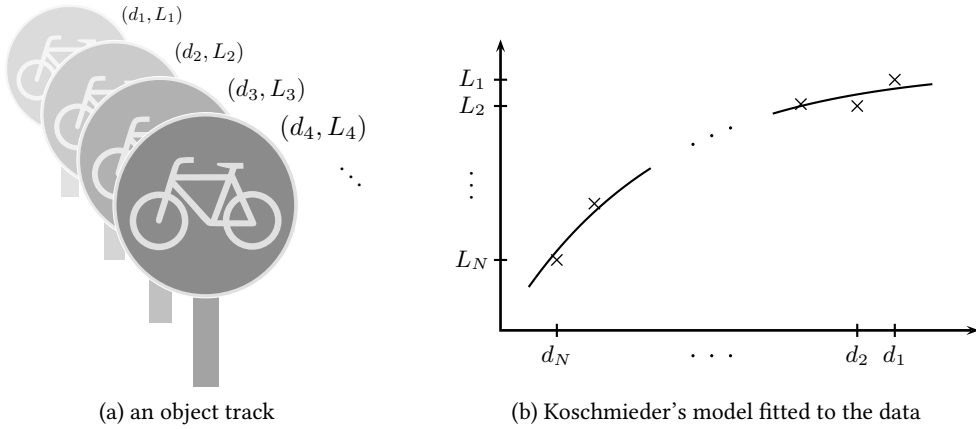


Figure 7.1: The luminance of an observed object changes w.r.t. the distance between the object and the observer. This relation can be described by Koschmieder's model.

## 7.1 Data Acquisition

The algorithm proposed in this chapter is based on luminance observations from objects at different distances to the observer, which requires objects to be moved relative to the camera or multiple cameras observing the same objects. In this context, the essential part of the data acquisition consists of the identification and linking of objects in different images, which is referred to as *tracking*. In order to apply radiative transfer models, for each of these observations a luminance value  $L_n^m$  and a distance value  $d_n^m$  have to be extracted:

$$\underbrace{(d_1^1, L_1^1), \dots, (d_{N_1}^1, L_{N_1}^1)}_{\text{1st object}}, \dots, \underbrace{(d_1^M, L_1^M), \dots, (d_{N_M}^M, L_{N_M}^M)}_{\text{Mth object}}, \quad (7.1)$$

where  $M \in \mathbb{N}$  denotes the number of object tracks and  $N_m \in \mathbb{N}$  the length of the  $m^{\text{th}}$  track,  $m \in \{1, \dots, M\}$ . Each object is equipped with its own (unknown) intrinsic luminance  $L_0^m$ . If the observation angle changes by a relevant degree during an observation, the method requires the object surfaces to be approximately Lambertian, so that the light radiated from the objects in the direction of the observer (intrinsic luminance) is comparable across the observation process (*cf.* Sec. 6.2). One should note that many non-natural surfaces such as that of road signs or cars are actually far from being Lambertian reflectors. Nevertheless, due to the diffusely in-scattered light in fog, most of them still can be considered as Lambertian emitters.

Tracking is an important task in many computer vision applications. Especially video-based driver assistance systems provide numerous useable object tracks, such as on road signs, vehicles, pedestrians or even generic objects. Temporally linked superpixel or (concatenated) flow vectors are further tracks available for tracking-based visibility estimation.

The same applies to the estimation of distances  $d_n^m$  towards the tracked entities, which can be acquired by various approaches. Most commonly, the scene's depth is reconstructed with the help of triangulation on corresponding points in different images of calibrated cameras (multiple view 3D reconstruction, such as structure from motion or stereo vision, *cf. e.g.* [Har2004]). Other approaches based on visual information utilize, among others, the change of region scales (*cf. e.g.*

[Wed2006]), images of different focus (*cf. e.g.* [Das1995]), depth learning on single images (*cf. e.g.* [Sax2008]), a-priori knowledge about observed objects (*cf. e.g.* [Gen2012]), shape collections (*cf. e.g.* [Su2014]) or other context information (*e.g.* simple geometry, such as a flat world). Apart from camera-based depth estimation, the distances can also be provided from specialized ranging sensors, such as radar, lidar or ultrasonic systems.

So, there are many approaches to detect and track objects in camera images and to extract the corresponding depth information. The resulting data quality essentially depends on the available hardware, on timing constraints and on other related circumstances. Since tracking and depth reconstruction are fundamental prerequisites for several applications in computer vision, they are nowadays still in the focus of research. In the next few years, data quality can therefore be expected to increase considerably.

However, the data acquisition is not a central topic of this work, wherefore the various data sources described above are not rigorously evaluated and compared. To nevertheless evaluate the proposed models and parameter estimation methods by feasibility tests on real world data (*cf. Sec. 7.6*), the tracking, including the object segmentation, is performed manually. The distance data  $d_n^m$  is acquired from a simple structure from motion algorithm and bundle adjusted as well as extrapolated with the help of ESC data regarding the inter-frame travel distance (*cf. Remark 18*).

Besides the distance values  $d_n^m$ , luminance values  $L_n^m$  have to be acquired from the tracked objects. This requires a method to select one representative luminance value  $L_n^m$  from the luminance distribution on the whole object segment. Due to imperfect segmentations and various forms of objects, this luminance distribution can be quite heterogeneous. For reasons of simplicity, in this work  $L_n^m$  is simply selected as the mean luminance over the segmented object. This is further motivated by the fact that Koschmieder's model (5.19) can be directly transferred from single luminance values to their mean. However, in cases of low-quality object segmentations, this luminance selection should be replaced by a more suitable one, *e.g.* by estimating the mode of the distribution which is less biased by outliers (*cf. e.g.* [Bic2002; Bic2006]). Among others, percentile luminances such as the median luminance could be a useful alternative as well (*cf.* [Mar2013]).

One should note that the setting required for tracking-based visibility estimation does not include specific road features. This is why, in contrast to the algorithms presented in chapters 8 and 9, this approach is rather independent of the driver assistance context.

**Remark 18** (ESC-Based Bundle Adjustment). Today's cars are usually equipped with a system called *electronic stability control* (ESC). Apart from its stabilizing properties in critical driving situations it measures as a byproduct the vehicle's travel distances and provides it to other components in the car via the vehicle bus and protocols such as the *Controller Area Network* (CAN). This information can be used to further improve the tracking distances of static objects, which (in this work) are acquired with the help of a structure from motion approach. The merging with ESC data basically is a supported *bundle adjustment*, which (without ESC data) is commonly used to retrospectively correct distances emerging from a piecewise estimation algorithm.

The ESC-based distance bundle adjustment is applied to each object track separately. For a given track of length  $N$  the structure from motion distances are denoted by  $d_1^{sfm}, \dots, d_N^{sfm}$  and the ESC travel distances between consecutive observations  $n$  and  $n+1$  are denoted by  $l_n, n = 1, \dots, N-1$ .

To merge this data, a model for the temporary vehicle trajectory is required. For that, the car is assumed to move on a planar curve of a constant *radius of curvature*  $|R|$  for the duration of the track observation, where  $R \in \mathbb{R}_{>0} \cup \mathbb{R}_{<0} \cup \{\infty\}$ . This is satisfied by cars which move on a

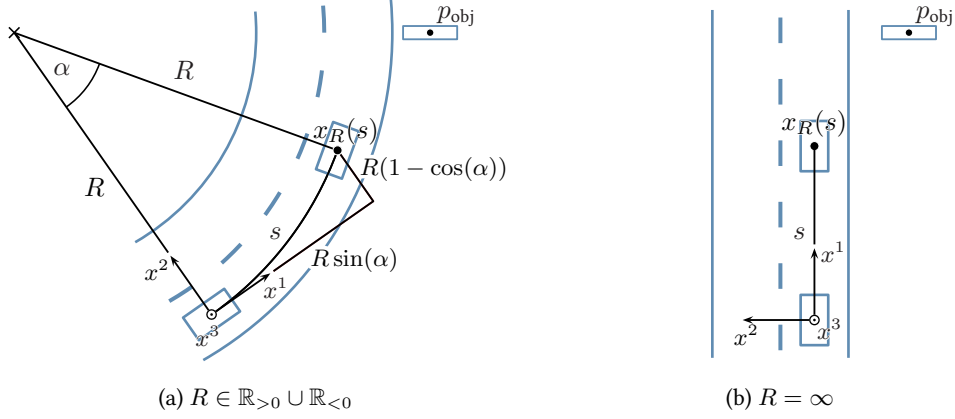


Figure 7.2: Notation for ESC-based distance bundle adjustment.

constantly bent curve ( $R \in \mathbb{R} \setminus \{0\}$ , cf. Fig. 7.2(a)) or straight ahead ( $R = \infty$ , cf. Fig. 7.2(b)). The straight-ahead case can be interpreted as limit scenario of  $R \rightarrow \infty$ . It is described in more detail in [Mar2013, Chapter 3] and shall be ignored at this point. A further improvement might be achieved by applying even more advanced trajectory models, such as clothoids (cf. e.g. [Gac2010]).

In the following, a positive radius  $R$  defines a curve with mathematical positive orientation (anti-clockwise), and a negative radius a curve with mathematical negative orientation (clockwise). The object position  $p_{\text{obj}} \in \mathbb{R}^3$  and the trajectory of the car  $x_R : \mathbb{R}_{\geq 0} \rightarrow \mathbb{R}^3$  are given in coordinates of the first observation. Now,  $x_R$  can be written in terms of the overall travel distance  $s$  as

$$x_R(s) = R \begin{pmatrix} \sin(s/R) \\ 1 - \cos(s/R) \\ 0 \end{pmatrix},$$

where  $s/R$  describes the overall travel angle  $\alpha$  (cf. Fig. 7.2(a)). The distance can be modeled with four parameters  $R$  and  $p_{\text{obj}} = (p_{\text{obj}}^1, p_{\text{obj}}^2, p_{\text{obj}}^3)$  as

$$d_{R,p_{\text{obj}}} : \mathbb{R}_{\geq 0} \rightarrow \mathbb{R}_{\geq 0}, \quad d_{R,p_{\text{obj}}}(s) = \sqrt{\left(x_R^1(s) - p_{\text{obj}}^1\right)^2 + \left(x_R^2(s) - p_{\text{obj}}^2\right)^2 + \left(x_R^3(s) - p_{\text{obj}}^3\right)^2}.$$

Computing the overall travel distance of the track by accumulating the inter-frame travel distances

$$s_1 = 0, \quad s_n = \sum_{k=1}^{n-1} l_k, \quad n = 2, \dots, N,$$

and fitting the distance model to the data with the help of a least-square approach

$$\left(R^{\text{opt}}, p_{\text{obj}}^{\text{opt}}\right) = \underset{(R, p_{\text{obj}})}{\operatorname{argmin}} \sum_{n=1}^N \left(d_{R,p_{\text{obj}}}(s_n) - d_n^{\text{sfm}}\right)^2,$$

leads to the bundle adjusted tracking distances

$$d_n := d_{R^{\text{opt}}, p_{\text{obj}}^{\text{opt}}}(s_n), \quad n = 1, \dots, N.$$

## 7.2 Model Selection

In order to implement a parameter estimation method based on the tracking data from Sec. 7.1, an atmospheric fog model is required which describes the relation between the luminances  $L$  and distances  $d$  depending on the extinction coefficient  $K$ . In the case of tracking data from a driver assistance camera that observes objects in front of the car, the assumption of horizontal vision seems to be natural. As stated in 5.4.1, a reliable model for this scenario is given by Koschmieder's model for horizontal vision

$$L(d) = L_0 e^{-Kd} + L_{\text{air}}(1 - e^{-Kd}), \quad (7.2)$$

with parameters  $K$ ,  $L_{\text{air}}$  and  $L_0$  representing the atmospheric density, the surrounding lighting conditions and the intrinsic object luminance, respectively.

It turns out that this model not only adequately describes tracking observations (*cf.* Sec. 7.6), but also leads to a likelihood objective function which can elegantly be minimized (*cf.* Sec. 7.4) for parameter estimation.

## 7.3 Optimization Problem

The question of how to interpret the observation data from Sec. 7.1 with the help of Koschmieder's model from Sec. 7.2 leads to an optimization problem often referred to as the inverse problem (*cf.* Sec. 6.3). The corresponding objective function can be stated as a weighted sum over squared residuals, where the weights allow for an incorporation of residual uncertainties. Minimizing this functional constitutes the parameter estimation and a fit of the model on the data (*cf.* Fig. 7.1(b)).

Each observation  $(d_n^m, L_n^m)$  in (7.1) is the outcome of a measurement process which can be interpreted as the sum of one term in accordance with Koschmieder's model (7.2) and another term constituting the measurement error. Assuming this error to be unbiased, normally distributed and solely caused by the the luminance measurement, the  $L_n^m$  values can be seen as the realizations of a random variable

$$L_n^m \sim \mathcal{N}\left(L_0^m e^{-Kd_n^m} + L_{\text{air}}(1 - e^{-Kd_n^m}); (\sigma_n^m)^2\right). \quad (7.3)$$

The uncertainty of a measurement  $L_n^m$  is expressed by its standard deviation  $\sigma_n^m$  (*cf.* Remark 20).

For  $M$  objects, (7.2) provides a distance-luminance model with  $M + 2$  parameters

$$p = (K, L_{\text{air}}, L_0^1, \dots, L_0^M).$$

A common approach, to infer from some measured data  $(d_n^m, L_n^m)$  onto the underlying parameters  $p$  is to maximize the likelihood function of the overall observation process (*maximum likelihood problem*). It maps  $p$  to the value of the overall probability density function  $f_p$  evaluated in the observed outcome  $(L_1^1 \dots, L_{N_M}^M)$ . Assuming the observations  $L_n^m$  to be independent of each

other, the likelihood function can be decomposed into the product of probability density functions of single observations

$$p \mapsto f_p(L_1^1, \dots, L_{N_M}^M) = \prod_{m=1}^M \prod_{n=1}^{N_m} f_{(K, L_{\text{air}}, L_0^m)}(L_n^m).$$

According to (7.3) these are normally distributed with an expected value fitting Koschmieder's model in  $d_n^m$  and standard deviation  $\sigma_n^m$ . This leads to the following likelihood function:

$$p \mapsto \prod_{m=1}^M \prod_{n=1}^{N_m} \frac{1}{\sqrt{2\pi}\sigma_n^m} \cdot \exp\left(\frac{1}{2} \left(\frac{L_n^m - [L_0^m e^{-Kd_n^m} + L_{\text{air}}(1 - e^{-Kd_n^m})]}{\sigma_n^m}\right)^2\right). \quad (7.4)$$

In this case, the maximum likelihood problem can more easily be accessed by applying a negative log to the likelihood function leading to an equivalent but simplified minimization problem:

$$\begin{aligned} & -\log(f_p(L_1^1, \dots, L_{N_M}^M)) \\ &= -\log\left(\prod_{m=1}^M \prod_{n=1}^{N_m} \frac{1}{\sqrt{2\pi}\sigma_n^m} \cdot \exp\left(\frac{1}{2} \left(\frac{L_n^m - [L_0^m e^{-Kd_n^m} + L_{\text{air}}(1 - e^{-Kd_n^m})]}{\sigma_n^m}\right)^2\right)\right) \\ &= \sum_{m=1}^M \sum_{n=1}^{N_m} \left[-\log(\sqrt{2\pi}\sigma_n^m) + \frac{1}{2} \left(\frac{L_n^m - [L_0^m e^{-Kd_n^m} + L_{\text{air}}(1 - e^{-Kd_n^m})]}{\sigma_n^m}\right)^2\right]. \end{aligned}$$

Therefore, the likelihood function in (7.4) is maximized if and only if the weighted least-square functional

$$p \mapsto \mathcal{F}(p) := \sum_{m=1}^M \sum_{n=1}^{N_m} \frac{1}{(\sigma_n^m)^2} \left([L_0^m e^{-Kd_n^m} + L_{\text{air}}(1 - e^{-Kd_n^m})] - L_n^m\right)^2 \quad (7.5)$$

is minimized.

**Remark 19** (Interpretation as Weighted Sum-of-Squares Objective Function). The likelihood functional defined in (7.5) can also be interpreted as a weighted sum-of-squares objective function. In cases of similar uncertainties, the maximum likelihood problem therefore differs only marginally from the very common least-square problem, which is motivated by the idea that in the ideal case the observed data can be perfectly described by the model and the set of true atmospheric

parameters. The resulting residual equations are

$$\begin{aligned} \text{object 1:} & \begin{cases} L_1^1 = L_{\text{air}} + (L_0^1 - L_{\text{air}})e^{-Kd_1^1}, \\ \vdots \\ L_{N_1}^1 = L_{\text{air}} + (L_0^1 - L_{\text{air}})e^{-Kd_{N_1}^1}, \\ \vdots \end{cases} \\ \text{object } M: & \begin{cases} L_1^M = L_{\text{air}} + (L_0^M - L_{\text{air}})e^{-Kd_1^M}, \\ \vdots \\ L_{N_M}^M = L_{\text{air}} + (L_0^M - L_{\text{air}})e^{-Kd_{N_M}^M}. \end{cases} \end{aligned} \quad (7.6)$$

Obviously, measurement noise and unsatisfied model assumptions lead to violations of these relations. Therefore, an exact solution of (7.6) has to be replaced by a functional that minimizes the overall error in the equation system. This is usually done by minimizing the sum-of-squares functional derived as the sum over the squared residua

$$r_n^m(K, L_{\text{air}}, L_0^m) := L_{\text{air}} + (L_0^m - L_{\text{air}})e^{-Kd_n^m} - L_n^m$$

w.r.t. the selected parameters:

$$(K, L_{\text{air}}, L_0^1, \dots, L_0^M) \mapsto \sum_{m=1}^M \sum_{n=1}^{N_m} (r_n^m(K, L_{\text{air}}, L_0^m))^2.$$

Choosing  $\sigma_n^m \equiv 1$ , this is a special case of  $\mathcal{F}$ .

**Remark 20** (Assignment of Uncertainties). The use of the standard deviations  $\sigma_n^m$  in (7.5) makes it possible to incorporate the uncertainties of the acquired data into the visibility estimation process. To select the  $\sigma_n^m$  in a meaningful way, a good understanding of the stochastic process of the distance and luminance acquisition is required. If this is difficult or if all data can be considered to be more or less of the same weight, it is a valid choice to set  $\sigma_n^m \equiv 1$  (cf. Remark 19).

In this work, the luminance uncertainty is modeled according to the fact that  $L_n^m$  represents the mean over a segmented object area in the image. Assuming the luminances of the segmented pixels to be i.i.d. and the segmentation error to be negligible, the variance in  $L_n^m$  is inversely proportional to the size of the segmented area, *i.e.*

$$\sigma_n^m \sim \left( \# \text{object pixels at } n^{\text{th}} \text{ frame of } m^{\text{th}} \text{ track} \right)^{-\frac{1}{2}}. \quad (7.7)$$

However, it could be useful to incorporate other uncertainties (*e.g.* from segmentation or tracking, or from a more sophisticated noise model) in  $\sigma_n^m$  as well.

**Remark 21** (2D-Uncertainty Objective Function). Modeling the stochastic process of measurement to be one-dimensionally represented in  $L$  does not properly reflect the actual two-dimensional measuring process in  $(d, L)$ . To nevertheless justify the one-dimensional approach one has to treat the uncertainty of the  $d$  measurements as fully included in the uncertainty of  $L$ .

Nevertheless, from a measuring theory point of view it is more convenient to derive the parameter estimation problem from a two-dimensional maximum likelihood approach. Given

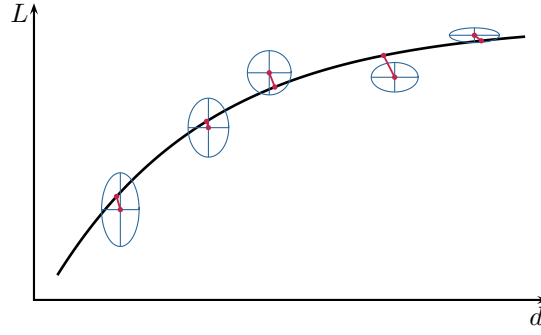


Figure 7.3: Example for the results from geometric fitting, including the ellipses of one standard deviation. The model parameters are chosen in a way that minimizes the sum of the squared Mahalanobis distances between the sampling points and the related model curve.

two-dimensional uncertainties in form of covariance matrices  $\Sigma_n^m \in \mathbb{R}^{2 \times 2}$  and assuming a Gaussian error model, the resulting objective function can be written as

$$(K, L_{\text{air}}, L_0^1, \dots, L_0^M) \mapsto \sum_{m=1}^M \sum_{n=1}^{N_m} \min_{d>0} \left[ \begin{pmatrix} d_n^m - d \\ L_n^m - L_{\text{Kos}}^m(d) \end{pmatrix}^T (\Sigma_n^m)^{-1} \begin{pmatrix} d_n^m - d \\ L_n^m - L_{\text{Kos}}^m(d) \end{pmatrix} \right], \quad (7.8)$$

where  $L_{\text{Kos}}^m(d)$  is an abbreviatory notation for Koschmieder's model term

$$L_{\text{Kos}}^m(d) = L_{\text{air}} + (L_0^m - L_{\text{air}})e^{-Kd}.$$

Each summand represents the minimal squared Mahalanobis distances with covariance matrix  $\Sigma_n^m$  (cf. e.g. [Mae2000]) between the data point  $(d_n^m, L_n^m)$  and its Mahalanobis projection to the model curve. This is often referred to as *geometric fitting* (cf. e.g. [Kan2008]). Fig. 7.3 shows an example of such a fit.

However, this approach is based on a much more complex objective function than the one proposed in (7.5), since for each evaluation of (7.8) several projection problems have to be solved. Moreover, it does not lead to a substantially increased estimation performance. Therefore, the idea of two-dimensional uncertainties is not followed up any further in this work.

## 7.4 Fast Minimization Approach

There are several well-known approaches to minimize the objective function  $\mathcal{F} : \mathbb{R}^{M+2} \rightarrow \mathbb{R}$  from (7.5). A useful overview can be found in, for instance, [Mad2004]. One of the most popular optimization algorithm is given by the method of gradient descent. Starting at  $p_0 \in \mathbb{R}^{M+2}$  the approximate minimizer  $p_n$  is updated by a residuum proportional to the negative gradient of  $\mathcal{F}$  in each iteration:

$$p_{n+1} := p_n - \varepsilon_n \nabla \mathcal{F}(p_n),$$

where the step size factor  $\varepsilon_n > 0$  and the stopping criteria can be chosen in various ways. Another common optimization algorithm is Newton's method which aims for solving  $\nabla \mathcal{F} = 0$

by iteratively solving

$$[\text{Hess } \mathcal{F}(p_n)] (p_{n+1} - p_n) := -\nabla \mathcal{F}(p_n).$$

Newton's method is converging much faster than gradient descent methods but suffers from only a narrow range of convergence (*cf. e.g.* [Gal2000]).

Since  $\mathcal{F}$  can be interpreted as a sum-of-squares objective function (*cf.* Remark 19 on page 80)

$$\mathcal{F}(p) = \sum_{n=1}^N r_n(p)^2, \quad N = N_1 + \dots + N_M,$$

specialized approaches can be used for its minimization. The Gauß-Newton algorithm, for example, replaces Hess  $\mathcal{F}$  in Newton's method by a more stable approximation which leads to the iterative approach

$$[J_r^T(p_n) J_r(p_n)] (p_{n+1} - p_n) = -[J_r^T(p_n)] r(p_n),$$

where  $r = (r_1, \dots, r_K) : \mathbb{R}^{M+2} \rightarrow \mathbb{R}^K$ , and  $J_r$  denotes the Jacobian matrix of  $r$ . To obtain a reliable and fast optimization approach, the Levenberg-Marquardt algorithm uses an iteratively adaptive combination of the Gauß-Newton and the gradient descent method. This leads to one of the most popular non-linear least square algorithms:

$$[J_r^T(p_n) J_r(p_n) + \alpha \mathcal{I}] (p_{n+1} - p_n) = -[J_r^T(p_n)] r(p_n),$$

where  $\mathcal{I}$  denotes the identity matrix, and  $\alpha > 0$  adaptively controls the weight of the gradient descent method.

However, the optimal choice of the minimization approach substantially depends on the structure of the objective function. Newton's method, for example, is always converging for globally convex functions, and the gradient descent method can be modified in the case of linear least square functionals such that it converges very efficiently with the help of optimal step sizes. Since tracking-based visibility estimation has to be applicable on economic real-time embedded camera systems it is important to analyze  $\mathcal{F}$  regarding the optimal choice of the minimizer.

In this section, a highly specialized and efficient minimization approach is derived from analytical properties of  $\mathcal{F}$ . Due to the partially linear character of Koschmieder's model (*cf.* Sec. 7.2), it is possible to analytically find the globally optimal parameter choice  $L_{\text{air}}, L_0^1, \dots, L_0^M$  for any  $K \neq 0$  (*cf.* Lemma 4 on page 86). The minimization of  $\mathcal{F}$  thus remains a one-dimensional minimization problem in  $K$ . The following analytical discussion follows this idea and provides the necessary details for an efficient implementation.

#### 7.4.1 Analytical Discussion

To infer from some observed distance and luminance data onto the underlying model parameters, the likelihood objective function  $\mathcal{F}$  (*cf.* Sec. 7.3) has to be minimized. In general, one cannot expect this to be explicitly doable. Therefore, it is important to understand  $\mathcal{F}$ 's behavior and to derive suitable methods for approximating its minimum.

In the following, let  $M \in \mathbb{N}$ ,  $N_m \in \mathbb{N}$ ,  $d_n^m \in \mathbb{R}_{>0}$ ,  $L_n^m \in \mathbb{R}$ ,  $\sigma_n^m \in \mathbb{R}_{>0}$  as described above, where  $m = 1, \dots, M$  and  $n = 1, \dots, N_m$  (*cf.* Sec. 7.1 and Sec. 7.3). For reasons of readability, an abbreviatory notation  $S_{\Theta}^m$  is introduced that represents sums over  $n$  with summands depending

on  $\Theta$  as described in Remark 24 on page 91; quite self-explanatory examples are

$$\begin{aligned} S_1^m &= \sum_{n=1}^{N_m} \frac{1}{(\sigma_n^m)^2}, \quad S_L^m = \sum_{n=1}^{N_m} \frac{L_n^m}{(\sigma_n^m)^2}, \quad S_e^m = \sum_{n=1}^{N_m} \frac{e^{-Kd_n^m}}{(\sigma_n^m)^2}, \quad S_{(1-e)}^m = \sum_{n=1}^{N_m} \frac{(1 - e^{-Kd_n^m})}{(\sigma_n^m)^2}, \\ S_{ed}^m &= \sum_{n=1}^{N_m} \frac{e^{-Kd_n^m} d_n^m}{(\sigma_n^m)^2}, \quad S_{LL}^m = \sum_{n=1}^{N_m} \frac{L_n^m L_n^m}{(\sigma_n^m)^2}, \quad S_{Led}^m = \sum_{n=1}^{N_m} \frac{L_n^m e^{-Kd_n^m} d_n^m}{(\sigma_n^m)^2}, \quad \dots \end{aligned} \quad (7.9)$$

Additionally,  $S_\Theta := \sum_{m=1}^M S_\Theta^m$  denote the sums over all object tracks. Furthermore, the Koschmieder term is abbreviated as

$$\mathcal{L}(K, L_{\text{air}}, L_0, d) := e^{-Kd} L_0 + (1 - e^{-Kd}) L_{\text{air}} = L_{\text{air}} + e^{-Kd} (L_0 - L_{\text{air}}),$$

where in unambiguous cases the arguments of  $\mathcal{L}$  are omitted. To allow for a more comfortable flow of reading, the proofs in this section are moved to Appendix D.

To investigate the properties of  $\mathcal{F}$  one often has to make use of its derivatives. The following lemma provides several formulations for subsequent use.

**Lemma 2** ( $\mathcal{F}$  and its Derivatives). *Let  $\mathcal{F}$  be as described above. Then, one has*

$$\begin{aligned} \mathcal{F} &= \sum_{m=1}^M \sum_{n=1}^{N_m} \frac{1}{(\sigma_n^m)^2} \left( [L_{\text{air}} + e^{-Kd_n^m} (L_0^m - L_{\text{air}})] - L_n^m \right)^2 = \sum_{m=1}^M \sum_{n=1}^{N_m} \frac{1}{(\sigma_n^m)^2} (\mathcal{L} - L_n^m)^2 \\ &= L_{\text{air}}^2 S_{(1-e)(1-e)} - 2L_{\text{air}} S_{L(1-e)} + S_{LL} + \sum_{m=1}^M \left[ 2L_{\text{air}} L_0^m S_{e(1-e)}^m + L_0^m L_0^m S_{ee}^m - 2L_0^m S_{Le}^m \right]. \end{aligned}$$

The first derivatives are given by

$$\begin{aligned} \frac{\partial \mathcal{F}}{\partial K} &= -2 \sum_{m=1}^M \sum_{n=1}^{N_m} \frac{1}{(\sigma_n^m)^2} (\mathcal{L} - L_n^m) (L_0^m - L_{\text{air}}) e^{-Kd_n^m} d_n^m, \\ \frac{\partial \mathcal{F}}{\partial L_{\text{air}}} &= 2 \sum_{m=1}^M \sum_{n=1}^{N_m} \frac{1}{(\sigma_n^m)^2} (\mathcal{L} - L_n^m) (1 - e^{-Kd_n^m}), \\ \frac{\partial \mathcal{F}}{\partial L_0^m} &= 2 \sum_{n=1}^{N_m} \frac{1}{(\sigma_n^m)^2} (\mathcal{L} - L_n^m) e^{-Kd_n^m}, \quad m = 1, \dots, M, \end{aligned}$$

or in terms of Remark 24 on page 91

$$\begin{aligned} \frac{\partial \mathcal{F}}{\partial K} &= 2L_{\text{air}}^2 S_{e(1-e)d} - 2L_{\text{air}} S_{Led} - 2 \sum_{m=1}^M \left[ L_0^m L_{\text{air}} (S_{ed}^m - 2S_{eed}^m) + L_0^m L_0^m S_{eed}^m - L_0^m S_{Led}^m \right], \\ \frac{\partial \mathcal{F}}{\partial L_{\text{air}}} &= 2L_{\text{air}} S_{(1-e)(1-e)} + 2 \sum_{m=1}^M L_0^m S_{e(1-e)}^m - 2S_L + 2S_{Le}, \\ \frac{\partial \mathcal{F}}{\partial L_0^m} &= 2L_{\text{air}} S_{e(1-e)}^m + 2L_0^m S_{ee}^m - 2S_{Le}^m, \quad m = 1, \dots, M. \end{aligned}$$

The second derivatives are given by

$$\begin{aligned}
\frac{\partial^2 \mathcal{F}}{\partial K \partial K} &= 2 \sum_{m=1}^M \sum_{n=1}^{N_m} \frac{1}{(\sigma_n^m)^2} \left[ (L_0^m - L_{air}) e^{-K d_n^m} d_n^m \right]^2 \\
&\quad + 2 \sum_{m=1}^M \sum_{n=1}^{N_m} \frac{1}{(\sigma_n^m)^2} (\mathcal{L} - L_n^m) (L_0^m - L_{air}) e^{-K d_n^m} d_n^m, \\
\frac{\partial^2 \mathcal{F}}{\partial K \partial L_{air}} &= -2 \sum_{m=1}^M \sum_{n=1}^{N_m} \frac{1}{(\sigma_n^m)^2} (1 - e^{-K d_n^m}) (L_0^m - L_{air}) e^{-K d_n^m} d_n^m \\
&\quad + 2 \sum_{m=1}^M \sum_{n=1}^{N_m} \frac{1}{(\sigma_n^m)^2} (\mathcal{L} - L_n^m) e^{-K d_n^m} d_n^m, \\
\frac{\partial^2 \mathcal{F}}{\partial K \partial L_0^m} &= -2 \sum_{n=1}^{N_m} \frac{1}{(\sigma_n^m)^2} e^{-K d_n^m} (L_0^m - L_{air}) e^{-K d_n^m} d_n^m \\
&\quad - 2 \sum_{n=1}^{N_m} \frac{1}{(\sigma_n^m)^2} (\mathcal{L} - L_n^m) e^{-K d_n^m} d_n^m, \\
\frac{\partial^2 \mathcal{F}}{\partial L_{air} \partial L_{air}} &= 2 \sum_{m=1}^M \sum_{n=1}^{N_m} \frac{1}{(\sigma_n^m)^2} (1 - e^{-K d_n^m})^2, \\
\frac{\partial^2 \mathcal{F}}{\partial L_{air} \partial L_0^m} &= 2 \sum_{n=1}^{N_m} \frac{1}{(\sigma_n^m)^2} (1 - e^{-K d_n^m}) e^{-K d_n^m}, \\
\frac{\partial^2 \mathcal{F}}{\partial L_0^m \partial L_0^l} &= 2 \delta_m^l \sum_{n=1}^{N_m} \frac{1}{(\sigma_n^m)^2} e^{-K d_n^m} e^{-K d_n^m},
\end{aligned}$$

or in terms of Remark 24 on page 91

$$\begin{aligned}
\frac{\partial^2 \mathcal{F}}{\partial K \partial K} &= 2L_{air}^2 (2S_{eadd} - S_{edd}) + 2L_{air} S_{Ledd} \\
&\quad + 2 \sum_{m=1}^M \left[ L_{air} L_0^m (S_{edd}^m - 4S_{eadd}^m) + 2L_0^m L_0^m S_{eadd}^m - L_0^m S_{Ledd}^m \right], \\
\frac{\partial^2 \mathcal{F}}{\partial K \partial L_{air}} &= -4L_{air} S_{e(1-e)d} + 2 \sum_{m=1}^M L_0^m (2S_{eed}^m - S_{ed}^m) - 2S_{Led}, \\
\frac{\partial^2 \mathcal{F}}{\partial K \partial L_0^m} &= 2L_{air} (2S_{eed}^m - S_{ed}^m) - 4L_0^m S_{eed}^m + 2S_{Led}^m, \\
\frac{\partial^2 \mathcal{F}}{\partial L_{air} \partial L_{air}} &= 2S_{(1-e)(1-e)}, \quad \frac{\partial^2 \mathcal{F}}{\partial L_{air} \partial L_0^m} = 2S_{e(1-e)}^m, \quad \frac{\partial^2 \mathcal{F}}{\partial L_0^m \partial L_0^l} = 2\delta_m^l S_{ee}^m.
\end{aligned}$$

*Proof.* This follows from straightforward calculations.  $\square$

It turns out that  $\mathcal{F}$  is neither convex nor coercive. Therefore, some of the most powerful existence and convergence theorems cannot be applied here. For later use, it is useful to understand in which way  $\mathcal{F}$  is non-coercive.

**Lemma 3** (Non-Convexity and Non-Coercivity of  $\mathcal{F}$ ). *Let  $\mathcal{F}$  be as described above. Let furthermore  $\mathcal{F}_{c,\tilde{L}}$  and  $\mathcal{F}_c$  be defined as*

$$K \mapsto \mathcal{F}_{c,\tilde{L}}(K) := \mathcal{F}(K, \tilde{L}, \dots, \tilde{L}), \quad \text{for any } \tilde{L} \in \mathbb{R},$$

which is  $\mathcal{F}$  restricted to  $L_{\text{air}} = L_0^1 = \dots = L_0^M = \tilde{L}$ , and

$$\mathcal{F}_c := \mathcal{F}_{c,\bar{L}}, \quad \text{where } \bar{L} := \frac{\sum_{m=1}^M \sum_{n=1}^{N_m} \frac{1}{(\sigma_n^m)^2} L_n^m}{\sum_{m=1}^M \sum_{n=1}^{N_m} \frac{1}{(\sigma_n^m)^2}} = \frac{S_L}{S_1}.$$

Then:

(a) For any  $\tilde{L}$  the function  $\mathcal{F}_{c,\tilde{L}}$  is constant, with

$$\mathcal{F}_c \equiv S_{LL} - \frac{S_L^2}{S_1} \leq \sum_{m=1}^M \sum_{n=1}^{N_m} \frac{1}{(\sigma_n^m)^2} (\tilde{L} - L_n^m)^2 \equiv \mathcal{F}_{c,\tilde{L}}.$$

(b)  $\mathcal{F}$  is not coercive, i.e.

$$\exists (p_n)_{n \in \mathbb{N}} \subset \mathbb{R}^{M+2}, \exists C > 0 : \quad |p_n| \rightarrow \infty, n \rightarrow \infty \quad \text{and} \quad |\mathcal{F}(p_n)| \leq C, \forall n \in \mathbb{N}.$$

(c)  $\mathcal{F}$  is not globally convex, i.e.

$$\exists p \in \mathbb{R}^{M+2}, \exists \xi \in \mathbb{R}^{M+2} \setminus \{0\} : \quad \xi^T \text{Hess } \mathcal{F}(p) \xi < 0.$$

*Proof.* The proof can be found in Appendix D on page 187. □

Although  $\mathcal{F}$  is neither convex nor coercive it provides a property that allows for a massive dimensional reduction in the search of its minimum. The linearity of Koschmieder's model (5.19) in all parameters but  $K$  makes it possible to replace the  $(M+2)$ -dimensional minimization by a 1-dimensional problem.

To achieve this, one has to study the behavior of  $\mathcal{F}$  for arbitrary but fixed  $K \in \mathbb{R}$ . The restriction of  $\mathcal{F}$  to the plane  $\{x = (x^1, \dots, x^{M+2}) \in \mathbb{R}^{M+2} : x^1 = K\}$  is denoted as  $\mathcal{F}_{f,K} : \mathbb{R}^{M+1} \rightarrow \mathbb{R}$

$$(L_{\text{air}}, L_0^1, \dots, L_0^M) \mapsto \mathcal{F}_{f,K}(L_{\text{air}}, L_0^1, \dots, L_0^M) := \mathcal{F}(K, L_{\text{air}}, L_0^1, \dots, L_0^M). \quad (7.10)$$

**Lemma 4** (Critical Points of  $\mathcal{F}_{f,K}$ ). *Let  $K \in \mathbb{R} \setminus \{0\}$  and  $\mathcal{F}_{f,K}$  be as described above. Then,  $\mathcal{F}_{f,K}$  has one and only one critical point  $(L_{\text{air}}, L_0^1, \dots, L_0^M) \in \mathbb{R}^{M+1}$  given by*

$$L_{\text{air}} = \frac{S_L - \sum_{m=1}^M \frac{S_e^m S_{Le}^m}{S_{ee}^m}}{S_1 - \sum_{m=1}^M \frac{S_e^m S_e^m}{S_{ee}^m}},$$

$$L_0^m = \frac{S_{Le}^m - L_{\text{air}} S_{e(1-e)}^m}{S_{ee}^m} = \frac{S_{Le}^m S_1 - S_{e(1-e)}^m S_L + \sum_{l=1}^M \frac{S_e^l}{S_{ee}^l} [S_{Le}^l S_{e(1-e)}^m - S_e^l S_{Le}^m]}{S_1 S_{ee}^m - S_{ee}^m \sum_{l=1}^M \frac{S_e^l S_e^l}{S_{ee}^l}}.$$

Furthermore,  $\mathcal{F}_{f,K}$  satisfies

$$\forall p \in \mathbb{R}^{M+1}, \forall \xi \in \mathbb{R}^{M+1} \setminus \{0\} : \quad \xi^T \text{Hess } \mathcal{F}_{f,K}(p) \xi > 0.$$

In particular,  $\mathcal{F}_{f,K}$  is strictly convex and uniquely minimized in  $(L_{\text{air}}, L_0^1, \dots, L_0^M)$ .

Let now  $K = 0$ . Then,  $\mathcal{F}_{f,K} = \mathcal{F}_{f,0}$  is constant in  $L_{\text{air}}$  and  $(L_{\text{air}}, L_0^1, \dots, L_0^M)$  is a critical point of  $\mathcal{F}_{f,0}$  if and only if

$$L_0^1 = \bar{L}^1 := S_L^1 / S_1^1, \dots, L_0^M = \bar{L}^M := S_L^M / S_1^M.$$

Therefore,  $\mathcal{F}_{f,0}$  has a unique line of critical points, at which it is constant and minimized:

$$\mathbb{R} \ni L_{\text{air}} \mapsto (L_{\text{air}}, \bar{L}^1, \dots, \bar{L}^M) \in \mathbb{R}^{M+1}.$$

*Proof.* The proof can be found in Appendix D on page 188.  $\square$

Based on Lemma 4 the following functions are well-defined:

$$\begin{aligned} L_{\text{air},\min} : \mathbb{R} \setminus \{0\} &\rightarrow \mathbb{R}, & K &\mapsto L_{\text{air},\min}(K) := \frac{S_L - \sum_{m=1}^M \frac{S_e^m S_{Le}^m}{S_{ee}^m}}{S_1 - \sum_{m=1}^M \frac{S_e^m S_e^m}{S_{ee}^m}}, \\ L_{0,\min}^m : \mathbb{R} \setminus \{0\} &\rightarrow \mathbb{R}, & K &\mapsto L_{0,\min}^m(K) := \frac{S_{Le}^m - L_{\text{air},\min}(K) S_{e(1-e)}^m}{S_{ee}^m}, \\ \mathcal{F}_{\min} : \mathbb{R} \setminus \{0\} &\rightarrow \mathbb{R}, & K &\mapsto \mathcal{F}_{\min}(K) := \mathcal{F}(K, L_{\text{air},\min}(K), L_{0,\min}^1(K), \dots, L_{0,\min}^M(K)). \end{aligned}$$

For later use,  $L_{\text{air},\min}$ 's numerator and denominator are denoted by

$$L_{\text{air}}^{\text{num}} \in C^\infty(\mathbb{R}), \quad L_{\text{air}}^{\text{num}} := S_L - \sum_{m=1}^M \frac{S_e^m S_{Le}^m}{S_{ee}^m} = \sum_{m=1}^M \frac{S_L S_{ee}^m - S_e^m S_{Le}^m}{S_{ee}^m}, \quad (7.11)$$

$$L_{\text{air}}^{\text{denom}} \in C^\infty(\mathbb{R}), \quad L_{\text{air}}^{\text{denom}} := S_1 - \sum_{m=1}^M \frac{S_e^m S_e^m}{S_{ee}^m} = \sum_{m=1}^M \frac{S_1 S_{ee}^m - S_e^m S_e^m}{S_{ee}^m}, \quad (7.12)$$

where the  $C^\infty$ -smoothness follows from (D.2) and elementary analysis. The derivatives of these terms, required in the following, can be found in Appendix E.

Any critical point of  $\mathcal{F}$ , with  $K \neq 0$ , has to lie on the curve

$$\mathbb{R} \setminus \{0\} \ni K \mapsto (K, L_{\text{air},\min}(K), L_{0,\min}^1(K), \dots, L_{0,\min}^M(K)) \in \mathbb{R}^{M+2}.$$

These critical points are minima of  $\mathcal{F}$  if and only if  $\mathcal{F}_{\min}$  is minimized in the associated  $K$  (cf. Lemma 6 on page 90). Therefore, in search of  $\mathcal{F}$ 's minima it is sufficient to understand the behavior of  $\mathcal{F}_{\min}$ ; examples for the shape of  $\mathcal{F}_{\min}$  can be found in Figures 7.4, 7.5 and 7.6. Based on this knowledge, it will be possible to implement an efficient minimization algorithm for  $\mathcal{F}$  (cf. 7.4.2).

**Lemma 5** (Properties of  $\mathcal{F}_{\min}$ ). *Let  $\mathcal{F}_{\min}$  be as described above and let some distances  $d_{n_1}^m$  and  $d_{n_2}^m$  differ for at least one  $m$ , i.e.*

$$\exists m \in \{1, \dots, M\}, \exists n_1, n_2 \in \{1, \dots, N_m\} : d_{n_1}^m \neq d_{n_2}^m. \quad (7.13)$$

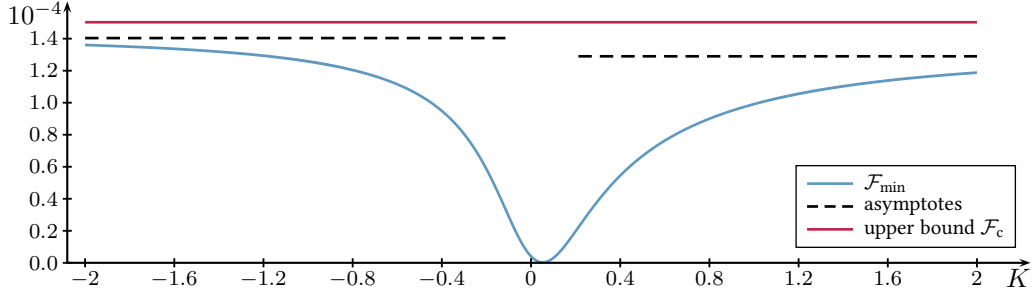


Figure 7.4: Example for  $\mathcal{F}_{\min}$  and  $\mathcal{F}_c$ . The minimum of  $\mathcal{F}_{\min}$  lies at about  $K = 0.0335 \text{ m}^{-1}$ , which corresponds to  $d_{\text{met}} \approx 89 \text{ m}$ .

Then, the following holds:

- (a)  $\mathcal{F}_{\min}$  is continuous on  $\mathbb{R} \setminus \{0\}$ , where 0 is a removable discontinuity.  
(b)  $\mathcal{F}_{\min} : \mathbb{R} \rightarrow \mathbb{R}$  can be written as

$$\mathcal{F}_{\min} = \left[ S_{LL} - \sum_{m=1}^M \frac{S_{Le}^m S_{Le}^m}{S_{ee}^m} \right] - \frac{\left( S_L - \sum_{m=1}^M \frac{S_e^m S_{Le}^m}{S_{ee}^m} \right)^2}{S_1 - \sum_{m=1}^M \frac{S_e^m S_e^m}{S_{ee}^m}},$$

where

$$\mathcal{F}_{\min}(0) = \left[ S_{LL} - \sum_{m=1}^M \frac{S_L^m S_L^m}{S_1^m} \right] - \frac{\left( S_{Ld} - \sum_{m=1}^M \frac{S_L^m S_d^m}{S_1^m} \right)^2}{S_{dd} - \sum_{m=1}^M \frac{S_d^m S_d^m}{S_1^m}}.$$

- (c)  $\mathcal{F}_{\min}$  is uniformly bounded by

$$0 \leq \mathcal{F}_{\min} \leq \mathcal{F}_c \equiv \sum_{m=1}^M \sum_{n=1}^{N_m} \frac{1}{(\sigma_n^m)^2} (\bar{L} - L_n^m)^2 = S_{LL} - \frac{S_L^2}{S_1}.$$

- (d)  $\mathcal{F}_{\min}$  has two horizontal asymptotes:

$$\lim_{K \rightarrow \infty} \mathcal{F}_{\min}(K) = \left[ S_{LL} - \sum_{m=1}^M \frac{(L_{\min}^m)^2}{(\sigma_{\min}^m)^2} \right] - \frac{\left( S_L - \sum_{m=1}^M \frac{L_{\min}^m}{(\sigma_{\min}^m)^2} \right)^2}{S_1 - \sum_{m=1}^M \frac{1}{(\sigma_{\min}^m)^2}},$$

$$\lim_{K \rightarrow -\infty} \mathcal{F}_{\min}(K) = \left[ S_{LL} - \sum_{m=1}^M \frac{(L_{\max}^m)^2}{(\sigma_{\max}^m)^2} \right] - \frac{\left( S_L - \sum_{m=1}^M \frac{L_{\max}^m}{(\sigma_{\max}^m)^2} \right)^2}{S_1 - \sum_{m=1}^M \frac{1}{(\sigma_{\max}^m)^2}},$$

where  $L_{\min}^m, L_{\max}^m, \sigma_{\min}^m$  and  $\sigma_{\max}^m$  correspond to the minimal and maximal  $d_n^m$  values, respectively:

$$n_{\min}^m := \operatorname{argmin}_{n \in \{1, \dots, N_m\}} d_n^m, \quad L_{\min}^m := L_{n_{\min}^m}^m, \quad \sigma_{\min}^m := \sigma_{n_{\min}^m}^m,$$

$$n_{\max}^m := \operatorname{argmax}_{n \in \{1, \dots, N_m\}} d_n^m, \quad L_{\max}^m := L_{n_{\max}^m}^m, \quad \sigma_{\max}^m := \sigma_{n_{\max}^m}^m.$$

(e)  $\mathcal{F}_{\min} \in C^\infty(\mathbb{R})$ , where

$$\begin{aligned}\mathcal{F}'_{\min}(K) &= \frac{\partial \mathcal{F}}{\partial K}(K, L_{air, \min}(K), L_{0, \min}^1(K), \dots, L_{0, \min}^M(K)) \\ &= 2 \sum_{m=1}^M \frac{S_{Led}^m S_{Le}^m S_{ee}^m - S_{eed}^m S_{Le}^m S_{Le}^m}{S_{ee}^m S_{ee}^m} \\ &\quad - \frac{2L_{air}^{num}(K)L_{air}^{num'}(K)L_{air}^{denom}(K) - (L_{air}^{num}(K))^2 L_{air}^{denom'}(K)}{(L_{air}^{denom})^2}\end{aligned}$$

and

$$\begin{aligned}\mathcal{F}'_{\min}(0) &= 2 \sum_{m=1}^M \frac{S_{Ld}^m S_L^m S_1^m - S_L^m S_L^m S_d^m}{S_1^m S_1^m} \\ &\quad - L_{air}^{num'}(0) \frac{6L_{air}^{num''}(0)L_{air}^{denom''}(0) - 2L_{air}^{num'}(0)L_{air}^{denom'''}(0)}{3(L_{air}^{denom''}(0))^2}\end{aligned}$$

and

$$\begin{aligned}\mathcal{F}''_{\min} &= 2 \sum_{m=1}^M \left[ \frac{-S_{Ledd}^m S_{Le}^m S_{ee}^m S_{ee}^m - S_{Led}^m S_{Led}^m S_{ee}^m S_{ee}^m + 4S_{Led}^m S_{Le}^m S_{eed}^m S_{ee}^m}{S_{ee}^m S_{ee}^m S_{ee}^m} \right. \\ &\quad \left. + \frac{2S_{Le}^m S_{Le}^m S_{eed}^m S_{ee}^m - 4S_{Le}^m S_{Le}^m S_{eed}^m S_{eed}^m}{S_{ee}^m S_{ee}^m S_{ee}^m} \right] \\ &\quad - \left[ \frac{2(L_{air}^{num'})^2 (L_{air}^{denom})^2 + (L_{air}^{num})^2 (L_{air}^{denom'})^2 + L_{air}^{num} L_{air}^{num''} (L_{air}^{denom})^2}{(L_{air}^{denom})^3} \right. \\ &\quad \left. - \frac{4L_{air}^{num} L_{air}^{num'} L_{air}^{denom} L_{air}^{denom'} + (L_{air}^{num})^2 L_{air}^{denom} L_{air}^{denom''}}{(L_{air}^{denom})^3} \right]\end{aligned}$$

and

$$\begin{aligned}\mathcal{F}''_{\min}(0) &= 2 \sum_{m=1}^M \left[ \frac{-S_{Ldd}^m S_L^m S_1^m S_1^m - S_{Ld}^m S_{Ld}^m S_1^m S_1^m + 4S_{Ld}^m S_L^m S_d^m S_1^m}{(S_1^m)^3} \right. \\ &\quad \left. + \frac{2S_L^m S_L^m S_{dd}^m S_1^m - 4S_L^m S_L^m S_d^m S_d^m}{(S_1^m)^3} \right] \\ &\quad - \left[ \frac{9(L_{air}^{num''}(0))^2 (L_{air}^{denom''}(0))^2 + 12L_{air}^{num'}(0)L_{air}^{num'''}(0) (L_{air}^{denom''}(0))^2}{9(L_{air}^{denom''}(0))^3} \right. \\ &\quad \left. + \frac{-12L_{air}^{num'}(0)L_{air}^{num''}(0)L_{air}^{denom''}(0)L_{air}^{denom'''}(0)}{9(L_{air}^{denom''}(0))^3} \right. \\ &\quad \left. + \frac{4(L_{air}^{num'}(0))^2 (L_{air}^{denom'''}(0))^2 - 3(L_{air}^{num'}(0))^2 L_{air}^{denom''}(0)L_{air}^{denom'''}(0)}{9(L_{air}^{denom''}(0))^3} \right].\end{aligned}$$

The required derivatives of  $L_{air}^{num}$  and  $L_{air}^{denom}$  are given in Appendix E.

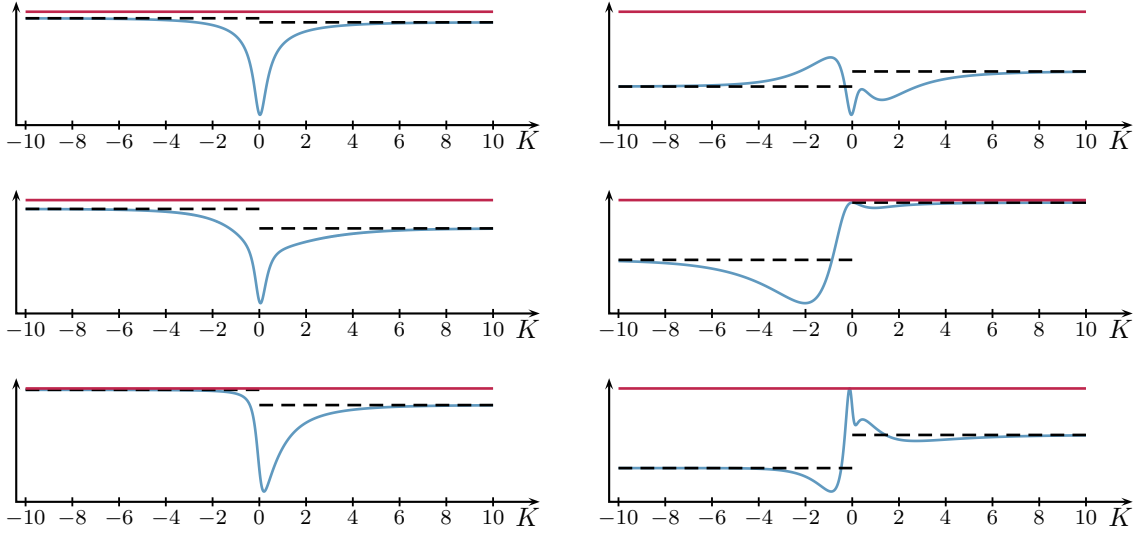


Figure 7.5: Examples for  $\mathcal{F}_{\min}$ . For all cases of somehow useful data  $\mathcal{F}_{\min}$  is quasiconvex (left). However, in contrast to the simple standard behavior,  $\mathcal{F}_{\min}$  can be almost arbitrarily shaped whenever the noise on the data largely exceeds the dynamic of the undisturbed signal (right).

*Proof.* The proof can be found in Appendix D on page 190.  $\square$

As mentioned above, the critical points of  $\mathcal{F}$  can be characterized by critical points of  $\mathcal{F}_{\min}$ . Therefore, the  $(M + 2)$ -dimensional exploration of  $\mathcal{F}$  regarding its minima can be replaced by a 1-dimensional minimum search on  $\mathcal{F}_{\min}$ . The following lemma summarizes the connection between  $\mathcal{F}$ 's and  $\mathcal{F}_{\min}$ 's critical points.

**Lemma 6** (Characterization of  $\mathcal{F}$ 's Critical Points). *Let  $\mathcal{F}_{\min}$  be as described above. Then, the following holds:*

(a)  $(K, L_{air}, L_0^m, \dots, L_0^M) \in \mathbb{R}^{M+2}$  is a critical point of  $\mathcal{F}$  if and only if

$$\begin{aligned} K \neq 0 \quad \wedge \quad & \mathcal{F}'_{\min}(K) = 0 \\ & \wedge \quad (L_{air}, L_0^1, \dots, L_0^M) = (L_{air, \min}(K), L_{0, \min}^1(K), \dots, L_{0, \min}^M(K)) \end{aligned}$$

or

$$\begin{aligned} K = 0 \quad \wedge \quad & (L_0^m, \dots, L_0^M) = (\bar{L}^1, \dots, \bar{L}^M) \quad \text{where} \quad \bar{L}^m = \frac{S_L^m}{S_1^m} \\ & \wedge \quad L_{air} \sum_{m=1}^M \left[ S_{Ld}^m - \frac{S_L^m S_d^m}{S_1^m} \right] = \sum_{m=1}^M \frac{S_L^m}{S_1^m} \left[ S_{Ld}^m - \frac{S_L^m S_d^m}{S_1^m} \right]. \end{aligned} \quad (7.14)$$

(b) For  $K \neq 0$ ,  $(K, L_{air}, L_0^m, \dots, L_0^M) \in \mathbb{R}^{M+2}$  is a (strict) local minimum of  $\mathcal{F}$  if and only if

$$\begin{aligned} \mathcal{F}'_{\min}(K) = 0 \quad \wedge \quad & \mathcal{F}''_{\min}(K) \geq 0 \quad (\text{strict case: } \mathcal{F}''_{\min}(K) > 0) \\ & \wedge \quad (L_{air}, L_0^1, \dots, L_0^M) = (L_{air, \min}(K), L_{0, \min}^1(K), \dots, L_{0, \min}^M(K)). \end{aligned}$$

(c) For  $K \neq 0$ ,  $\mathcal{F}$  has no local maximum.

*Proof.* The proof can be found in Appendix D on page 197.  $\square$

**Remark 22** (Critical Point Constraint for  $L_{\text{air}}$  in  $K = 0$ ). The constraint (7.14) is equivalent to

$$\begin{aligned} & \left[ S_{\text{Ld}} - \sum_{m=1}^M \frac{S_{\text{L}}^m S_{\text{d}}^m}{S_1^m} = 0 \quad \wedge \quad \sum_{m=1}^M \frac{S_{\text{L}}^m}{S_1^m} \left( S_{\text{Ld}} - \frac{S_{\text{L}}^m S_{\text{d}}^m}{S_1^m} \right) = 0 \right] \\ \vee & \left[ S_{\text{Ld}} - \sum_{m=1}^M \frac{S_{\text{L}}^m S_{\text{d}}^m}{S_1^m} \neq 0 \quad \wedge \quad L_{\text{air}} = \frac{\sum_{m=1}^M \frac{S_{\text{L}}^m}{S_1^m} \left( S_{\text{Ld}} - \frac{S_{\text{L}}^m S_{\text{d}}^m}{S_1^m} \right)}{\sum_{m=1}^M \left( S_{\text{Ld}} - \frac{S_{\text{L}}^m S_{\text{d}}^m}{S_1^m} \right)} \right]. \end{aligned}$$

**Remark 23** ( $L_{\text{air},\min}$  at 0). In contrast to  $L_{0,\min}$  and  $\mathcal{F}_{\min}$ , the discontinuity of  $L_{\text{air},\min}$  in 0 can only be removed if and only if

$$S_{\text{Ld}} - \sum_{m=1}^M \frac{S_{\text{L}}^m S_{\text{d}}^m}{S_1^m} = 0.$$

This, for instance, is true for  $L_n^m$  all being equal. However, this is a rare case and cannot be expected for noisy data.

**Remark 24** (Sum Notations  $S_{\Theta}^m$ ,  $S_{\Theta}$ ). For the analytical discussion of  $\mathcal{F}$  and to allow for an efficient implementation of the proposed minimization algorithm in 7.4.2, an abbreviatory notation  $S_{\Theta}^m$  is introduced. The subscript  $\Theta$  has to be a word over the alphabet  $\mathcal{A} := \{1, \text{L}, \text{e}, (1-\text{e}), \text{d}\}$ . The term  $S_{\Theta}^m$  represents a sum over  $n$ , where each symbol  $s_k \in \mathcal{A}$  in  $\Theta = s_1 s_2 \dots$  corresponds to a factor of the summand:

$$S_{\Theta}^m = S_{s_1 s_2 \dots}^m := \sum_{n=1}^{N_m} \frac{f(s_1) f(s_2) \dots}{(\sigma_n^m)^2},$$

where

$$f(1) = 1, \quad f(\text{L}) = L_n^m, \quad f(\text{e}) = e^{-K d_n^m}, \quad f(1-\text{e}) = 1 - e^{-K d_n^m}, \quad f(\text{d}) = d_n^m.$$

Additionally,  $S_{\Theta} := \sum_{m=1}^M S_{\Theta}^m$  denote the respective sums over all object tracks. Examples for sums  $S_{\Theta}^m$  can be found in (7.9).

## 7.4.2 Derived Algorithms

Based on 7.4.1 it is now possible to derive highly efficient algorithms for the minimization of  $\mathcal{F}$ .

Firstly, the so-called *fastMLE* algorithm is briefly introduced (already published in [Len2014]). In order to solve the one-dimensional equation (7.18), Newton's method is used, which leads to a simple and quite reliable parameter estimation.

Beyond this naïve approach, a more sophisticated algorithm is introduced which takes advantage of further insights from 7.4.1. In this way, it is possible to take into account the range of convergence of Newton's method and to handle the numerically unstable neighborhood of 0. Although the so-called *advFastMLE* algorithm appears to be more complex (*cf.* Fig. 7.7), the run-time turns out to be basically equal to the *fastMLE*'s (*cf.* Fig. 7.21), which can be explained by a new low-cost initial Newton step based on the careful discussion of  $\mathcal{F}_{\min}$  at 0 (*cf.* Lemma 5 on page 87).

**Fast Maximum Likelihood Parameter Estimation (fastMLE).** Due to Lemma 2 on page 84 and as demonstrated in the proof of Lemma 4 on page 86 (cf. (D.1)), the critical point equations  $\nabla \mathcal{F}(K, L_{\text{air}}, L_0^1, \dots, L_0^M) = 0$  are equivalent to

$$0 = -\frac{1}{2} \frac{\partial \mathcal{F}}{\partial K} = L_{\text{air}}^2 (S_{\text{eed}} - S_{\text{ed}}) + L_{\text{air}} S_{\text{Led}} + \sum_{m=1}^M [L_{\text{air}} L_0^m (S_{\text{ed}}^m - 2S_{\text{eed}}^m) - L_0^m S_{\text{ed}}^m + L_0^m L_0^m S_{\text{eed}}^m], \quad (7.15)$$

$$\wedge \begin{pmatrix} S_{\text{L}} \\ S_{\text{Le}}^1 \\ \vdots \\ S_{\text{Le}}^M \end{pmatrix} = \begin{pmatrix} S_1 - S_{\text{e}} & S_{\text{e}}^1 & \dots & S_{\text{e}}^M \\ S_{\text{e}}^1 - S_{\text{ee}}^1 & S_{\text{ee}}^1 & & \\ \vdots & & \ddots & \\ S_{\text{e}}^M - S_{\text{ee}}^M & & & S_{\text{ee}}^M \end{pmatrix} \begin{pmatrix} L_{\text{air}} \\ L_0^1 \\ \vdots \\ L_0^M \end{pmatrix}, \quad (7.16)$$

which for  $K \neq 0$  can be uniquely solved in  $L_{\text{air}}$  and  $L_0^m$  by successively applying

$$L_{\text{air}} = \frac{S_{\text{L}} - \sum_{m=1}^M \frac{S_{\text{e}}^m S_{\text{Le}}^m}{S_{\text{ee}}^m}}{S_1 - \sum_{m=1}^M \frac{S_{\text{e}}^m S_{\text{e}}^m}{S_{\text{ee}}^m}}, \quad L_0^m = \frac{S_{\text{Le}}^m + L_{\text{air}} (S_{\text{ee}}^m - S_{\text{e}}^m)}{S_{\text{ee}}^m}. \quad (7.17)$$

Substituting  $L_0^m$  and  $L_{\text{air}}$  in equation (7.15) leads to a one-dimensional equation in  $K$ . In terms of 7.4.1 this can be written as

$$0 = \chi(K) := -\frac{1}{2} \frac{\partial \mathcal{F}}{\partial K}(K, L_{\text{air}, \min}(K), L_{0, \min}^1(K), \dots, L_{0, \min}^M(K)). \quad (7.18)$$

Therefore, (7.18) is satisfied for a  $K \neq 0$  if and only if

$$\exists L_{\text{air}}, L_0^1, \dots, L_0^M : \quad \nabla \mathcal{F}(K, L_{\text{air}}, L_0^1, \dots, L_0^M) = 0.$$

Assuming a starting value close enough to such a critical point, equation (7.18) can be solved efficiently by applying Newton's method, iterating  $K \leftarrow K - \chi(K)/\chi'(K)$  (cf. Algorithm 1). The starting value is set to  $K = 10^{-3} \text{ m}^{-1}$  ( $d_{\text{met}} \approx 3000 \text{ m}$ ) and all meteorological visibilities above 3000 m are understood as unlimited. The main stopping criterion is the relative change in the estimated  $d_{\text{met}}$  being smaller than 1 %:

$$\frac{|d_{\text{met}} - d_{\text{met}}^{\text{old}}|}{\min\{d_{\text{met}}, d_{\text{met}}^{\text{old}}\}} \stackrel{(3.5)}{=} \frac{|K - K_{\text{old}}|}{\min\{K, K_{\text{old}}\}} < 10^{-2}. \quad (7.19)$$

Although the algorithm usually converges after 3 iterations, a maximum number of 10 iterations is allowed.

It should also be noted that, in contrast to standard minimization techniques, only one starting value has to be specified, which simplifies both implementation and application of fastMLE.

**Advanced Fast Maximum Likelihood Parameter Estimation (advFastMLE).** Although the fastMLE algorithm already provides a suitable method for tracking-based visibility estimation, it still can be improved by making use of further insights from the analytical discussion in 7.4.1. One of the main problems of fastMLE can be found in the fact that it does not properly handle the discontinuities of  $L_{\text{air}, \min}$ ,  $L_{0, \min}$  and in turn  $\mathcal{F}_{\min}$  in  $K = 0$ . While  $L_{0, \min}$ 's discontinuity can be

**Algorithm 1** Fast Maximum Likelihood Parameter Estimation

---

```

1: procedure FASTMLE( $d_n^m, L_n^m, \sigma_n^m$ )
2:    $K \leftarrow 10^{-3}$ 
3:    $curlter \leftarrow 1$  ▷ current iteration
4:   repeat
5:     compute  $\exp(-K d_n^m)$  ▷ computationally most expensive step
6:     compute  $S_*^*(K)$  ▷ using  $\exp(-K d_n^m), L_n^m, d_n^m, \sigma_n^m$ 
7:     compute  $L_{\text{air},\min}(K), L'_{\text{air},\min}(K)$  ▷ using  $S_*^*(K)$ 
8:     compute  $L_{0,\min}^m(K), L_{0,\min}^{m'}(K)$  ▷ using  $L_{\text{air},\min}(K), L'_{\text{air},\min}(K), S_*^*(K)$ 
9:     compute  $\chi(K), \chi'(K)$  ▷ using  $L_{\text{air},\min}(K), L'_{\text{air},\min}(K), L_{0,\min}^m(K), L_{0,\min}^{m'}(K), S_*^*(K)$ 

10:     $K_{\text{old}} \leftarrow K$ 
11:     $K \leftarrow K_{\text{old}} - \chi(K)/\chi'(K)$ 
12:    if  $K < 10^{-3} \text{ m}^{-1}$  then
13:      return 0 ▷ unlimited meteorological visibility
14:    end if
15:     $curlter \leftarrow curlter + 1$ 
16:  until  $curlter > 10 \vee |K_{\text{old}} - K| < 10^{-2} \cdot \min\{K, K_{\text{old}}\}$  ▷ cf. (7.19)
17:  return  $K$ 
18: end procedure

```

---

removed in 0, one cannot expect this behavior from  $L_{\text{air},\min}$  (cf. Remark 23), i.e. usually one has  $|L_{\text{air},\min}(K)| \rightarrow \infty$  for  $K \rightarrow 0$ . This is why line 7 in Algorithm 1 leads to numerical instabilities close to 0, wherefore fastMLE has to be stopped for  $K < 10^{-3} \text{ m}^{-1}$ .

In contrast to that, the advFastMLE is directly based on  $\mathcal{F}_{\min}$  and its explicit derivatives provided in Lemma 5 on page 87. It turns out that in this way the numerical instabilities can be reduced to an about  $10^4$  times smaller interval around 0. Running simulations based on double precision (64bit) floating-point numbers, the largest observed instability for fastMLE lays at about  $10^{-4} \text{ m}^{-1}$ , whereas for advFastMLE no instability occurred beyond  $10^{-8} \text{ m}^{-1}$ .

Another advantage of advFastMLE is a low-cost first iteration due to the use of  $K = 0$  as the starting value. Thanks to Lemma 5(e) on page 88,  $\mathcal{F}_{\min}(0)$ ,  $\mathcal{F}'_{\min}(0)$  and  $\mathcal{F}''_{\min}(0)$  can be computed explicitly without the need of any exp-evaluations, which usually constitute the computationally most expensive steps of an iteration. Since Newton's method is an extremely fast converging algorithm (usually converges in 3 steps here) even one single low-cost step significantly increases the performance.

The only assumption that is made to derive the advFastMLE algorithm is  $\mathcal{F}_{\min}$  being quasiconvex. This property can be observed across all reliable examples and is further discussed in 7.4.3. Based on this assumption, the domain of  $\mathcal{F}_{\min}$  can be divided into three disjoint intervals

$$\begin{aligned}
I_L &:= \{K \in \mathbb{R} : \mathcal{F}'_{\min}(K) < 0 \wedge \mathcal{F}''_{\min}(K) < 0\}, \\
I_{\text{mid}} &:= \{K \in \mathbb{R} : \mathcal{F}''_{\min}(K) \geq 0\}, \\
I_R &:= \{K \in \mathbb{R} : \mathcal{F}'_{\min}(K) > 0 \wedge \mathcal{F}''_{\min}(K) < 0\},
\end{aligned} \tag{7.20}$$

where, due to the quasiconvexity of  $\mathcal{F}_{\min}$  and its uniform boundedness (cf. Lemma 5(c) on page

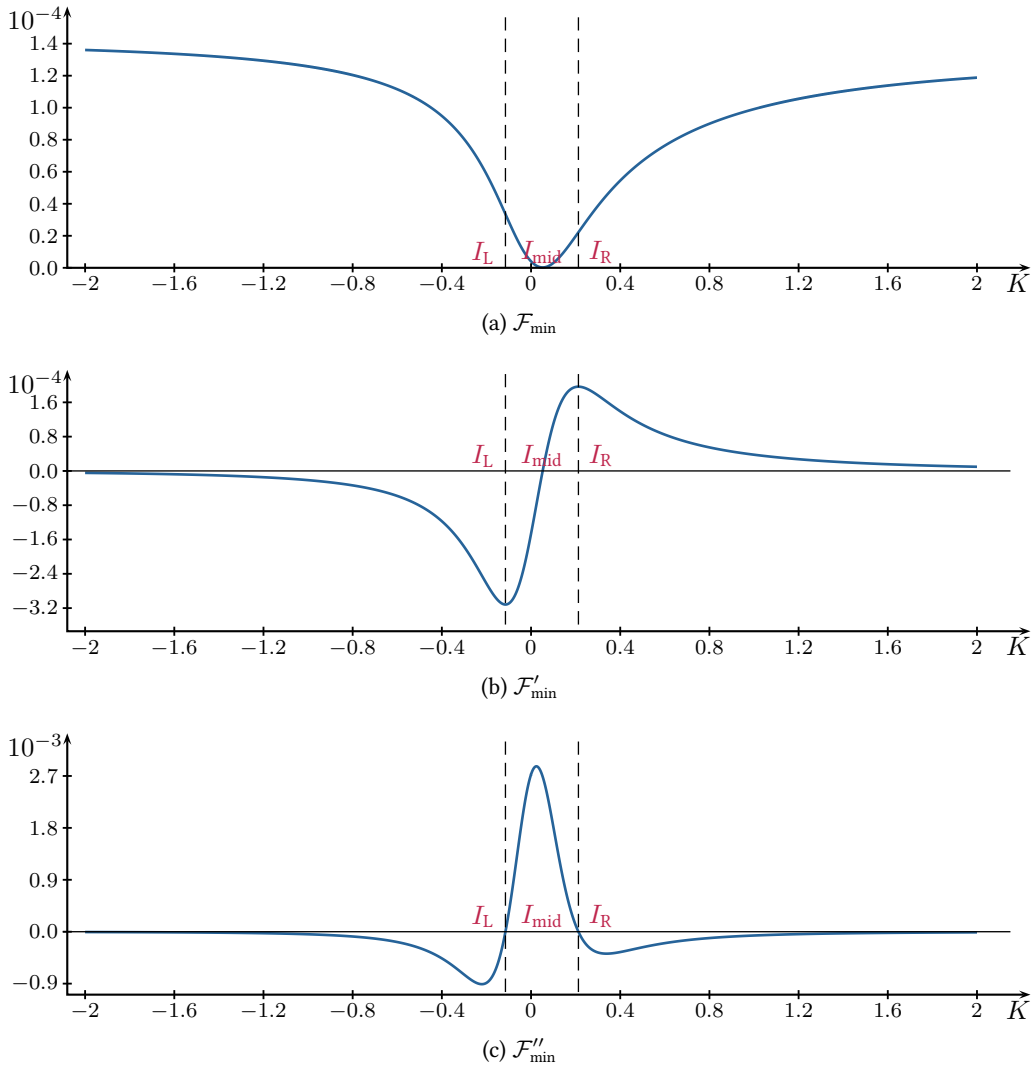


Figure 7.6: Left, middle and right interval for a quasiconvex and uniform bounded  $\mathcal{F}_{\min}$ .

88), one has

$$I_L < I_{\text{mid}} < I_R \quad \text{and} \quad I_L \dot{\cup} I_{\text{mid}} \dot{\cup} I_R = \mathbb{R},$$

also *cf.* Fig. 7.6. Moreover, the setting of quasiconvexity and uniform boundedness in particular leads to a guaranteed existence of a unique minimum of  $\mathcal{F}_{\min}$ .

In order to approximate this minimum by Newton's method, one has to start within its range of convergence. Obviously, this range of convergence is a subset of  $I_{\text{mid}}$ , wherefore advFastMLE switches to a bisection approach whenever  $K \in I_L \cup I_R$  or the latest Newton iteration has not been successful. Furthermore, a search range is initially defined by a left bound  $K_L := 0$  and a right bound  $K_R := 3 \text{ m}^{-1}$ . If the minimum of  $\mathcal{F}_{\min}$  is not situated within this search range, the algorithm returns *out of range*.

The advFastMLE algorithm in the first place tries to start a Newton iteration in  $K_L$ . However, within the bisection mode it updates the left and the right side of the search range. Switching back to the Newton iteration the algorithm continues its work on the latest updated value  $K_L$  or

$K_R$ . This is represented by the  $K_\Theta$  notation, where  $\Theta \in \{L, R\}$ .

Whenever there is no need to, the advFastMLE algorithm avoids the evaluation of  $\mathcal{F}_{\min}$  in  $K_R$ . However, in some cases  $\mathcal{F}_{\min}$  has to be evaluated in  $K_R$  as this is required to check whether the minimum of  $\mathcal{F}_{\min}$  lies beyond  $K_R$  and thus not in the search range. To remember whether the right side of the search range has already been checked, the flag `rsc_flag`  $\in \{true, false\}$  is introduced.

All details about advFastMLE can be found in the flowchart Fig. 7.7.

**Remark 25** ((7.18) in Terms of  $\mathcal{F}_{\min}$ ). Although the numerical computation of the Newton step in fastMLE and advFastMLE are substantially different, they are equivalent from an analytical point of view. This is due to (D.7), which yields  $\chi(K) = \mathcal{F}'_{\min}(K)/2$ . Therefore, it might be reasonable to use  $\chi(K)$  and  $\chi'(K)$  for  $K$  large enough, since their computation is slightly cheaper than the computation of  $\mathcal{F}'_{\min}$  and  $\mathcal{F}''_{\min}$ .

**Remark 26** (Predicted Starting Values). In a sequence of visibility estimations within narrow time frames it is reasonable to assume a slowly changing atmosphere. Instead of taking the starting values for fastMLE and advFastMLE as fixed values  $10^{-3}$  and 0, respectively, one could thus also use a predicted value based on the preceding observations. Due to inaccuracies of the estimations and a possible non-smoothness of the atmosphere the best approach is probably to simply use the latest successful estimation of  $K$  as new starting value.

**Remark 27** (Case:  $M = 1$ ). For the case  $M = 1$ , many of the terms in the analytical discussion and the algorithm from above can be rearranged and simplified, such as

$$L_{\text{air,min}} = \frac{S_L - \sum_{m=1}^M \frac{S_e^m S_{Le}^m}{S_{ee}^m}}{S_1 - \sum_{m=1}^M \frac{S_e^m S_e^m}{S_{ee}^m}} = \frac{S_L S_{ee} - S_e S_{Le}}{S_1 S_{ee} - S_e S_e}.$$

Since single object tracks are a typical scenario, it might be useful to take a closer look at this case. This could lead to a simplified and deeper analytical discussion as well as a more efficient implementation. One can expect some of the open problems in 7.4.3 to be solvable more easily for this case than for the general case.

### 7.4.3 Open Questions and Conjectures

Even after the quite deep analytical discussion on  $\mathcal{F}$  and  $\mathcal{F}_{\min}$  in 7.4.1, a number of more or less relevant open questions are remaining. It is not only an interesting but also a promising task to take care of these problems in the future. Since some of them might be hidden beneath the theoretical discussion above, they are pointed out explicitly in the following.

**Existence.** Although one can find explicit bounds (and even explicit asymptotes) on the continuous function  $\mathcal{F}_{\min}$ , a valid argument for the general existence of a local or even global minimum is still missing. Until now, no case could be observed where the existence assumption has been violated. Nevertheless, depending on the data it is easily conceivable that e.g. one of the asymptotes is decreasing to a value below the rest of  $\mathcal{F}_{\min}$ , i.e. e.g.  $\lim_{\hat{K} \rightarrow \infty} \mathcal{F}_{\min}(\hat{K}) < \mathcal{F}_{\min}(K)$  for all  $K \in \mathbb{R}$ . It would be interesting to find criteria on the data excluding these cases or even to find a general proof that the existence of a global or local minimum can be guaranteed.

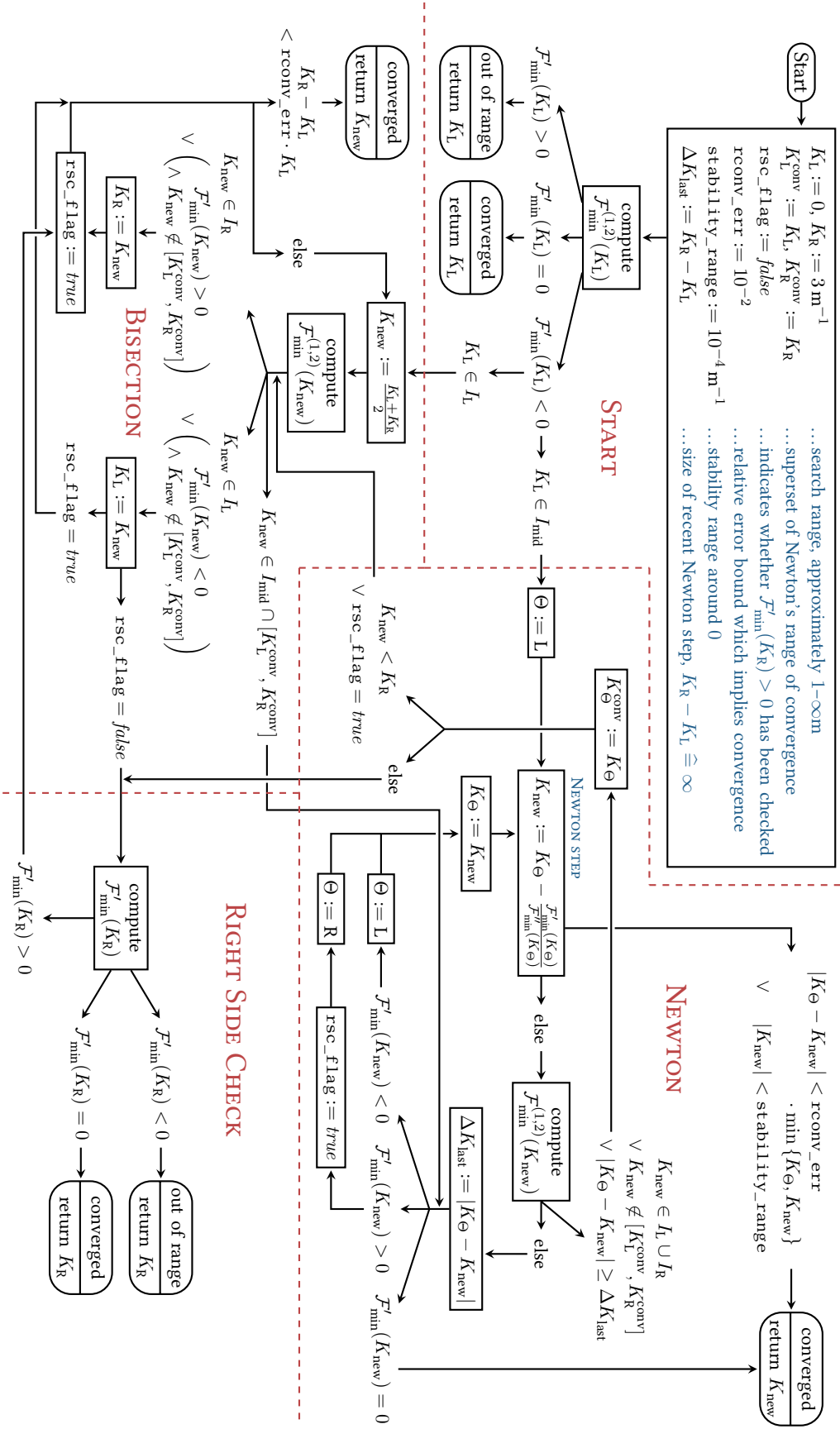


Figure 7.7: Flowchart for Advanced Fast Maximum Likelihood Parameter Estimation (advFastMLE)

**Uniqueness.** As can be seen in Fig. 7.5, there are cases where  $\mathcal{F}_{\min}$  shows a quite chaotic behavior with more than just one local minimum. In all reasonable cases, where the data quality allows for a useful estimation of  $K$ , however, the minimum of  $\mathcal{F}_{\min}$  seems to be unique. This is indicated by tests on the simplicity of  $\mathcal{F}_{\min}$  as provided below (cf. e.g. Fig. 7.8). One can observe the chaotic behavior especially when the noise on the data largely exceeds the dynamic of the undisturbed signal. Therefore, it might be useful to find a criterion on the signal-to-noise ratio that guarantees a simple unique minimum. Another observation from numerical experiments is that monotonous data seems to guarantee this simple behavior of  $\mathcal{F}_{\min}$ . The use of this observation, however, would require further investigations on the optimal way to make the data monotone, the impact on the estimation results and a proof for the implication between monotonicity and uniqueness. This will not be part of this work.

**Quasiconvexity.** Another property that can be expected for good-natured data is the quasiconvexity of  $\mathcal{F}_{\min}$ . One should note that quasiconvexity combined with the a-priori bounds from Lemma 5 on page 87 in particular implies the existence and uniqueness properties from above. Similar to what has been said for the uniqueness, numerical experiments suggest that quasiconvexity is a very likely property that might even be given for all cases of monotonous data or almost monotonous data.

**Simplicity.** Since the quasiconvexity of  $\mathcal{F}_{\min}$  cannot numerically be checked without further analytical investigations, another property is introduced which can be understood as quasiconvexity and boundedness (implying uniqueness and existence) of  $\mathcal{F}_{\min}$  on a test set of sampling points chosen as

$$\mathcal{S}_{\text{check}} := \{-1 \text{ m}^{-1}, -0.99 \text{ m}^{-1}, \dots, 3.99 \text{ m}^{-1}, 4 \text{ m}^{-1}\}.$$

According to (7.20), this so-called *simplicity* of  $\mathcal{F}_{\min}$  is formally given whenever there exist successively arranged intervals  $I_L < I_{\text{mid}} < I_R$ , s.t.  $\mathbb{R} = I_L \dot{\cup} I_{\text{mid}} \dot{\cup} I_R$  and for all  $K \in \mathcal{S}_{\text{check}}$

$$\begin{aligned} K \in I_L &\Leftrightarrow \mathcal{F}'_{\min}(K) < 0 \wedge \mathcal{F}''_{\min}(K) < 0, \\ K \in I_{\text{mid}} &\Leftrightarrow \mathcal{F}''_{\min}(K) \geq 0, \\ K \in I_R &\Leftrightarrow \mathcal{F}'_{\min}(K) > 0 \wedge \mathcal{F}''_{\min}(K) < 0. \end{aligned}$$

To figure out in which cases one can or cannot expect the simplicity of  $\mathcal{F}_{\min}$ , noise-free artificial distance-luminance data for single objects is created by the simulation framework described in Fig. 7.20. Afterwards, the luminance signal is disturbed by additive Gaussian noise of a level relative to the luminance range of the observation, i.e.

$$L_{\text{noisy},n}^m \sim L_{\text{undisturbed},n}^m + \text{noiselevel} \cdot \left( \max_n L_{\text{undisturbed},n}^m - \min_n L_{\text{undisturbed},n}^m \right) \cdot \mathcal{N}(0, 1).$$

A large number of simulations is performed for different values for  $N$ ,  $d_{\text{met}}$  and the noise level. The results are provided in Fig. 7.8. One can see that up to a noise level of about 20 % one can reliably expect simplicity.

However, in the work on data automatically extracted from camera images one has to include the handling of bad corner cases. The algorithm should thus be able to recognize most of those cases which could otherwise lead to useless and misleading results. To achieve this, one has to decide directly from the distance-luminance data whether simplicity can be expected. According to the observations from Fig. 7.8, the noise level could be a good features for a decision like this.

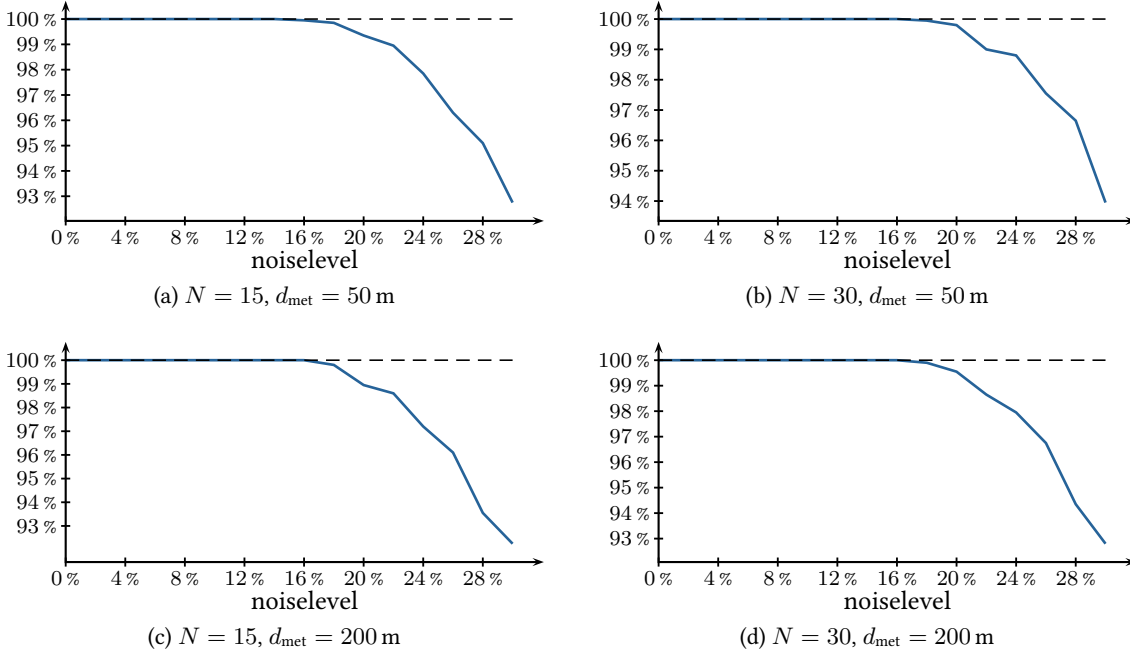


Figure 7.8: Numerical tests on simplicity for different values for  $N$ ,  $d_{\text{met}}$  and the noise level. The probability of simplicity is estimated from 2000 simulations for each noise level in each plot. The number of objects is set to  $M = 1$ .

If the noise level relative to the dynamic range of the signal is small enough, one can expect the resulting  $\mathcal{F}_{\text{min}}$  to be simple. Another desirable property of such a feature is the invariance under linear transformation of the luminance data. The resulting classifier would thus be independent of linear transformations due to different camera models or data representations.

One feature satisfying these constraints is the normalized estimated standard deviation (*cf.* Appendix C)

$$f_{\text{std}} = \frac{1}{\max_n L_n - \min_n L_n} \sqrt{\frac{1}{2(N-1)} \sum_{n=1}^{N-1} (L_{n+1} - L_n)^2}.$$

This feature is fast to compute and invariant under linear transformations. Fig. 7.9 shows the resulting relation between the feature  $f_{\text{std}}$  and  $\mathcal{F}_{\text{min}}$ 's simplicity for several simulations. A strict threshold based on this feature could, for instance, be set to the smallest  $f_{\text{std}}$  where non-simplicity occurs. In order to evaluate the usefulness of such a threshold, the number of useful samples has to be considered as well. In this context, a samples is said to be *useful* when  $K$  can be estimated up to a relative error of 30%. The percentage of useful samples for which  $f_{\text{std}}$  lies below the threshold is given in Fig. 7.9. From this, one can see that excluding observations based on  $f_{\text{std}}$  guarantees simplicity in most of the cases, without losing too much useful information.

**Accuracy.** In order to assess an estimated meteorological visibility, it is desirable to find meaningful error bounds on this value. Since systematic errors in the distance-luminance data are hard to detect, these absolute error bounds seem to be impossible to achieve (up to trivial bounds). Therefore, it could be useful to at least implement an estimator for the accuracy which might be

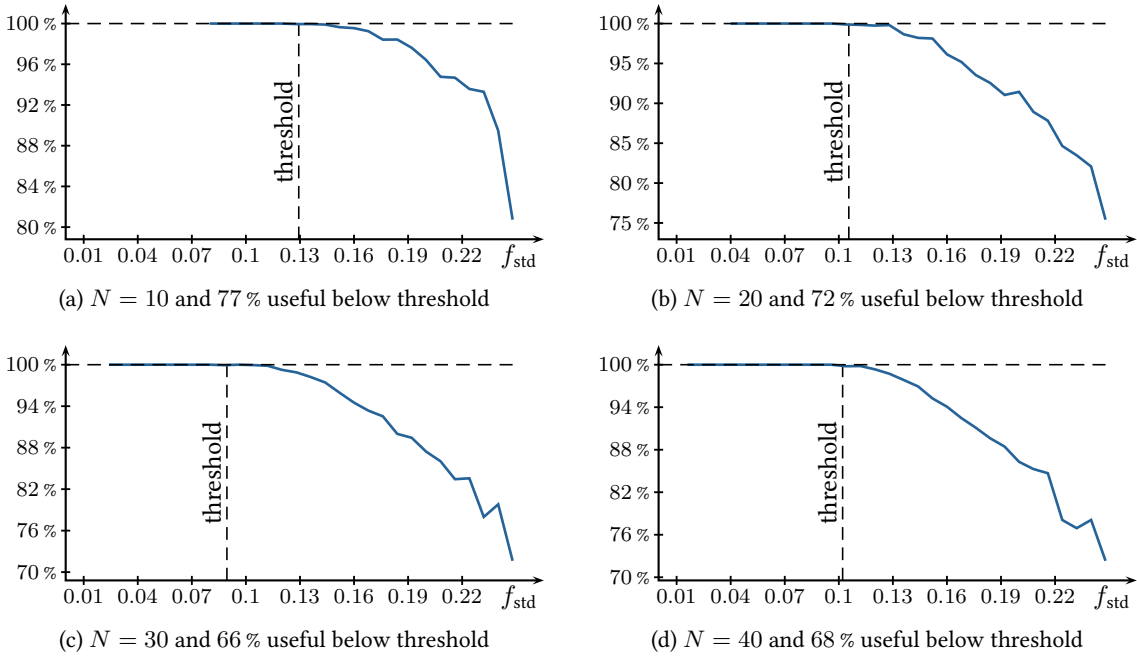


Figure 7.9:  $f_{\text{std}}$  is a feature that could be used to decide whether the tracking data leads to simplicity of  $\mathcal{F}_{\min}$ . The plots show the percentage of simplicity w.r.t. the feature  $f_{\text{std}}$ . Each plot is based on 50000 simulations for randomly varying  $d_{\text{met}}$  between 5 m and 1000 m and noise levels between 0 % and 40 %. The dashed vertical line shows the  $f_{\text{std}}$  threshold where the smallest non-simple sample has been observed. The percentage of useful samples left of this border are given below the plots; a sample is called useful if  $K$  can be estimated up to a relative error of 30 %.

based on the relative noise level or the residual errors for each data point.

**Case:  $K = 0$ .** The idea of minimizing the one-dimensional  $\mathcal{F}_{\min}$  instead of the higher-dimensional  $\mathcal{F}$  is essentially based on the equivalence of (strict) local minima shown in Lemma 6(b) on page 90. However, this is so far restricted to  $K \neq 0$ . Therefore, questions remain on the behavior in  $K = 0$ , such as whether a local minimum of  $\mathcal{F}_{\min}$  in 0 also implies a local minimum in  $\mathcal{F}$ .

One should note that many of these problems (namely the existence, uniqueness, quasiconvexity and the case  $K = 0$ ) can be avoided by a regularization term as introduced in Sec. 7.5.

## 7.5 $L_{\text{air}}$ Stabilization

Thanks to the discussion in earlier sections, the minimization of the objective function  $\mathcal{F}$  has become relatively efficient. However, this discussion does not cover the general capabilities of  $\mathcal{F}$  in the context of parameter estimation. One experiment on the feasibility of tracking-based visibility estimation as introduced above can be found in Sec. 7.6. It shows that for a sufficiently large number of data points a useful value  $d_{\text{met}}$  can be estimated.

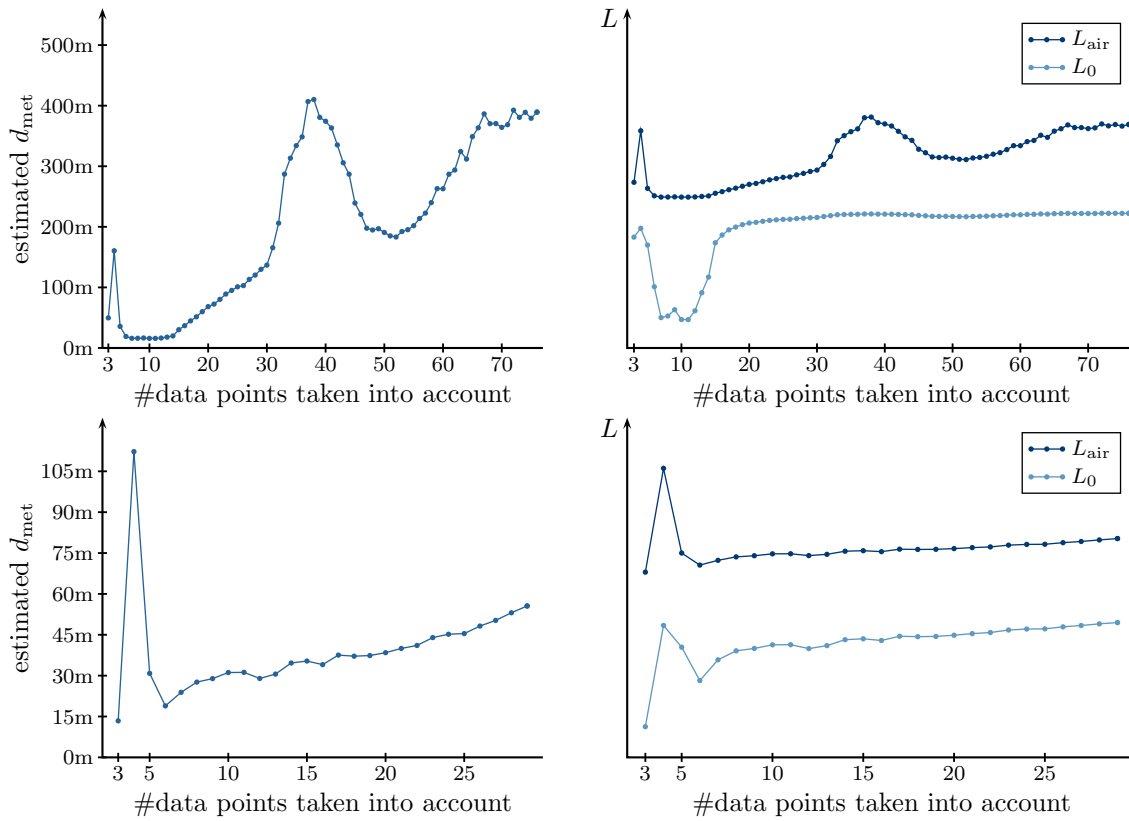


Figure 7.10:  $K$ ,  $L_{\text{air}}$  and  $L_0$  are estimated from a real data set, whereby the number of data points taken into account (starting at measurement  $n = 1$ ) is varied. One can observe the behavior of  $L_{\text{air}}$  and  $d_{\text{met}}$  to be strongly correlated. The large variations in the estimation can be substantially reduced by  $L_{\text{air}}$  stabilization, which can be seen in Fig. 7.12.

Nevertheless, an experiment repeating the parameter estimation on successively reduced data points reveals that this cannot be expected for shorter tracklengths (*cf.* Fig. 7.10). With a decreased number of data points the parameter estimation clearly becomes more and more unstable. On the one hand, these problems can be reduced by increasing the data quality and length of tracks, which indeed is one important challenge for the future. On the other hand, short tracks should not be discarded generally. By combining multiple short tracks (and in turn increasing  $M$ ), the estimation might become more stable as well (*cf.* Remark 30 on page 104).

Another stabilizing approach arises from the observation that the parameters  $L_{\text{air}}$  and  $K$  slide to instability hand in hand (*cf.* Fig. 7.10).  $L_{\text{air}}$  and  $K$  are strongly correlated to each other, wherefore stabilizing  $L_{\text{air}}$  would probably lead to a stabilized estimation of  $K$  as well. This of course requires additional information on  $L_{\text{air}}$  which constitutes the major challenge of this idea.

Fortunately, in the context of Koschmieder's model for horizontal vision, the air light parameter  $L_{\text{air}}$  theoretically corresponds to the luminance which incides to the observer from an infinite horizontal direction. This could allow for  $L_{\text{air}}$  measurements directly from the camera images. This is verified by a small experiment illustrated in Fig. 7.11. Based on a reliable  $L_{\text{air}}$  estimation from a long track, the corresponding regions where  $L_{\text{air}}$  could have been measured from the camera image are highlighted.



Figure 7.11: Highlighting of positions in a camera image that correspond to the  $L_{\text{air}}$  estimation. Dark blue: up to 5% relative difference, medium blue: up to 10% relative difference, light blue: up to 20% relative difference.

Moreover, extracting the luminance close to the horizon is not the only way to estimate  $L_{\text{air}}$ . Since  $L_{\text{air}}$  is a less mutable quantity than  $d_{\text{met}}$ , one can expect it to be stable over an extended period of time. Therefore, former estimations of  $L_{\text{air}}$  could be incorporated in a continuous estimation of  $L_{\text{air}}$ .

In the following, the externally measured air light parameter is denoted as  $\hat{L}_{\text{air}}$ . To incorporate it into the maximum likelihood parameter estimation, a penalization term  $(L_{\text{air}} - \hat{L}_{\text{air}})^2$  is added to the objective function  $\mathcal{F}$  from (7.5). This leads to the stabilized functional

$$p \mapsto \hat{\mathcal{F}}(p) := \mathcal{F}(p) + w_{\text{air}} \left( \hat{L}_{\text{air}} - L_{\text{air}} \right)^2, \quad p = (K, L_{\text{air}}, L_0^1, \dots, L_0^M). \quad (7.21)$$

The weighting factor  $w_{\text{air}} > 0$  should be selected according to the reliability of  $\hat{L}_{\text{air}}$ . Fortunately, most of the relevant properties of  $\mathcal{F}$  remain true for  $\hat{\mathcal{F}}$ . Analogously to 7.4.1, one can find that  $\hat{\mathcal{F}}$  restricted to any hyperplane  $\{p \in \mathbb{R}^{M+2} : K = \text{const.}\}$  is strictly convex and has exactly one minimum given by

$$\begin{aligned} \hat{L}_{\text{air},\min} : \mathbb{R} \rightarrow \mathbb{R}, \quad K \mapsto \hat{L}_{\text{air},\min}(K) &:= \frac{S_{\text{L}} - \sum_{m=1}^M \frac{S_{\text{e}}^m S_{\text{Le}}^m}{S_{\text{ee}}^m} + w_{\text{air}} \hat{L}_{\text{air}}}{S_{\text{1}} - \sum_{m=1}^M \frac{S_{\text{e}}^m S_{\text{e}}^m}{S_{\text{ee}}^m} + w_{\text{air}}}, \\ \hat{L}_{0,\min}^m : \mathbb{R} \rightarrow \mathbb{R}, \quad K \mapsto \hat{L}_{0,\min}^m(K) &:= \frac{S_{\text{Le}}^m - \hat{L}_{\text{air},\min}(K) S_{\text{e}(1-\text{e})}^m}{S_{\text{ee}}^m}. \end{aligned}$$

Furthermore, the analogous terms  $\hat{\mathcal{F}}_{\min}$ ,  $\hat{L}_{\text{air}}^{\text{num}}$ ,  $\hat{L}_{\text{air}}^{\text{denom}}$  are defined by

$$\begin{aligned} K &\mapsto \hat{\mathcal{F}}_{\min}(K) := \mathcal{F}(K, \hat{L}_{\text{air},\min}(K), \hat{L}_{0,\min}^1(K), \dots, \hat{L}_{0,\min}^M(K)), \\ K &\mapsto \hat{L}_{\text{air}}^{\text{num}}(K) := S_L - \sum_{m=1}^M \frac{S_e^m S_{Le}^m}{S_{ee}^m} + w_{\text{air}} \hat{L}_{\text{air}} = L_{\text{air}}^{\text{num}}(K) + w_{\text{air}} \hat{L}_{\text{air}}, \\ K &\mapsto \hat{L}_{\text{air}}^{\text{denom}}(K) := S_1 - \sum_{m=1}^M \frac{S_e^m S_e^m}{S_{ee}^m} + w_{\text{air}} = L_{\text{air}}^{\text{denom}}(K) + w_{\text{air}}. \end{aligned}$$

In contrast to the  $w_{\text{air}} = 0$  case,  $\hat{L}_{\text{air},\min}$  and  $\hat{L}_{0,\min}^m$  are well defined on  $\mathbb{R}$  including 0. This can be shown with the help of the Cauchy-Schwarz inequality (analogous to (D.6)):

$$\hat{L}_{\text{air}}^{\text{denom}}(K) = S_1 - \sum_{m=1}^M \frac{S_e^m S_e^m}{S_{ee}^m} + w_{\text{air}} = \sum_{m=1}^M \frac{S_1 S_{ee}^m - S_e^m S_e^m}{S_{ee}^m} + w_{\text{air}} \geq w_{\text{air}} > 0.$$

Now, analogous to the proof of Lemma 5 on page 87,  $\hat{\mathcal{F}}_{\min}$ ,  $\hat{\mathcal{F}}'_{\min}$  and  $\hat{\mathcal{F}}''_{\min}$  can be written as

$$\begin{aligned} \hat{\mathcal{F}}_{\min} &= \hat{L}_{\text{air},\min}^2 L_{\text{air}}^{\text{denom}} - 2\hat{L}_{\text{air},\min} L_{\text{air}}^{\text{num}} + \left[ S_{LL} - \sum_{m=1}^M \frac{S_{Le}^m S_{Le}^m}{S_{ee}^m} \right], \\ \hat{\mathcal{F}}'_{\min} &= 2\hat{L}_{\text{air},\min} \hat{L}'_{\text{air},\min} L_{\text{air}}^{\text{denom}} + \hat{L}_{\text{air},\min}^2 L_{\text{air}}^{\text{denom}'} - 2\hat{L}'_{\text{air},\min} L_{\text{air}}^{\text{num}} - 2\hat{L}_{\text{air},\min} L_{\text{air}}^{\text{num}'} \\ &\quad + 2 \sum_{m=1}^M \frac{S_{Led}^m S_{Le}^m S_{ee}^m - S_{eed}^m S_{Le}^m S_{Le}^m}{S_{ee}^m S_{ee}^m}, \\ \hat{\mathcal{F}}''_{\min} &= 2\hat{L}'_{\text{air},\min} \hat{L}''_{\text{air},\min} L_{\text{air}}^{\text{denom}} + 2\hat{L}_{\text{air},\min} \hat{L}''_{\text{air},\min} L_{\text{air}}^{\text{denom}} + 4\hat{L}_{\text{air},\min} \hat{L}'_{\text{air},\min} L_{\text{air}}^{\text{denom}'} \\ &\quad + \hat{L}_{\text{air},\min}^2 L_{\text{air}}^{\text{denom}''} - 2\hat{L}''_{\text{air},\min} L_{\text{air}}^{\text{num}} \\ &\quad - 4\hat{L}'_{\text{air},\min} L_{\text{air}}^{\text{num}'} - 2\hat{L}_{\text{air},\min} L_{\text{air}}^{\text{num}''} \\ &\quad + 2 \sum_{m=1}^M \left[ \frac{-S_{Ledd}^m S_{Le}^m S_{ee}^m S_{ee}^m - S_{Led}^m S_{Le}^m S_{ee}^m S_{ee}^m + 4S_{Led}^m S_{Le}^m S_{eed}^m S_{ee}^m}{S_{ee}^m S_{ee}^m S_{ee}^m} \right. \\ &\quad \left. + \frac{2S_{Le}^m S_{Le}^m S_{eed}^m S_{ee}^m - 4S_{Le}^m S_{Le}^m S_{eed}^m S_{eed}^m}{S_{ee}^m S_{ee}^m S_{ee}^m} \right], \end{aligned}$$

where

$$\begin{aligned} \hat{L}'_{\text{air},\min} &= \left[ \frac{\hat{L}_{\text{air}}^{\text{num}}}{\hat{L}_{\text{air}}^{\text{denom}}} \right]' = \frac{\hat{L}_{\text{air}}^{\text{num}'} \hat{L}_{\text{air}}^{\text{denom}} - \hat{L}_{\text{air}}^{\text{denom}'} \hat{L}_{\text{air}}^{\text{num}}}{\hat{L}_{\text{air}}^{\text{denom}} \hat{L}_{\text{air}}^{\text{denom}}} = \frac{L_{\text{air}}^{\text{num}'} \hat{L}_{\text{air}}^{\text{denom}} - L_{\text{air}}^{\text{denom}'} \hat{L}_{\text{air}}^{\text{num}}}{\hat{L}_{\text{air}}^{\text{denom}} \hat{L}_{\text{air}}^{\text{denom}}}, \\ \hat{L}''_{\text{air},\min} &= \frac{L_{\text{air}}^{\text{num}''} \hat{L}_{\text{air}}^{\text{denom}} \hat{L}_{\text{air}}^{\text{denom}} - L_{\text{air}}^{\text{denom}''} \hat{L}_{\text{air}}^{\text{num}} \hat{L}_{\text{air}}^{\text{denom}}}{\hat{L}_{\text{air}}^{\text{denom}} \hat{L}_{\text{air}}^{\text{denom}} \hat{L}_{\text{air}}^{\text{denom}}} \\ &\quad + \frac{-2L_{\text{air}}^{\text{denom}'} L_{\text{air}}^{\text{num}'} \hat{L}_{\text{air}}^{\text{denom}} + 2L_{\text{air}}^{\text{denom}'} L_{\text{air}}^{\text{denom}'} \hat{L}_{\text{air}}^{\text{num}}}{\hat{L}_{\text{air}}^{\text{denom}} \hat{L}_{\text{air}}^{\text{denom}} \hat{L}_{\text{air}}^{\text{denom}}}. \end{aligned}$$

An algorithm similar to fastMLE or advFastMLE (*cf.* 7.4.2) can be used to minimize  $\hat{\mathcal{F}}_{\min}$ .

For  $w_{\text{air}} \rightarrow \infty$  the situation becomes even more elegant from an analytical point of view.  $L_{\text{air},\min}$

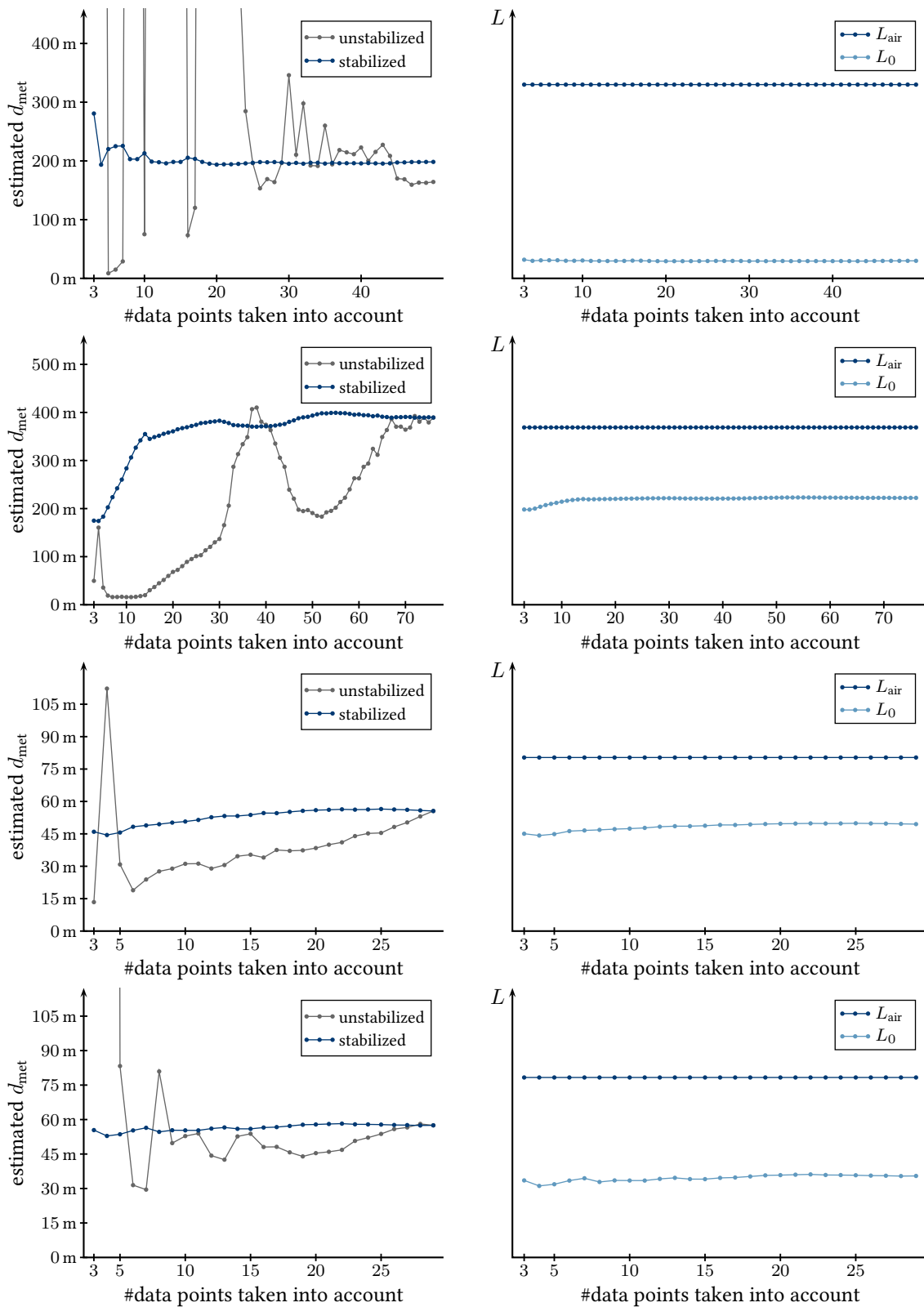


Figure 7.12: Stabilization experiment on real data for  $w_{\text{air}} = \infty$ .  $K$ ,  $L_{\text{air}}$  and  $L_0$  are estimated for a varying number of data points taken into account (starting at measurement  $n = 1$ ).

and  $L_{0,\min}$  are then given by

$$K \mapsto \hat{L}_{\text{air},\min}(K) = \hat{L}_{\text{air}}, \quad K \mapsto \hat{L}_{0,\min}^m(K) = \frac{S_{\text{Le}}^m - \hat{L}_{\text{air}} S_{\text{e}(1-\text{e})}^m}{S_{\text{ee}}^m}$$

and  $\hat{\mathcal{F}}_{\min}$  can simply be written as (cf. proof of Lemma 5 on page 87)

$$\hat{\mathcal{F}}_{\min} = \hat{L}_{\text{air}}^2 \left[ S_1 - \sum_{m=1}^M \frac{S_{\text{e}}^m S_{\text{e}}^m}{S_{\text{ee}}^m} \right] - 2\hat{L}_{\text{air}} \left[ S_{\text{L}} - \sum_{m=1}^M \frac{S_{\text{Le}}^m S_{\text{e}}^m}{S_{\text{ee}}^m} \right] + \left[ S_{\text{LL}} - \sum_{m=1}^M \frac{S_{\text{Le}}^m S_{\text{Le}}^m}{S_{\text{ee}}^m} \right]. \quad (7.22)$$

It turns out that this functional has a simpler and more predictable analytical and numerical behavior than in the finite case. An example for the visibility estimation results based on different values for  $w_{\text{air}}$  are provided in Fig. 7.13.

The major drawback of  $w_{\text{air}} = \infty$  can be found in the fact that  $L_{\text{air}}$  cannot be estimated anymore. It has to be determined independently of the visibility optimization. Therefore, errors in  $\hat{L}_{\text{air}}$  cannot be compensated by the other data terms. The results of an experiment investigating the error propagation from  $\hat{L}_{\text{air}}$  to the estimated  $d_{\text{met}}$  can be found in Fig. 7.14. However, this might be a price worth to be paid compared to the error arising from instabilities occurring otherwise. In an overall framework, one could continuously switch between different visibility estimation methods depending on the confidence of the available data.

**Remark 28** (Minima of  $\hat{\mathcal{F}}$  and  $\hat{\mathcal{F}}_{\min}$ ). Besides the very important stabilizing properties of the penalization term introduced in (7.21), the global property of  $\hat{\mathcal{F}}$  to be convex on each  $K$ -plane guarantees that minima of  $\hat{\mathcal{F}}_{\min}$  correspond to minima of  $\hat{\mathcal{F}}$ . Therefore, a difficult analytical problem of the relation between  $\mathcal{F}_{\min}$  and  $\mathcal{F}$  at 0 (which could not be solved in Lemma 6 on page 90) can be avoided here (cf. 7.4.3).

**Remark 29** (Instability At 0). As stated above, neither  $\hat{\mathcal{F}}_{\min}$  nor  $\hat{L}_{\text{air},\min}$  or  $\hat{L}_{0,\min}^m$  are suffering from singularities at  $K = 0$  anymore. This simplifies not only the analytical discussion, but also eliminates the numerical instability at 0 that had to be considered in the fastMLE and advFastMLE algorithms (cf. 7.4.2). This constitutes another benefit of the use of an  $L_{\text{air}}$  regularization term.

**Remark 30** (Special Case: Short Tracks). A reliable parameter estimation for short object tracks with methods provided in Sec. 7.4 only works in cases of very low noise. However, there are interesting approaches to discuss for the special cases where  $N = 2$  or  $N = 3$ . These approaches could become useful when low-noise data or large sets of short object tracks (e.g. from an optical flow vector field) are available. In this remark, only one special case with two observations on one object and  $w_{\text{air}} = \infty$  is discussed, for which the minimization problem can be accessed explicitly.

Having two data points and an externally measured  $L_{\text{air}} = \hat{L}_{\text{air}}$  available, one can minimize  $\hat{\mathcal{F}}_{\min}$  from (7.22) explicitly. Since  $\hat{\mathcal{F}}_{\min}$  is a sum of positively weighted quadratic terms, it becomes 0 in  $(K, L_0)$  if and only if all terms are 0. Denoting  $L_n := L_n^1$ ,  $d_n := d_n^1$  ( $n \in \{1, 2\}$ ) and canceling the standard deviations results in

$$L_1 = \hat{L}_{\text{air}} + (L_0 - \hat{L}_{\text{air}})e^{-Kd_1}, \quad L_2 = \hat{L}_{\text{air}} + (L_0 - \hat{L}_{\text{air}})e^{-Kd_2}. \quad (7.23)$$

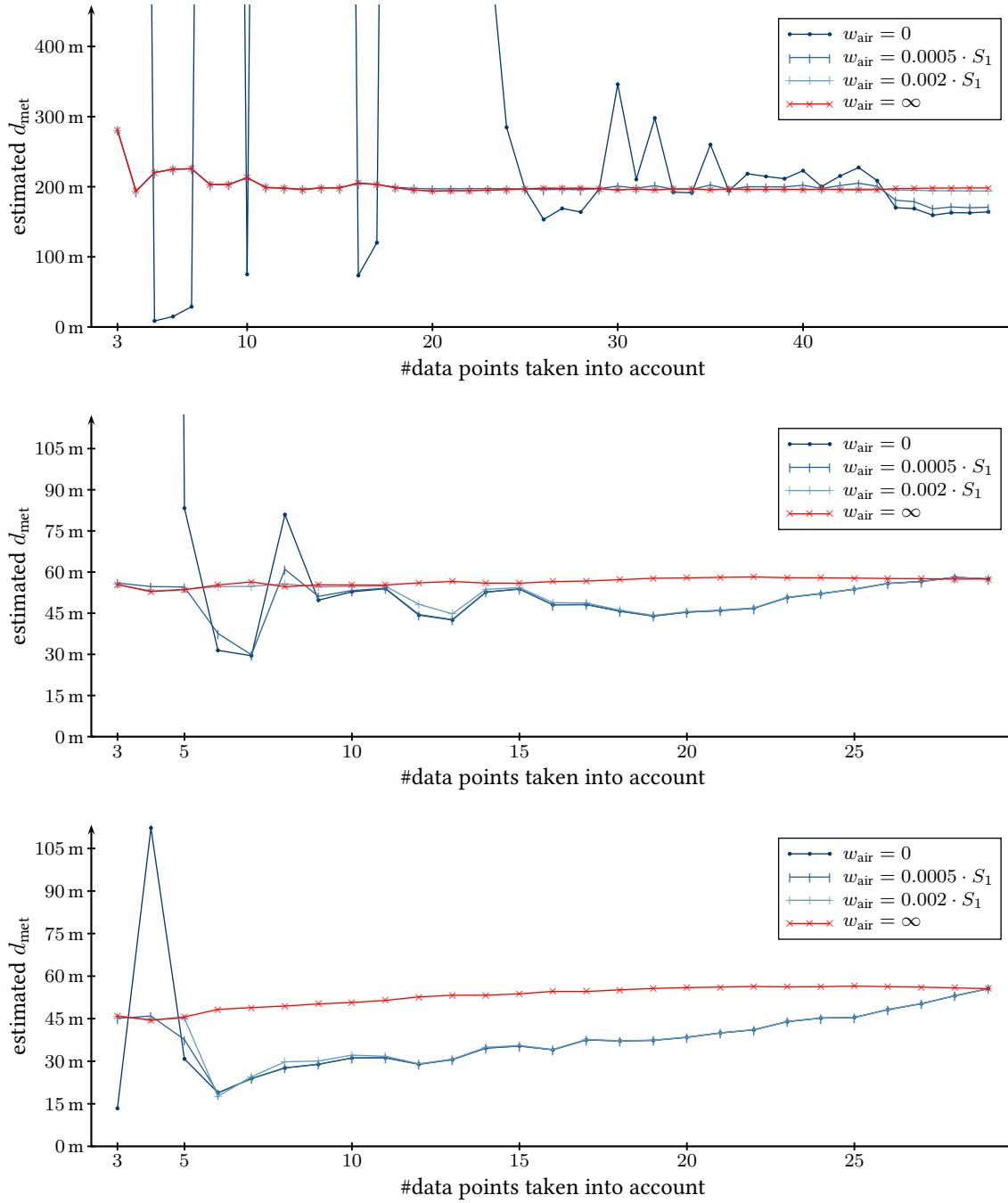


Figure 7.13: Stabilization experiment on real data for different  $w_{\text{air}}$ .

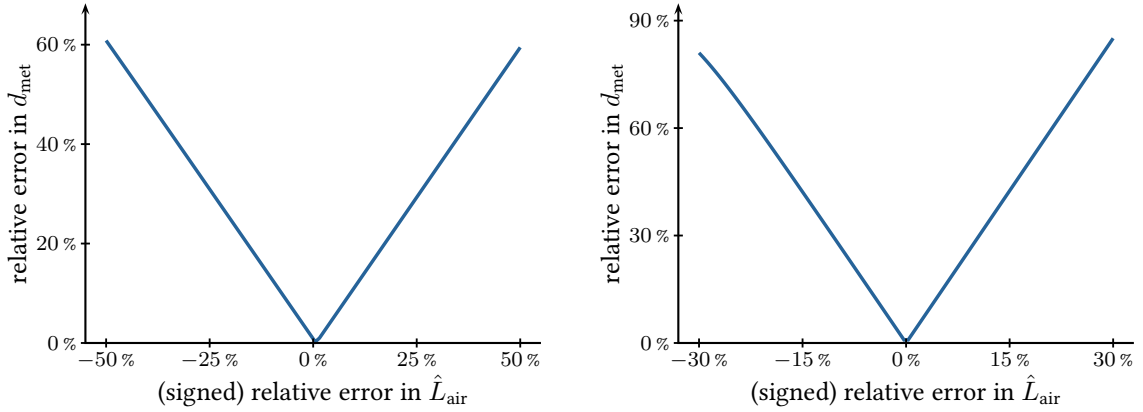


Figure 7.14: Example for error propagation from estimation error in  $\hat{L}_{\text{air}}$  onto estimation error in  $d_{\text{met}}$ . Example parameters:  $M = 1$ ,  $N = 30$ ,  $w_{\text{air}} = \infty$ , without noise. The plots are based on two different example sets of real world data points.

If  $L_1 = L_2$ , the set of solutions of (7.23) is

$$\left\{ (L_0, K) : L_0 = \hat{L}_{\text{air}}, K \in \mathbb{R} \right\} \cup \left\{ (L_0, K) : L_0 \in \mathbb{R}, K = 0 \right\},$$

so either nothing can be concluded or  $K = 0$ . Since objects with intrinsic luminance  $L_{\text{air}}$  are very unlikely, it is reasonable to interpret this situation generally as  $K = 0$ , or  $d_{\text{met}} = \infty$ .

If  $L_1 \neq L_2$ , there exist solutions if and only if  $L_1, L_2 < \hat{L}_{\text{air}}$  or  $L_1, L_2 > \hat{L}_{\text{air}}$ . In all other cases a solution would lead to a contradiction: Assume  $(a, b) \in \{(1, 2), (2, 1)\}$ ,  $(L_0, K)$  a solution to (7.23), and  $L_a \leq \hat{L}_{\text{air}} < L_b$ . Then,

$$\begin{aligned} \underbrace{L_a - \hat{L}_{\text{air}}}_{\leq 0} &= (L_0 - \hat{L}_{\text{air}}) \underbrace{e^{-Kd_a}}_{> 0} \Rightarrow L_0 - \hat{L}_{\text{air}} \leq 0, \\ \underbrace{L_b - \hat{L}_{\text{air}}}_{> 0} &= (L_0 - \hat{L}_{\text{air}}) \underbrace{e^{-Kd_b}}_{> 0} \Rightarrow L_0 - \hat{L}_{\text{air}} > 0, \end{aligned}$$

a contradiction. Analogously for  $L_a < \hat{L}_{\text{air}} \leq L_b$ . In all other cases where  $L_1, L_2 < \hat{L}_{\text{air}}$  or  $L_1, L_2 > \hat{L}_{\text{air}}$ , one can find the unique solution for (7.23) by combining both equations

$$\begin{aligned} \frac{L_1 - \hat{L}_{\text{air}}}{e^{-Kd_1}} = \frac{L_2 - \hat{L}_{\text{air}}}{e^{-Kd_2}} &\Leftrightarrow \frac{L_2 - \hat{L}_{\text{air}}}{L_1 - \hat{L}_{\text{air}}} = \frac{e^{-Kd_2}}{e^{-Kd_1}} \Leftrightarrow \frac{L_2 - \hat{L}_{\text{air}}}{L_1 - \hat{L}_{\text{air}}} = e^{K(d_1 - d_2)} \\ &\Leftrightarrow K = \frac{1}{d_1 - d_2} \log \left( \frac{L_2 - \hat{L}_{\text{air}}}{L_1 - \hat{L}_{\text{air}}} \right). \end{aligned}$$

Note that this equation supports the interpretation  $K = 0$  for  $L_1 = L_2$ .

## 7.6 Further Evaluation

Several examples and experiments are already provided within the above discussion: Examples for the shape of  $\mathcal{F}_{\text{min}}$  can be found in Fig. 7.4 and Fig. 7.5, and the results of an experiment checking

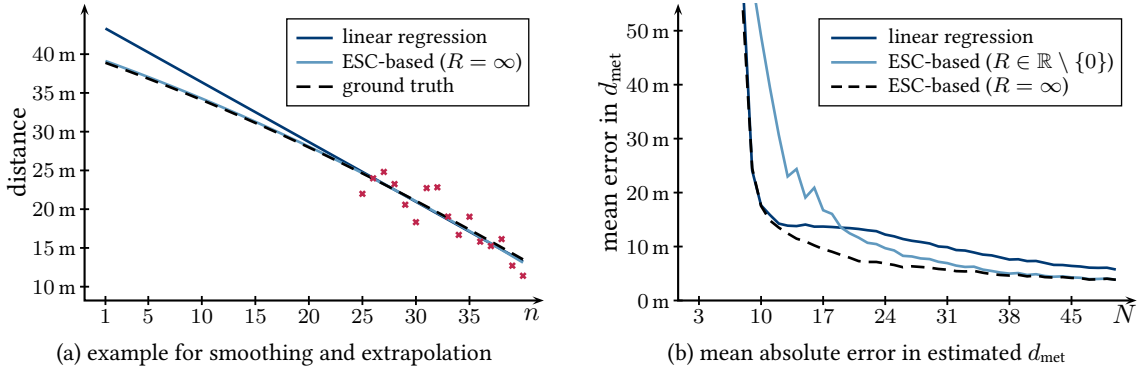


Figure 7.15: ESC-based bundle adjustment can be used for reliable extrapolation and smoothing of the structure from motion distances  $d_n^{\text{sfm}}$ . (a) and (b) provide a comparison between ESC-based bundle adjustment ( $R = \infty$  model and  $R \in \mathbb{R} \setminus \{0\}$  model) and naïve linear regression. General setting: initial velocity  $p_v = 0.5$  m/frame, acceleration  $p_a = 0.0086$  m/(frame)<sup>2</sup>, ground truth radius  $R = \infty$ , Gaussian distance noise 8%,  $p_{\text{obj}}^2 = -5$  m,  $p_{\text{obj}}^3 = 0.5$  m. Setting in (a):  $N = 40$ . Setting in (b):  $d_{\text{met}} = 50$  m,  $N \in \{3, 4, \dots, 50\}$ , 2000 test data sets per  $N$ .

the quasiconvexity of  $\mathcal{F}_{\min}$  for various synthetic data is given in Fig. 7.8 and Fig. 7.9. In the same experiment the fastMLE and advFastMLE algorithms (cf. 7.4.2) and their implementations are extensively tested. Several experiments on the estimation stability with and without the  $L_{\text{air}}$  regularization term are provided in Fig. 7.10, Fig. 7.12 and Fig. 7.13, all of them based on real data. Other experiments on  $L_{\text{air}}$  stabilization can be found in Fig. 7.11 and Fig. 7.14.

In this section, further experiments are carried out which, among others, include Monte Carlo simulations, estimations on the computational effort of fastMLE and advFastMLE, and feasibility tests on real data.

**ESC-Based Bundle Adjustment.** ESC-based bundle adjustment can be used to smoothen and extrapolate distances data (cf. Remark 18 on page 77). Different experiments are provided that test the performance on synthetic data with ground truth available. The travel distances  $s_n$  are computed from an initial velocity  $p_v$  and a constant acceleration  $p_a$ :

$$s_n = (n-1)p_v + \frac{(n-1)^2}{2}p_a.$$

Fig. 7.15 reveals that the extrapolation and smoothing via ESC-based bundle adjustment outperforms the results from a naïve linear regression. Especially for extrapolation and non-constant velocities, the additional ESC data is beneficial for distance smoothing and, in turn, for the  $d_{\text{met}}$  estimation based on these distances. Fig. 7.16 compares the zero-curvature ( $R = \infty$ ) and the non-zero-curvature ( $R \in \mathbb{R} \setminus \{0\}$ ) models (cf. Fig. 7.2) for different simulated curve radii. It turns out that even for curves with a large curvature, the non-zero-curvature model does not have a substantial advantage over the zero-curvature model. Therefore, it might be useful to always assume  $R = \infty$ . This becomes even more reasonable if the ESC yaw rate or the steering angle of the wheels are used to discard data that is captured in situations where the steering angle exceeds

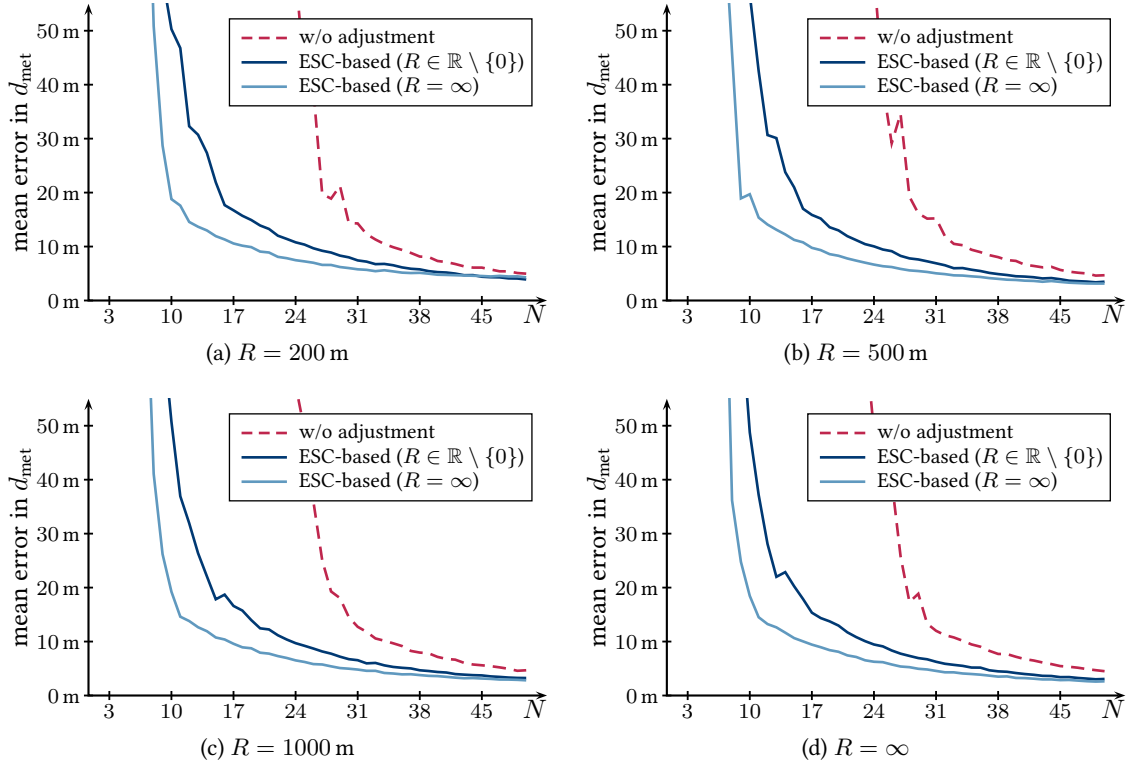


Figure 7.16: Mean absolute  $d_{\text{met}}$  estimation error for different simulated radii of curvature. Setting: initial velocity  $p_v = 0.5$  m/frame, acceleration  $p_a = 0.0086$  m/(frame)<sup>2</sup>, Gaussian distance noise 8%,  $p_{\text{obj}}^2 = -5$  m,  $p_{\text{obj}}^3 = 0.5$  m,  $N \in \{3, 4, \dots, 50\}$ , 2000 test data sets per  $N$ .

a certain threshold.

**Monte Carlo Simulations.** To evaluate the model and the estimation capabilities based on exact ground truth, Monte Carlo simulations are used to provide most realistic images. The road is assumed to be an infinitely expanded and perfectly absorbing plane and the sun to be a uniform light source at a given height level  $H_{\text{atm}}$  above the ground. The homogeneous fog in the atmosphere is represented by a certain extinction coefficient  $K$  and each scattering event is simulated by the Henyey-Greenstein mean scattering phase function from (4.12) and an asymmetry parameter of  $g = 0.85$ . Each photon travels backwards randomly, starting at the camera, and is scattered multiple times, a maximum of 300 scatterings is allowed. All details about the Monte Carlo simulation are provided in 8.6.1.

The framework from 8.6.1 is extended here by virtual targets in front of the camera. In each simulation one target is situated at a height  $H_{\text{tar}}$  above the road plane and at a certain distance in front of the camera. The camera is installed at a height  $H_{\text{cam}}$ . Examples for the resulting images of the target at different distances are shown in Fig. 7.17.

Fig. 7.18 provides the visibility estimation results based on the Monte Carlo images for different  $H_{\text{tar}} \in H_{\text{cam}} + \{-1 \text{ m}, -0.5 \text{ m}, 0 \text{ m}, 0.5 \text{ m}, 1 \text{ m}\}$ . As expected from 5.4.1, for the case of exact horizontal vision ( $H_{\text{cam}} = H_{\text{tar}}$ ) the model perfectly fits the simulated data points, and  $d_{\text{met}}$  is well reconstructed by the tracking-based algorithm. The quality of the  $d_{\text{met}}$  estimation increases

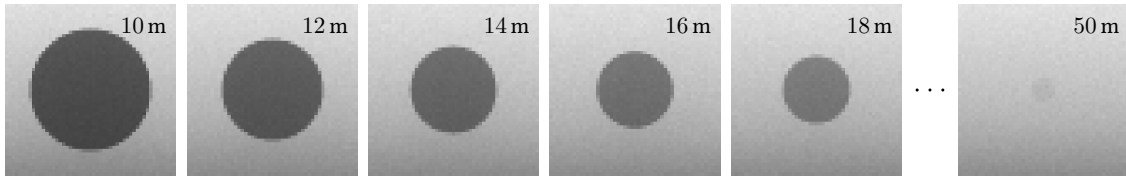


Figure 7.17: Synthetic images from the Monte Carlo simulation. The target is situated at varying distances from 10 to 50 m. Setting:  $d_{\text{met}} = 50$  m,  $H_{\text{tar}} = H_{\text{cam}} = 1.5$  m, 40 000 photons/pixel,  $H_{\text{atm}} = 4d_{\text{met}}$ ,  $f = 1200$  px,  $\xi = 0^\circ$ , half resolution in  $u$  and in  $v$ , the target's diameter is 0.6 m.

as more and more data points are successively taken into account.

In the case of non-horizontal vision ( $H_{\text{tar}} \neq H_{\text{cam}}$ ), a systematic estimation error seems to be introduced. As expected, this error becomes worse with increasing  $|H_{\text{tar}} - H_{\text{cam}}|$ . This agrees with the findings from Chap. 8, where luminances at the road surface are used for visibility estimation, *i.e.*  $H_{\text{tar}} = 0$  m. For these road surface luminance curves, the estimation results are significantly improved if the effects of non-horizontal vision are taken into account. Therefore, it might be useful to introduce a systematic error correction for the tracking-based algorithm in the future as well.

**Feasibility Experiment on Real Data.** To evaluate the tracking-based visibility approach on real-world data, the objects are manually segmented at the camera images and the distances are computed with the help of a simple structure-from-motion algorithm (*cf.* Sec. 7.1). The distance values are further bundle-adjusted with the help of the ESC data, where the radius of curvature is assumed to be  $R = \infty$  (*cf.* Remark 18 on page 77 and Fig. 7.15).

Since no reference measurement sensor is available, the estimated meteorological visibility ( $d_{\text{met}}^{\text{track}}$ ) is compared to a coarse estimation from visual inspection of the camera images ( $d_{\text{met}}^{\text{coarse}}$ ). If available, the tracking-based estimation is compared to the RSLC-based estimation as presented Chap. 8 ( $d_{\text{met}}^{\text{RSLC, 1st}}$ ,  $d_{\text{met}}^{\text{RSLC, 2nd}}$ ).

The results are provided in Fig. 7.19. It shows that Koschmieder's model fits the distance-luminance data very well. Even large meteorological visibilities are acceptably estimated. In most cases RSLC-based algorithms are not applicable since the road or the sky is obstructed by, for example, other traffic participants, curves or bridges. On the other hand, the tracking-based algorithm requires observable objects, wherefore both algorithms beneficially complement each other.

One should note that the results presented here and in Sec. 7.5 only show the general feasibility of tracking-based visibility estimation on real data. It remains an open task to systematically and quantitatively check the accuracy of the estimation results. This not only requires a reliable and mobile reference measurement sensor, but also the use of automated tracking, segmentation and ranging of objects.

**Simulation Framework.** In this chapter a large number of synthetic tracks are used for the discussion and evaluation of the introduced methods. These data points cannot be generated by sophisticated physical simulations in a tolerable amount of time. Therefore, the ground truth data is directly generated from Koschmieder's model for horizontal vision (5.19). This is

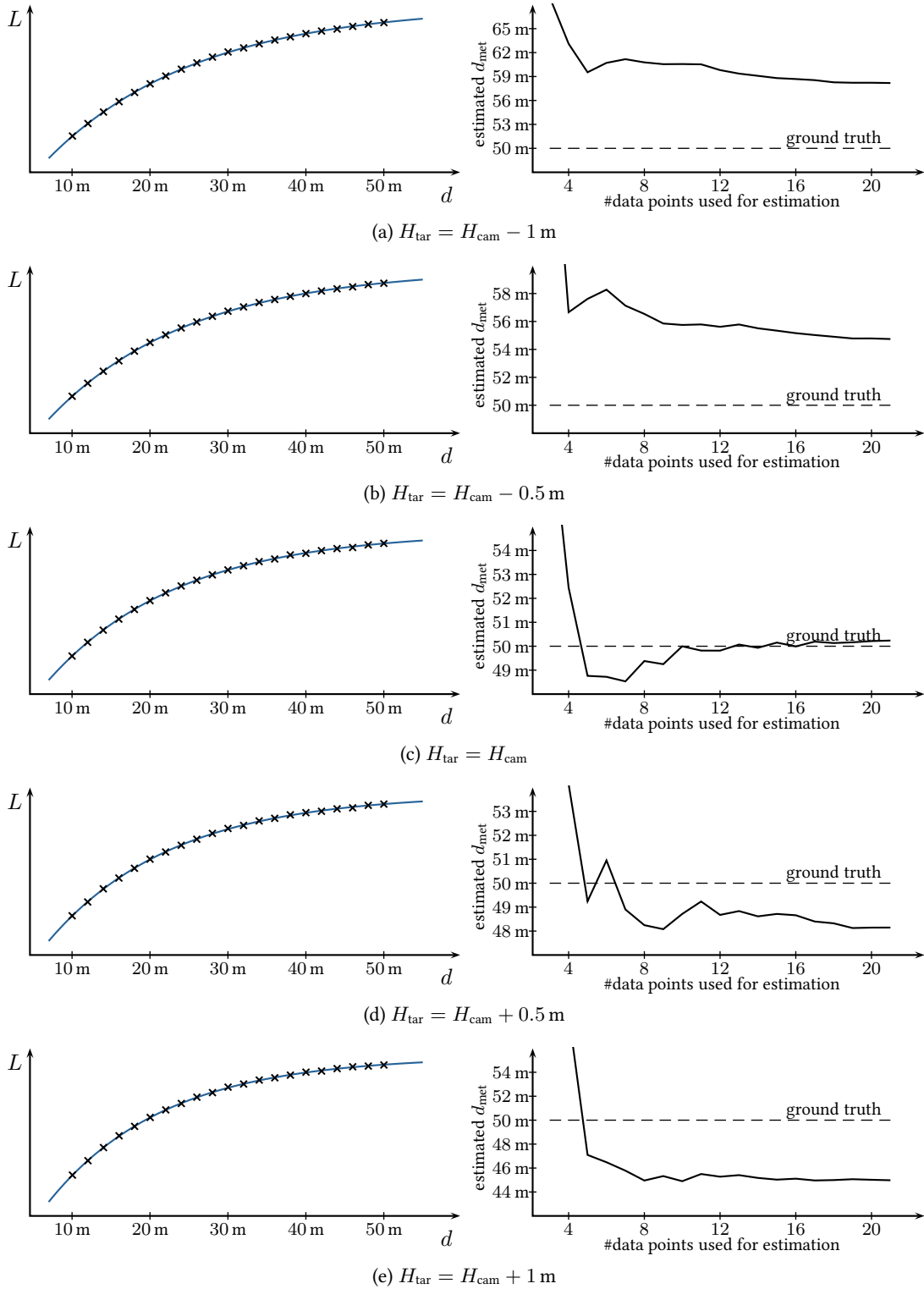


Figure 7.18: Results of Monte Carlo simulations for targets at different heights. Left: Fit of Koschmieder's model. Right: Results from tracking-based visibility estimation. Setting: target distances varying from 10 to 50 m,  $d_{\text{met}} = 50 \text{ m}$ , 40 000 photons/pixel,  $H_{\text{atm}} = 4d_{\text{met}}$ ,  $f = 1200 \text{ px}$ ,  $\xi = 0^\circ$ , half resolution in  $u$  and in  $v$ , the target's diameter is 0.6 m.

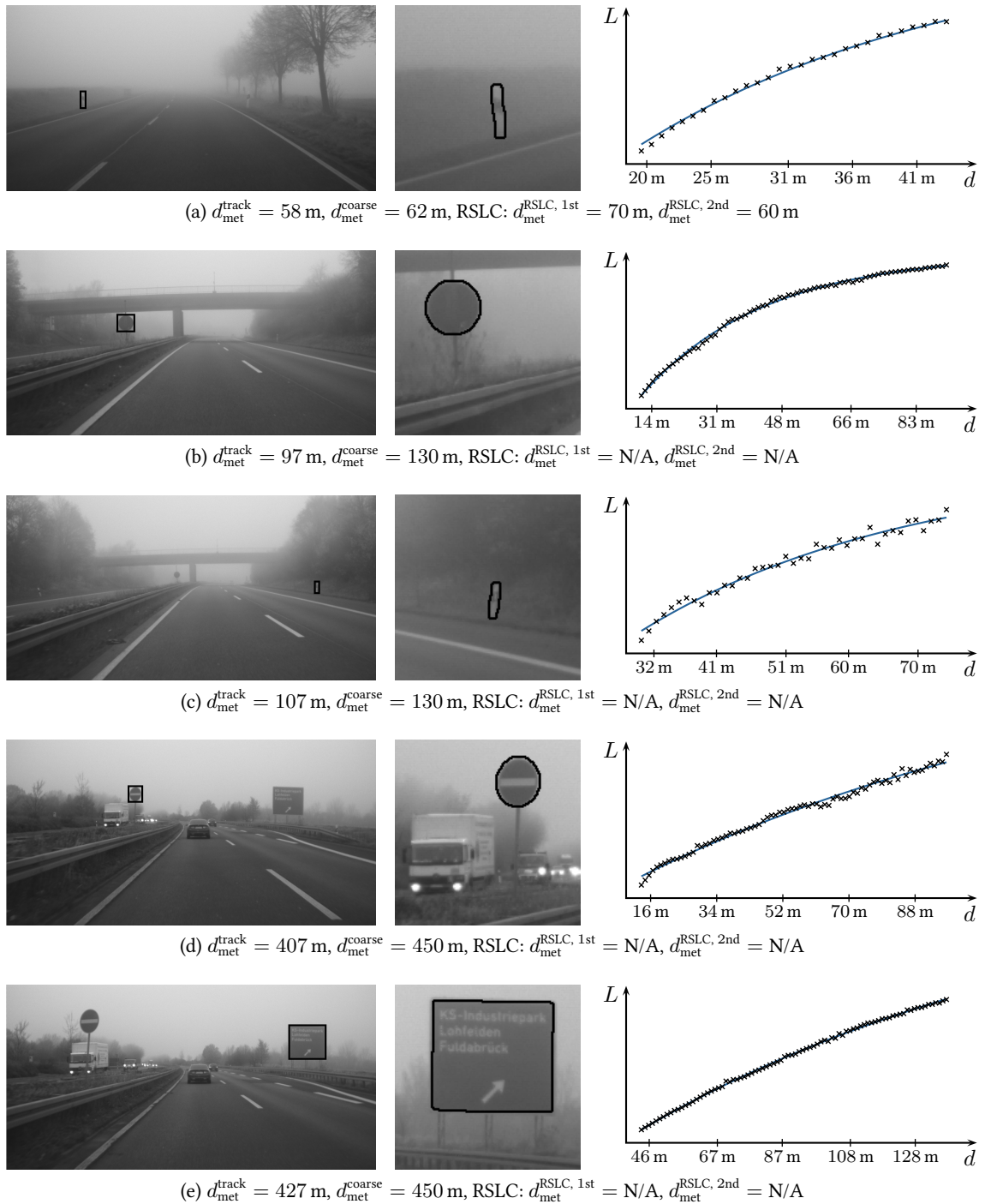


Figure 7.19: The meteorological visibility estimated by: the tracking-based algorithm ( $d_{\text{met}}^{\text{track}}$ ), a coarse visual inspection ( $d_{\text{met}}^{\text{coarse}}$ ), the first-order RSLC-based algorithm from Sec. 8.2 ( $d_{\text{met}}^{\text{RSLC}, 1\text{st}}$ ), the second-order RSLC-based algorithm from Sec. 8.3 ( $d_{\text{met}}^{\text{RSLC}, 2\text{nd}}$ ). Right: Fit of Koschmieder’s model to the distance-luminance data.

indeed a reasonable approach since for horizontal vision Koschmieder’s model represents the full radiative transfer model under just a few assumptions (*cf.* the theoretical discussion in 5.4.1, or the numerical results in Fig. 7.18).

All the other parameters of the simulation are coordinated by a simulation framework presented in the diploma thesis of Johannes Martini [Mar2013]. He considers different kinds of geometric scenarios, world positions of the objects, speed vectors of the camera, intrinsic camera parameters and sizes of objects. Camera-specific noise and additional Gaussian noise can be added to the luminance and distance values. The track lengths and the atmospheric parameters can be chosen arbitrarily. More details can be found in [Mar2013] and in Fig. 7.20, which summarizes the workflow of the framework.

However, for most of the experiments in this work a very simple scenario of objects frontally heading towards the camera is sufficient. A discussion of all influences of the numerous scenario parameters would go beyond the scope of this thesis. Such a discussion is partially provided in [Mar2013, Chap. 3].

**Computational Effort.** The parameter estimation for tracking-based visibility estimation is one of the most emphasized topics in this work. It can be approached by the likelihood objective function  $\mathcal{F}$  introduced in Sec. 7.3 and the fast minimization methods fastMLE and advFastMLE provided in Sec. 7.4. For evaluation, these algorithms are compared to standard minimization techniques as described in the introduction of Sec. 7.4, namely Newton’s method, the Gauß-Newton method, the gradient descent and the Levenberg-Marquardt algorithm.

It turns out that the Newton and Gauß-Newton methods suffer from an unusably small range of convergence. Even for slightly disturbed data,  $K$ , and in turn  $d_{\text{met}}$ , cannot be suitably estimated. The method of gradient descent is more stable, but also becomes inapplicable due to its extremely slow convergence (by a factor  $\gg 1000$ ). This is why quantitatively fastMLE and advFastMLE are only compared to the more state-of-the-art Levenberg-Marquardt algorithm (*cf.* [Mar1963]).

The run-time evaluation is performed by counting the basic operations within optimized implementations of the three algorithms. Based on the specification of a Cortex-A9 floating-point unit (*cf.* [ARM2010]), these numbers are multiplied with the required number of cycles per operation and summed up to an overall number of cycles. The number of cycles is further divided by the FPU’s cycles per second to estimate the computation time of each algorithm. This approach constitutes only a coarse estimation of the real computation times, but nevertheless should be a quite fair measure for comparison. This is especially true since the major computation steps in all algorithms are similar.

Fig. 7.21 shows the results of the comparison. As expected, the fastMLE and advFastMLE are remarkably faster than the Levenberg-Marquardt algorithm. To achieve a similar accuracy, the  $(M + 2)$ -dimensional minimization seems in general to require a much larger number of iterations than the 1-dimensional approaches from 7.4.2. The fastMLE and advFastMLE converge in a comparable amount of time. For parameter estimation, one thus has the factual choice between the easy-to-implement fastMLE and the more complex advFastMLE that provides a better range of convergence.

Hence, the tracking-based algorithm benefits from a well-understood and fast parameter estimation. Together with an increasing quality and variety of distance and luminance data from camera systems, it constitutes a powerful way of visibility estimation for future driver assistance systems.

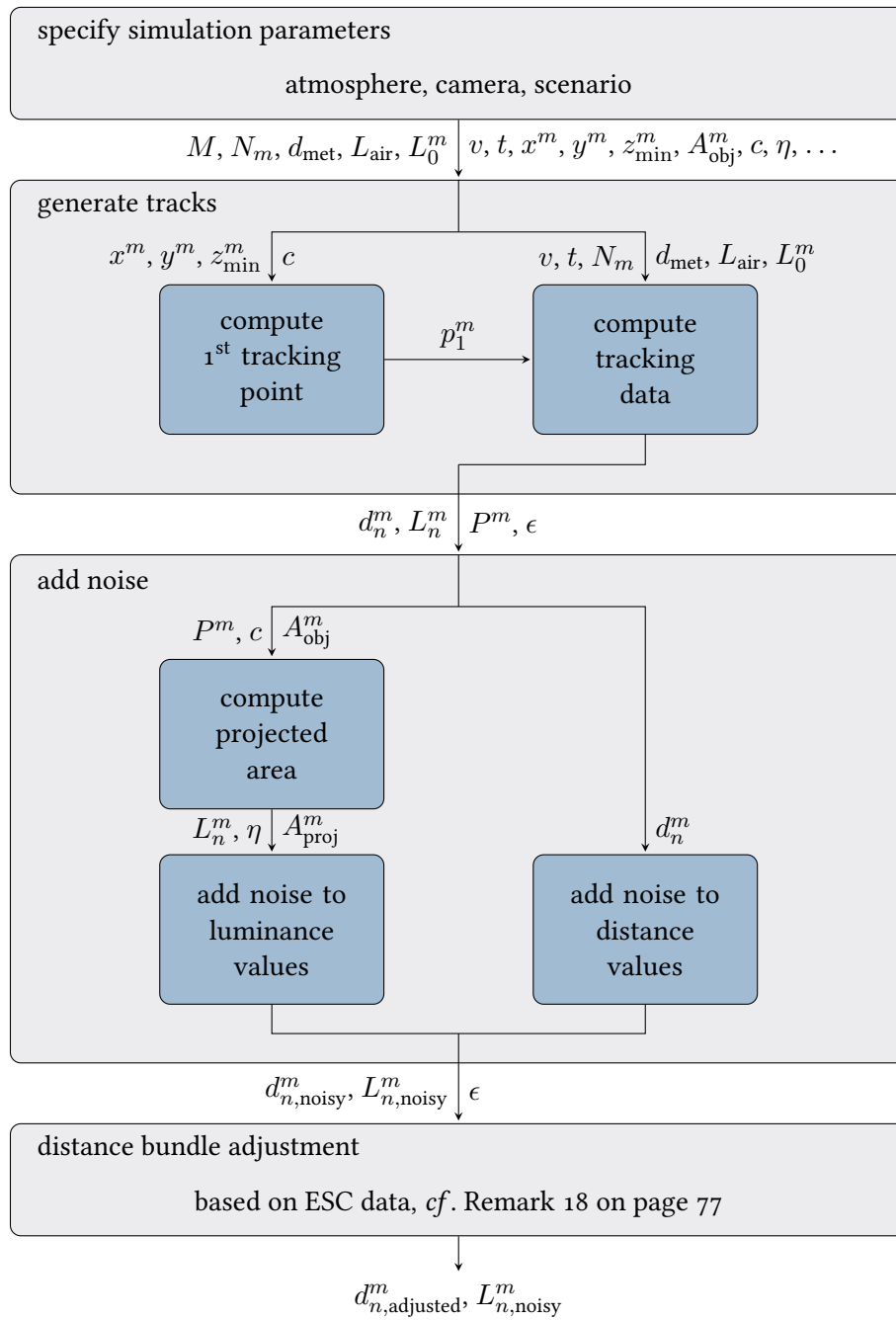


Figure 7.20: Workflow of simulation framework (based on [Mar2013, Fig. 3.2]). Notation:  $c$  = intrinsic camera parameters;  $\eta$  = luminance noise model;  $A_{\text{obj}}^m$  = 2-dimensional world object dimension;  $A_{\text{proj}}^m$  = 2-dimensional projected object dimension;  $v$  = velocity;  $t$  = trajectory;  $(x^m, y^m, z^m) = p_1^m$  closest tracking point ( $z^m$  is chosen minimally in a way that  $z^m \geq z_{\text{min}}^m$  and  $p_1^m$  can be projected to the virtual imager);  $P^m$  = simulated tracking world coordinates;  $\epsilon$  = simulated ESC data.

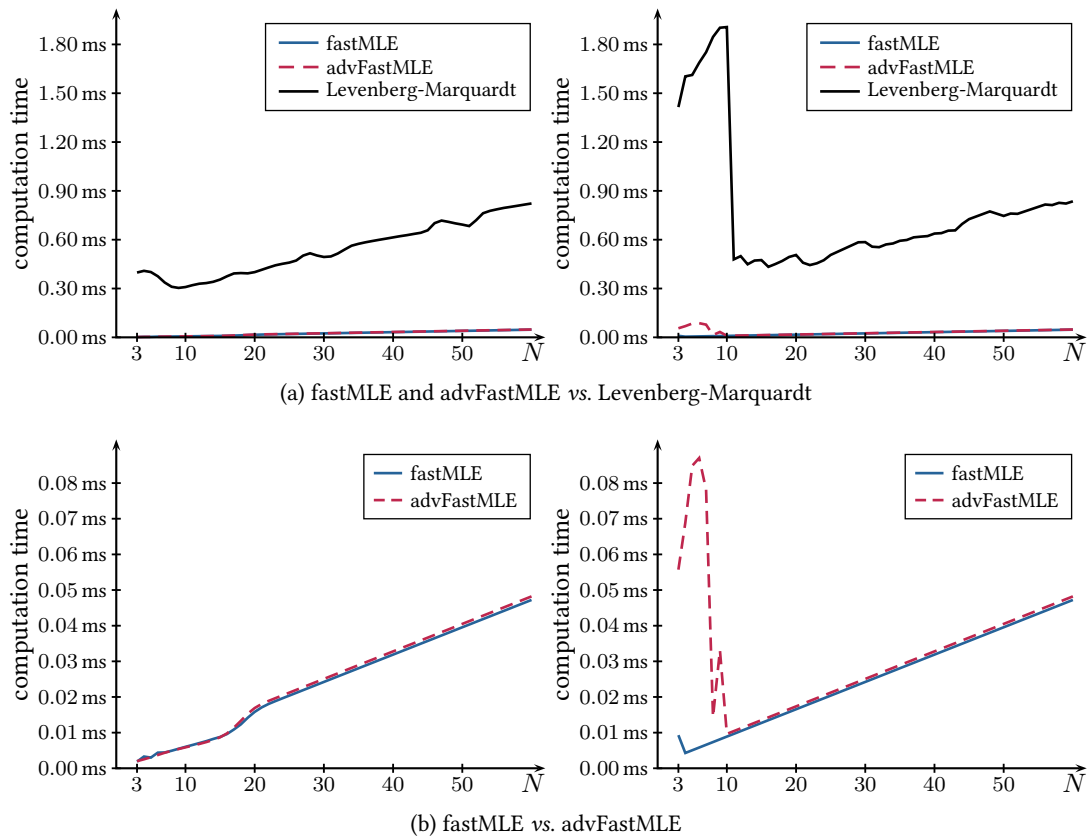


Figure 7.21: Comparison of computational effort for tracking-based parameter estimation. For each  $N$  the experiment is repeated 10000 times. The mean (left) and the maximum (right) of the computation times are compared. The bottom plots provide a closer look at the differences between fastMLE and advFastMLE.

# Chapter 8

---

## Algorithm Based on Road Surface Luminance Curves

### Contents

---

8.1	Data Acquisition . . . . .	116
8.2	First-Order: Koschmieder's Model . . . . .	120
8.3	Second-Order: Improved Fog Model . . . . .	121
8.3.1	In-Scattering Luminance Model . . . . .	123
8.3.2	Geometry . . . . .	124
8.3.3	Second-Order Model . . . . .	125
8.3.4	Notes on the Parameter Estimation . . . . .	125
8.4	Higher-Order Models . . . . .	130
8.5	Inflection Point Estimation from Observation Data . . . . .	135
8.6	Further Experiments and Evaluation . . . . .	136
8.6.1	Monte Carlo Simulation . . . . .	136
8.6.2	Further Numerical Experiments . . . . .	138
8.6.3	Real World Examples . . . . .	147

---

One of the most common driving situations consists of a vehicle driving along a long and easily accessible road without too much traffic. Especially in dense fog this often allows the driver to observe the road and the sky touching or even merging at the horizon. Based on this observation Hautière *et al.* [Hau2006c] introduced another visibility estimation approach (*cf.* 6.1.1). In contrast to the tracking-based algorithm from Chap. 7, not many observations of objects at different distances are required, but one observation of the homogeneous and depth-extended road. From this, a luminance curve is extracted from the top to the bottom of the image, called the *road surface luminance curve* (RSLC). The parameter estimation can be realized with the help of a relation between this curve's inflection point and the extinction coefficient  $K$ .

The main contribution of this work is to make use of the full potential of the luminance curve model. Motivated by the finding that Koschmieder's model for horizontal vision not satisfactorily describes real-world RSLC observations, an improved model taking into account effects of non-horizontal vision is introduced (*cf.* Sec. 8.3). Iterating this idea even leads to higher-order models that converge to the exact solution of the corresponding radiative transfer problem (*cf.* Sec. 8.4). It turns out that especially in dense fog the estimation capabilities of RSLC-based methods can be

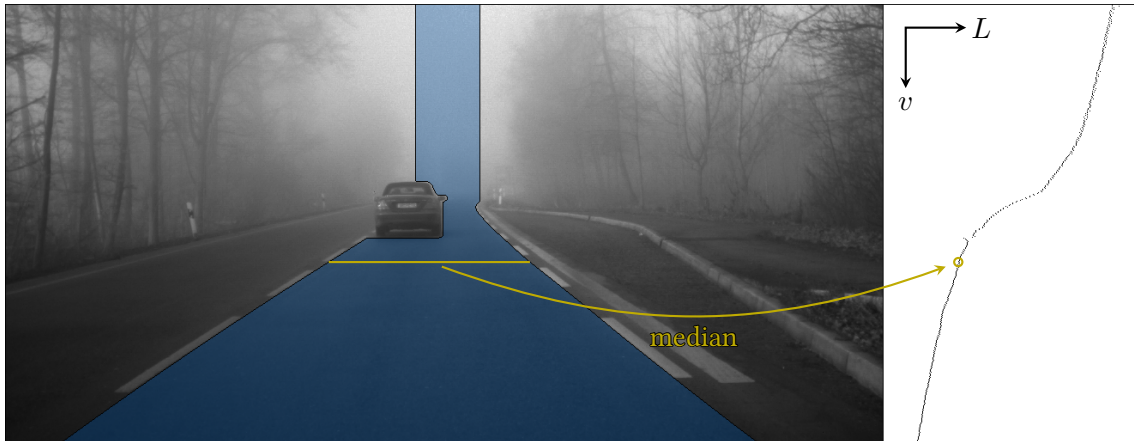


Figure 8.1: The road surface luminance curve (RSLC) is extracted line by line from the segmented region in the middle of the camera frame.

substantially increased by applying more accurate models.

## 8.1 Data Acquisition

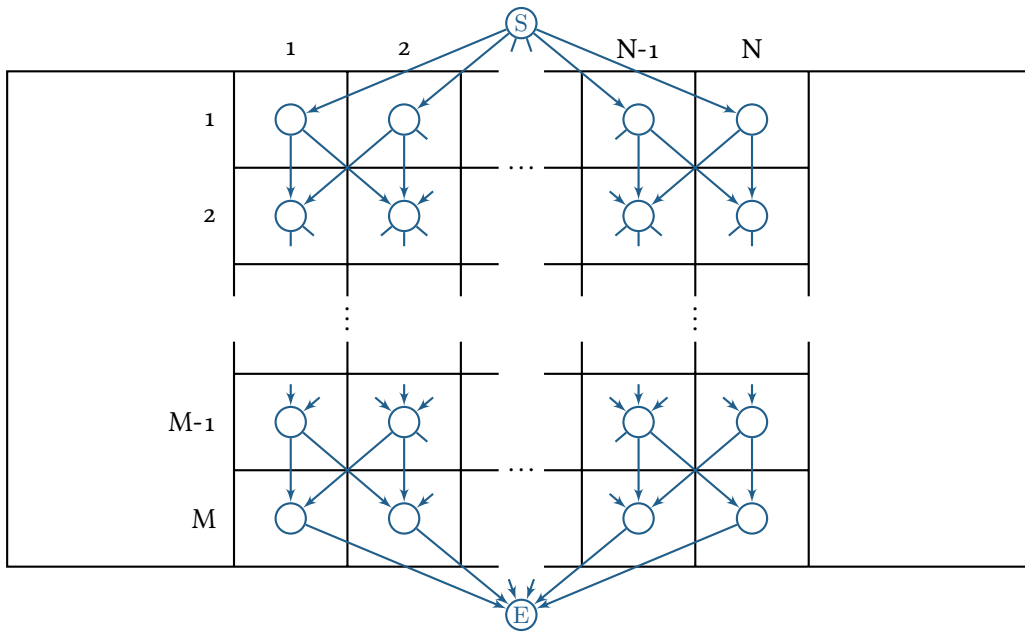
The observation data that is used for visibility estimation in this chapter consists of a vertical luminance profile of the road and the sky in the camera image. If no objects are blocking the view, this luminance profile can be extracted from the top to the bottom of the image and is called *road surface luminance curve* (RSLC). Based on segmented parts of the road and the sky it is obtained from

$$v \mapsto L(v) := \text{median luminance at (segmented part of) line } v \text{ (cf. Fig. 8.1).}$$

Some approaches for RSLC acquisition can be found in works presenting frameworks for RSLC-based visibility assessment, such as [Hau2006c] and [Bro2009]. They basically find parts of the road and the sky by expansion algorithms starting at the bottom of the camera image. However, RSLC extraction mainly consists of a segmentation problem, which is a well-known and widely discussed standard task in computer vision. Examples for road and sky segmentation can be found in [Alv2012] and [Ghe2015], but any other segmentation method could also be discussed in this context.

As already mentioned, a comprehensive coverage of all possible road and sky segmentation methods would go beyond the scope of this work. Instead, two purposeful approaches are employed for RSLC extraction:

In all cases where the visibility measurement quality must not be essentially disturbed by non-optimal segmentation, the segmentation is done manually. To realize this, a comfortable tool has been implemented that interpolates labeled points at the roadside and vertically extends its endpoints to the top of the image (cf. e.g. Fig. 6.1, Fig. 8.1 and Fig. 8.24). Obstructing objects can be masked out.

Figure 8.2: directed graph  $(\mathcal{V}, \mathcal{E})$ 

The second segmentation method is a novel and automatic one that is tailored to the RSLC context and takes into account the requirements of real-time embedded systems. The middle part of the image is divided into (potentially overlapping) segments and an in some sense optimal path from the top to the bottom of the image is explored. The resulting segmentation is used for RSLC extraction afterwards.

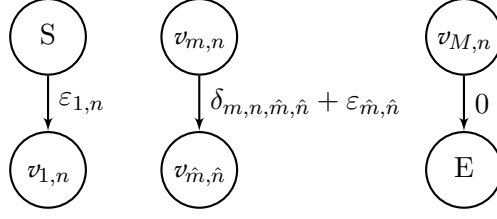
The choice in which way the image is divided is essentially influenced by the trade-off between smaller and larger segments, resulting in either more flexible or more smoothing effects. This decision is up to the developer, who knows the behavior and limits of the camera he is working with.

In this work, the image is split into rectangles induced by horizontal and vertical lines at positions

$$\begin{aligned} 1 = v_{r,0} < \dots < v_{r,M} = v_{\max}, & \quad (\text{horizontal}) \\ u_{r,0} < \dots < u_{r,N}, & \quad (\text{vertical}) \end{aligned}$$

where  $v_{\max}$  denotes the number of rows in the camera image (height). Now, the aim is to select for each of the  $M$  rectangle rows one of the  $N$  column tiles such that the overall selection results in an optimal RSLC. Different criteria can be applied to decide which rectangle path is the optimal one. Some of them, such as a minimal noise criterion or a monotonicity criterion, can be broken down to local decisions and thus transformed to a graph-related problem. This will allow for a fast optimal path selection.

To construct the corresponding weighted and directed graph  $\mathcal{G} = (\mathcal{V}, \mathcal{E}, w)$ , each tile  $(m, n) \in \{1, \dots, M\} \times \{1, \dots, N\}$  is assigned to one node  $v_{m,n} \in \mathcal{V}$ . Additionally, a start node  $S \in \mathcal{V}$  and an end node  $E \in \mathcal{V}$  are introduced, connected to the first and the last row, respectively (*cf.* Fig. 8.2), *i.e.*  $(S, v_{1,n}) \in \mathcal{E}$  and  $(v_{M,n}, E) \in \mathcal{E}$  for all  $n \in \{1, \dots, N\}$ . The remaining edges are directed

Figure 8.3: edge weights  $w$ 

connections between consecutive layers taking into account a path connectivity constraint, *i.e.* for all  $(m, n), (\hat{m}, \hat{n}) \in \{1, \dots, M\} \times \{1, \dots, N\}$  one has

$$(v_{m,n}, v_{\hat{m},\hat{n}}) \in \mathcal{E} \quad \Leftrightarrow \quad \hat{m} = m + 1 \quad \wedge \quad \mathcal{C}(n, \hat{n}) = 1,$$

where  $\mathcal{C}$  is 1 if and only if column  $n$  and column  $\hat{n}$  are allowed to be connected. Unless stated otherwise,  $\mathcal{C}$  is chosen to enforce a geometrically connected path in the following. That means the resulting path is allowed to jump at most one column per row, namely

$$\{1, \dots, N\}^2 \ni (n, \hat{n}) \mapsto \mathcal{C}(n, \hat{n}) = \begin{cases} 1 & , \text{if } |n - \hat{n}| \leq 1 \\ 0 & , \text{otherwise} \end{cases}. \quad (8.1)$$

Now, each path  $p$  from the start node S to the end node E corresponds to a valid segmentation choice

$$(n_1, \dots, n_M) \quad \leftrightarrow \quad p = (S, v_{1,n_1}, \dots, v_{M,n_M}, E). \quad (8.2)$$

In order to find an optimal path, one has to specify an objective function first. The objective function proposed here rates the noise and monotonicity of the corresponding RSLC. Based on Appendix C, the noise variance is estimated from the sum of squared neighbor differences

$$s_{\text{noise}}(L) := \frac{1}{2(v_{\max} - 1)} \sum_{v=1}^{v_{\max}-1} (L(v+1) - L(v))^2.$$

The non-monotonicity can be scored by a similar term

$$s_{\text{mon}}(L) := \frac{1}{2(v_{\max} - 1)} \sum_{v=1}^{v_{\max}-1} (\max\{L(v+1) - L(v), 0\})^2,$$

which penalizes any non-decreasing case  $L(v+1) > L(v)$ . From this, the overall objective function can be constructed as

$$(n_1, \dots, n_M) \mapsto s_{\text{noise}}(L_{n_1, \dots, n_M}) + s_{\text{mon}}(L_{n_1, \dots, n_M}), \quad (8.3)$$

where  $L_{n_1, \dots, n_M}$  denotes the RSLC corresponding to segmentation  $(n_1, \dots, n_M)$ . Based on (8.2), the minimization of (8.3) can be formulated in terms of graph theory. This results in a classical shortest path problem which is to find a path  $(S, v_{1,n_1}, \dots, v_{M,n_M}, E)$  that minimizes the sum over the path's edge weights. These edge weights  $w : \mathcal{E} \rightarrow \mathbb{R}_{\geq 0}$  are given in terms of the inner

node costs  $\varepsilon_{m,n}$  and the intermediate node costs  $\delta_{m,n,\hat{m},\hat{n}}$  as

$$w(S, v_{1,n}) = \varepsilon_{1,n}, \quad w(v_{m,n}, v_{\hat{m},\hat{n}}) = \varepsilon_{\hat{m},\hat{n}} + \delta_{m,n,\hat{m},\hat{n}}, \quad w(v_{M,n}, E) = 0 \quad (\text{cf. Fig. 8.3}).$$

In order to represent the objective function (8.3) the inner and intermediate costs are defined as

$$\begin{aligned} \varepsilon_{m,n} &:= \frac{1}{2(v_{\max} - 1)} \sum_{v=v_{r,m-1}+1}^{v_{r,m}-1} \text{sq}(L_n(v+1) - L_n(v)) \\ &\quad + \frac{1}{2(v_{\max} - 1)} \begin{cases} \text{sq}(L_n(2) - L_n(1)) & , \text{ if } m = 1 \\ 0 & , \text{ otherwise } \end{cases}, \\ \delta_{m,n,\hat{m},\hat{n}} &:= \frac{1}{2(v_{\max} - 1)} \text{sq}(L_n(v_{r,m}) - L_{\hat{n}}(v_{r,\hat{m}})), \end{aligned}$$

where  $L_n := L_{n,\dots,n}$  denotes the RSLC according to the  $n^{\text{th}}$  column, and  $x \mapsto \text{sq}(x) := \max\{\sqrt{2}x, |x|\}^2$ , a modified square operator that allows for the combination of  $s_{\text{noise}}$  and  $s_{\text{mon}}$ .

The shortest path problem constructed above can efficiently be solved by a modified Dijkstra algorithm [Dij1959] that iteratively obtains the shortest paths from the start node to each layer (cf. Algorithm 2). Examples of the results are shown in Fig. 8.4.

---

**Algorithm 2** Modified Dijkstra Algorithm for Shortest Rectangle Path

---

```

1: procedure SHORTESTRECTANGLEPATH( $\varepsilon_{m,n}, \delta_{m,n,\hat{m},\hat{n}}$ )
2:    $\triangleright$  layer-wise shortest path extraction:
3:    $C(1, n) \leftarrow \varepsilon_{1,n}$   $\triangleright C(m, n)$ ... costs of shortest path from S to  $v_{m,n}$ 
4:   for  $m \leftarrow 2$  to  $M$  do
5:     for  $n \leftarrow 1$  to  $N$  do
6:        $c_{\min} \leftarrow \infty$   $\triangleright$  currently minimal costs
7:       for all  $n_p \in \{1, \dots, N\}$  with  $\mathcal{C}(n_p, n) = 1$  do
8:          $c_{\text{this}} \leftarrow C(m-1, n_p) + \delta_{m-1,n_p,m,n}$   $\triangleright$  costs of this predecessor
9:         if  $c_{\min} > c_{\text{this}}$  then
10:            $c_{\min} \leftarrow c_{\text{this}}$ 
11:            $P(m, n) \leftarrow n_p$   $\triangleright P(m, n)$ ... shortest path predecessor of  $v_{m,n}$ 
12:         end if
13:       end for
14:        $C(m, n) \leftarrow c_{\min} + \varepsilon_{m,n}$   $\triangleright$  node costs  $\varepsilon_{m,n}$  independent of predecessor
15:     end for
16:   end for
17:    $\triangleright$  recurse over predecessors to determine shortest path:
18:    $n_M \leftarrow \text{argmin}_{n=1,\dots,N} C(M, n)$ 
19:   for  $m \leftarrow M-1$  to 1 do
20:      $n_m \leftarrow P(m+1, n_{m+1})$ 
21:   end for
22:   return  $(n_1, \dots, n_M)$ 
23: end procedure

```

---

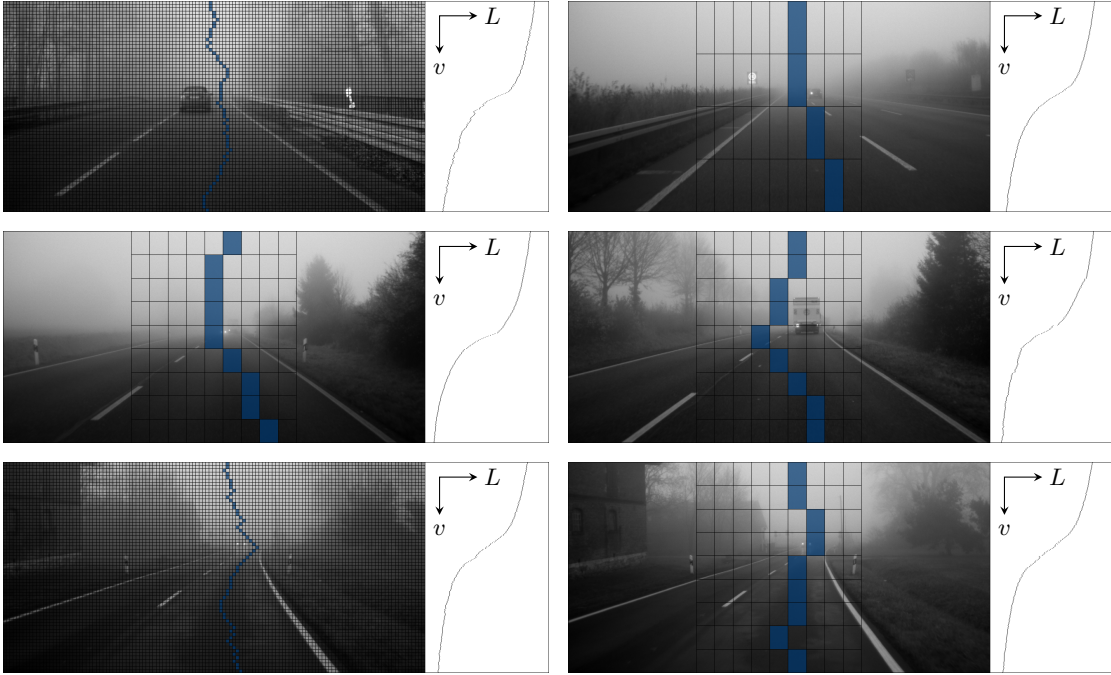


Figure 8.4: Examples for the output of Algorithm 2 using different grid sizes.

Additionally, the outcoming optimal score can further be used as a confidence measure for the extracted RSLC. In cases where the noise and non-monotonicity are too high in relation to the overall dynamic of the luminance curve, the RSLC extraction might have failed and can be rejected. An anti-confidence measure could thus look like

$$L \mapsto \frac{\sqrt{s_{\text{noise}}(L) + s_{\text{mon}}(L)}}{|L(1) - L(v_{\text{max}})|}. \quad (8.4)$$

## 8.2 First-Order: Koschmieder's Model

To utilize the road surface luminance curve (RSLC) for visibility estimation, a model has to be found that describes the RSLC in terms of atmospheric parameters (*cf.* Sec. 6.3). The first to introduce such a model were Hautière *et al.* [Hau2006c]. Based on the assumption of a flat and homogeneously dark road, they apply Koschmieder's model for horizontal vision (*cf.* 5.4.1)

$$L^{\text{Kos}}(v) := e^{-Kd(v)} L_0 + (1 - e^{-Kd(v)}) L_{\text{air}}, \quad (8.5)$$

where  $L_0$  represents the constant intrinsic road luminance. The distance  $d$  between the camera and the street at image row  $v$  is derived from reasonable assumptions about the camera's and world's geometry:

$$d(v) = \begin{cases} \frac{c}{v-v_h} & , \text{ if } v > v_h \\ \infty & , \text{ if } v \leq v_h \end{cases}, \quad (8.6)$$

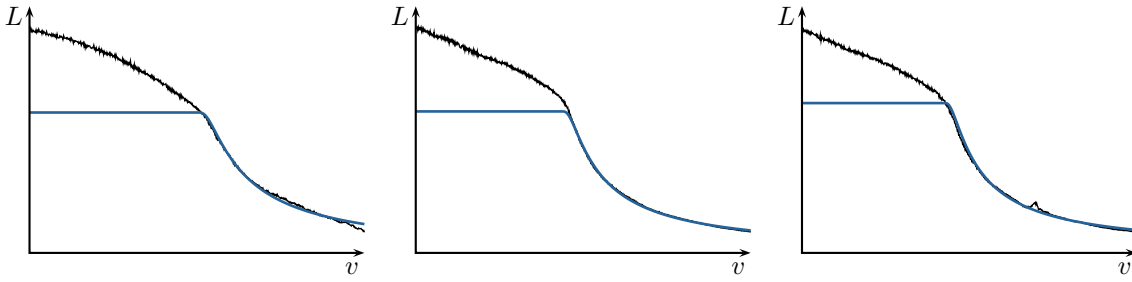


Figure 8.5: Koschmieder's model is not capable of describing real-world RSLCs adequately.

where  $c$  represents a camera constant depending on the intrinsic camera parameters, the pitch angle  $\xi$  and the height  $H_{\text{cam}}$  of the camera installed above the road plane (*cf.* Fig. 8.7);  $v_h$  denotes the road plane's horizon in image coordinates.

The key observation for RSLC-based parameter estimation is that  $L^{\text{Kos}}$  has an inflection point  $v_i$  that exactly corresponds to the parameters  $(K, L_{\text{air}}, L_0)$  in an explicit way (*cf.* [Hau2006c, (16), (20) and (21)]), more precisely

$$(K, L_{\text{air}}, L_0) \stackrel{\text{bijective correspondence}}{\leftrightarrow} (v_i, L^{\text{Kos}}(v_i), \partial_v L^{\text{Kos}}(v_i)). \quad (8.7)$$

As already mentioned in 6.1.1,  $K$  and  $v_i$  are even linearly related by  $K = 2(v_i - v_h)/c$ .

Hautière *et al.* provide an explicit method to estimate the meteorological visibility  $d_{\text{met}}$  directly from the RSLC's inflection point  $v_i$ . Therefore, the main computational costs of the entire approach consists of extracting the luminance curve (*cf.* Sec. 8.1) and its inflection point (*cf.* Sec. 8.5). However, the overall estimation error is composed of the errors arising not only from the RSLC and inflection point extraction, but also from the employed model. In fact, a closer look at the class of luminance curves  $v \mapsto L^{\text{Kos}}(v)$  defined in (8.5) and (8.6) reveals that the model is not capable of sufficiently describing the RSLC observation. In particular, the fact that  $L^{\text{Kos}}$  remains constant above the horizon does not reflect reality (*cf.* Fig. 8.5).

The reason for this is that Koschmieder's model assumes that the amount of ambient light (or air light) scattered into the line of sight is constant in direction and location. This is approximately true for horizontal vision, but changes with the angle of view. This raises the question of how much improvement in measurement accuracy could be achieved by further developing the RSLC model, and whether more accurate models are still applicable for driver assistance purposes. These are the motivating questions for the following sections (*cf.* Sec. 8.3 and Sec. 8.4).

### 8.3 Second-Order: Improved Fog Model

According to the radiative transfer theory (*cf.* 5.3.1), in a perfectly scattering and homogeneous atmosphere the transmission of light in direction  $\sigma = (\sigma^1, \sigma^2, \sigma^3)^T \in \mathbb{S}^2$  over a distance  $d \in \mathbb{R}_{\geq 0}$  can be expressed as

$$L(\sigma, d) = e^{-Kd} L_0 + \int_0^d K e^{-Ks} \int_{\mathbb{S}^2} L_{\text{in}}(p(s), \omega) \psi(\sigma, \omega) dS(\omega) ds. \quad (8.8)$$

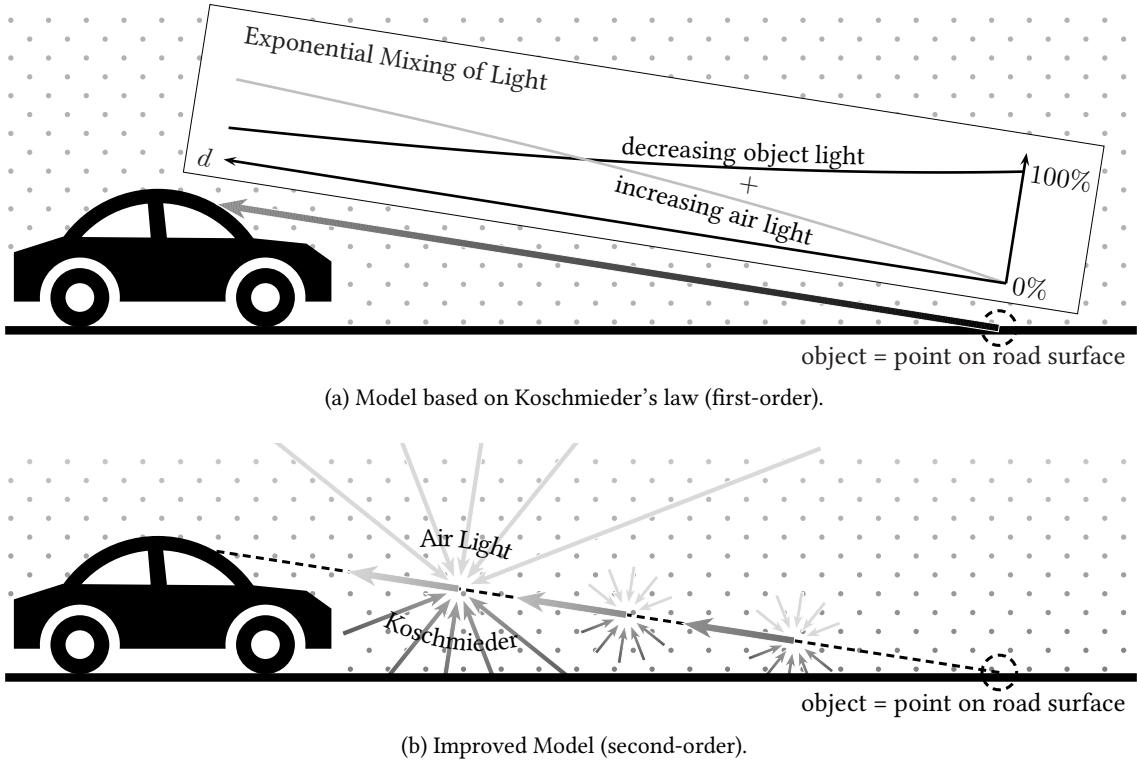


Figure 8.6: Two models for the transmission of light through fog: While Koschmieder's model explains it as an exponential mixing of light, the improved model considers the in-scattered light to be dependent on location and direction on the line of sight. The improved model uses Koschmieder's model to determine the in-scattered light at every position along the line of sight.

Here, the first term represents the exponentially attenuated intrinsic luminance  $L_0$ , and the second term represents the air light scattered into the optical path in direction of the observer  $p_{\text{obs}} \in \mathbb{R}^3$ . At any point of the *line of sight*

$$[0, d] \ni s \mapsto p(s) := p_{\text{obs}} - s\sigma \in \mathbb{R}^3, \quad (8.9)$$

the amount of in-scattered light is determined by the in-scattering luminance  $L_{\text{in}}$  weighted by the phase function  $\psi$  and integrated over all directions, namely  $\int_{\mathbb{S}^2} L_{\text{in}}(p(s), \omega) \psi(\sigma, \omega) dS(\omega)$ . It is easy to see that the light transport model (8.8) turns into Koschmieder's model if  $L_{\text{in}}$  is assumed to be constant in the spatial domain (cf. 5.4.1).

To derive an improved RSLC model, the in-scattering light  $L_{\text{in}}$  has to be chosen more appropriately. This problem is at least as complex as determining  $L$  itself. However, according to 5.4.2, the radiative transfer relation given in (8.8) leads to an upgraded model compared to the model used for  $L_{\text{in}}$ . So far, the best explicit radiative transfer model is given by Koschmieder, which therefore is used as the model for the in-scattering function here (cf. Fig. 8.6). In this way, the RSLC model is improved from the first to the second order.

### 8.3.1 In-Scattering Luminance Model

In order to model the light  $L_{\text{in}}$  that is scattered into the line of sight, the road is assumed to be an infinitely expanded plane. Applying Koschmieder's model (5.19) results in

$$L_{\text{in}}(p(s), \omega) = \begin{cases} L_{\text{air}} & , \text{if } \omega^3 \leq 0 \\ e^{-K \frac{h(s)}{\omega^3}} L_0 + \left(1 - e^{-K \frac{h(s)}{\omega^3}}\right) L_{\text{air}} & , \text{if } \omega^3 > 0 \end{cases}, \quad (8.10)$$

where  $h(s)$  denotes the height of  $p(s)$  above the ground and  $\omega = (\omega^1, \omega^2, \omega^3)^T \in \mathbb{S}^2$  the direction of in-scattered light (cf. Fig. 8.7).

Substituting (8.10) into (8.8), applying the  $\mathbb{S}^2$  parametrization  $\Phi$  from Remark 10 on page 39 and using the fact that the phase function is normalized, (4.4) leads to the second-order model:

$$\begin{aligned} L(\sigma, d) &= e^{-Kd} L_0 + \int_0^d K e^{-Ks} \int_{\mathbb{S}^2} L_{\text{in}}(p(s), \omega) \psi(\sigma, \omega) dS(\omega) ds \\ &= e^{-Kd} L_0 + \int_0^d K e^{-Ks} \int_0^\pi \int_0^{2\pi} L_{\text{in}}(p(s), \omega) \psi(\sigma, \Phi(\varphi, \theta)) \sin(\theta) d\varphi d\theta ds \\ &= e^{-Kd} L_0 + \int_0^d K e^{-Ks} \int_{\frac{\pi}{2}}^\pi \int_0^{2\pi} L_{\text{air}} \psi(\sigma, \Phi(\varphi, \theta)) \sin(\theta) d\varphi d\theta ds \\ &\quad + \int_0^d K e^{-Ks} \int_0^{\frac{\pi}{2}} \int_0^{2\pi} \left[ e^{-K \frac{h(s)}{\cos(\theta)}} L_0 \right. \\ &\quad \quad \quad \left. + \left(1 - e^{-K \frac{h(s)}{\cos(\theta)}}\right) L_{\text{air}} \right] \psi(\sigma, \Phi(\varphi, \theta)) \sin(\theta) d\varphi d\theta ds \\ &= e^{-Kd} L_0 + L_{\text{air}} \int_0^d K e^{-Ks} \int_0^\pi \int_0^{2\pi} \psi(\sigma, \Phi(\varphi, \theta)) \sin(\theta) d\varphi d\theta ds \\ &\quad + (L_0 - L_{\text{air}}) \int_0^d K e^{-Ks} \int_0^{\frac{\pi}{2}} \int_0^{2\pi} e^{-K \frac{h(s)}{\cos(\theta)}} \psi(\sigma, \Phi(\varphi, \theta)) \sin(\theta) d\varphi d\theta ds \\ &= e^{-Kd} L_0 + L_{\text{air}} \int_0^d K e^{-Ks} ds + (L_0 - L_{\text{air}}) \mathcal{T}_K(\sigma, d) \\ &= e^{-Kd} L_0 + (1 - e^{-Kd}) L_{\text{air}} + (L_0 - L_{\text{air}}) \mathcal{T}_K(\sigma, d), \end{aligned} \quad (8.11)$$

where an abbreviatory notation

$$\mathcal{T}_K(\sigma, d) := \int_0^d K e^{-Ks} \int_0^{\frac{\pi}{2}} \int_0^{2\pi} e^{-K \frac{h(s)}{\cos(\theta)}} \psi(\sigma, \Phi(\varphi, \theta)) \sin(\theta) d\varphi d\theta ds$$

is introduced. It is interesting to note that the increase of complexity compared to the first-order model lies in exactly the integral term  $(L_0 - L_{\text{air}}) \mathcal{T}_K(\sigma, d)$ ; the first two terms of the improved model match Koschmieder's model and are independent of  $\sigma$ .

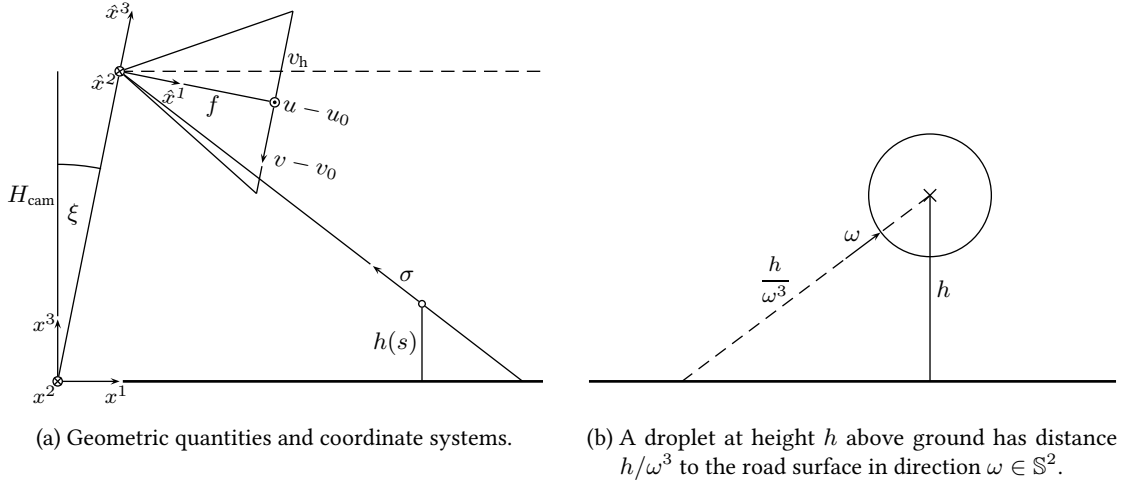


Figure 8.7: Notation and geometry.

### 8.3.2 Geometry

In order to transfer the improved model from world coordinates  $(x^1, x^2, x^3)^T$  to image coordinates  $(u, v)^T$ , the world's and camera's geometry have to be specified (*cf.* Fig. 8.7). As mentioned before, the road is assumed to be an infinitely expanded plane; the camera is mounted at height  $H_{\text{cam}}$  above ground and pitched by an angle  $\xi$ . In camera coordinates  $(\hat{x}^1, \hat{x}^2, \hat{x}^3)^T$ , an image point  $(u, v)^T$  becomes

$$(f, u_0 - u, v_0 - v)^T,$$

determined by the focal length  $f$  and the principle point  $(u_0, v_0)^T$ . Furthermore,  $(u, v)^T$  can be expressed in world coordinates  $(x^1, x^2, x^3)^T$  by translation and rotation of the camera coordinates:

$$p_{\text{obs}} + \begin{pmatrix} \cos(\xi) & 0 & \sin(\xi) \\ 0 & 1 & 0 \\ -\sin(\xi) & 0 & \cos(\xi) \end{pmatrix} \begin{pmatrix} f \\ u_0 - u \\ v_0 - v \end{pmatrix} = p_{\text{obs}} - \begin{pmatrix} \sin(\xi)(v - v_0) - \cos(\xi)f \\ u - u_0 \\ \cos(\xi)(v - v_0) + \sin(\xi)f \end{pmatrix}.$$

In particular,  $\sigma(u, v)$  is given by

$$\sigma(u, v) = \frac{1}{\sqrt{f^2 + (u - u_0)^2 + (v - v_0)^2}} \begin{pmatrix} \sin(\xi)(v - v_0) - \cos(\xi)f \\ u - u_0 \\ \cos(\xi)(v - v_0) + \sin(\xi)f \end{pmatrix}. \quad (8.12)$$

Furthermore, the camera origin in world coordinates is situated at

$$p_{\text{obs}} = \begin{pmatrix} \tan(\xi)H_{\text{cam}} \\ 0 \\ H_{\text{cam}} \end{pmatrix}.$$

This allows for determining the height of  $p(s)$  above the road (*cf.* (8.9)):

$$h(s) = H_{\text{cam}} - s\sigma^3. \quad (8.13)$$

The image's row of the horizon  $v_h$  is defined by  $\sigma^3(u, v_h) = 0$ , which can be evaluated explicitly:

$$\cos(\xi)(v_h - v_0) + \sin(\xi)f = 0 \quad \Leftrightarrow \quad v_h = v_0 - \tan(\xi)f.$$

Due to (8.13) and for  $v > v_h$ , the pixel's distance  $d(u, v)$  is determined by  $H_{\text{cam}} - d(u, v)\sigma^3(u, v) = 0$  and thus

$$d(u, v) = \begin{cases} \infty & , \text{ if } v \leq v_h \\ \frac{H_{\text{cam}}}{\sigma^3(u, v)} & , \text{ if } v > v_h \end{cases}. \quad (8.14)$$

### 8.3.3 Second-Order Model

The last step formulating the explicit RSLC model is to choose a phase function  $\psi$ . The shape of the scattering distribution differs from particle to particle. Depending on the drop-size distribution, the macroscopic phase function can be described as an average representation of scatterers (cf. 4.3.2). In the context of fog, the Henyey-Greenstein phase function (4.12) is commonly used to approximate this average scattering distribution

$$\psi^{\text{HG}}(\sigma, \omega) = \frac{1}{4\pi} \frac{1 - g^2}{(1 - 2g\langle\sigma, \omega\rangle + g^2)^{\frac{3}{2}}},$$

where  $g \in [0.8, 0.9]$  denotes the asymmetry parameter and  $\sigma$  and  $\omega$  are directed inwards and outwards, respectively (cf. Fig. 4.4). One should note that most of the following insights are independent of the chosen phase function.

Finally, inserting (8.12) and (8.14) in (8.11) yields the improved RSLC model

$$v \mapsto L^{\text{2nd}}(v) = L_{\text{air}} + (L_0 - L_{\text{air}}) \left[ e^{-Kd(u, v)} + \mathcal{T}_K(\sigma(u, v), d(u, v)) \right], \quad (8.15)$$

where

$$\mathcal{T}_K(\sigma, d) = \int_0^d K e^{-Ks} \int_0^{\frac{\pi}{2}} \int_0^{2\pi} e^{-K \frac{h(s)}{\cos(\theta)}} \psi^{\text{HG}}(\sigma, \Phi(\varphi, \theta)) \sin(\theta) d\varphi d\theta ds. \quad (8.16)$$

This model depends on several parameters; the *system parameters*  $H_{\text{cam}}$ ,  $\xi$ ,  $f$ ,  $u_0$ ,  $v_0$  and  $u$ , which are assumed as being given (e.g. from calibration and algorithms estimating the camera motion); and the *atmospheric parameters*  $K$ ,  $L_{\text{air}}$ ,  $L_0$  and  $g$ . Apart from  $u_0$  and  $u$ , which are ignored in [Hau2006c] for reasons of simplicity, the parameter  $g$  is the only new parameter appearing in the second-order RSLC model. In the following, an abbreviatory notation  $L^{\text{2nd}}(v; p_1, p_2, \dots)$  is used whenever  $L^{\text{2nd}}$  is discussed w.r.t. the parameters  $p_1, p_2, \dots$ , for instance  $L^{\text{2nd}}(v; K, L_0, L_{\text{air}})$  or  $L^{\text{2nd}}(v; f, H_{\text{cam}})$ .

### 8.3.4 Notes on the Parameter Estimation

***K-v<sub>i</sub> Relation.*** Similar to Koschmieder's model, linear transformations applied to the improved model exactly correspond to changes in the luminance parameters  $L_0$  and  $L_{\text{air}}$ . On the one hand,

for all  $\alpha, \beta \in \mathbb{R}$  and any  $v$  one has

$$\begin{aligned} \alpha L^{\text{2nd}}(v; L_{\text{air}}, L_0) + \beta &= \alpha \left[ L_{\text{air}} + (L_0 - L_{\text{air}}) \left[ e^{-Kd} + \mathcal{T}_K(\sigma, d) \right] \right] + \beta \\ &= [\alpha L_{\text{air}} + \beta] + ([\alpha L_0 + \beta] - [\alpha L_{\text{air}} + \beta]) \left[ e^{-Kd} + \mathcal{T}_K(\sigma, d) \right] \\ &= L^{\text{2nd}}(v; \alpha L_{\text{air}} + \beta, \alpha L_0 + \beta). \end{aligned}$$

On the other hand, for any  $L_{\text{air}}, L_0, \hat{L}_{\text{air}}$  and  $\hat{L}_0$  (with  $L_0 \neq L_{\text{air}}$ ), the corresponding second-order luminance curves are linearly related; more precisely,  $L^{\text{2nd}}(\cdot; \hat{L}_{\text{air}}, \hat{L}_0) \equiv \alpha L^{\text{2nd}}(\cdot; L_{\text{air}}, L_0) + \beta$ , where

$$\alpha = \frac{\hat{L}_{\text{air}} - \hat{L}_0}{L_{\text{air}} - L_0}, \quad \beta = \frac{\hat{L}_0 L_{\text{air}} - \hat{L}_{\text{air}} L_0}{L_{\text{air}} - L_0}.$$

This is not only a basic requirement for all models working with intensities instead of luminances (cf. Sec. 6.4), but also reveals the independence of  $v_i$  from  $L_{\text{air}}$  and  $L_0$ . Therefore, given all system parameters,  $v_i$  only depends on the two remaining atmospheric parameters  $K$  and  $g$ .

However, there does not seem to be a way to estimate  $g$  from an observed luminance curve without performing a full model fit. In order to avoid this computationally expensive optimization procedure, the asymmetry parameter is set to a fixed value

$$g := 0.85.$$

Fortunately,  $g$ 's effect on  $v_i$  seems to be almost negligible compared to  $K$ 's. Numerical experiments suggest that keeping  $g$  constant produces a worst-case error of about 3.5% (cf. Fig. 8.17). Now that  $g$  and all system parameters are fixed, for every  $K$ , there exists exactly one  $v_i$  independent of  $L_{\text{air}}$  and  $L_0$ . Further experiments support the presumption that  $K \mapsto v_i(K)$  is monotone and in particular bijective (cf. Fig. 8.15). Therefore, it can be utilized for parameter estimation by inversion. In contrast to the first-order model from Sec. 8.2, the mapping  $v_i \mapsto K(v_i)$  cannot be formulated explicitly. The increased complexity of the new model thus has to be broken down to precomputed look-up tables (see below).

Similar to (8.7), it is possible to additionally estimate the atmospheric parameters  $L_{\text{air}}$  and  $L_0$  from  $(v_i, L^{\text{2nd}}(v_i), \partial_v L^{\text{2nd}}(v_i))$  via

$$L_{\text{air}} = L^{\text{2nd}}(v_i; L_{\text{air}}, L_0) - D L^{\text{2nd}}(v_i; 0, 1), \quad L_0 = D + L_{\text{air}}, \quad D := \frac{\partial_v L^{\text{2nd}}(v_i; L_{\text{air}}, L_0)}{\partial_v L^{\text{2nd}}(v_i; 0, 1)},$$

taking advantage of the simplicity of  $L^{\text{2nd}}(v_i; 0, 1)$  (cf. (8.15)):

$$L^{\text{2nd}}(v_i; 0, 1) = e^{-Kd(u,v)} + \mathcal{T}_K(\sigma(u, v), d(u, v)).$$

In the following, the inflection-point-based parameter estimation is referred to as  $v_i$ -fit.

**Inflection Point Estimation from Noisy Observation Data.** One necessary part of the parameter estimation and data acquisition is the extraction of the inflection point  $v_i$  from an observed road surface luminance curve. This is an important source of error during the overall measurement of  $d_{\text{met}}$ . A further discussion can be found in Sec. 8.5 and 8.6.2 (cf. Fig. 8.16).

**Integral Evaluation.** The main computational cost for calculating the second-order RSLC model lies in the triple integral in (8.16). Due to the fundamental theorem of calculus,  $\mathcal{T}_K$  is continuous

and even differentiable in  $d$ . Applying further Fubini's theorem and Lebesgue's dominated convergence theorem to  $\mathcal{T}_K(\sigma, d')$  for  $d' \rightarrow d$  allows for replacing of the triple integral with a numerical more cost-effective double integral, even for  $d = \infty$ :

$$\begin{aligned} \mathcal{T}_K(\sigma, d) &= \lim_{d' \rightarrow d} \mathcal{T}_K(\sigma, d') \\ &= \lim_{d' \rightarrow d} \int_0^{d'} K e^{-Ks} \int_0^{\frac{\pi}{2}} \int_0^{2\pi} e^{-K \frac{h(s)}{\cos(\theta)}} \psi^{\text{HG}}(\sigma, \Phi(\varphi, \theta)) \sin(\theta) d\varphi d\theta ds \\ &= \lim_{d' \rightarrow d} \int_0^{\frac{\pi}{2}} \int_0^{d'} K e^{-Ks} e^{-K \frac{h(s)}{\cos(\theta)}} ds \int_0^{2\pi} \psi^{\text{HG}}(\sigma, \Phi(\varphi, \theta)) d\varphi \sin(\theta) d\theta \\ &= \int_0^{\frac{\pi}{2}} \int_0^d K e^{-Ks} e^{-K \frac{h(s)}{\cos(\theta)}} ds \int_0^{2\pi} \psi^{\text{HG}}(\sigma, \Phi(\varphi, \theta)) d\varphi \sin(\theta) d\theta. \end{aligned}$$

To avoid numerical handling of infinity, the first inner integral can be explicitly evaluated for  $d = \infty$ :

$$\begin{aligned} \int_0^{\infty} K e^{-Ks} e^{-K \frac{h(s)}{\cos(\theta)}} ds &= \lim_{d' \rightarrow \infty} \int_0^{d'} K e^{-Ks} e^{-K \frac{H_{\text{cam}} - s\sigma^3}{\cos(\theta)}} ds \\ &= e^{-K \frac{H_{\text{cam}}}{\cos(\theta)}} \lim_{d' \rightarrow \infty} \int_0^{d'} K e^{-Ks \left(1 - \frac{\sigma^3}{\cos(\theta)}\right)} ds \\ &= e^{-K \frac{H_{\text{cam}}}{\cos(\theta)}} \lim_{d' \rightarrow \infty} \left[ - \left(1 - \frac{\sigma^3}{\cos(\theta)}\right)^{-1} e^{-Ks \left(1 - \frac{\sigma^3}{\cos(\theta)}\right)} \right]_{s=0}^{d'} \quad (8.17) \\ &= \left(1 - \frac{\sigma^3}{\cos(\theta)}\right)^{-1} e^{-K \frac{H_{\text{cam}}}{\cos(\theta)}} = \frac{\cos(\theta)}{\cos(\theta) - \sigma^3} e^{-K \frac{H_{\text{cam}}}{\cos(\theta)}}. \end{aligned}$$

One should note that  $\sigma^3 \leq 0$  for  $d = \infty$  and  $\cos(\theta) > 0$  on  $(0, \pi/2)$ . In the case of  $d < \infty$ , a similar evaluation could be done for the integral, which in contrast to the  $d = \infty$  case would lead to problems at  $\cos(\theta) = \sigma^3$ . This could be further approached by applying l'Hôpital's rule, which in turn leads to an inconvenient numerical case differentiation. Therefore, for  $d < \infty$  an numerical evaluation of the integral is preferable.

**Quadrature for  $d < \infty$ .** To evaluate the integrals in  $\mathcal{T}_K$  numerically, *Simpson's rule* (also referred to as *three-point Newton-Cotes quadrature rule*)

$$\int_x^{x+h} f(\tau) d\tau \approx \frac{h}{6} \left[ f(x) + 4f\left(x + \frac{h}{2}\right) + f(x+h) \right]$$

is applied. Thereby the intervals  $[0, \pi/2]$ ,  $[0, d]$  and  $[0, 2\pi]$  are split up into  $N_\theta$ ,  $N_s$ ,  $N_\varphi$  subintervals of equal length, respectively, where

$$h_\theta := \frac{\pi}{2N_\theta}, \quad h_s := \frac{d}{N_s}, \quad h_\varphi := \frac{2\pi}{N_\varphi}.$$

For reasons of clarity, let

$$T_1(s, \theta) := K e^{-K \left( \frac{h(s)}{\cos(\theta)} + s \right)}, \quad T_2(s, \theta) := \psi^{\text{HG}}(\sigma, \Phi(\varphi, \theta)).$$

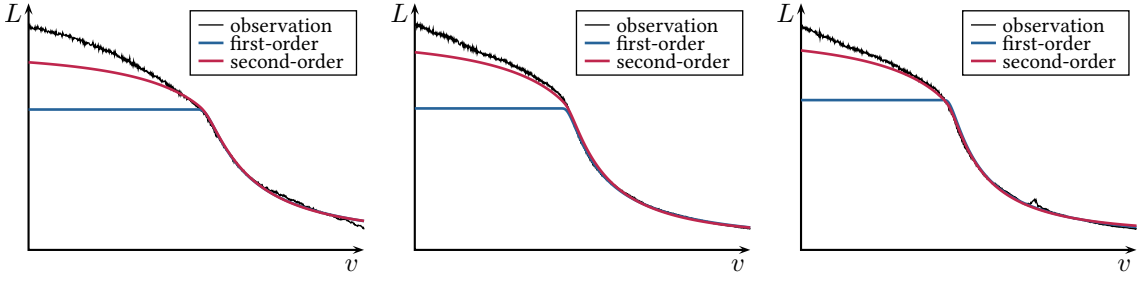


Figure 8.8: Examples for first-order and second-order  $v_i$ -fits. The second-order model fits the data more appropriately than the first-order model, but it still leaves room for improvement. This is addressed by the higher-order models introduced in Sec. 8.4.

Now, repeatedly applying Simpson's rule to all subintervals yields

$$\begin{aligned}
 \mathcal{T}_K(\sigma, d) &= \int_0^{\frac{\pi}{2}} \int_0^d T_1(s, \theta) ds \int_0^{2\pi} T_2(\varphi, \theta) d\varphi \sin(\theta) d\theta \\
 &\approx \frac{h_\theta}{6} \sum_{n=0}^{2N_\theta} w_{\theta,n} \sin(\theta_n) \int_0^d T_1(s, \theta_n) ds \int_0^{2\pi} T_2(\varphi, \theta_n) d\varphi \\
 &\approx \frac{h_\theta h_s h_\varphi}{216} \sum_{n=0}^{2N_\theta} w_{\theta,n} \sin(\theta_n) \sum_{m=0}^{2N_s} w_{s,m} T_1(s_m, \theta_n) \sum_{l=0}^{2N_\varphi} w_{\varphi,l} T_2(\varphi_l, \theta_n),
 \end{aligned}$$

where the quadrature weights  $w_{\theta,n}$ ,  $w_{s,m}$  and  $w_{\varphi,l}$  are 1, 4, 2, 4, 2,  $\dots$ , 2, 4, 2, 4, 1 and the quadrature interpolation points are given as

$$\theta_n := n \frac{h_\theta}{2}, \quad s_m := m \frac{h_s}{2}, \quad \varphi_l := l \frac{h_\varphi}{2}.$$

**Quadrature for  $d = \infty$ .** The case  $d = \infty$  can be treated analogously to the  $d < \infty$  case, whereby (8.17) has to be taken into account.

**Symmetry in  $u - u_0$ .** As one might expect from the geometry, the model is symmetric in  $u$  around  $u_0$ , i.e. for any  $v$  and  $u_\Delta$

$$L^{\text{2nd}}(v; u = u_0 + u_\Delta) \equiv L^{\text{2nd}}(v; u = u_0 - u_\Delta).$$

This can easily be proven by a substitution  $(\varphi, \theta) \rightarrow (2\pi - \varphi, \theta)$ .

**Efficient Look-up Tables.** In contrast to the first-order model from Sec. 8.2, the relation between  $v_i$  and  $K$  for the second-order model is not given in an explicit way. Since its computation seems to be too expensive for an online solution, it is useful to find an efficient way to store  $v_i \mapsto K(v_i; L_0, L_{\text{air}}, H_{\text{cam}}, \xi, f, u_0, v_0, u, g)$ . The luminance parameters  $L_0$  and  $L_{\text{air}}$  can be ignored due to the invariance discussed at the beginning of 8.3.4. The asymmetry parameter  $g$  is set to 0.85 as explained above and in Fig. 8.17.  $f$  and  $v_0$  are intrinsic parameters that are assumed to be constant here. Furthermore, as shown above, the extinction coefficient depends on  $u$  and  $u_0$  only in the form of  $|u - u_0|$ .

Therefore, it remains to precompute a look-up table of the form  $v_i \mapsto K(v_i; H_{\text{cam}}, \xi, |u - u_0|)$ .

This can be done in various ways. One of them shall be demonstrated here for the following test set:

$$\begin{aligned}
 d_{\text{met}} &\in \{20 \text{ m}, 30 \text{ m}, \dots, 490 \text{ m}, 500 \text{ m}\}, \\
 H_{\text{cam}} &\in \{1.250 \text{ m}, 1.255 \text{ m}, \dots, 1.295 \text{ m}, 1.300 \text{ m}\}, \\
 \xi &\in \{0^\circ, 0.1^\circ, \dots, 4.9^\circ, 5^\circ\}, \\
 u &\in \{u_0, u_0 \pm 10 \text{ px}, \dots, u_0 \pm 190 \text{ px}, u_0 \pm 200 \text{ px}\}.
 \end{aligned} \tag{8.18}$$

Since the range of  $v_i$  varies w.r.t. the system parameters, the look-up table is (counterintuitively) constructed for the inverse mapping  $K \mapsto v_i(K)$ . Another benefit of this inverse mapping is that  $d_{\text{met}}$  is evenly sampled according to (8.18). The look-up query for given data  $(v_i, H_{\text{cam}}, \xi, |u - u_0|)$  would thus consist in a simple one-dimensional binary search in the respective  $K$ - $v_i$  list. For this naïve look-up table concept  $49 \cdot 51 \cdot 11 \cdot 21$   $v_i$  values have to be stored together with the  $49 + 51 + 11 + 21$  parameter values described in (8.18) which sums up to 577401 values. This motivates the idea to further compress the look-up table in order to save memory. This can be approached in various ways. The compression concept proposed in this work is based on the observation from 8.6.2 that for a fixed set of parameters the relation  $v_i \mapsto K(v_i)$  has a quite linear character (cf. Fig. 8.15). Therefore, it is useful to formulate the  $v_i$ - $K$  relation for each parameter setting  $(H_{\text{cam}}, \xi, |u - u_0|)$  as

$$K(v_i) = \alpha v_i + \beta - \varepsilon(v_i),$$

where  $\varepsilon(v_i)$  denotes the error term and  $\alpha$  and  $\beta$  are chosen for the mapping to be exact at  $K = 0.15 \text{ m}^{-1}$  ( $d_{\text{met}} \approx 20 \text{ m}$ ) and  $K = 0.006 \text{ m}^{-1}$  ( $d_{\text{met}} \approx 500 \text{ m}$ ), i.e.

$$0.15 = \alpha v_i(0.15) + \beta, \quad 0.006 = \alpha v_i(0.006) + \beta.$$

Furthermore, Fig. 8.18 suggests a quite simple dependency of  $\alpha$  and  $\beta$  on the parameters  $H_{\text{cam}}, \xi, |u - u_0|$ . This motivates the idea to further approximate the overall  $v_i$ - $K$  relation by

$$\begin{aligned}
 \alpha(H_{\text{cam}}, \xi, u) &= \sum_{n_H=0}^2 \sum_{n_\xi=0}^2 \sum_{n_u=0}^2 c_{n_H, n_\xi, n_u}^\alpha H_{\text{cam}}^{n_H} \xi^{n_\xi} u^{n_u}, \\
 \beta(H_{\text{cam}}, \xi, u) &= \sum_{n_H=0}^3 \sum_{n_\xi=0}^3 \sum_{n_u=0}^3 c_{n_H, n_\xi, n_u}^\beta H_{\text{cam}}^{n_H} \xi^{n_\xi} u^{n_u}.
 \end{aligned}$$

In order to compensate the slightly non-linear character of the  $v_i$ - $K$  relation, the error term  $\varepsilon(v_i)$  can be approximated by a mapping  $K \mapsto \varepsilon^{\text{avg}}(K)$ . For each  $K$  from (8.18), this mapping is computed as the average error term  $\varepsilon$  over all system parameters. To apply this correction term to a given  $v_i$ , one has to compute the linear approximation  $K^{\text{lin}} := \alpha v_i + \beta$  first. The correction term  $\varepsilon^{\text{avg}}$  has then to be applied to  $K^{\text{lin}}$  in order to achieve a more appropriate estimation of  $K$ .

In this way, only  $2 \cdot 49$  values for  $\varepsilon^{\text{avg}}$  and  $3^3 + 4^3$  values for the  $\alpha$ - $\beta$  interpolation coefficients have to be stored. For the example given above, this drastically reduces the number of values to be stored to 189. The maximum relative estimation error in  $d_{\text{met}}$  generated by this reduction technique turns out to be below 0.9% on the test set (8.18). Without the non-linearity correction introduced by  $\varepsilon^{\text{avg}}$ , this would be more than 7%.

## 8.4 Higher-Order Models

In Sec. 8.3, it has been outlined that based on the radiative transfer theory an existing luminance model can be improved by utilizing it as the in-scattering luminance model. It stands to reason that this idea can be iterated in order to incrementally improve the luminance models. More precisely, one can write

$$L^0(x, \sigma) := L_{\text{air}},$$

$$L^{n+1}(x, \sigma) := L_0(x, \sigma)e^{-Kd(x, \sigma)} + \int_0^{d(x, \sigma)} Ke^{-Ks} \int_{\mathbb{S}^2} L^n(x - s\sigma, \omega) \psi(\sigma, \omega) dS(\omega) ds.$$

These recursively defined models are extensively discussed in 5.4.2 and Theorem 2 on page 50. Among other important properties, convergence of  $L^n$  as  $n \rightarrow \infty$  towards the exact solution of the full radiative boundary problem is shown (see Sec. 5.2). In this sense it becomes clearer why Hautière *et al.*'s model (see Sec. 8.2) and the improved model (see Sec. 8.3) can be interpreted as first-order and second-order RSLC models, respectively. It also motivates why the second-order model is indeed a more appropriate model than the first-order one (*cf.* Fig. 8.8).

Higher-order RSLC models can be derived by applying the recursively defined luminance models to a plane-parallel scenario. According to Sec. 5.5, the plane-parallel radiative boundary problem can be written as

$$\bar{L}(H, \mu) = L_0(H, \mu)e^{-Kd(H, \mu)} + \int_0^{d(H, \mu)} Ke^{-Ks} \int_{-1}^1 \bar{L}(H + s\mu, \hat{\mu}) \bar{\psi}(\mu, \hat{\mu}) d\hat{\mu} ds, \quad (8.19)$$

where  $(H, \mu)$  is related to  $(x, \sigma)$  via the  $x^3$ -plane-parallel transformation

$$H : \mathbb{R}^3 \times \mathbb{S}^2 \rightarrow \mathbb{R}, \quad (x, \sigma) \mapsto x^3,$$

$$\mu : \mathbb{R}^3 \times \mathbb{S}^2 \rightarrow [-1, 1], \quad (x, \sigma) \mapsto \sigma^3;$$

and  $\bar{L}$  denotes the plane-parallel representation of the luminance function

$$\bar{L} : [0, H_{\text{atm}}] \times [-1, 1] \rightarrow [0, \infty), \quad L(x, \sigma) = \bar{L}(H(x, \sigma), \mu(x, \sigma));$$

and  $\bar{\psi}$  denotes the plane-parallel phase function

$$\bar{\psi}(\mu, \hat{\mu}) = \int_0^{2\pi} \hat{\psi} \left( \mu \hat{\mu} + \sqrt{1 - \mu^2} \sqrt{1 - \hat{\mu}^2} \cos(\varphi) \right) d\varphi,$$

where  $\hat{\psi}(\langle \omega, \hat{\omega} \rangle) = \psi(\omega, \hat{\omega})$ . The boundary conditions at height levels 0 and  $H_{\text{atm}}$  (*cf.* Fig. 8.9) are given by

$$\forall \mu \in [0, 1] : \bar{L}(0, \mu) = L_0,$$

$$\forall \mu \in [-1, 0] : \bar{L}(H_{\text{atm}}, \mu) = L_{\text{air}},$$

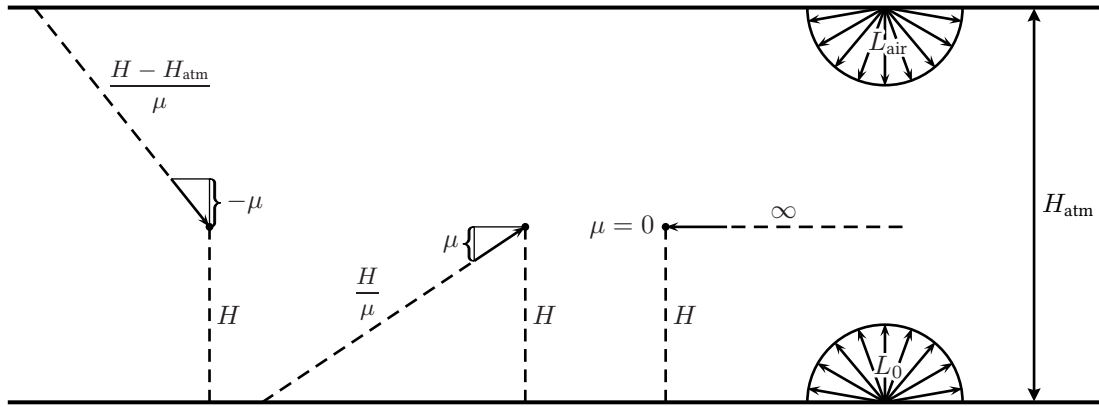
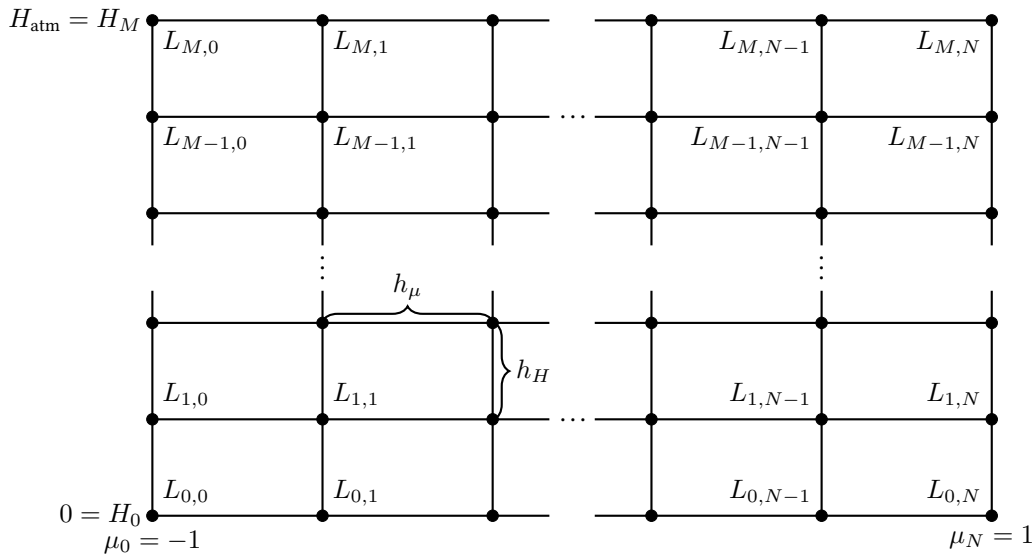


Figure 8.9: Plane-parallel boundary conditions.

Figure 8.10: Discrete representation of  $\bar{L}$  on  $[0, H_{\text{atm}}] \times [-1, 1]$ .

which leads to  $d(H, \mu)$  and  $L_0(H, \mu)$  being given as

$$L_0(H, \mu) = \begin{cases} L_{\text{air}} & , \text{ if } \mu \leq 0 \\ L_0 & , \text{ if } \mu > 0 \end{cases}, \quad d(H, \mu) = \begin{cases} \frac{H - H_{\text{atm}}}{\mu} & , \text{ if } \mu < 0 \\ \infty & , \text{ if } \mu = 0 \\ \frac{H}{\mu} & , \text{ if } \mu > 0 \end{cases}$$

With each step from the  $n^{\text{th}}$ -order to the  $(n + 1)^{\text{th}}$ -order model, the analytical complexity is substantially increased. As a consequence, an explicit analytical discussion seems to be impracticable. Nevertheless, the higher-order models can still be deployed using numerical approximations.

To achieve this, the domain  $[0, H_{\text{atm}}] \times [-1, 1]$  is equidistantly split up into  $M \cdot N$  rectangles (*cf.*

Fig. 8.10):

$$\begin{aligned} 0 = H_0 < \dots < H_m = mh_H < \dots < H_M = H_{\text{atm}}, & \quad h_H = \frac{H_{\text{atm}}}{M}, \\ -1 = \mu_0 < \dots < \mu_n = -1 + nh_\mu < \dots < \mu_N = 1, & \quad h_\mu = \frac{2}{N}. \end{aligned}$$

$\bar{L}$  is numerically represented by  $L_h$ , which is discretely defined through  $L_h(H_m, \mu_n) = L_{m,n}$  and bilinearly interpolated in between, i.e. on  $[H_m, H_{m+1}] \times [\mu_n, \mu_{n+1}]$  it is

$$L_h(H, \mu) = c_{00} + c_{10}H_{\text{rel}} + c_{01}\mu_{\text{rel}} + c_{11}H_{\text{rel}}\mu_{\text{rel}},$$

where the relative representations of  $H$  and  $\mu$  are given by

$$H_{\text{rel}} = \frac{H - H_m}{h_H}, \quad \mu_{\text{rel}} = \frac{\mu - \mu_n}{h_\mu},$$

and the coefficients  $c_{ij}$  are derived from

$$\begin{aligned} L_{m,n} &= c_{00} + c_{10} \cdot 0 + c_{01} \cdot 0 + c_{11} \cdot 0 \cdot 0, \\ L_{m+1,n} &= c_{00} + c_{10} \cdot 1 + c_{01} \cdot 0 + c_{11} \cdot 1 \cdot 0, \\ L_{m,n+1} &= c_{00} + c_{10} \cdot 0 + c_{01} \cdot 1 + c_{11} \cdot 0 \cdot 1, \\ L_{m+1,n+1} &= c_{00} + c_{10} \cdot 1 + c_{01} \cdot 1 + c_{11} \cdot 1 \cdot 1, \end{aligned}$$

which leads to

$$\begin{aligned} c_{00} &= L_{m,n}, \quad c_{10} = L_{m+1,n} - L_{m,n}, \quad c_{01} = L_{m,n+1} - L_{m,n}, \\ c_{11} &= L_{m+1,n+1} - L_{m+1,n} - L_{m,n+1} + L_{m,n}. \end{aligned}$$

To represent the zeroth-order model, all  $L_{m,n}$  have to be set to  $L_{\text{air}}$  initially, s.t.  $L_h \equiv L_{\text{air}}$ .

In order to derive the approximate higher-order models,  $L_h$  is inserted into (8.19). Similar to 8.3.4, the triple integral has to be evaluated numerically. For this, each integration direction is disassembled into  $N_{\hat{\mu}}$ ,  $N_s$  and  $N_\varphi$  intervals of equal lengths

$$h_{\hat{\mu}} = \frac{2}{N_{\hat{\mu}}}, \quad h_s = \frac{d(H, \mu)}{N_s}, \quad h_\varphi = \frac{2\pi}{N_\varphi},$$

respectively. With the help of Fubini's theorem and Simpson's rule, the integral can be numerically evaluated by

$$\begin{aligned} & \int_0^{d(H, \mu)} K e^{-Ks} \int_{-1}^1 \bar{L}(H + s\mu, \hat{\mu}) \bar{\psi}(\mu, \hat{\mu}) d\hat{\mu} ds \\ &= \int_{-1}^1 \left[ \int_0^{d(H, \mu)} K e^{-Ks} \bar{L}(H + s\mu, \hat{\mu}) ds \right] \left[ \int_0^{2\pi} \hat{\psi} \left( \mu \hat{\mu} + \sqrt{1 - \mu^2} \sqrt{1 - \hat{\mu}^2} \cos(\varphi) \right) d\varphi \right] d\hat{\mu} \\ &\approx \frac{h_{\hat{\mu}} h_s h_\varphi}{216} \sum_{n_{\hat{\mu}}=0}^{2N_{\hat{\mu}}} w_{\hat{\mu}}(n_{\hat{\mu}}) \left[ \sum_{n_s=0}^{2N_s} w_s(n_s) Q_1(n_s, n_{\hat{\mu}}) \right] \left[ \sum_{n_\varphi=0}^{2N_\varphi} w_\varphi(n_\varphi) Q_2(n_\varphi, n_{\hat{\mu}}) \right], \end{aligned} \quad (8.20)$$

where  $w_s, w_{\hat{\mu}}, w_\varphi$  denote the weights 1, 4, 2, 4, 2, ..., 2, 4, 2, 4, 1 and

$$Q_1(n_s, n_{\hat{\mu}}) = K e^{-K n_s \frac{h_s}{2}} L_h \left( H - n_s \frac{h_s}{2} \mu, -1 + n_{\hat{\mu}} \frac{h_{\hat{\mu}}}{2} \right),$$

$$Q_2(n_\varphi, n_{\hat{\mu}}) = \hat{\psi} \left( \mu \left( -1 + n_{\hat{\mu}} \frac{h_{\hat{\mu}}}{2} \right) + \sqrt{1 - \mu^2} \sqrt{1 - \left( -1 + n_{\hat{\mu}} \frac{h_{\hat{\mu}}}{2} \right)^2} \cos \left( n_\varphi \frac{h_\varphi}{2} \right) \right).$$

To avoid a cumbersome handling of infinity, the case  $\mu = 0$  is specially treated by

$$\bar{L}(H, 0) = \int_0^\infty K e^{-Ks} ds \int_{-1}^1 \bar{L}(H, \hat{\mu}) \bar{\psi}(0, \hat{\mu}) d\hat{\mu} = \int_{-1}^1 \bar{L}(H, \hat{\mu}) \bar{\psi}(0, \hat{\mu}) d\hat{\mu},$$

which is numerically approximated analogously to the case  $\mu \neq 0$ .

Furthermore, it is useful to normalize the discrete  $\hat{\psi}$ , motivated by the phase function's normalization property in the continuous case, which is

$$\int_{-1}^1 \int_0^{2\pi} \hat{\psi} \left( \mu \hat{\mu} + \sqrt{1 - \mu^2} \sqrt{1 - \hat{\mu}^2} \cos(\varphi) \right) d\varphi d\hat{\mu} = 1.$$

This leads to a normalized version of (8.20)

$$\int_{-1}^1 \left[ \int_0^{d(H, \mu)} K e^{-Ks} \bar{L}(H - s\mu, \hat{\mu}) ds \right] \left[ \int_0^{2\pi} \hat{\psi} \left( \mu \hat{\mu} + \sqrt{1 - \mu^2} \sqrt{1 - \hat{\mu}^2} \cos(\varphi) \right) d\varphi \right] d\hat{\mu}$$

$$\approx \frac{h_s}{6} \frac{\sum_{n_{\hat{\mu}}=0}^{2N_{\hat{\mu}}} w_{\hat{\mu}}(n_{\hat{\mu}}) \left[ \sum_{n_s=0}^{2N_s} w_s(n_s) Q_1(n_s, n_{\hat{\mu}}) \right] \left[ \sum_{n_\varphi=0}^{2N_\varphi} w_\varphi(n_\varphi) Q_2(n_\varphi, n_{\hat{\mu}}) \right]}{\sum_{n_{\hat{\mu}}=0}^{2N_{\hat{\mu}}} w_{\hat{\mu}}(n_{\hat{\mu}}) \sum_{n_\varphi=0}^{2N_\varphi} w_\varphi(n_\varphi) Q_2(n_\varphi, n_{\hat{\mu}})}$$

Since the integrands do not have to be evaluated at any further points, the computational costs for the normalization are negligible. Moreover, due to the anisotropic shape of  $\psi^{\text{HG}}$ , the normalization step stabilizes the numerical integration significantly (*cf.* Fig. 8.23). The explicit normalization factor ensures the use of valid discrete phase functions and incorporates additional information to the integration which helps reduce the quadrature error.

Examples for higher-order light distributions are given in Fig. 8.11. From these, one can easily compute the corresponding RSLCs by positioning a virtual camera (with specified height, pitch angle and intrinsic camera parameters) within each light distribution (*cf.* Fig. 8.12). It is interesting to see that both figures are consistent with Theorem 2 on page 50: For order 0 the light distribution and thus the RSLC are constant. For order 1 and order 2 the resulting RSLCs match the explicit first-order and second-order RSLC models derived in Sec. 8.2 and Sec. 8.3, respectively. Despite the large number of discretizations, these curves perfectly coincide. One can also observe the predicted monotonicity, boundedness and convergence behavior.

**Remark 31** (Parameter estimation based on  $K$ - $v_i$  relation). Due to Theorem 2(g) on page 50, the relation between the inflection point  $v_i$  of higher-order models and  $K$  is independent of  $L_{\text{air}}$  and  $L_0$ . Hence, similar to the first-order and second-order case (*cf.* 8.3.4), a fast parameter estimation method based on look-up tables could be implemented. Unfortunately, due to the high complexity of large-order models, creating look-up tables seems to be an extremely costly task. However,

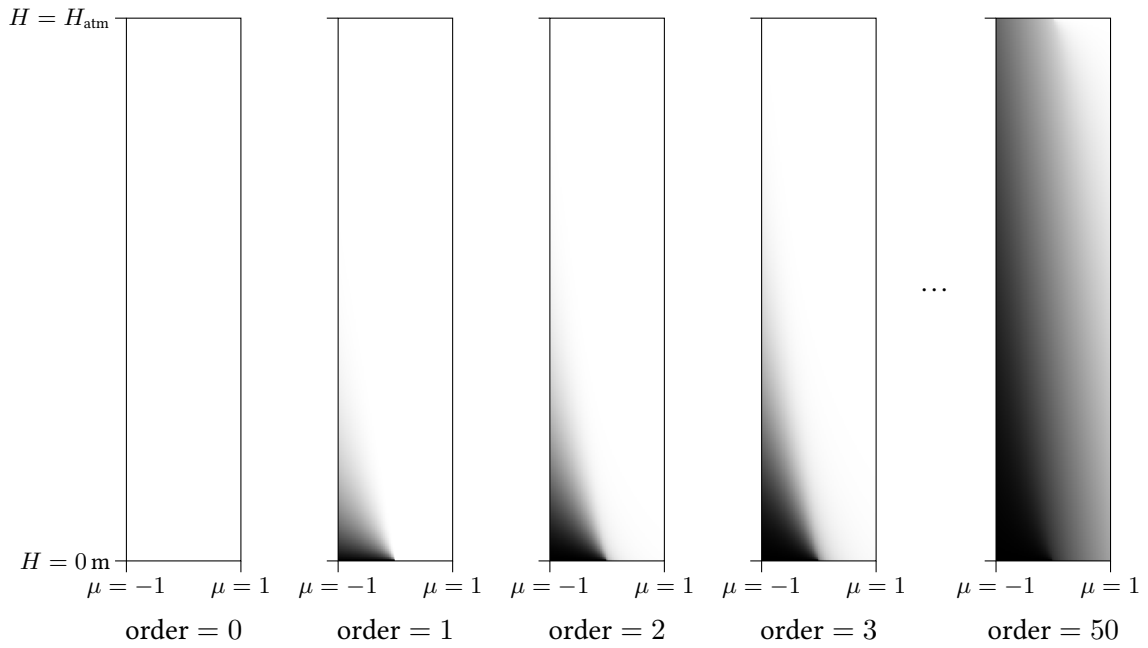


Figure 8.11: Higher-order light distributions in  $H$  and  $\mu$ . Setting:  $d_{\text{met}} = 40$  m,  $L_0 = \text{black}$ ,  $L_{\text{air}} = \text{white}$ ,  $H_{\text{atm}} = 120$  m,  $M = 480$ ,  $N = 100$ ,  $N_s = 80$ ,  $N_{\hat{\mu}} = 30$ ,  $N_{\varphi} = 30$ .

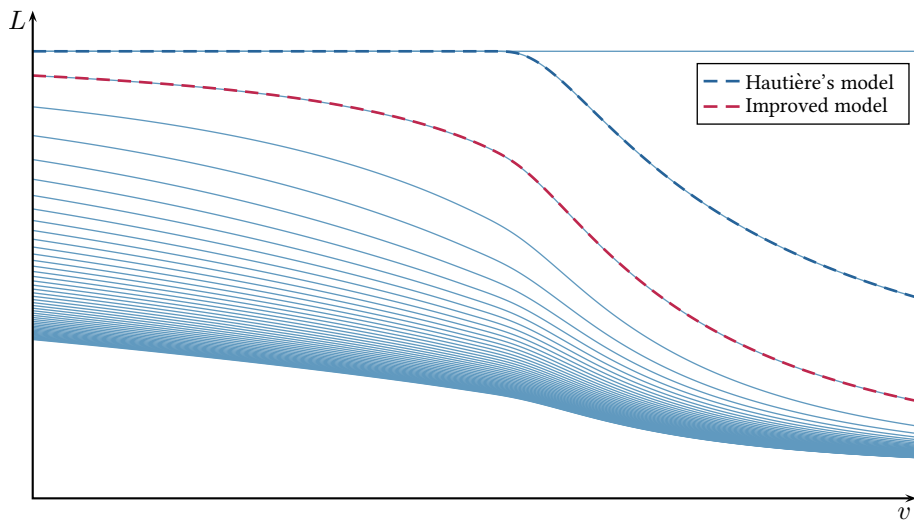


Figure 8.12: Higher-order RSLCs extracted from the light distributions in Fig. 8.11 with the help of a virtual camera, where  $H_{\text{cam}} = 1.5$  m,  $\xi = 0^\circ$ ,  $f = 1200$  px,  $u_0 = 0$  px,  $v_0 = 256$  px,  $v_{\text{max}} = 512$  px.

even taking the second-order model instead of the first-order one is a substantial improvement in visibility estimation (*cf.* Fig. 8.19).

### 8.5 Inflection Point Estimation from Observation Data

The visibility estimation methods proposed in this chapter are mostly based on a mapping from the RSLC’s inflection point  $v_i$  to the corresponding extinction coefficient  $K$  of the atmosphere (*cf.* Sec. 8.2 and Sec. 8.3). Therefore, the robust extraction of inflection points from noisy data is an important part of the parameter estimation. This requires the search for extrema in the first derivative of the RSLC data. Unfortunately, the estimation of derivatives from noisy signals is one of the most challenging tasks in the field of numerics. A recommendable summary of this topic can be found in [Kno2012].

The derivative approximations of the noisy data are usually obtained from local fits of generic functions, such as polynomials or splines. The major difficulty of selecting the fitting method and parameters consists in the common trade-off between smoothing and the extraction of the signal dynamics. Therefore, the optimal choice substantially depends on the data quality, the number of data points and the dynamics of the underlying signal. The methods for inflection point estimation thus has to be adapted to the specific camera system, which, amongst others, includes its orientation to the world, its resolution, its signal-to-noise ratio and its available computing capacity.

In this work, *splines* (*cf. e.g.* [Boo1978]) are used for the smoothing of the luminance curve, since splines combine numerical and analytical simplicity with a high flexibility. The non-smooth RSLC is given by the data points

$$(1, L_1), \dots, (v_{\max}, L_{v_{\max}}).$$

The splines are based on an equidistant knot sequence

$$1 = v_{k,0} < \dots < v_{k,N_k} = v_{\max},$$

s.t. the *basic splines*  $B_{l,k}$  (B-splines) of order  $k$  are recursively defined via

$$v \mapsto B_{l,1}(v) := \begin{cases} 1 & , v \in [v_{k,l}, v_{k,l+1}) \\ 0 & , \text{otherwise} \end{cases},$$

$$v \mapsto B_{l,k}(v) := \left[ \frac{v - v_{k,l}}{v_{k,l+k-1} - v_{k,l}} \right] B_{l,k-1}(v) + \left[ 1 - \frac{v - v_{k,l+1}}{v_{k,l+k-1} - v_{k,l+1}} \right] B_{l+1,k-1}(v).$$

The splines of order  $k$  are defined as the linear combination of the  $k^{\text{th}}$ -order B-splines:

$$v \mapsto \sum_{l=k-1}^{N_k-k} c_l B_{l,k}(v), \quad \text{where } c_l \in \mathbb{R}.$$

Now, the smoothing of the RSLC’s data points can be realized with the help of a least-square spline fit to the data. In order to avoid overfitting, a common approach is to incorporate a penalization term to the minimization, aiming to keep the derivatives small. One of the most successful penalization concepts is described by Eilers and Marx [Eil1996], who use penalties based on finite

differences of the spline coefficients, leading to the following objective function:

$$(c_{k-1}, \dots, c_{N_k-k}) \mapsto \sum_{v=1}^{v_{\max}} \left[ L_v - \sum_{l=k-1}^{N_k-k} c_l B_{l,k}(v) \right]^2 + w_p \sum_{l=k_d+k-1}^{N_k-k} \left( \Delta^{k_d} c_l \right)^2, \quad (8.21)$$

where  $w_p$  denotes the weight of the penalization term and  $k_d$  the order of coefficient differences. The finite differences are recursively defined via

$$\Delta^1 c_l := c_l - c_{l-1}, \quad \Delta^{k_d} c_l := \Delta^{k_d-1} c_l - \Delta^{k_d-1} c_{l-1}.$$

In [Eil1996], it is shown that the minimization problem of (8.21) leads to a linear equation system that can be solved efficiently.

For the camera setting used in this work, using 3<sup>rd</sup>-order splines turns out to be a suitable choice of parameters, with the number of nodes set to  $N_k = 50$ , and a difference order of  $k_d = 2$ . As proposed by Eilers and Marx, the large number of nodes does not lead to an overfitting, thanks to the penalty term, which for  $k_d = 2$  corresponds to keeping the second derivative of the fitting curve small. This, of course, also depends on the choice of the penalty weighting  $w_p$ . For the experiments in this work, it is chosen by *generalized cross-validation* (gcv) as presented in [Eil1996, (29)]. Since this requires several optimization steps, the use of a fixed  $w_p$  is suggested for real-time purposes. The optimal choice for  $w_p$  mainly depends on the signal-to-noise ratio, wherefore it might be useful to introduce a precomputed optimal SNR-to- $w_p$  mapping. This is especially useful as the gcv measure is not optimized for the purpose of inflection point extraction. The noise level could be estimated from the signal with the help of the sum of squared differences, as proposed in Appendix C.

## 8.6 Further Experiments and Evaluation

Several experiments are already described in the theory part, such as in Fig. 8.4, where examples for the results of the best rectangle path are provided; in Fig. 8.5, where it can be seen that the first-order model does not satisfyingly fit the RSLC observation data; in Fig. 8.8, where the first- and the second-order model are compared regarding their fitting capabilities, in Fig. 8.11 and Fig. 8.12, which visualize the convergence of the higher-order approximate luminance and RSLC models.

In this section, further evaluations on the differences between the first-order, second-order and higher-order models are provided. From this, it can be seen that there is a relevant improvement from taking the effects of non-horizontal vision into account (*cf.* 8.6.1 and 8.6.2). Although the general feasibility of RSLC-based visibility estimation has already been proven in the literature (*cf.* *e.g.* [Hau2008a]), experimental results based on real-world data are depicted in 8.6.3. Besides these improvement and feasibility evaluations, further tests on numerical and model issues are provided.

### 8.6.1 Monte Carlo Simulation

The higher-order approximate models proposed in Sec. 8.4 are based on the extensive analytical theory introduced in Chap. 5. It starts with the radiative transfer equation (*cf.* Sec. 5.1), requires a

clear concept of the boundary conditions (*cf.* Sec. 5.2) and an appropriate integral reformulation (*cf.* Sec. 5.3), and finally leads to the analytical form of approximate solutions to the full RTT boundary problem (*cf.* Sec. 5.4). Furthermore, to derive higher-order RSLC models, the approximations are transformed to the plane-parallel case (*cf.* Sec. 5.5). Since an explicit analytical discussion of the resulting models seems to be impracticable, numerical approximations have to be used instead (*cf.* Sec. 8.4). These numerical approximations make use of five discretizations, namely in  $H$ , in  $\mu$ , and in the three integral domains for  $s$ ,  $\hat{\mu}$  and  $\varphi$ .

Therefore, it is not evident from the derivation that the resulting higher-order RSLCs still properly represent the solution of the radiative boundary problem. To examine the quality of the higher-order models, a Monte Carlo simulation is implemented that, in contrast to the radiative approach, is based on the particle property of light (*cf.* Sec. 4.2).

To achieve this, a virtual camera is positioned at a certain height  $H_{\text{cam}}$  above the road. The road is assumed to be an infinitely expanded plane with a constant albedo between 0% and 100%. The road albedo represents the probability for an incident photon to be reflected instead of being absorbed by the road surface. The sun is assumed to be a uniform light source at a given height level  $H_{\text{atm}}$  above the ground. The atmosphere between the road surface and the sky plane is assumed to consist of homogeneous fog with a certain extinction coefficient  $K > 0$ . Each scattering event is simulated with the help of the Henyey-Greenstein phase function from (4.12) and an asymmetry parameter  $g := 0.85$ .

In order to generate a simulated camera image for this setting, an equal number of photons is traced back for each pixel direction. Each photon thus travels backwards randomly, starting at the camera, and is scattered multiple times (maximal 300 scattering events allowed). Each scattering event is determined by three random numbers that describe the length of the scattering-free path ( $p_{\text{len}}$ ) and the angle and direction of the next scattering event ( $\mu$  and  $\varphi$ ).

The length of the scattering-free path  $p_{\text{len}}$  can be interpreted as continuous random variable. Due to the homogeneous atmosphere it is exponentially distributed, s.t. for any  $d \in \mathbb{R}_{\geq 0}$  one has

$$P(p_{\text{len}} \leq d) = 1 - \exp(-Kd).$$

The rate parameter is given by the extinction coefficient  $K$ . For the implementation, the random variable  $p_{\text{len}}$  can be sampled from a uniform distribution with the help of inversion sampling, *i.e.*

$$1 - \exp(-Kp_{\text{len}}) \sim \mathcal{U}(0, 1) \quad \text{or} \quad p_{\text{len}} \sim -\frac{\log(\mathcal{U}(0, 1))}{K}.$$

This can analogously be done for the scattering direction. In the case of the Henyey-Greenstein phase function, the cosine of the scattering angle  $\mu$  can be determined by explicit inversion sampling

$$\mu \sim \frac{1}{2g} \left[ 1 + g^2 - \left( \frac{1 - g^2}{1 - g + 2g\mathcal{U}(0, 1)} \right)^2 \right].$$

Given a specific  $\mu$ , the remaining equally likely directions in  $\mathbb{S}^2$  lie on a circle orthogonal to the incident direction of the photon. From another uniformly distributed angle  $\varphi \sim \mathcal{U}(0, 2\pi)$ , it is thus possible to determine the photon's new three-dimensional direction.

Whenever a backward traveling photon hits the road surface, it is either absorbed or reflected according to the albedo. Since up to linear changes the luminances and in turn the RSLCs are

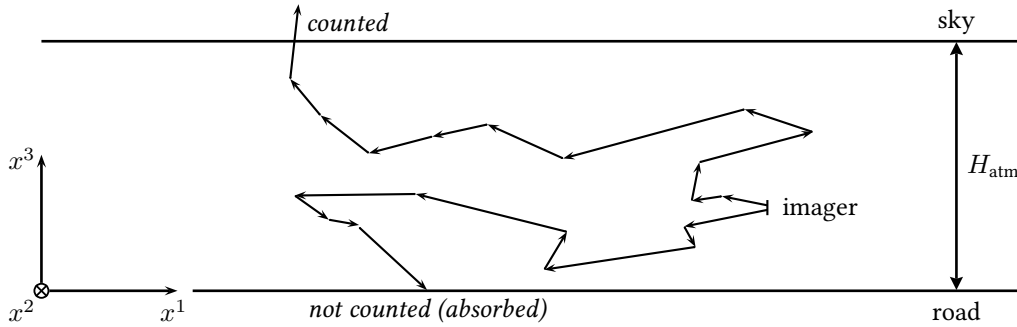


Figure 8.13: Virtual photons are traced back from the camera. If they reach the sky plane, they are counted as originating from the sun.

independent of the road plane's albedo, it is chosen to be 0 in this implementation. This slightly speeds up the simulation since the photon's travel is definitely stopped whenever it reaches the road surface. It is considered to be a photon that does not exist and thus is not counted. In contrast to that, a backward traveling photon hitting the sky plane is considered to be a photon that originates from the light source. In this case it is counted. This is depicted in Fig. 8.13.

Fig. 8.14 shows how compatible the higher-order models are to the Monte Carlo results. It reveals the remarkable consistency between both approaches, which is especially noteworthy due to the different and non-trivial way both results have been derived. This involves not only that the Monte Carlo simulation is based on the particle property of light and the higher-order models are based on the wave property of light. It also validates the extensive theoretical derivation and numerical approximations (including five different discretizations) of higher-order models in Chap. 5 and Sec. 8.4.

### 8.6.2 Further Numerical Experiments

**$K$ - $v_i$  Relation.** The base for RSLC-based visibility estimation is the bijective relation between the luminance curve's inflection point  $v_i$  and the atmosphere's extinction coefficient  $K$ . To use this relation for visibility estimation, it is important to have a rough idea of its shape. Fig. 8.15 visualizes examples for the  $K$ - $v_i$  and the corresponding  $d_{\text{met}}$ - $v_i$  relations based on the second-order model and for different parameter setting.

On the one hand, it can be clearly seen from the  $d_{\text{met}}$ - $v_i$  plots that the estimation accuracy drastically decreases with increasing meteorological visibility, since  $v_i$  approaches  $v_h$ . Above a certain visibility, the RSLC-based  $d_{\text{met}}$  estimation thus becomes impracticable. For the camera setting and  $v_i$  estimation used in this work, this threshold is at about 200 m.

On the other hand, Fig. 8.15 also reveals that RSLC-based methods are well-suited for dense fog (here maybe  $d_{\text{met}} < 100$  m). This is even more true since the data acquisition (RSLC extraction) and the model assumptions (such as the homogeneous and flat road) are closer to reality in situations of dense fog. Fortunately, the most accurate visibility estimation is required especially for dense fog at about 50 m in the context of driver assistance application (*cf.* Sec. 3.3). Moreover, current driver assistance cameras rarely exceed a range of 200 m, wherefore fog of this density is

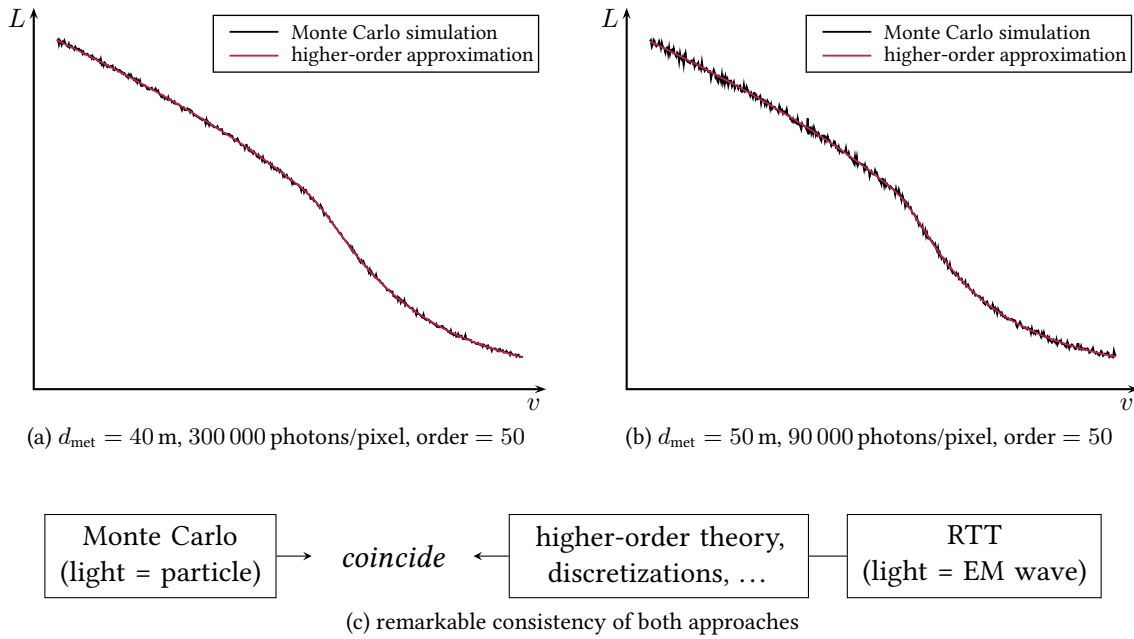


Figure 8.14: The RSLC approximations from the Monte Carlo simulation and a 50<sup>th</sup>-order model coincide. Detailed setting:  $H_{\text{atm}} = 6d_{\text{met}}$ ,  $M = 480$ ,  $N = 100$ ,  $N_s = 80$ ,  $N_{\hat{\mu}} = 30$ ,  $N_{\varphi} = 30$ ,  $H_{\text{cam}} = 1.5 \text{ m}$ ,  $\xi = 0^\circ$ ,  $f = 1200 \text{ px}$ ,  $u_0 = u$ ,  $v_0 = 256 \text{ px}$ ,  $v_{\text{max}} = 512 \text{ px}$ .

just a marginal problem.

However, this is an important finding on the estimation confidence and should be taken into account for the combination with other visibility estimation methods, such as the tracking-based (*cf.* Chap. 7) or the pRSLC-based (*cf.* Chap. 9) approaches.

**Robustness to Errors in  $v_i$ .** Motivated by the finding above, the estimation robustness to errors in  $v_i$  shall be studied in a more quantitative way. Fig. 8.16 shows the impact of an error in the  $v_i$  estimation on the estimated  $d_{\text{met}}$ . As suggested by Fig. 8.15, errors in  $v_i$  are more tolerable for dense than for light fog scenarios. Based on what can be seen in Fig. 8.19, this cannot be expected to be substantially different for higher-order models. The inflection point is always bounded by  $v_h$ .

**Fixed  $g = 0.85$ .** Another experiment is provided that studies the impact of choosing  $g = 0.85$  fixed instead of estimating it together with  $K$ . The maximum relative error in  $d_{\text{met}}$  caused by the fixed  $g$  is computed on the following test parameter sets:

$$\begin{aligned}
 H_{\text{cam}} &\in \mathcal{T}_{H_{\text{cam}}} := \{1.250 \text{ m}, 1.255 \text{ m}, \dots, 1.300 \text{ m}\}, \\
 \xi &\in \mathcal{T}_{\xi} := \{0^\circ, 0.1^\circ, \dots, 5^\circ\}, \\
 u &\in \mathcal{T}_u := \{u_0, u_0 \pm 10 \text{ px}, u_0 \pm 20 \text{ px}, \dots, u_0 \pm 200 \text{ px}\}, \\
 g &\in \mathcal{T}_g := \{0.8, 0.81, \dots, 0.9\},
 \end{aligned} \tag{8.22}$$

while the intrinsic camera parameters  $f = 1200 \text{ px}$ ,  $u_0 = 512 \text{ px}$ ,  $v_0 = 256 \text{ px}$  are fixed.

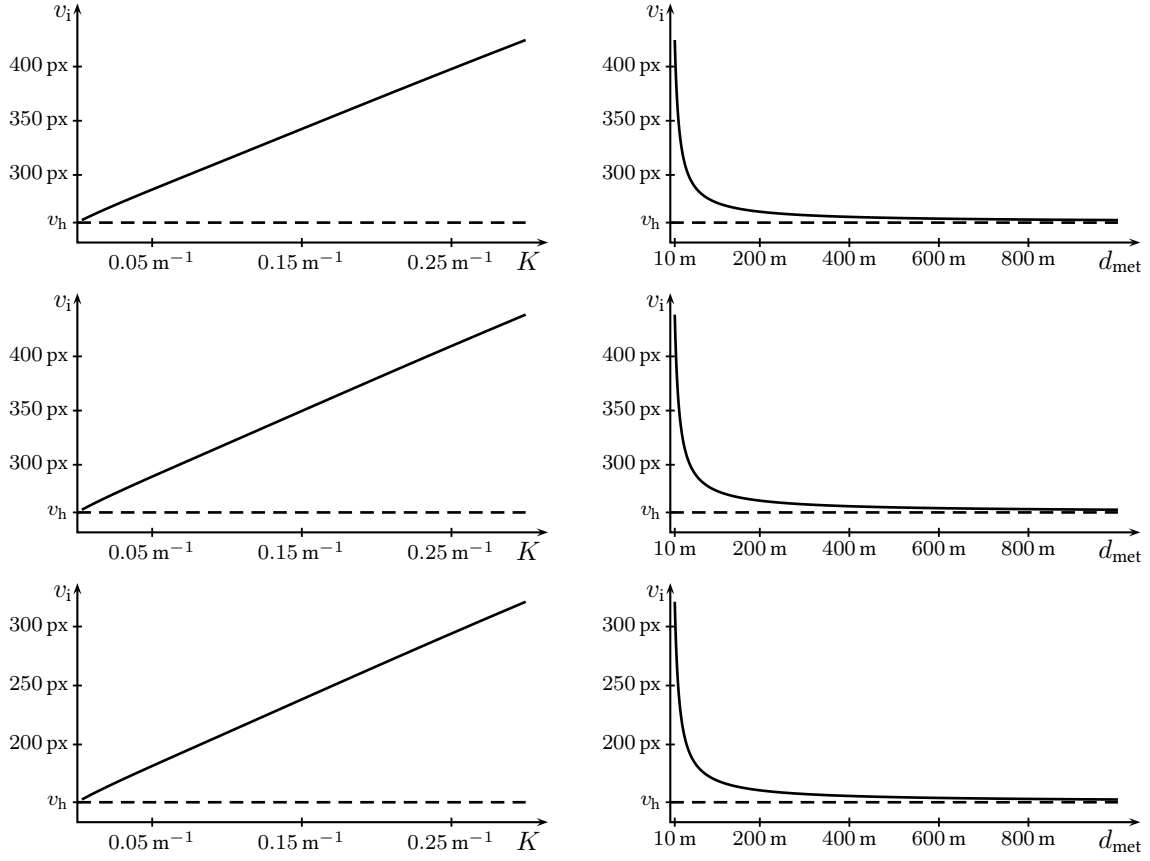


Figure 8.15:  $K$ - $v_i$  relation and  $d_{\text{met}}$ - $v_i$  relation based on the second-order RSLC model and for fixed system parameters; top:  $H_{\text{cam}} = 1.25$  m,  $\xi = 0^\circ$ ,  $f = 1200$  px,  $u_0 = u = 512$  px,  $v_0 = 256$  px; mid:  $H_{\text{cam}} = 1.25$  m,  $\xi = 0^\circ$ ,  $f = 1300$  px,  $u_0 = u = 512$  px,  $v_0 = 256$  px; bottom:  $H_{\text{cam}} = 1.25$  m,  $\xi = 5^\circ$ ,  $f = 1200$  px,  $u_0 = u = 512$  px,  $v_0 = 256$  px.

Fig. 8.17(a) shows the maximum error w.r.t.  $d_{\text{met}}$ . In a non-rigorous notation, one could describe the plotted relation by

$$d_{\text{met}} \mapsto \max_{g \in \mathcal{T}_g} \max_{p \in \mathcal{T}_{H_{\text{cam}}} \times \mathcal{T}_\xi \times \mathcal{T}_u} \left[ \frac{d_{\text{met}}^{\text{est}} [v_i(d_{\text{met}}, g, p), g = 0.85, p] - d_{\text{met}}}{d_{\text{met}}} \right], \quad (8.23)$$

*i.e.* for all choices of parameters from the test sets, the  $v_i$  is computed from the model and used for the  $d_{\text{met}}$  estimation with fixed  $g = 0.85$ . It can be seen that the  $g = 0.85$  assumption leads to an acceptable estimation error of maximally  $\approx 3\%$  for the test set in (8.23).

For the setting causing the largest error, the  $g$  dependence is explicitly plotted in Fig. 8.17(b), namely  $[0.8, 0.9] \ni g \mapsto K(v_i; g)$ , where  $d_{\text{met}}(v_i; 0.85) \approx 110$  m.

**Dependencies on System Parameters.** Except for  $L_{\text{air}}$  and  $L_0$ , the relation  $v_i \mapsto K(v_i)$  depends on all system parameters. Since  $(H_{\text{cam}}, \xi, f, u_0, v_0, u) \mapsto K(v_i; H_{\text{cam}}, \xi, f, u_0, v_0, u)$  is difficult to visualize, only the one-dimensional relations are plotted here, *i.e.*  $p \mapsto K(v_i; p)$  or  $p \mapsto d_{\text{met}}(v_i; p)$ , for  $p \in \{H_{\text{cam}}, \xi, f, u_0, v_0, u\}$  and fixed  $v_i$ . The result can be found in Fig. 8.18.

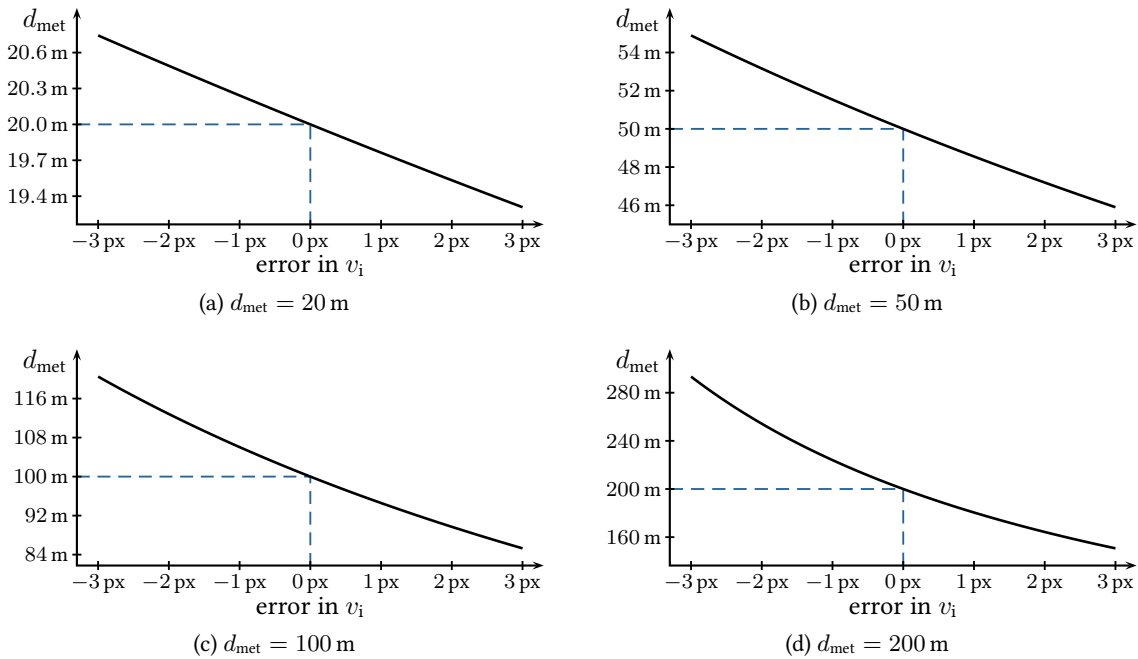


Figure 8.16: Estimation robustness to  $v_i$  perturbations based on the second-order model. Setting:  $H_{\text{cam}} = 1.25 \text{ m}$ ,  $\xi = 0^\circ$ ,  $f = 1200 \text{ px}$ ,  $u_0 = u$ ,  $v_0 = 256 \text{ px}$ ,  $g = 0.85$ .

This gives a rough feeling for the visibility estimation errors arising from perturbations in the system parameters. In addition, it indicates that  $(H_{\text{cam}}, \xi, f, u_0, v_0, u) \mapsto K(v_i; H_{\text{cam}}, \xi, f, u_0, v_0, u)$  is a quite smooth mapping, which is advantageous for compact look-up tables as introduced in 8.3.4.

As one could expect, the estimation strongly depends on the parameters  $\xi$  and  $v_0$ , which both have a significant impact on the important estimation term  $v_h - v_0$ . In contrast,  $|u - u_0|$  has only a small impact, which is useful since the road surface luminance curve is extracted from different columns in the image.

**Higher-Order Model Experiments.** The validity of higher-order models in general is shown using the Monte Carlo simulation provided in 8.6.1 and Fig. 8.14. In order to assess how much the higher-order models improve the visibility estimation, the impact of the model order on the inflection point position has to be studied. Fig. 8.19 shows the behavior of  $v_i$  w.r.t. the RSLC model's order for different cases of meteorological visibility. This reveals that the second-order model already leads to substantially improved estimation results, since by far the largest  $v_i$  gap can be found between the first-order and the second-order models. This justifies the use of second-order models, which combine a good approximation of the correct  $v_i$ - $K$  relation and a still practicable way of computation.

Similar to Fig. 8.8, an overall comparison of the fitting to the correct RSLC curve from the Monte Carlo simulation can be found in Fig. 8.20. It is clearly visible why the inflection point position is largely improved by the second-order model. In the left part of the curve (sky luminances), several iterations are required to approach the Monte Carlo results. On the right side (road luminances), the models appropriately fit the correct RSLC. Close to the inflection point, the first-order and the

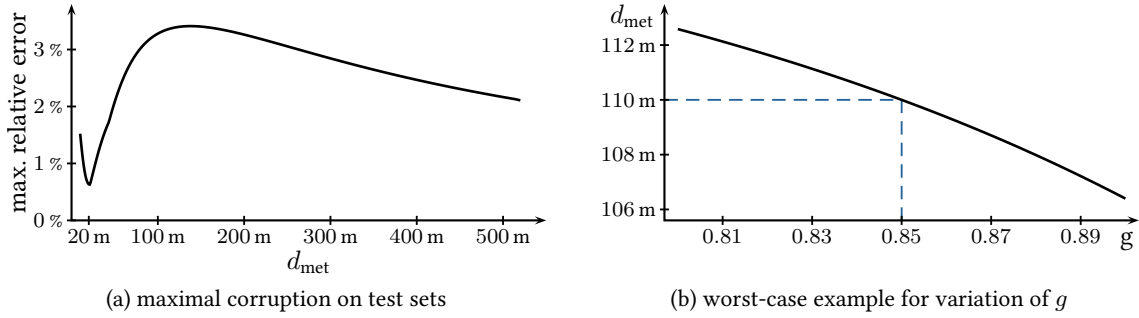


Figure 8.17: Fixing  $g = 0.85$  corrupts the results only marginally. In (a), the maximum relative error of visibility estimation (8.23) based on test sets from (8.22) is provided. In (b), the variation of the estimated  $d_{\text{met}}$  w.r.t. varying  $g$  is depicted for a fixed setting. The setting was chosen to represent a case close to the maximum in (a), which is  $v_i \approx 273$  px,  $H_{\text{cam}} = 1.25$  m,  $\xi = 0^\circ$ ,  $f = 1200$  px,  $u_0 = u$ ,  $v_0 = 256$  px.

second-order models differ significantly.

**First-Order vs. Second-Order.** From Fig. 8.19 it can be seen that applying the second-order model instead of the first-order model significantly reduces the systematical model error within the visibility estimation. To get a feeling of how much the visibility estimation can be improved, the estimation results have to be compared. Fig. 8.21 shows the results of visibility estimation based on the first-order and the second-order model (left), and their relative difference  $d_{\text{met}}^{2\text{nd}} \mapsto |d_{\text{met}}^{2\text{nd}} - d_{\text{met}}^{1\text{st}}|/d_{\text{met}}^{2\text{nd}}$  (right). For all visibilities, one can observe a substantial difference between both estimation results.

**Log-Normal Phase Function.** A look at Fig. 8.17 reveals that RSLC-based visibility estimation only marginally depends on the asymmetry parameter  $g$ . This enables a valuable simplification of the approach, since otherwise  $g$  would have to be estimated along with  $K$ , requiring more than a precomputed look-up table for the  $v_i$ - $K$  relation and thus being impracticable.

However, even the Henyey-Greenstein phase function with an optimally chosen parameter  $g$  is only a weak representation of a more realistic scattering phase function in natural fog (*cf.* Remark 8 on page 35). This motivates the question on the impact of a more realistic phase function on the RSLC and the  $v_i$ - $K$  relation. To give a feeling of the severity of this problem, a second-order RSLC is computed based on the average Mie phase function for a log-normal drop-size distribution as presented in Remark 8 on page 35. The parameters are chosen as

$$\mathcal{N}_0 = 10^9 \text{ m}^{-3}, \quad S = 1.4241, \quad r_m = 2 \mu\text{m}, \quad (8.24)$$

and wavelength  $\lambda = 0.55 \mu\text{m}$ . The scattering coefficient  $K_s$  (which approximately equals  $K$ ), the average asymmetry parameter  $g$  and the liquid water content LWC can be computed with the help of (4.5), (4.7) and (4.15) as

$$K \approx K_s \approx 0.035894 \text{ m}^{-1}, \quad d_{\text{met}} \approx 83.46 \text{ m}, \quad g \approx 0.8272, \quad \text{LWC} \approx 0.059 \text{ g m}^{-3}.$$

The resulting average Mie phase function compared to the Henyey-Greenstein phase function

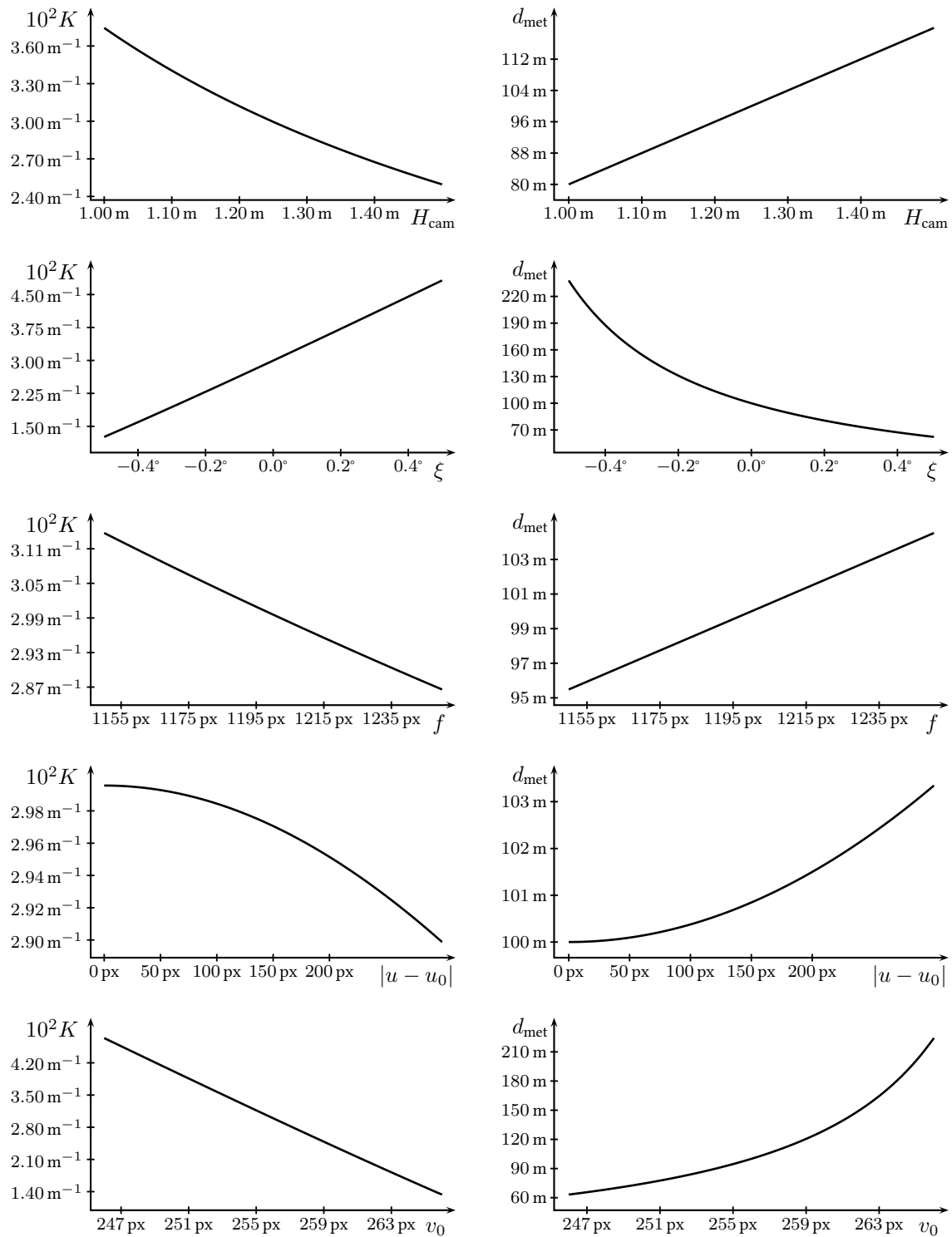


Figure 8.18:  $K$  and  $d_{\text{met}}$  w.r.t. different system parameters. Basic setting:  $d_{\text{met}} = 100$  m,  $H_{\text{cam}} = 1.25$  m,  $\xi = 0^\circ$ ,  $f = 1200$  px,  $u_0 = u$ ,  $v_0 = 256$  px,  $g = 0.85$ .

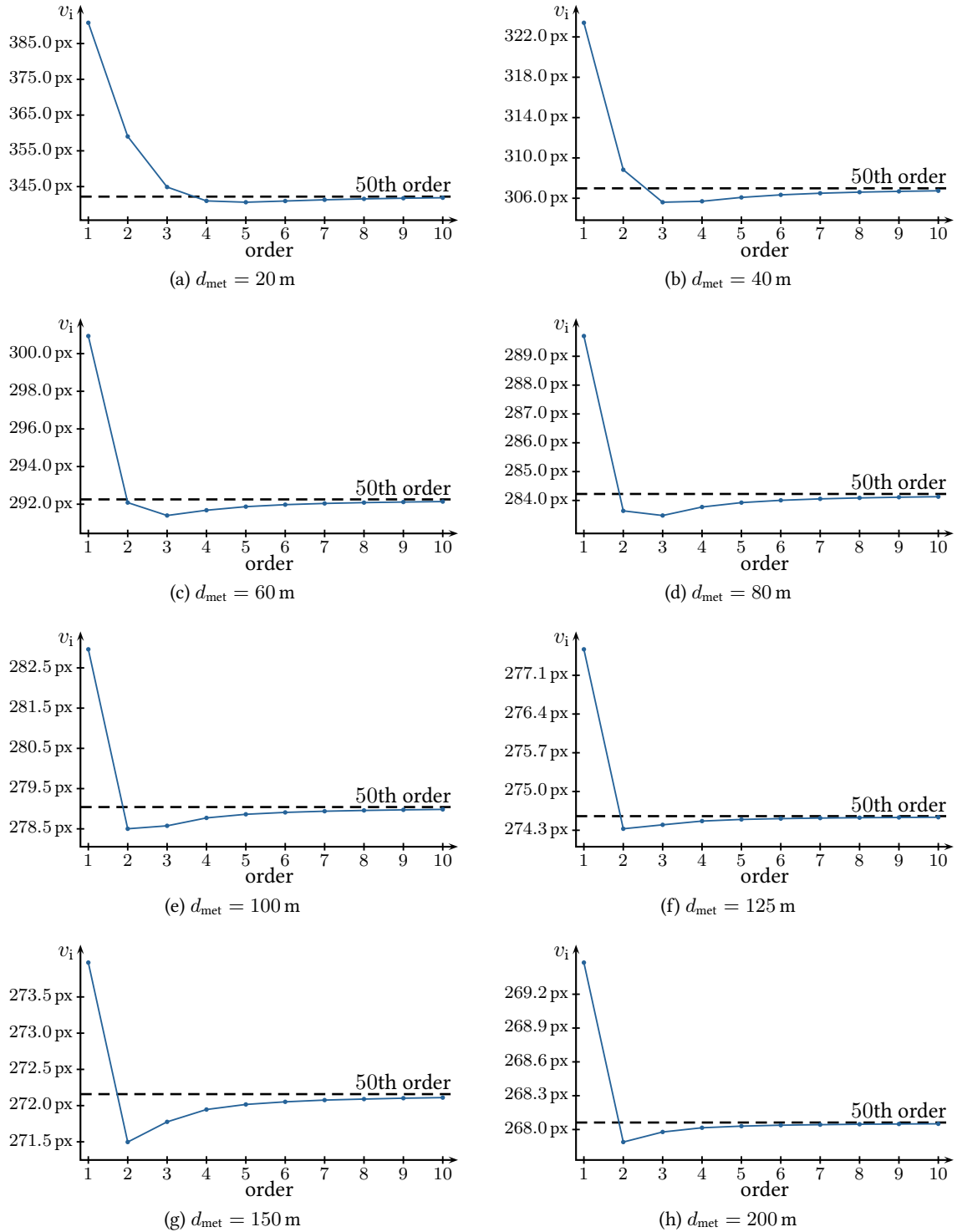


Figure 8.19: Convergence of the inflection point position for higher-order models. Simulation parameters:  $H_{\text{atm}} = 3d_{\text{met}}$ ,  $M = 200$ ,  $N = 400$ ,  $N_s = 80$ ,  $N_{\hat{\mu}} = 30$ ,  $N_{\varphi} = 30$ . Setting for virtual camera:  $H_{\text{cam}} = 1.5$  m,  $\xi = 0^\circ$ ,  $f = 1200$  px,  $u_0 = u$ ,  $v_0 = 256$  px.

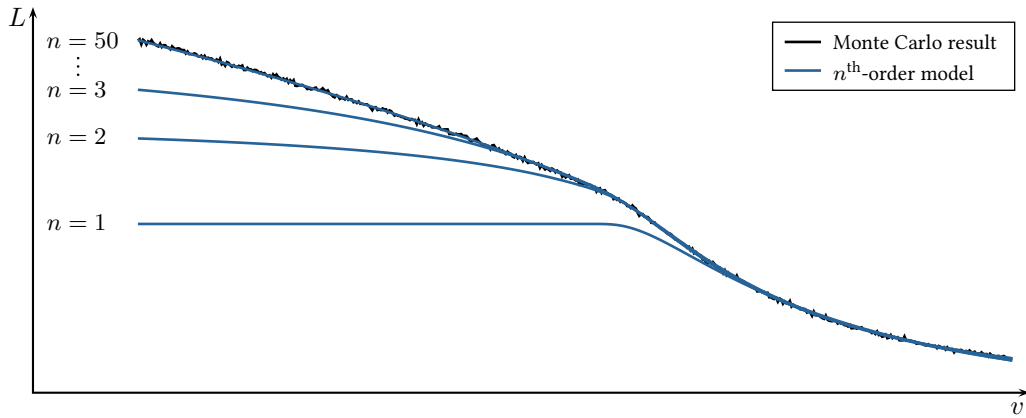


Figure 8.20:  $n^{\text{th}}$ -order models converging to the Monte Carlo result. Setting: Monte Carlo: 300 000 photons/pixel; higher-order models:  $M = 480$ ,  $N = 100$ ,  $N_s = 80$ ,  $N_{\hat{\mu}} = 30$ ,  $N_{\varphi} = 30$ ; both:  $d_{\text{met}} = 40$  m,  $H_{\text{cam}} = 1.5$  m,  $\xi = 0^\circ$ ,  $f = 1200$  px,  $u_0 = u$ ,  $v_0 = 256$  px,  $v_{\text{max}} = 512$  px,  $H_{\text{atm}} = 240$  m.

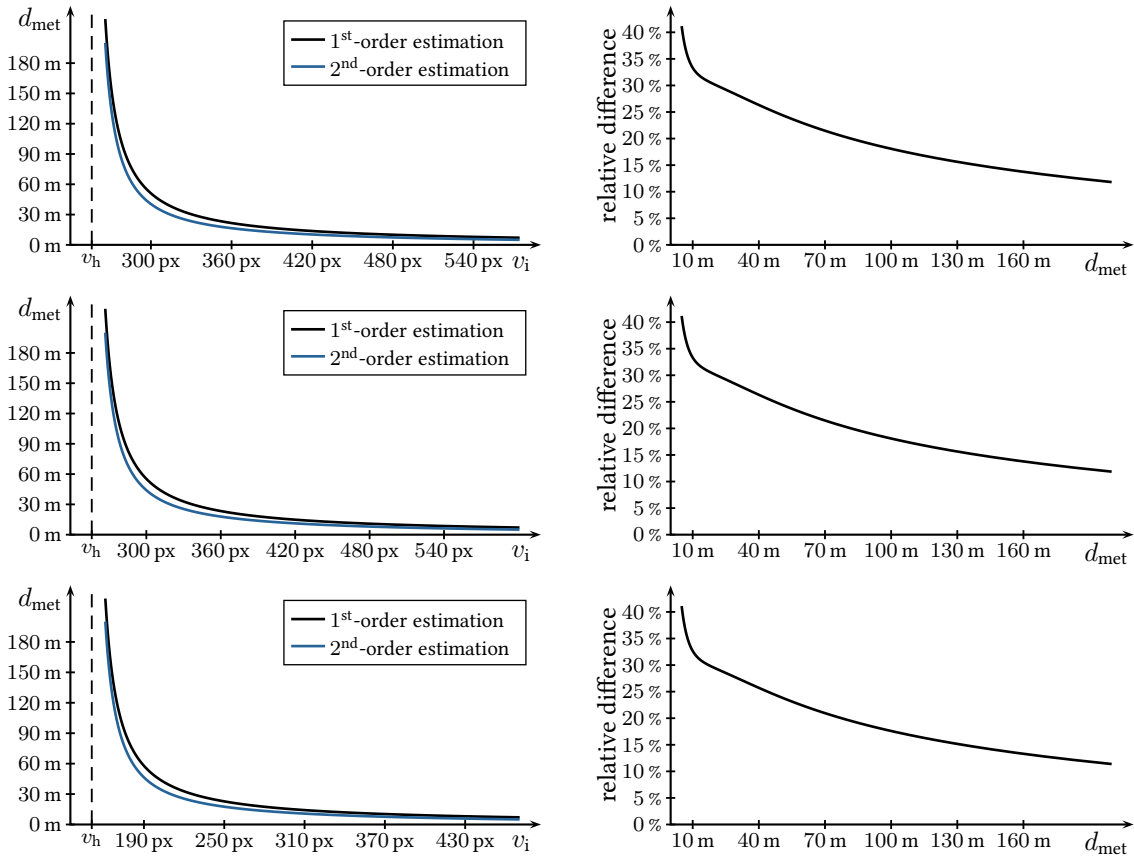


Figure 8.21: Difference between first-order and second-order estimation. Left: absolute estimation results. Right: relative difference. Setting: top:  $H_{\text{cam}} = 1.25$  m,  $\xi = 0^\circ$ ,  $f = 1200$  px,  $u_0 = u = 512$  px,  $v_0 = 256$  px; mid:  $H_{\text{cam}} = 1.25$  m,  $\xi = 0^\circ$ ,  $f = 1300$  px,  $u_0 = u = 512$  px,  $v_0 = 256$  px; bottom:  $H_{\text{cam}} = 1.25$  m,  $\xi = 5^\circ$ ,  $f = 1200$  px,  $u_0 = u = 512$  px,  $v_0 = 256$  px.

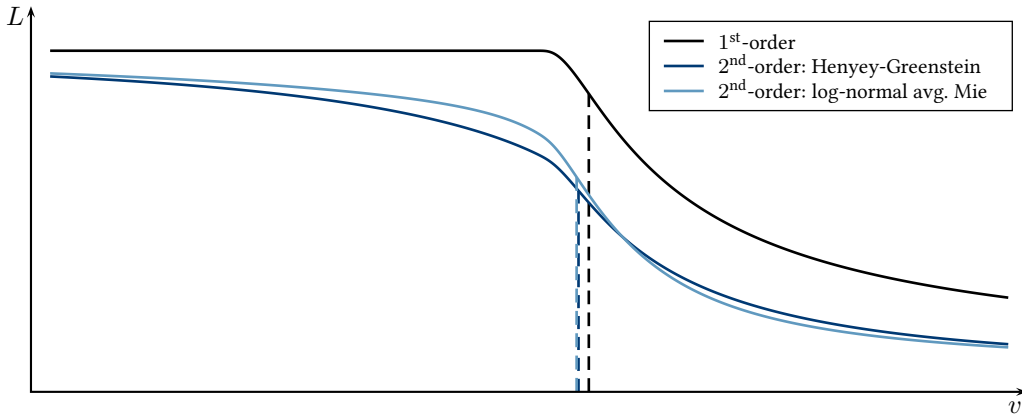


Figure 8.22: Comparison of RSLCs (and their inflection points) that differ in order and phase function. The setting is given in (8.24) and (8.25).

can be found in Fig. 4.11. From this it becomes apparent that both functions differ substantially, revealing how much algorithms based on the Henyey-Greenstein phase model might be improvable.

To get a feeling for the impact of the differing phase functions on RSLC-based visibility estimation, the road surface luminance curves for both phase functions are shown in Fig. 8.22 for a usual set of camera parameters

$$H_{\text{cam}} = 1.5 \text{ m}, \quad \xi = 0^\circ, \quad f = 1200 \text{ px}, \quad u_0 = u = 512 \text{ px}, \quad v_0 = 256 \text{ px}. \quad (8.25)$$

Although the resulting second-order RSLCs differ significantly, the inflection point positions lie close together compared to the difference to the first-order inflection point:

$$\begin{aligned} \text{first-order:} \quad v_i &= 288.3 \text{ px}, \\ \text{second-order (Henyey-Greenstein):} \quad v_i &= 282.8 \text{ px}, \\ \text{second-order (log-normal avg. Mie):} \quad v_i &= 281.8 \text{ px}. \end{aligned}$$

This once again encourages the use of the second-order model even if the underlying phase functions are not well known. Moreover, it is still to be clarified whether wavelength averaging and higher-order models might even reduce the error arising from the simplifying use of  $\psi^{\text{HG}}$ .

However, the careful study of more appropriate phase functions leaves room for further improvement of RSLC-based visibility estimation in the future. Fortunately, the theory of second-order and higher-order RSLC models is independent of the actual phase function. The only problem arising is the need for finer discretizations due to the more complexly shaped phase functions.

**Quadrature Normalization.** The numerical evaluation of higher-order models with the help of (8.19) requires the computation of an integral term in  $\hat{\mu}$ ,  $s$  and  $\varphi$  for each luminance computation. Since an error from the numerical integration directly leads to an error in the luminance, this has to be done most accurately. To compare the standard quadrature approach (8.20) to its normalized version, some exemplary second-order luminances  $L_{m,n}$  are computed from a first-order light

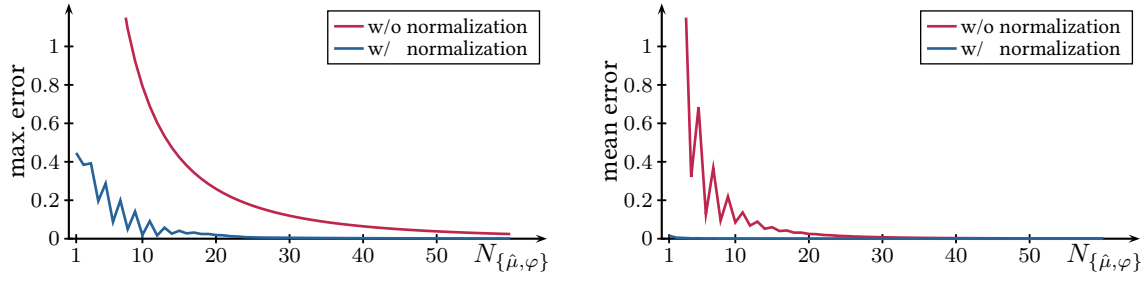


Figure 8.23: Maximum and mean error due to numerical integration for  $N_\varphi = N_{\hat{\mu}} \in \{1, \dots, 60\}$ .

field. For this experiment, the simulation parameters are chosen as

$$\{L_0\} = 0, \quad \{L_{\text{air}}\} = 1, \quad d_{\text{met}} = 40 \text{ m}, \quad H_{\text{atm}} = 120 \text{ m}, \quad g = 0.85, \quad h_H = 0.5 \text{ m}, \quad h_\mu = \frac{1}{20}.$$

The number of sub-intervals  $N_\varphi$  and  $N_{\hat{\mu}}$  are simultaneously increased. Fig. 8.23 shows the resulting mean error

$$\frac{1}{(M+1)(N+1)} \sum_{m=0}^M \sum_{n=0}^N \left| L_{m,n} - \bar{L}^{\text{2nd}}(H_m, \mu_n) \right|$$

as well as the resulting maximum error

$$\max_{(m,n) \in \{0, \dots, M\} \times \{0, \dots, N\}} \left| L_{m,n} - \bar{L}^{\text{2nd}}(H_m, \mu_n) \right|.$$

From this it can be seen that the numerical integration is remarkably improved by the normalization. At the same time, the additional computational effort for the normalization factor is almost negligible, since the required values  $Q_2(n_\varphi, n_{\hat{\mu}})$ ,  $n_\varphi = 0, \dots, N_\varphi$ ,  $n_{\hat{\mu}} = 0, \dots, N_{\hat{\mu}}$ , are already available from the standard quadrature. Hence, it is strongly advisable to make use of the normalized quadrature approach.

### 8.6.3 Real World Examples

The estimation of meteorological visibility based on road surface luminance curves has been introduced and further developed by Hautière, Negru *et al.* in several works, such as [Hau2006c], [Neg2013] and [Neg2014]. In all cases, the RSLC's inflection point position  $v_i$  is mapped to the atmosphere's extinction coefficient  $K$  with the help of Koschmieder's model. Different experiments are provided that reveal the feasibility for  $d_{\text{met}}$  estimation based on real-world camera images. In [Hau2008a], even a more exact experiment based on reference targets next to the road is used to prove the validity of this approach. This is why RSLC-based visibility estimation can be assumed to be established and reasonably validated not only for synthetic, but also for real-world data.

The evaluation in this chapter concentrates on the systematic model errors and model validation with the help of numerical experiments provided in 8.6.1 and 8.6.2. A comprehensive evaluation of RSLC-based visibility estimation based on reference sensors and a large number of real-world

sequences goes beyond the scope of this work. However, to give a feeling for the data and for the comparison with the approaches in chapters 7 and 9, the visibility estimation is done on a set of real-world sequences as well. The camera images are captured by the driver assistance front camera presented in Sec. 6.2. The vertical road surface and sky segmentation is performed manually as described in the beginning of Sec. 7.1. The camera's pitch angle, and in turn  $v_h$ , is computed from the road features' vanishing point under the assumption of a negligible roll angle. Fig. 8.24 shows the results for a number of single frames taken from different sequences.

Another experiment is provided in Fig. 8.25, where two sequence of 420 frames each are evaluated in this way. Without further postprocessing, the estimated  $d_{\text{met}}$  fluctuates significantly but acceptably. Since the estimated pitch angle and the estimated visibility locally correspond to each other, one can expect some of the fluctuations to arise due to the inaccurate estimation of the pitch angle. In order to demonstrate at least a most simple temporal filtering, an exponential smoothing is applied to the  $d_{\text{met}}$  signal with a smoothing factor 0.1, *i.e.* each new estimation is combined with the last filtered estimation by a weighted sum with factors 0.1 and 0.9, respectively. These experiments demonstrate the robustness of RSLC-based visibility estimation even on real-world data.

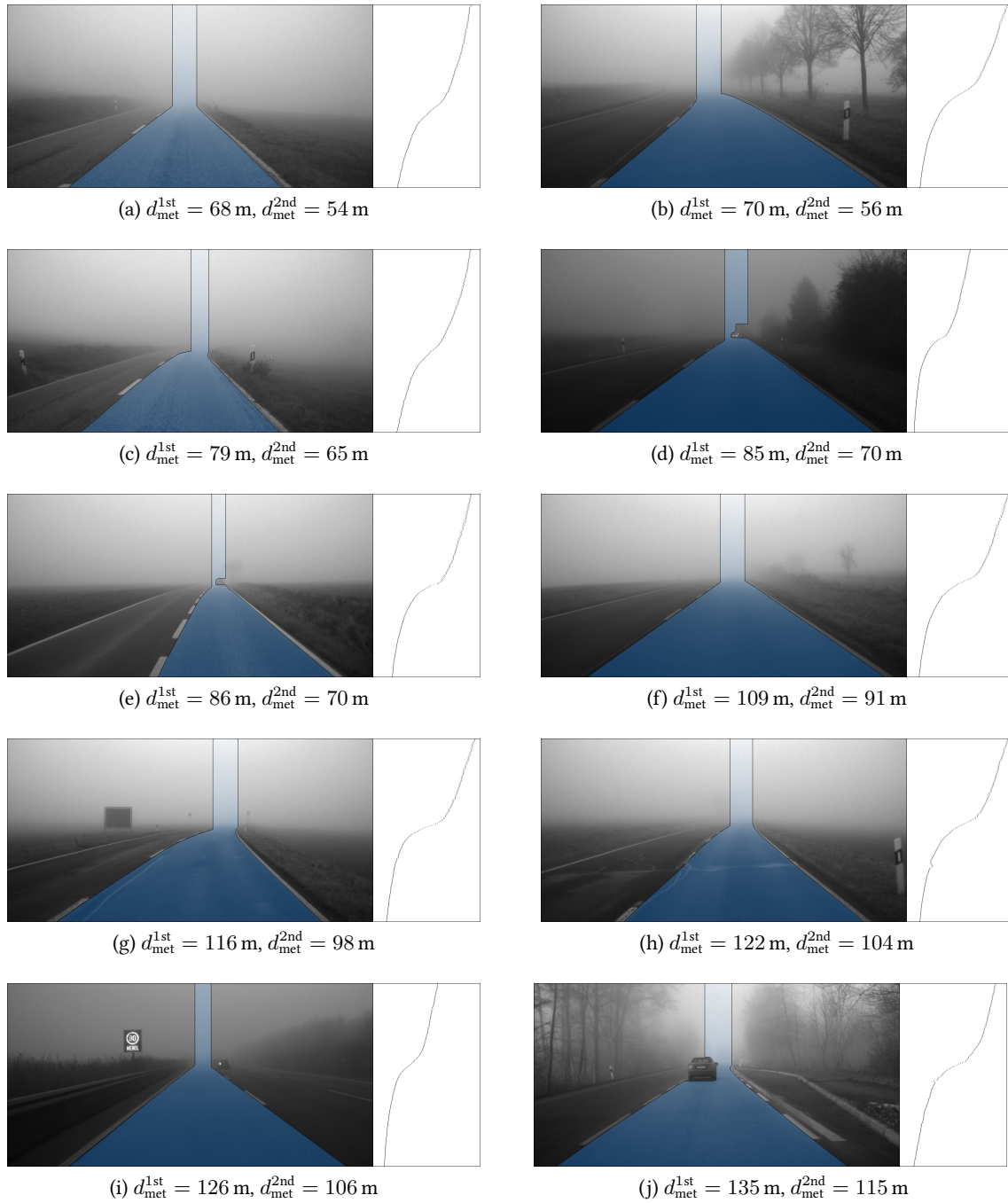


Figure 8.24: Examples for road surface luminance curves and the RSLC-based estimation results based on the first-order and second-order models. These are the same examples as later used for Fig. 9.2.

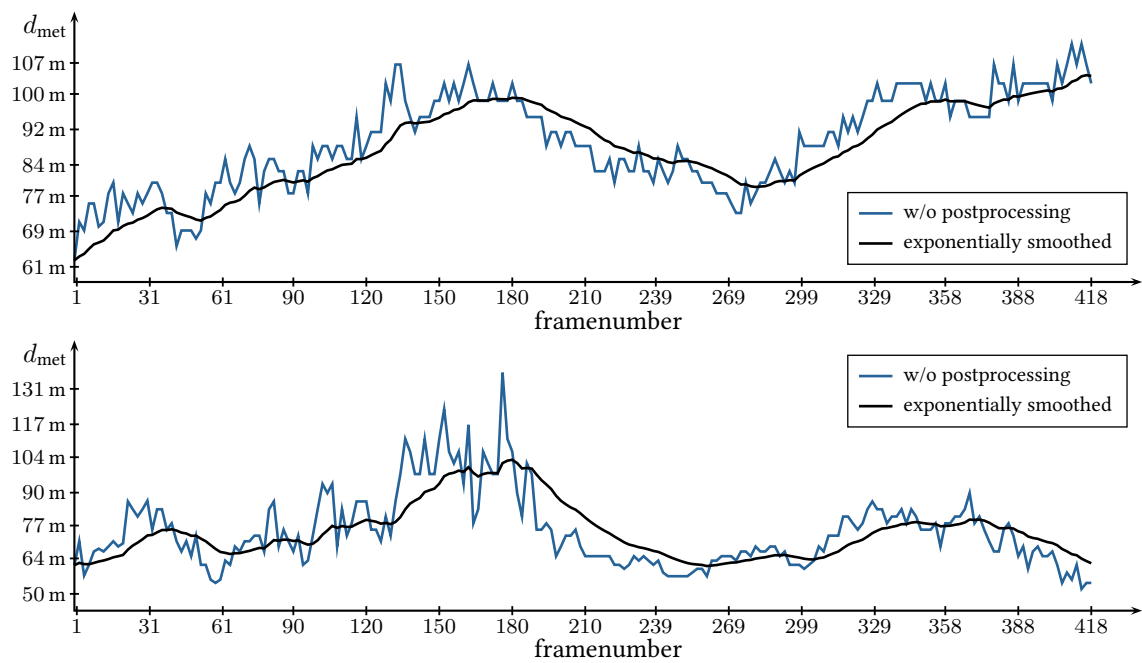


Figure 8.25: Two sequences of RSLC-based visibility estimations (second-order).

# Chapter 9

---

## Algorithm Based on Partial Road Segments

### Contents

---

9.1	Data Acquisition . . . . .	152
9.2	Model Selection . . . . .	153
9.3	Optimization Problem . . . . .	153
9.4	Experimental Results . . . . .	153

---

Especially in dense fog, the road surface luminance curve (RSLC) algorithm as presented in Chap. 8 constitutes a powerful visibility estimation approach. It works on single frames and benefits from a simple data acquisition on static road surveillance as well as driver assistance front cameras. The major drawback is the requirement of a non-obstructed view up to the horizon. In the case of obstructed roads, other algorithms such as the tracking-based visibility estimation presented in Chap. 7 could take the place of the RSLC-based algorithm.

As an alternative, a further algorithm could serve as fall-back solution in cases of obstructed roads. Taking the non-obstructed part of the road in front of the ego-car to extract at least a *partial road surface luminance curve* (pRSLC), Koschmieder's model can be used for a coarse parameter estimation (*cf.* Fig. 9.1). This approach becomes applicable for real time purposes with the help of the fast parameter estimation method presented in Sec. 7.4. The extraction of the pRSLC can be the by-product of the RSLC data acquisition and the distances to the road can be taken from a road surface model, such as a flat-world assumption or more complex models provided by the camera framework, or from other depth information obtained by for instance stereo vision. Therefore, this approach represents an ideal addition to a visibility estimation framework that continuously has to provide visibility information.

However, in contrast to the RSLC-based algorithm, the pRSLC-based approach obviously violates the horizontal vision assumption and is sensitive to inhomogeneities of the preceding road. It should thus only be considered as a fall-back solution and not as an equivalent alternative to RSLC-based visibility estimation.



Figure 9.1: The pRSLC-based visibility estimation can be used as a fall-back solution for the RSLC-based algorithm proposed in Chap. 8, in cases of a partially obstructed road.

## 9.1 Data Acquisition

The data required for this algorithm consist of distance-luminance pairs

$$(d_1, L_1), \dots, (d_N, L_N), \quad (9.1)$$

describing the luminance and distance to  $N \in \mathbb{N}$  different segments of the unobstructed road surface. Each segment should approximately have inherently equal distances to the road agreeing with the actual distance value in (9.1). According to the discussion above the segments can be the unobstructed road line segments that (partially) define the road surface luminance curve in Sec. 8.1 (*cf.* Fig. 8.1). The luminance values  $L_n$  can be extracted as the median of each road segment. The distance values  $d_n$  can be defined with the help of a flat-world assumption (*cf.* (8.14)) or using a more precise road surface luminance model that might be provided by the camera system. Alternatively, the road depth could also be obtained from stereo vision or other depth sensors.

Depending on the RSLC extraction method, the partial road surface luminance curve extraction can be implemented as a simple extension of the RSLC data acquisition that recognizes the obstructed road as discontinuity or undefined sections in the luminance curve. Then, the smooth beginning of the curve can be used as pRSLC. This makes the data acquisition of (9.1) a low-cost by-product of the RSLC algorithm. In particular, if the RSLC extraction fails even though the road is not completely obstructed, the pRSLC algorithm can still be used for visibility estimation on the successfully segmented parts of the road.

## 9.2 Model Selection

Although the acquisition of road luminances with a driver assistance camera violates the assumption of horizontal vision, Koschmieder's model (5.19)

$$L(d) = L_0 e^{-Kd} + L_{\text{air}} (1 - e^{-Kd})$$

is used to describe the distance-luminance pairs from (9.1). This can be justified by the fall-back character of pRSLC-based visibility estimation and by the need for a real-time capable parameter estimation (*cf.* Sec. 9.3). A feasibility experiment in Sec. 9.4 indicates that this model reasonably fits the data and delivers acceptable parameter estimation results.

## 9.3 Optimization Problem

Like the tracking-based algorithm in Chap. 7, the pRSLC-based visibility estimation uses Koschmieder's model to describe distance-luminance pairs. This leads to an optimization problem equivalent to that defined for the one-object tracking-based approach.

**Objective Function.** The negative log-likelihood objective function is given by (7.5) in the case  $M = 1$ :

$$(K, L_{\text{air}}, L_0) \mapsto \mathcal{F}(K, L_{\text{air}}, L_0) := \sum_{n=1}^N \frac{1}{(\sigma_n)^2} \left( \left[ e^{-Kd_n} L_0 + (1 - e^{-Kd_n}) L_{\text{air}} \right] - L_n \right)^2,$$

where the standard deviation  $\sigma_n$  represents the uncertainty of the  $n^{\text{th}}$  measurement,  $n \in \{1, \dots, N\}$ . In order to maximize the likelihood of  $(K, L_{\text{air}}, L_0)$  according to the observed distance-luminance data, the functional  $\mathcal{F}$  has to be minimized (*cf.* Sec. 7.3).

**Uncertainty Selection.** The uncertainties could simply be taken as  $\sigma_n = 1$ . It might lead to better results to derive them more sophisticatedly by *e.g.* taking the interior luminance standard deviation of the  $n^{\text{th}}$  segment instead. This could help reduce the statistical weight of the overrepresented nearby parts of the road, which are more affected by road inhomogeneities.

**Parameter Estimation.** The minimization of  $\mathcal{F}$  is extensively discussed in Sec. 7.4. Even for a large  $N$ , these methods allow for a fast parameter estimation, which makes pRSLC-based visibility estimation applicable for real-time purposes.

## 9.4 Experimental Results

To compare the results from the pRSLC-based algorithm to the results from the first- and second-order RSLC-based algorithms (*cf.* Sec. 8.2 and Sec. 8.3), the experiment uses frames that allow for completely extractable road surface luminance curves. The distance is taken from a flat-world assumption (*cf.* (8.14)) and the uncertainties are chosen as  $\sigma_n = 1$ .

The results of the Koschmieder's model fit and the estimated visibility distances for different maximum distances  $d_{\text{max}}$  are provided in Fig. 9.2. It can be seen that the pRSLC-based fall-back approach yields reasonable results if a sufficiently large part of the road is freely accessible.

In addition, in some examples it can be observed that the data in a range close to the camera is overrepresented, leading to poor fitting results at larger distances. This problem might be overcome by a choice of the weights  $\sigma_n^m$  that is inverse proportional to the distance-dependent data density. One could also think of an  $L_{\text{air}}$  stabilization as proposed in Sec. 7.5. However, the idea of a pRSLC-based fall-back solution shall only be sketchily proposed here. Therefore, tests on an extended data base or further steps on the optimization of this approach would go beyond the scope of this work.

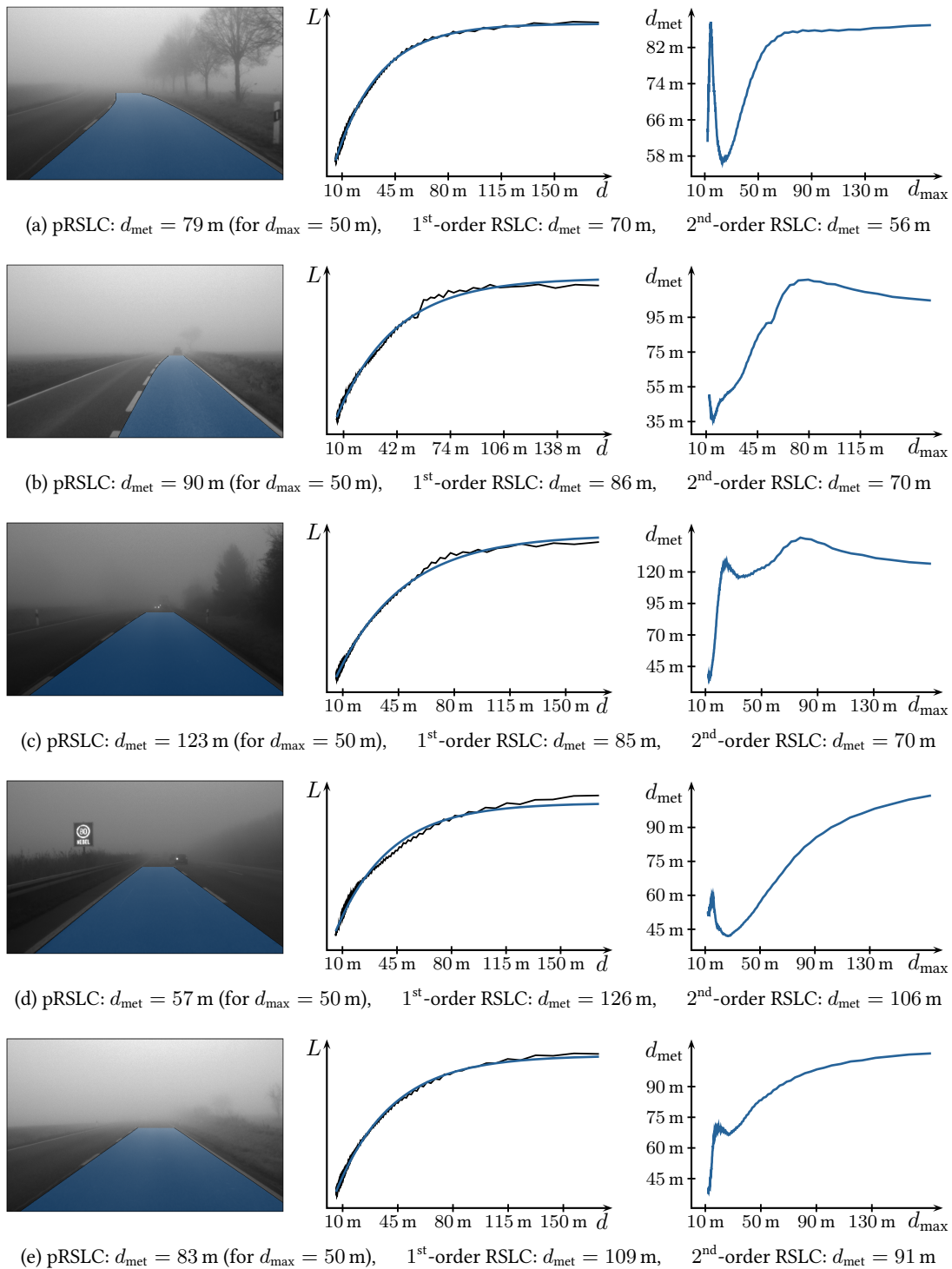


Figure 9.2: Page 1/2. Results of pRSLC-based visibility estimation. Left: Partially segmented road from which the luminances are extracted line by line. The marked area indicates the image region that is processed in the case of  $d_{\text{met}} = 50$  m. Middle: Fit of Koschmieder's model on the distance-luminance values. Right: Visibility estimation results w.r.t. the maximally considered distances.

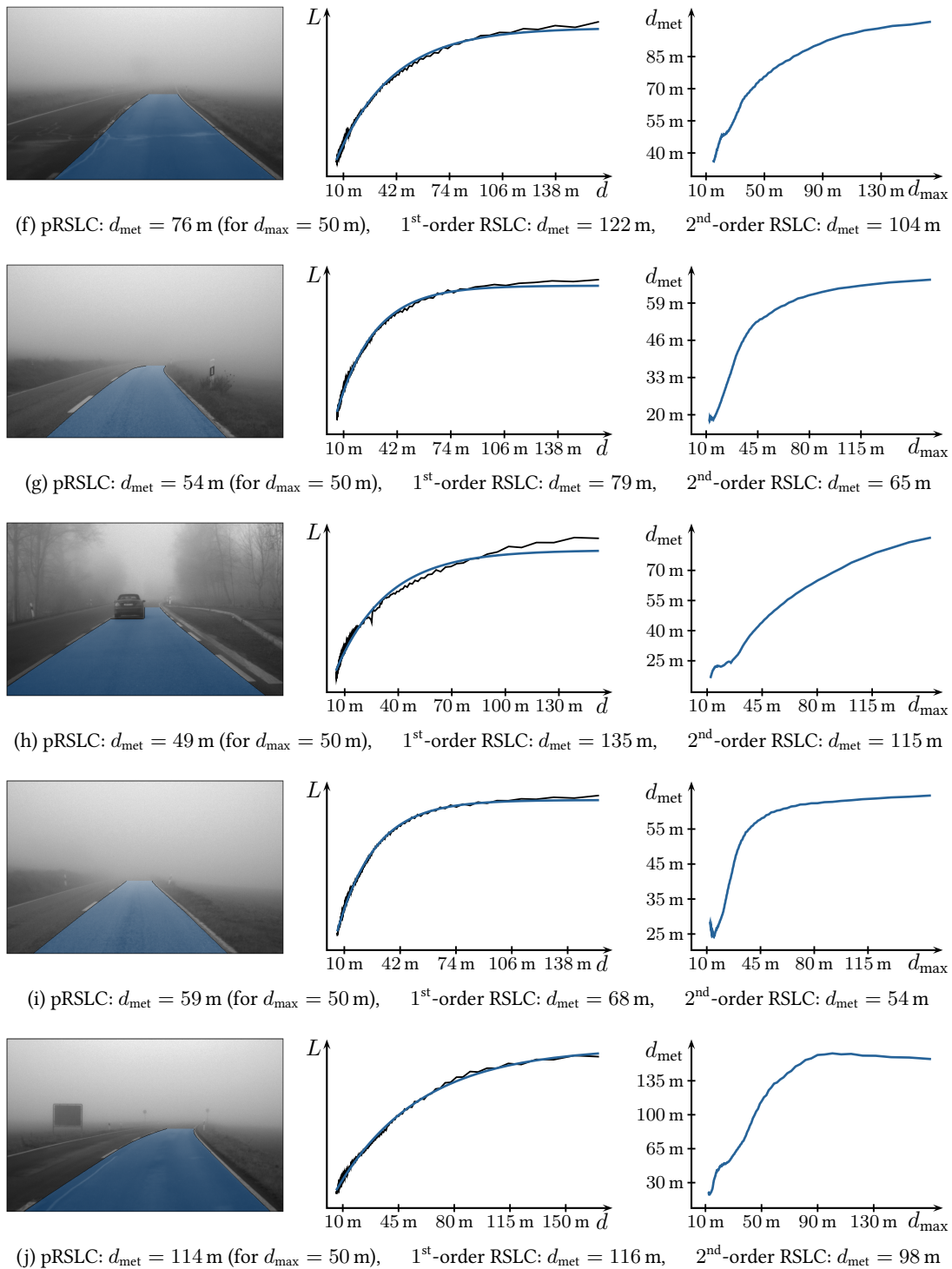


Figure 9.2: Page 2/2. Results of pRSLC-based visibility estimation. Left: Partially segmented road from which the luminances are extracted line by line. The marked area indicates the image region that is processed in the case of  $d_{\text{met}} = 50$  m. Middle: Fit of Koschmieder's model on the distance-luminance values. Right: Visibility estimation results w.r.t. the maximally considered distances.

---

## Conclusions and Outlook

Looking back at the chapters of this work, it can be summarized as a rigorous study of the quantitative assessment of visibility conditions in homogeneous daytime fog. After setting out the motivation behind the research and providing an introduction to meteorological visibility, the transport of light through fog is discussed on a microscopic as well as on a macroscopic scale. Based on the carefully derived models, different algorithms are introduced which have the potential to be part of a modern and comprehensive visibility assessment framework for future driver assistance cameras.

In the following, the major findings of this thesis are brought together in a short retrospective discussion. The models and algorithms are summarized, focusing on their advantages and disadvantages. Looking ahead, the author's personal suggestions and expectations with regard to the future developments within the respective fields of visibility assessment are incorporated into this discussion. From this it becomes clear that this work is just one first step towards a reliable visibility estimation based on automotive camera systems.

***About Light Transport Through Fog.*** Part II of this work provides a systematic overview of the aspects of light transport through fog. The part is introduced with the definition and discussion of the meteorological visibility  $d_{\text{met}}$  as the physical quantity which most appropriately describes the visibility conditions in homogeneous daytime fog (*cf.* Sec. 3.1). It is shown that surprisingly many applications could be implemented based on a reliable estimation of  $d_{\text{met}}$  (*cf.* Sec. 3.3). Taking a look at the ambiguities in the literature regarding the definition of visibility (*cf.* *e.g.* Table 3.1), this work hopefully can help to establish one common definition that is used in future studies.

In order to assess atmospheric visibility conditions in fog, it is furthermore advisable to comprehend not only the macroscopic process of light transport through fog, but also the microscopic interaction of light and tiny fog droplets. In Chap. 4, the Mie theory is revisited, which most exactly describes the scattering and absorption of light by single spherical particles as well as for particle volumes. In this way several common assumptions about microscopic scattering and absorption in fog are verified. This includes the assumptions that scattering of light in fog does not depend on the wavelength and is free of absorption. Thanks to the carefully compiled Mie formulas, it is explicitly shown how the single particle scattering theory and a certain drop-size distribution can be combined to derive the fog's volume scattering behavior which is mainly represented by the extinction coefficient  $K$  and the phase function  $\psi$ .

One example for the resulting phase function based on a log-normal drop-size distribution is provided in Remark 8 on page 35. This experiment has shown that the Henyey-Greenstein phase function model (4.12) only roughly represents a realistic scattering phase function. Due to its analytical simplicity and the fact that it only depends on the asymmetry parameter  $g$ , it represents one of the most popular phase function models. For the same reasons, the Henyey-Greenstein phase function is used throughout this work as well. One experiment is provided in Sec. 8.6.2 and Fig. 8.22 which addresses the impact of this decision on the overall visibility estimation

results. Although this impact has been revealed to be acceptable compared to other sources of estimation errors, it should definitively be the aim of future investigations to study more realistic phase function models in the context of visibility estimation. Moreover, it still has to be clarified whether wavelength averaging and the use of higher-order models (*cf.* Sec. 8.4) could possibly reduce the error arising from the use of the simple Henyey-Greenstein phase function model.

In Part II of this work, the most relevant chapter regarding visibility estimation is the discussion on the radiative transfer theory in Chap. 5. Based on the stationary, monochromatic and emission-free version of the radiative transfer equation (5.2), the classical radiative transfer problem (5.9) has been formulated to describe the macroscopic process of light transport through fog. It is shown that this integro-differential problem can be replaced by an integral equation (5.16), which is equivalent to the classical formulation in the space of uniformly bounded and measurable functions  $\mathfrak{B}$  (*cf.* Theorem 1 on page 47). From this integral formulation, a sequence of light transport models is derived, which are the outcome of a fixed-point iteration for the integral operator  $\mathcal{T}$  (*cf.* Sec. 5.4). In Theorem 2 on page 50, it is proven that these higher-order models satisfy a number of beneficial analytical properties such as their convergence towards an exact solution of the radiative transfer problem and their linearity w.r.t. to the luminance parameters  $L_0$  and  $L_{\text{air}}$ .

It has also been demonstrated that Koschmieder's model is equivalent to the first of these higher-order models, which even provides the exact solution to the radiative boundary problem in the special case of horizontal vision through a plane-parallel atmosphere. One should also note that Koschmieder's model only depends on the fog's extinction coefficient  $K$ , not on the specific volume scattering phase function. Both properties combined with the model's analytical simplicity make Koschmieder's model a reasonable choice for cases of approximately horizontal vision. In addition, the plane-parallel version of the radiative boundary problem is briefly revisited in Sec. 5.5 for subsequent use in the context of road surface luminance curves.

**About Model-Based Visibility Estimation.** Based on the light transport models provided in Chap. 5, several algorithms for estimating the meteorological visibility with the help of a driver assistance front camera are introduced in Part III of this work (*cf.* Fig. \* on the next page). These algorithms are organized according to the image content required for the estimation of the meteorological visibility. This has led to three groups of algorithms: firstly, making use of tracked objects (*cf.* Chap. 7), secondly the road surface luminance curve (*cf.* Chap. 8) and thirdly a partial segmentation of the road (*cf.* Chap. 9). In all approaches, the parameter estimation from the image data consists in solving the inverse problem (*cf.* Sec. 6.3) based on the most appropriate and applicable light transport model.

The first and novel visibility estimation approach proposed in this work makes use of luminance and distance observations on tracked objects in the camera image (*cf.* Sec. 7.1). Assuming that these objects mainly originate from horizontal vision, Koschmieder's model is applied to assess the tracking observations with a maximum likelihood objective function  $\mathcal{F}$  (*cf.* Sec. 7.2 and Sec. 7.3). Based on a comprehensive analytical discussion of  $\mathcal{F}$  in Sec. 7.4, it is revealed that the objective function can be minimized by an easy-to-implement and fast algorithm which is applicable for real-time purposes. Since this minimization approach clearly outperforms classical methods, such as the Levenberg-Marquardt method, this may be considered one of the major findings of this work. However, as suggested by the numerical experiments on synthetic and real data, a reliable and stable visibility estimation based on  $\mathcal{F}$  requires long and good object tracks. This problem is addressed by the  $L_{\text{air}}$  stabilization, introduced in Sec. 7.5. If additional information on the air

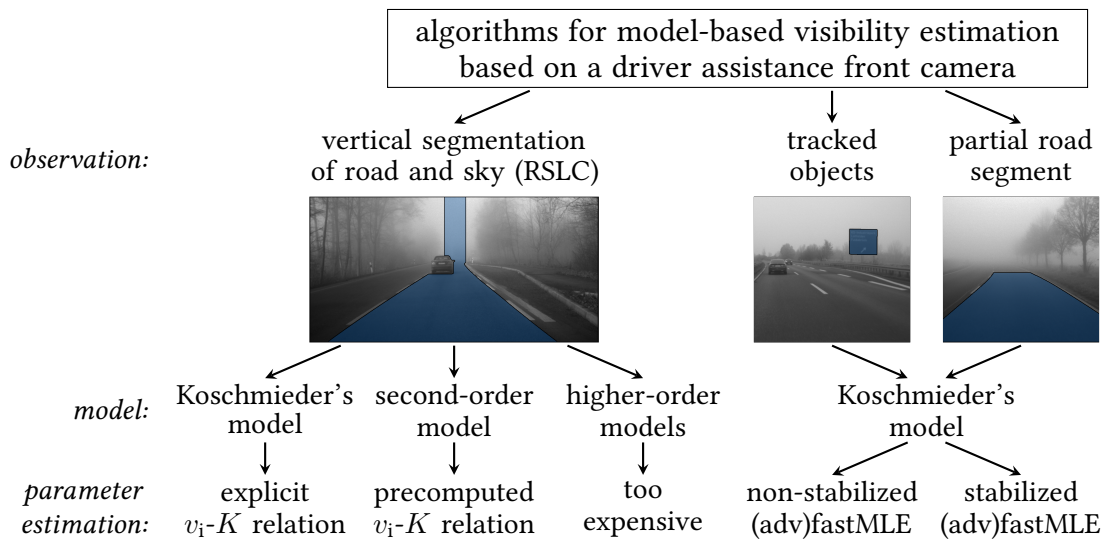


Figure 8: overview of algorithms for model-based visibility estimation proposed in this work

light parameter  $L_{\text{air}}$  was available, which could be directly estimated from the camera image, it would allow for a substantially stabilized visibility estimation. It thus seems to be the way of choice to estimate  $K$  and  $L_{\text{air}}$  simultaneously for a tracking-based visibility estimation in a driver assistance camera.

Nevertheless, many open issues remain for further developments regarding tracking-based visibility estimation. Although general feasibility based on the camera data is proven in Sec. 7.6, it has still to be verified that the tracking data extracted by real-time ADAS algorithms is of sufficient quality for the visibility estimation. However, it can be assumed that tracking-based visibility estimation based on camera images is possible, since one can expect current and future driver assistance cameras to provide numerous usable object tracks (e.g. on road signs or vehicles), generic superpixel tracks, or concatenated flow vectors of an increasing quality. The main question will be which of the data or data combinations turns out to be the most suitable for tracking-based visibility estimation. Further pending points concern the analytical properties of  $\mathcal{F}$ . They are summarized in 7.4.3. Solving these questions would mainly allow for the provision of reliable information on the estimation confidence, which indeed is highly desirable. Besides, several parts and potential extensions of the current approach demand further investigations. This mainly includes the selection of the luminance values from the object segments in Sec. 7.1, the assignment of the uncertainties in Remark 20 on page 81, the estimation of  $L_{\text{air}}$  for the stabilization in Sec. 7.5 and a correction of the systematic error arising from not perfectly horizontal vision (cf. Fig. 7.17).

In Chap. 8, the second approach for visibility estimation is presented. According to the idea of Hautière *et al.* in [Hau2006c], the image data used for this algorithm is based on a vertically connected segmentation of parts of the road and the sky in the image. From this image segment, the so-called road surface luminance curve (RSLC) can be extracted as the line-wise median of luminances (cf. Fig. 8.1). Before this work, Hautière *et al.* already demonstrated in [Hau2006c] that for Koschmieder's model the RSLC's inflection point position  $v_i$  uniquely corresponds to the underlying extinction coefficient  $K$  of the model curve. However, in Fig. 8.5 it is shown that Koschmieder's model does not adequately describe real world luminance curve observations since they crucially violate the assumption of horizontal vision.

Motivated by this finding, improved RSLC models are derived from the higher-order light transport models introduced in Chap. 5. For this derivation, the road is modeled as an infinitely expanded and homogeneous plane (*cf.* Sec. 8.4). Although this seems to be a tough assumption, one has to keep in mind that it is only used to more appropriately model the in-scattered light on the line of sight between the camera and the road (*cf.* Fig. 8.6). Especially in cases of dense fog, this is a reasonable assumption which can help to replace the air light constancy implicitly assumed by the use of Koschmieder's model (*cf.* 5.4.1).

One of the most crucial findings is that, analogous to the first-order case, all higher-order models (and even the exact solution of the plane-parallel radiative boundary problem) still allow for a unique mapping between  $v_i$  and  $K$ . Even though this relation could not be brought to a closed-form analytical expression for models of order  $\geq 2$ , it can still be exploited for a fast online parameter estimation. To achieve this, the increased model complexity is broken down to precomputed look-up tables. Unfortunately, the generation of such look-up tables based on the numerical methods introduced in Sec. 8.4 seems to be impracticable. Each higher-order model evaluation requires an expensive simulation of the full (discretely represented) luminance distribution. However, at least for the second-order RSLC model, it has been possible to derive an explicit formulation which allows for a fast computation of the luminance curve and in turn the required  $K$ - $v_i$  relation (*cf.* Sec. 8.3). Moreover, it is shown that the second-order model already removes most of the systematic visibility estimation errors arising from the horizontal vision assumption of Koschmieder (*cf.* 8.6.2 and Fig. 8.19). In addition, Fig. 8.21 demonstrates that the use of second-order models relevantly improves the visibility estimation results. Therefore, the major finding on RSLC-based visibility estimation is that taking into account the effects of non-horizontal vision is feasible as well as beneficial.

In addition, the extensive experimental evaluations in Sec. 8.6 reveal that the estimation capabilities of RSLC-based methods in general rapidly decrease when the meteorological visibility increases (*cf.* *e.g.* Fig. 8.15 and Fig. 8.16). Assuming a driver assistance camera similar to the MPC from Sec. 6.2, the border of useful estimation results is about 200 m. This effect is reinforced by the fact that the assumption of a flat and homogeneous road is more acceptable for dense than for light fog. Even though this limitation seems to be acceptable for driver assistance applications one should be aware of it when implementing an automatic visibility estimation system based on road surface luminance curves. Probably, for cases of light fog, an RSLC-based visibility estimation has to be replaced by different approaches.

The most relevant future challenges of RSLC-based visibility estimation, however, can be found in an improved inflection point estimation, an advanced generation of look-up tables, and the introduction of a road surface depth correction. From the experience in this work the extraction of an inflection point from noisy RSLCs is still one of the major sources of visibility estimation errors, especially in cases of medium or light fog. Furthermore, the generation of look-up tables for higher-order models is still too expensive. This problem might be solvable by explicit analytical formulations of higher-order models, similar to the second-order case. Finally, one can expect the use of depth correction for non-flat road surfaces to be a valuable advancement even if the in-scattered light is still modeled by the flat-world assumption. Each of these open issues seems thus to be a promising subject for future investigations.

The last algorithm proposed in this work is presented in Chap. 9. It can be considered to be a combination of the tracking-based and RSLC-based approaches from chapters 7 and 8. In cases where the RSLC cannot be extracted to the whole, the remaining road segment is shown to be useable for a visibility estimation based on Koschmieder's model. Since this approach disregards

the effects due to non-horizontal vision, it has to be considered to be more a useful fall-back solution than a fully valuable algorithm. For use in future driver assistance cameras, it seems to be reasonable to provide this method with reliable road depth information and to improve the selection of uncertainties  $\sigma_n^m$  in order to reduce the effects from currently overrated low-distance parts of the road.

Finally, there are several improvements which are desirable for all algorithms proposed in this work. First of all it is always helpful to improve the input data to the algorithms, which includes not only depth estimations, more accurate object tracks and segmentations, but also the image quality in general. As it is a crucial assumption, it is extremely important to aim for a most linear imager characteristic which might require an additional (photometric) calibration. This also involves the luminous sensitivity having to be constant across the whole imager. Furthermore, for all algorithms it seems to be helpful to introduce confidence measures based on experience or analytical investigations. These measures could be helpful for the combined use of different visibility estimation approaches.

**Combined Approaches.** As stated above, the algorithms for model-based visibility estimation exhibit different advantages and disadvantages. While RSLC-based algorithms, for example, rely on an unobstructed view up to the horizon, tracking-based algorithms explicitly benefit from crowded situations with many trackable objects available. At the same time, tracking-based algorithms require not only stable object tracks and segmentations, but also reliable depth estimations, which is a challenging task, in particular for monocular cameras and moving objects. RSLC-based visibility estimation, however, is inherently restricted to road traffic scenarios, while tracking-based approaches can be applied more flexibly. This restriction is further amplified by the assumption of a flat and homogeneous dark road which should be at least approximately satisfied. On the other hand, RSLC-based methods are well-suited for visibility estimation in dense fog and should thus not be neglected. This is especially true, because tracking-based visibility estimation only seems to be stable for excellent tracking data or additional information on the air light parameter. One should also note that, in contrast to the tracking-based approach, algorithms based on road surface luminance curves only require a single frame for the parameter estimation and can therefore also be applied to stationary cameras such as those used for traffic or weather surveillance.

From this it becomes clear that the different approaches could be a valuable supplement to each other. In order to design a robust and reliable framework for model-based visibility estimation, the different algorithms probably have to be combined. Thanks to the different sources of data this includes not only a higher availability and accuracy, but could also be useful for mutual validation. Depending on the confidence of the available data one could, for example, continuously switch between different visibility estimation methods and provide a joint visibility result together with a joint confidence measure. Another important question is whether such a framework should be combined with an additional fog detection to trigger the visibility estimation in the first place. It is also conceivable that the results from one of the model-based visibility estimators have a sufficiently high significance to distinguish cases of a clear atmosphere, haze or light fog from cases of relevantly reduced visibility. The optimal combination of algorithms, however, largely depends on the camera system used for the estimation of meteorological visibility.

**Future Fields of Visibility Assessment.** In this work, the assessment of visibility conditions in homogeneous daytime fog is at the center of considerations. This, of course, is only a first step towards creating a framework for automated and comprehensive weather and visibility recognition as required for future driver assistance systems and autonomously driving vehicles. The biggest

challenge of future fog assessment lies in handling nighttime situations and inhomogeneous fog.

In cases of nighttime fog the visibility conditions are not dominated by contrast reduction, as is the case for daytime fog, but by effects of self-glare and diffusion. Therefore, the meteorological visibility as defined in Sec. 3.1 cannot automatically be considered to be an adequate visibility definition for nighttime situations. Furthermore, as stated in [Gal2009], the extinction coefficient does not sufficiently describe the grade of visibility reduction due to backscattering and halos. In order to assess the visibility conditions in nighttime fog based on physical models, one should first of all attempt to define an appropriate visibility measure.

The same is true for substantially inhomogeneous fog and smoke, which suffer from a locally varying extinction coefficient. The definition of meteorological visibility cannot offhandedly be applied to these scenarios. In fact, visibility measurement constitutes an ill-posed tomography problem for severe inhomogeneities. Since fog, however, can never be expected to be perfectly homogeneous, it should be part of future investigations to identify perturbation results which provide information on the usability of the definition and estimation algorithms for  $d_{\text{met}}$  in cases of slightly disturbed atmospheres.

Other sight impairments which can be caused by difficult light situations or any disturbances within the optical path range from glare, snow or wet road surfaces to total darkness and cracks in the windshield. It is likely that the effects of these sight impairments in the camera image cannot entirely be described by useful physical models as it is the case for homogeneous daytime fog. Therefore, future work should aim to find ways of enhancing gradual blindness detection based on, for instance, generic image features and machine learning approaches. Another field of study should focus on improving visibility estimation by combining different sensor technologies.

This outlook shows that the area of visibility estimation faces numerous fascinating challenges and has considerable potential for development. Over the next years one can expect this area to be further driven by the trend towards autonomous driving and the associated need for an assessment of the sensor's operability. This involves providing estimations on as much physical information related to the environmental conditions as possible. This work makes a valuable contribution towards achieving this.

---

# Appendix A. Notation

In this work, a number of more or less common mathematical symbols, operators, terms, abbreviations and theorems are used, which might not be present to the reader. In order to avoid ambiguities, the noteworthy notation of this thesis is summarized in the following.

## ***Mathematical Abbreviations.***

LHS	left hand side (of an equation)
RHS	right hand side (of an equation)
PDE	partial differential equation
ODE	ordinary differential equation
w.r.t.	with respect to
w.l.o.g.	without loss of generality
w/	with
w/o	without
N/A	not available
s.t.	such that
i.i.d.	identically and independently distributed (in the context of random variables)
iff	if and only if
a.e.	almost everywhere (measure theory)
$\forall$	for all
$\exists$	there exist(s)

Other abbreviations can be looked up in the Index.

## ***Mathematical Symbols, Operators and their Notation.***

$\mathbb{N}$  *Natural Numbers.*  $\mathbb{N} := \{1, 2, 3, \dots\}$ .

$\mathbb{N}_0$  *Non-Negative Integers.*  $\mathbb{N}_0 := \mathbb{N} \cup \{0\}$ .

$\mathbb{Z}$  *Integers.*  $\mathbb{Z} := \mathbb{N}_0 \cup (-\mathbb{N})$ .

$\mathbb{Q}$  *Rational Numbers.*  $\mathbb{Q} := \{p/q : p \in \mathbb{Z}, q \in \mathbb{N}\}$ .

$\mathbb{R}$  *Real Numbers.* The real numbers  $\mathbb{R}$  are defined as the metric completion of the rational numbers  $\mathbb{Q}$ , which can be constructed as the quotient set

$$\mathbb{R} := \left\{ (q_n)_{n \in \mathbb{N}} \in \mathbb{Q}^{\mathbb{N}} : (q_n) \text{ is a Cauchy sequence} \right\} / \sim,$$

where the equivalence relation  $\sim$  is defined by

$$(q_n) \sim (p_n) \quad :\Leftrightarrow \quad |q_n - p_n| \rightarrow 0, \quad \text{for } n \rightarrow \infty.$$

- $\mathbb{R}_{>0}$  *Positive Real Numbers.*  $\mathbb{R}_{>0} := (0, \infty) = \{x \in \mathbb{R} : x > 0\}$ .
- $\mathbb{R}_{\geq 0}$  *Non-Negative Real Numbers.*  $\mathbb{R}_{\geq 0} := [0, \infty) = \{x \in \mathbb{R} : x \geq 0\}$ .
- $i$  *Imaginary Unit.*  $i := \sqrt{-1}$ .
- $\mathbb{C}$  *Complex Numbers.*  $\mathbb{C} := \mathbb{R} + i\mathbb{R}$ .
- $\Re, \Im$  *Real/Imaginary Part.* For any  $z \in \mathbb{C}$  there exist unique numbers  $\Re(z), \Im(z) \in \mathbb{R}$ , s.t.

$$z = \Re(z) + i\Im(z).$$

$\Re(z)$  and  $\Im(z)$  are called the *real part of  $z$*  and the *imaginary part of  $z$* , respectively.

- $\bar{z}$  *Complex Conjugate.* For  $z \in \mathbb{C}$  it is  $\bar{z} := \Re(z) - i\Im(z)$ .
- $\dot{\cup}$  *Mutually Disjoint Union.* For  $n \in \mathbb{N}$  and sets  $M, M_1, \dots, M_n$  it is
- $$M_1 \dot{\cup} \dots \dot{\cup} M_n = M \quad :\Leftrightarrow \quad M_1 \cup \dots \cup M_n = M \quad \wedge \quad \forall k \neq l : M_k \cap M_l = \emptyset.$$

- $\mathcal{G}$  *Graph.* A weighted and directed graph  $\mathcal{G} = (\mathcal{V}, \mathcal{E}, w)$  consists of a set of *nodes or vertices*  $\mathcal{V}$ , a set of *edges*  $\mathcal{E} \subseteq \mathcal{V} \times \mathcal{V}$  and the *edge weights*  $w : \mathcal{E} \rightarrow \mathbb{R}$ .
- $\mathbb{R}^{m \times n}$  *Matrices.* For  $m, n \in \mathbb{N}$  it is  $\mathbb{R}^{m \times n}$  the set of real  $m \times n$  matrices.
- $\mathcal{I}$  *Identity Matrix.*  $\mathcal{I}$  denotes a quadratic matrix that is 1 at the (main) diagonal entries and 0 otherwise. Its size should always be clear from the context.
- $\succ, \succeq$  *Definiteness of a Matrix.* For  $n \in \mathbb{N}$  and a symmetric matrix  $M \in \mathbb{R}^{n \times n}$  it is

$$M \succ 0 \quad :\Leftrightarrow \quad \forall x \in \mathbb{R}^n \setminus \{0\} : x^T M x > 0, \quad (\text{positive definite})$$

$$M \succeq 0 \quad :\Leftrightarrow \quad \forall x \in \mathbb{R}^n \setminus \{0\} : x^T M x \geq 0, \quad (\text{positive semi-definite})$$

$$M \preceq 0 \quad :\Leftrightarrow \quad \forall x \in \mathbb{R}^n \setminus \{0\} : x^T M x \leq 0, \quad (\text{negative definite})$$

$$M \prec 0 \quad :\Leftrightarrow \quad \forall x \in \mathbb{R}^n \setminus \{0\} : x^T M x < 0. \quad (\text{negative semi-definite})$$

$\det$  *Determinant.* For  $n \in \mathbb{N}$  and a matrix  $M \in \mathbb{R}^{n \times n}$ , the determinant of  $M$  is written as  $\det(M)$ .

$\text{SO}$  *Special Orthogonal Group.* For  $n \in \mathbb{N}$  it is

$$\text{SO}(n) := \text{SO}(n; \mathbb{R}) := \{R \in \mathbb{R}^{n \times n} : R^T R = \mathcal{I}, \det(R) = 1\}.$$

To actually make  $\text{SO}(n)$  an algebraic group, it is equipped with the standard matrix multiplication.

$\langle \cdot, \cdot \rangle$  *Euclidean Scalar Product.* For  $N \in \mathbb{N}$  and  $x, y \in \mathbb{R}^N$  it is

$$\langle x, y \rangle := \sum_{n=1}^N x^n y^n.$$

$|\cdot|$  *Euclidean Norm.* For  $N \in \mathbb{N}$  and  $x \in \mathbb{R}^N$  it is

$$|x| := \sqrt{\langle x, x \rangle}.$$

For  $z \in \mathbb{C}$  it is  $|z| := \sqrt{\Re(z)^2 + \Im(z)^2}$ .

$B_\varepsilon(\cdot)$  *Open (Euclidean) Ball.* For  $n \in \mathbb{N}$ ,  $x \in \mathbb{R}^n$  and  $\varepsilon > 0$  it is

$$B_\varepsilon(x) := \{y \in \mathbb{R}^n : |x - y| < \varepsilon\}.$$

$\mathbb{S}^n$  *Unit Sphere in  $\mathbb{R}^{n+1}$ .* For  $n \in \mathbb{N}$  it is  $\mathbb{S}^n := \{x \in \mathbb{R}^{n+1} : |x| = 1\}$ .

$\mathbb{S}_{>0}^n$  *Open Upper Unit Hemisphere in  $\mathbb{R}^{n+1}$ .*  $\mathbb{S}_{>0}^n := \mathbb{S}^n \cap (\mathbb{R}^n \times \mathbb{R}_{>0})$ .

$\mathbb{S}_{\geq 0}^n$  *Closed Upper Unit Hemisphere in  $\mathbb{R}^{n+1}$ .*  $\mathbb{S}_{\geq 0}^n := \mathbb{S}^n \cap (\mathbb{R}^n \times \mathbb{R}_{\geq 0})$ .

$\cdot \times \cdot$  *(Gibbs') Cross Product.* For  $x, y \in \mathbb{R}^3$  it is

$$x \times y := \begin{pmatrix} x^2 y^3 - x^3 y^2 \\ x^3 y^1 - x^1 y^3 \\ x^1 y^2 - x^2 y^1 \end{pmatrix}.$$

$\mathcal{N}(\cdot, \cdot)$  *Normal Distribution.* Given an expected value  $\mu$ , a variance  $\sigma^2$  and a random variable  $X$ , the standard notation  $X \sim \mathcal{N}(\mu, \sigma^2)$  has to be understood as  $X$  being normally distributed with the corresponding moments.

$\mathcal{U}(\cdot, \cdot)$  *Continuous Uniform Distribution.* Given an interval  $[a, b] \subset \mathbb{R}$  and a random variable  $X$ , the standard notation  $X \sim \mathcal{U}(a, b)$  has to be understood as  $X$  being continuously uniform distributed on  $[a, b]$ .

$\delta$ : *Kronecker Delta.* For  $n, m \in \mathbb{N}$  the Kronecker delta indicates whether  $n$  and  $m$  are equal:

$$\delta_n^m := \begin{cases} 1 & , \text{ if } n = m \\ 0 & , \text{ otherwise } \end{cases}.$$

$\pi$  *Pi.* An exception can be found in Sec. 4.3, where  $\pi_n$  denote angular eigenfunctions of scattering processes.

$e$  *Euler's Number.*

In the following, let  $M$  be a set,  $V$  be a vector space over a field  $\mathbb{K}$ ,  $d : V \times V \rightarrow \mathbb{R}$  be a metric on  $V$ , and  $U \subseteq V$  be any arbitrary but fixed subset of  $V$ .

$M^{\mathbb{N}}$  *Set of Sequences in  $M$ .*  $M^{\mathbb{N}} := \{(m_n)_{n \in \mathbb{N}} : m_n \in M, \forall n \in \mathbb{N}\}$ . As it is a standard convention,  $(m_n)_{n \in \mathbb{N}} \subset M$  will be understood as  $(m_n)_{n \in \mathbb{N}} \in M^{\mathbb{N}}$ .

$v^n$  *Components Notation.* If not stated otherwise, for  $N \in \mathbb{N}$  and  $v \in V^N$ , the  $n^{\text{th}}$  component of  $v$  is denoted as  $v^n$ , i.e.  $v = (v^1, \dots, v^N)$ .

$\|\cdot\|$  *Norm on  $V$ .* Let  $\mathbb{K} \in \{\mathbb{R}, \mathbb{C}\}$ . A function  $\|\cdot\| : V \rightarrow \mathbb{R}$  is called *norm* iff for all  $v_1, v_2 \in V$  and  $z \in \mathbb{K}$  it is  $\|v_1\| \geq 0$ , and  $\|v_1\| = 0$  iff  $v_1 = 0$ , and  $\|v_1 + v_2\| \leq \|v_1\| + \|v_2\|$ , and  $\|zv_1\| = |z|\|v_1\|$ . An example for a norm on  $V = \mathbb{R}^n$ ,  $n \in \mathbb{N}$ , is given by the Euclidean norm  $|\cdot|$  as defined above. A norm always induces a metric by  $(x, y) \mapsto \|x - y\|$ .

sup *Supremum.* Let  $M \subseteq \mathbb{R}$  be a subset of the real numbers. Then, there exists a unique number  $\sup(M) \in \mathbb{R} \cup \{-\infty, \infty\}$  satisfying

$$\forall m \in M : \sup(M) \geq m \quad \wedge \quad \forall x < \sup(M), \exists m \in M : m \geq x.$$

This number is called *supremum of  $M$* . For a function  $f : M \rightarrow \mathbb{R}$  the *supremum of  $f$*  is defined by

$$\sup(f) := \sup \{f(m) : m \in M\}.$$

inf *Infimum.* Let  $M \subseteq \mathbb{R}$  be a subset of the real numbers. Then, there exists a unique number  $\inf(M) \in \mathbb{R} \cup \{-\infty, \infty\}$  satisfying

$$\forall m \in M : \inf(M) \leq m \quad \wedge \quad \forall x > \inf(M), \exists m \in M : m \leq x.$$

This number is called *infimum of  $M$* . For a function  $f : M \rightarrow \mathbb{R}$  the *infimum of  $f$*  is defined by

$$\inf(f) := \inf \{f(m) : m \in M\}.$$

diam *Diameter of  $U$ .*  $\text{diam}(U) := \sup \{d(u_1, u_2) : u_1, u_2 \in U\}$ .

$\bar{U}$  *Closure of  $U$  (in  $V$ ).*  $\bar{U} := \{v \in V : \forall \varepsilon > 0, \exists u \in U, \text{ s.t. } d(u, v) < \varepsilon\}$ .

$\partial U$  *Boundary of  $U$  (in  $V$ ).*  $\partial U := \bar{U} \cap \overline{V \setminus U}$ .

**Topological Terms.** In the following, let  $V$  be a vector space with a metric  $d$  and  $U \subseteq V$ .

$V$  is called *Banach space* iff  $d$  is induced by a norm and all Cauchy sequences  $(v_n)_{n \in \mathbb{N}} \in V^{\mathbb{N}}$  are converging in  $V$ .

$U$  is said to be *open (in  $V$ )* iff

$$\forall u \in U, \exists \varepsilon > 0 : \{v \in V : d(v, u) < \varepsilon\} \subseteq U.$$

$U$  is said to be *closed (in  $V$ )* iff  $V \setminus U$  is an open subset of  $V$ .

$U$  is said to be *connected* iff for all open subsets  $U_1, U_2 \subseteq V$ ,

$$(U_1 \cap U) \dot{\cup} (U_2 \cap U) = U \quad \Rightarrow \quad (U_1 \cap U) = \emptyset \vee (U_2 \cap U) = \emptyset.$$

$U$  is called a *domain* iff  $U$  is open, connected and non-empty.

Let  $\mathbb{K} \in \{\mathbb{R}, \mathbb{C}\}$ . Then,  $U$  is said to be *convex* iff

$$\forall u, v \in U, \forall \alpha \in (0, 1) : \alpha u + (1 - \alpha)v \in U.$$

$U$  is said to be (*sequentially*) *compact* iff for all  $(u_n)_{n \in \mathbb{N}} \in U^{\mathbb{N}}$  there exists a subsequence which converges in  $U$ .

Note: If not stated otherwise, analytical and topological terms and definitions (such as convergence or Cauchy sequence) that rely on a metric over  $\mathbb{Q}^n$ ,  $\mathbb{R}^n$  or  $\mathbb{C}^n$ ,  $n \in \mathbb{N}$ , shall always be understood as induced by the Euclidean metric.

**Functions and Function Spaces.** In the following, let  $k \in \mathbb{N} \cup \{\infty\}$ ,  $m, n \in \mathbb{N}$  and  $\Omega \subseteq \mathbb{R}^n$  be open. The following standard function spaces are used in this work:

- $C^0$  *Continuous Functions.* The function spaces  $C^0(\Omega; \mathbb{R}^m)$  and  $C^0(\bar{\Omega}; \mathbb{R}^m)$  consist of all continuous functions  $f : \Omega \rightarrow \mathbb{R}^m$  and  $f : \bar{\Omega} \rightarrow \mathbb{R}^m$ , respectively. In addition, it can be abbreviated as  $C^0(\Omega) := C^0(\Omega; \mathbb{R})$  and  $C^0(\bar{\Omega}) := C^0(\bar{\Omega}; \mathbb{R})$ .
- $\|\cdot\|_{C^0}$   *$C^0$  Norm.* For  $f \in C^0(\Omega; \mathbb{R}^m)$  one can define

$$\|f\|_{C^0} := \sup_{x \in \Omega} |f(x)|.$$

For  $\Omega$  bounded, this constitutes a norm on  $C^0(\bar{\Omega}; \mathbb{R}^m)$ , which is also called *maximum* or *infinity norm*. For not uniformly bounded functions it takes the value  $\infty$ .  $\|\cdot\|_{C^0}$  can not only be applied to continuous functions. It, for instance, is finite for arbitrary uniformly bounded functions.

- $C^k$   *$k$ -Times Continuously Differentiable Functions.* The function space  $C^k(\Omega; \mathbb{R}^m)$  consists of the functions  $f : \Omega \rightarrow \mathbb{R}^m$  that are  $k$ -times differentiable with all derivatives of order  $\leq k$  being continuous on  $\Omega$ .  $C^k(\bar{\Omega}; \mathbb{R}^m)$  consists of all functions in  $C^k(\Omega; \mathbb{R}^m)$  that are continuously extendable to  $\bar{\Omega}$  for all derivatives of order  $\leq k$ . In addition, it can be abbreviated as  $C^k(\Omega) := C^k(\Omega; \mathbb{R})$  and  $C^k(\bar{\Omega}) := C^k(\bar{\Omega}; \mathbb{R})$ .
- $\|\cdot\|_{C^k}$   *$C^k$  Norm.* For  $\Omega$  bounded, a norm on  $C^k(\bar{\Omega}; \mathbb{R}^m)$  is introduced, which for  $f \in C^k(\bar{\Omega}; \mathbb{R}^m)$  is defined as

$$\|f\|_{C^k} := \sum_{\substack{l_1, \dots, l_n=0 \\ l_1 + \dots + l_n \leq k}}^k \left\| \left( \frac{\partial}{\partial x_1} \right)^{l_1} \cdots \left( \frac{\partial}{\partial x_n} \right)^{l_n} f \right\|_{C^0}$$

- $\mathfrak{B}$  *Bounded and Lebesgue Measurable Functions.* The space of uniformly bounded and Lebesgue measurable functions  $f : \Omega \rightarrow \mathbb{R}$  is denoted by  $\mathfrak{B}(\Omega)$ . Due to the uniform boundedness, this vector space can be equipped with the maximum norm  $\|\cdot\|_{C^0}$ . It is directly related to the function space of essentially bounded and measurable functions  $\mathbb{L}^\infty(\Omega)$ , which is described in Remark 14 on page 47.

A function  $f : \mathbb{R}^n \rightarrow \mathbb{R}$  is said to be *coercive* iff

$$\forall (x_k)_{k \in \mathbb{N}} \subset \mathbb{R}^n : |x_k| \rightarrow \infty \Rightarrow f(x_k) \rightarrow \infty, \quad k \rightarrow \infty.$$

Further terms and symbols regarding derivatives of multivariate functions:

- $\nabla f$  *Gradient.* For  $n \in \mathbb{N}$ ,  $\Omega \subseteq \mathbb{R}^n$  open, and  $f \in C^1(\Omega)$  it is

$$\nabla f := \left( \frac{\partial f}{\partial x^1}, \dots, \frac{\partial f}{\partial x^n} \right)^T.$$

$x \in \Omega$  is called *critical point* of  $f$  iff  $\nabla f(x) = 0$ .

$J_f$  *Jacobian Matrix.* For  $m, n \in \mathbb{N}$ ,  $\Omega \subseteq \mathbb{R}^n$  open,  $f \in C^1(\Omega; \mathbb{R}^m)$  and  $x \in \Omega$  it is

$$J_f(x) := \begin{pmatrix} \frac{\partial f^1}{\partial x^1}(x) & \cdots & \frac{\partial f^1}{\partial x^n}(x) \\ \vdots & & \vdots \\ \frac{\partial f^m}{\partial x^1}(x) & \cdots & \frac{\partial f^m}{\partial x^n}(x) \end{pmatrix}.$$

$\text{Hess}(\cdot)$  *Hess Matrix.* For  $n \in \mathbb{N}$ ,  $\Omega \subseteq \mathbb{R}^n$  open, and  $f \in C^2(\Omega)$  it is

$$\text{Hess}(f) := \begin{pmatrix} \frac{\partial^2 f}{\partial x^1 \partial x^1} & \cdots & \frac{\partial^2 f}{\partial x^1 \partial x^n} \\ \vdots & & \vdots \\ \frac{\partial^2 f}{\partial x^n \partial x^1} & \cdots & \frac{\partial^2 f}{\partial x^n \partial x^n} \end{pmatrix}.$$

Due to the equality of mixed partials (Schwarz' theorem), this matrix is symmetric.

**Convex Functions.** Let  $N \in \mathbb{N}$  and  $\Omega \subseteq \mathbb{R}^N$  be a convex domain.

A function  $f : \Omega \rightarrow \mathbb{R}$  is called *convex* iff

$$\forall x, y \in \Omega, x \neq y, \alpha \in (0, 1) : f(\alpha x + (1 - \alpha)y) \leq \alpha f(x) + (1 - \alpha)f(y),$$

which for  $f \in C^2(\Omega)$  is equivalent to

$$\forall x \in \Omega : \text{Hess } f(x) \succeq 0 \quad (\text{positive-semidefinite}).$$

A function  $f : \Omega \rightarrow \mathbb{R}$  is called *strictly convex* iff

$$\forall x, y \in \Omega, x \neq y, \alpha \in (0, 1) : f(\alpha x + (1 - \alpha)y) < \alpha f(x) + (1 - \alpha)f(y).$$

If a function  $f \in C^2(\Omega)$  satisfies

$$\forall x \in \Omega : \text{Hess } f(x) \succ 0 \quad (\text{positive-definite}),$$

it is in particular strictly convex.

A function  $f : \Omega \rightarrow \mathbb{R}$  is called *quasiconvex* iff

$$\forall x, y \in \Omega, x \neq y, \alpha \in (0, 1) : f(\alpha x + (1 - \alpha)y) \leq \max \{f(x), f(y)\}.$$

A function  $f : \Omega \rightarrow \mathbb{R}$  is called *strictly quasiconvex* iff

$$\forall x, y \in \Omega, x \neq y, \alpha \in (0, 1) : f(\alpha x + (1 - \alpha)y) < \max \{f(x), f(y)\}.$$

**Curves.** Let  $n \in \mathbb{N}$ ,  $k \in \mathbb{N}_0 \cup \{\infty\}$ ,  $I \subset \mathbb{R}$  be an open interval in  $\mathbb{R}$ . A function  $\gamma \in C^0(I; \mathbb{R}^n)$  is called *curve in  $\mathbb{R}^n$* . For  $k$ -times differentiable curves  $\gamma \in C^k(I; \mathbb{R}^n)$ ,  $k \in \mathbb{N}_0$ , its derivatives can be written as  $\dot{\gamma}, \ddot{\gamma}, \dots$ , or alternatively  $\gamma^{(l)}$ , where  $l \in \{1, \dots, k\}$ .

A curve  $\gamma \in C^1(I; \mathbb{R}^n)$  is said to be *parametrized by the arc length* iff  $|\dot{\gamma}| \equiv 1$ .

Let  $\gamma \in C^2(I; \mathbb{R}^2)$ , i.e.  $\gamma$  is a two-times differentiable and planar curve. Then, there exists a

theorem	example source
Cauchy-Schwarz inequality	[Gra1999, 6.2]
Cramer's rule	[Gra1999, 5.5]
Rodrigues' rotation formula	[Dai2015, (11)]
Schwarz's theorem	[Wal2002, 3.3]
product rule	[Wal2002, 3.4]
chain rule	[Wal2002, 3.10]
Leibniz's integral rule	[Abr1964, 3.3.7]
measure and integration theory	[Els2011]
linearity of integration	[Els2011, IV, §3]
Lebesgue's dominated convergence theorem	[Els2011, IV, §5]
Fubini's theorem	[Els2011, V, §2]
Fubini-Tonelli theorem	[Els2011, V, §2]
Simpson's rule	[Fre2007, 3.1]

Table A.1: standard theorems used in this work

unique function  $\kappa : I \rightarrow \mathbb{R}$  that satisfies

$$\begin{pmatrix} \ddot{\gamma}^1 \\ \ddot{\gamma}^2 \end{pmatrix} = \kappa \begin{pmatrix} -\dot{\gamma}^2 \\ \dot{\gamma}^1 \end{pmatrix}.$$

$\kappa$  is called *curvature of  $\gamma$* . For  $t \in I$  the value  $1/\kappa(t)$  is called the *radius of curvature in  $\gamma(t)$* .

**Error Discussion.** In the context of a correct and a disturbed quantity  $x \in \mathbb{R}$  and  $x_{\text{err}} \in \mathbb{R}$ , the term *relative error* shall always be understood as

$$\left| \frac{x_{\text{err}} - x}{x} \right| \in \mathbb{R}_{\geq 0} \cup \{\infty\},$$

where  $0/0$  has to be interpreted as  $0$ .

**Standard Theorems.** Table A.1 provides references for established theorems repeatedly referred to in this work.



---

## Appendix B. Selected Theorems

The following three results, used in this work, can be expected to be well-known but it is difficult to find reasonable formulations or proofs for them in the literature.

### B.1 L'Hôpital's Rule for Higher-Order Derivatives

The following theorem basically states that discontinuities that can be removed by l'Hôpital's rule are as smooth as the numerator and the denominator function allow them to be. Here, the theorem is given as  $C^\infty$  formulation.

**Theorem 3** (L'Hôpital's Rule for Higher Order Derivatives). *Let  $I \subset \mathbb{R}$  be an open interval,  $u, v \in C^\infty(I)$ ,  $M \in \mathbb{N}_0$ ,  $x_0 \in I$ , where  $v \neq 0$  on  $I \setminus \{x_0\}$ , and*

$$\forall m \in \{0, \dots, M\} : \quad u^{(m)}(x_0) = v^{(m)}(x_0) = 0, \quad \text{and} \quad v^{(M+1)}(x_0) \neq 0.$$

*Then, the discontinuity of  $u/v$  in  $x_0$  can be removed infinitely smooth, i.e.*

$$x \mapsto f(x) := \begin{cases} \frac{u(x)}{v(x)} & , x \in I \setminus \{x_0\} \\ \frac{u^{(M+1)}(x_0)}{v^{(M+1)}(x_0)} & , x = x_0 \end{cases} \in C^\infty(I).$$

*Proof.* Obviously, from  $u, v \in C^\infty(I)$  and  $0 \notin v(I \setminus \{x_0\})$  it follows  $f \in C^\infty(I \setminus \{x_0\})$ .

Let now for all  $n \in \mathbb{N}_0$  the  $u_n, v_n$  and  $M_n$  be recursively defined as

$$v_0 := v, \quad v_{n+1} := v_n^2, \quad u_0 := u, \quad u_{n+1} := u'_n v_n - u_n v'_n, \quad M_0 := M, \quad M_{n+1} := 2M_n + 1.$$

*STEP 1:* It is shown for all  $n \in \mathbb{N}_0$  that

$$f^{(n)}(x) = \frac{u_n(x)}{v_n(x)}, \quad \forall x \in I \setminus \{x_0\}. \quad (\text{B.1})$$

*Proof by induction:* The base case ( $n = 0$ ) directly follows from definitions:

$$f^{(0)}(x) = f(x) = \frac{u(x)}{v(x)} = \frac{u_0(x)}{v_0(x)}.$$

For the induction step, assume for a given  $n \in \mathbb{N}_0$  that  $f^{(n)}(x) = u_n(x)/v_n(x)$  for all  $x \in I \setminus \{x_0\}$ .

Then, (B.1) holds true for  $n + 1$  as well (by applying the product rule):

$$f^{(n+1)}(x) = \left[ f^{(n)}(x) \right]' = \left[ \frac{u_n(x)}{v_n(x)} \right]' = \frac{u_n'(x)v_n(x) - u_n(x)v_n'(x)}{v_n(x)^2} = \frac{u_{n+1}(x)}{v_{n+1}(x)}.$$

*STEP 2:* It is shown for all  $n \in \mathbb{N}_0$  that

$$\forall m \in \{0, \dots, M_n\} : \quad u_n^{(m)}(x_0) = v_n^{(m)}(x_0) = 0, \quad \text{and} \quad v^{(M_{n+1})}(x_0) \neq 0. \quad (\text{B.2})$$

*Proof by induction:* The base case directly follows from the assumptions on  $u$  and  $v$ . For the induction step, let (B.2) be true for an arbitrary  $n \in \mathbb{N}_0$ . Then, one can show that it holds true for  $n + 1$  as well: From iterating the product rule it follows for any  $m \in \mathbb{N}_0$

$$u_{n+1}^{(m)}(x_0) = \sum_{k=0}^m \binom{m}{k} \left[ u_n^{(k+1)}(x_0)v_n^{(m-k)}(x_0) - u_n^{(k)}(x_0)v_n^{(m-k+1)}(x_0) \right]. \quad (\text{B.3})$$

For  $m \leq M_{n+1} - 1$  one has

$$\begin{aligned} (k+1) + (m-k) &= m+1 \leq M_{n+1} = 2M_n + 1 \quad \Rightarrow \quad k+1 \leq M_n \vee m-k \leq M_n, \\ k + (m-k+1) &= m+1 \leq M_{n+1} = 2M_n + 1 \quad \Rightarrow \quad k \leq M_n \vee m-k+1 \leq M_n. \end{aligned}$$

Therefore, from (B.3) and (B.2) for  $n$  it follows  $u_{n+1}^{(m)}(x_0) = 0$ . Analogously, for  $m \leq M_{n+1}$  one has

$$v_{n+1}^{(m)} = \sum_{k=0}^m \binom{m}{k} v_n^{(k)} v_n^{(m-k)} = 0.$$

For  $m = M_{n+1}$  one has

$$u_{n+1}^{(M_{n+1})}(x_0) = \underbrace{\left[ \binom{2M_n+1}{M_n} - \binom{2M_n+1}{M_n+1} \right]}_{=0} u_n^{(M_{n+1})}(x_0)v_n^{(M_{n+1})}(x_0) = 0.$$

Furthermore, one has

$$v_{n+1}^{(M_{n+1}+1)} = \sum_{k=0}^{2M_n+2} \binom{m}{k} v_n^{(k)} v_n^{(m-k)} = \binom{2M_n+2}{M_n+1} v_n^{(M_{n+1})} v_n^{(M_{n+1})} \neq 0.$$

*STEP 3:* Finally, with the help of (B.1), (B.2) and l'Hôpital's rule it follows for any  $n \in \mathbb{N}$

$$\lim_{x \nearrow x_0} f^{(n)}(x) = \lim_{x \nearrow x_0} \frac{u_n(x)}{v_n(x)} = \frac{u_n^{(M_{n+1})}(x_0)}{v_n^{(M_{n+1})}(x_0)} = \lim_{x \searrow x_0} \frac{u_n(x)}{v_n(x)} = \lim_{x \searrow x_0} f^{(n)}(x).$$

□

## B.2 First-Order Linear Initial Value Problems

The following theorem is so essential that the fact it could only be found in the unpublished *Analysis 2* lecture notes from Hans-Christoph Grunau is especially surprising.

**Theorem 4** (Existence, Uniqueness and Explicit Solution). *Let  $I \subseteq \mathbb{R}$  be an open interval and  $a, b : I \rightarrow \mathbb{R}$  be continuous functions. Let further  $x_0, c_0 \in \mathbb{R}$ . Then, the linear first-order initial value problem*

$$f'(x) = a(x)f(x) + b(x), \quad x \in I, \quad f(x_0) = c_0 \quad (\text{B.4})$$

has a unique solution which is explicitly given by

$$f(x) = c_0 \exp\left(\int_{x_0}^x a(\tau) d\tau\right) + \int_{x_0}^x b(\sigma) \exp\left(\int_{\sigma}^x a(\tau) d\tau\right) d\sigma. \quad (\text{B.5})$$

*Proof.* Without explicit constants and explicit integral borders in (B.5) this theorem can be found in several textbooks (cf. e.g. [Nag2011, Theorem 1 on page 51]). The validity of (B.5) can easily be checked by substituting it into (B.4).  $\square$

## B.3 Sphere Parametrization with Arbitrary Orientation

The standard parametrization  $\Phi$  of the sphere  $\mathbb{S}^2$  as provided in Remark 10 on page 39 is given by

$$\Phi : (0, 2\pi) \times (0, \pi) \rightarrow \mathbb{S}^2, \quad (\varphi, \theta) \mapsto \begin{pmatrix} \sin(\theta) \cos(\varphi) \\ \sin(\theta) \sin(\varphi) \\ \cos(\theta) \end{pmatrix}.$$

In this parametrization, the north pole  $\Phi(0, 0)$  is given by  $(0, 0, 1)^T$ . In many applications, such as the parametrization of a rotated hemisphere or for the use as parametrization in a surface integral, a sphere parametrization may be required which provides an arbitrary orientation. This is explicitly discussed in the following.

Let  $\sigma \in \mathbb{S}^2 \setminus \{(0, 0, 1)^T, (0, 0, -1)^T\}$ . To obtain a parametrization  $\Phi_\sigma$  with north pole  $\Phi_\sigma(0, 0) = \sigma$ , the standard parametrization is rotated with the help of Rodrigues' rotation formula (cf. e.g. [Dai2015, (11)]). The rotation axis is given through the normal vector

$$\nu = \frac{(0 \ 0 \ 1)^T \times \sigma}{|(0 \ 0 \ 1)^T \times \sigma|} = \frac{1}{\sqrt{\sigma^1 \sigma^1 + \sigma^2 \sigma^2}} \begin{pmatrix} -\sigma^2 \\ \sigma^1 \\ 0 \end{pmatrix},$$

and the rotation angle  $\hat{\theta} \in [0, \pi]$  is represented by its cosine  $\mu$

$$\mu := \cos(\hat{\theta}) = \left\langle \begin{pmatrix} 0 \\ 0 \\ 1 \end{pmatrix}, \sigma \right\rangle = \sigma^3, \quad \sqrt{1 - \mu^2} \stackrel{\hat{\theta} \in [0, \pi]}{=} \sin(\hat{\theta}).$$

The rotation formula yields

$$\Phi_\sigma = \mu\Phi + \sqrt{1-\mu^2}\nu \times \Phi + (1-\mu)\langle \nu, \Phi \rangle \nu,$$

and therefore

$$\Phi_\sigma = \frac{1}{\sigma^1\sigma^1 + \sigma^2\sigma^2} \begin{pmatrix} \mu(\sigma^1\sigma^1 + \sigma^2\sigma^2)\Phi^1 + \sqrt{1-\mu^2}\sqrt{\sigma^1\sigma^1 + \sigma^2\sigma^2}\sigma^1\Phi^3 - (1-\mu)\sigma^2(-\sigma^2\Phi^1 + \sigma^1\Phi^2) \\ \mu(\sigma^1\sigma^1 + \sigma^2\sigma^2)\Phi^2 + \sqrt{1-\mu^2}\sqrt{\sigma^1\sigma^1 + \sigma^2\sigma^2}\sigma^2\Phi^3 + (1-\mu)\sigma^1(-\sigma^2\Phi^1 + \sigma^1\Phi^2) \\ \mu(\sigma^1\sigma^1 + \sigma^2\sigma^2)\Phi^3 - \sqrt{1-\mu^2}\sqrt{\sigma^1\sigma^1 + \sigma^2\sigma^2}(\sigma^2\Phi^2 + \sigma^1\Phi^1) \end{pmatrix}.$$

Together with

$$\sqrt{\sigma^1\sigma^1 + \sigma^2\sigma^2} = \sqrt{1 - \sigma^3\sigma^3} = \sqrt{1 - \mu^2} \quad \text{and} \quad \frac{1-\mu}{1-\mu^2} = \frac{1}{1+\mu}$$

this leads to

$$\Phi_\sigma = \begin{pmatrix} \sigma^1\Phi^3 + \sigma^3\Phi^1 - \frac{1}{1+\mu}\sigma^2(-\sigma^2\Phi^1 + \sigma^1\Phi^2) \\ \sigma^2\Phi^3 + \sigma^3\Phi^2 + \frac{1}{1+\mu}\sigma^1(-\sigma^2\Phi^1 + \sigma^1\Phi^2) \\ \sigma^3\Phi^3 - \sigma^2\Phi^2 - \sigma^1\Phi^1 \end{pmatrix}. \quad (\text{B.6})$$

Treating 0/0 as 0, the parametrization (B.6) even works in the trivial cases

$$\sigma \in \{(0, 0, 1)^T, (0, 0, -1)^T\}.$$

The corresponding rotation matrix is given by

$$\begin{aligned} R_\sigma &= \begin{pmatrix} \sigma^3 + \frac{1}{1+\mu}\sigma^2\sigma^2 & -\frac{1}{1+\mu}\sigma^1\sigma^2 & \sigma^1 \\ -\frac{1}{1+\mu}\sigma^1\sigma^2 & \sigma^3 + \frac{1}{1+\mu}\sigma^1\sigma^1 & \sigma^2 \\ -\sigma^1 & -\sigma^2 & \sigma^3 \end{pmatrix} \in \text{SO}(3) \\ &= \begin{pmatrix} \sigma^3 & 0 & \sigma^1 \\ 0 & \sigma^3 & \sigma^2 \\ -\sigma^1 & -\sigma^2 & \sigma^3 \end{pmatrix} + \frac{1}{1+\mu} \begin{pmatrix} \sigma^2\sigma^2 & -\sigma^1\sigma^2 & 0 \\ -\sigma^1\sigma^2 & \sigma^1\sigma^1 & 0 \\ 0 & 0 & 0 \end{pmatrix} \end{aligned} \quad (\text{B.7})$$

One should note that for  $\sigma = (0, 0, -1)^T$  the matrix  $R_\sigma$  is formally not a rotation matrix, since  $\det(R_\sigma) = -1$ . Due to the hairy ball theorem this cannot be avoided in a closed formulation (cf. discussion in Remark 12 on page 41).

One special property of the rotated parametrization can be found in its relation to  $\sigma$ :

$$\begin{aligned} \langle \Phi_\sigma, \sigma \rangle &= \sigma^1\sigma^1\Phi^3 + \sigma^1\sigma^3\Phi^1 - \frac{1}{1+\mu}\sigma^1\sigma^2(-\sigma^2\Phi^1 + \sigma^1\Phi^2) \\ &\quad + \sigma^2\sigma^2\Phi^3 + \sigma^2\sigma^3\Phi^2 + \frac{1}{1+\mu}\sigma^2\sigma^1(-\sigma^2\Phi^1 + \sigma^1\Phi^2) \\ &\quad + \sigma^3\sigma^3\Phi^3 - \sigma^3\sigma^2\Phi^2 - \sigma^3\sigma^1\Phi^1 \\ &= (\sigma^1\sigma^1 + \sigma^2\sigma^2 + \sigma^3\sigma^3)\Phi^3 = \Phi^3 = \cos(\theta), \end{aligned}$$

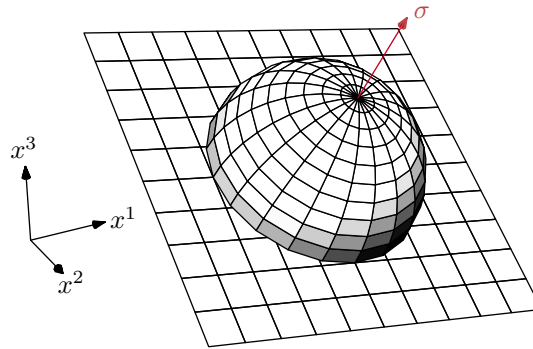


Figure B.1: Example for a (translated) hemisphere with an arbitrary north pole  $\sigma$ .

which can directly be derived from  $R_\sigma^{-1}$ 's orthogonality

$$\langle \Phi_\sigma, \sigma \rangle = \langle R_\sigma \Phi, \sigma \rangle = \langle R_\sigma^{-1} R_\sigma \Phi, R_\sigma^{-1} \sigma \rangle = \left\langle \Phi, \begin{pmatrix} 0 \\ 0 \\ 1 \end{pmatrix} \right\rangle = \cos(\theta). \quad (\text{B.8})$$

It also holds that

$$\left| \frac{\partial \Phi_\sigma}{\partial \varphi} \times \frac{\partial \Phi_\sigma}{\partial \theta} \right| = \left| R_\sigma \frac{\partial \Phi}{\partial \varphi} \times R_\sigma \frac{\partial \Phi}{\partial \theta} \right| = \left| \frac{\partial \Phi}{\partial \varphi} \times \frac{\partial \Phi}{\partial \theta} \right| = \sin(\theta). \quad (\text{B.9})$$



---

## Appendix C. Fast Noise Variance Estimation on Smooth Signals

Given a number of independent samples of the same stochastic process, it is well known from elementary statistics how to estimate their first and second moments in terms of sample mean and sample (co)variance (*cf. e.g.* [Was2004]). However, in order to estimate the noise's variance from samples of a non-constant noisy signal this estimation method cannot be applied. The most commonly used approaches for noise variance estimation are based on denoising (*e.g.* by fitting splines to the data, *cf. e.g.* Sec. 8.5). Thereby, the noise variance can be estimated directly from the difference of the noisy and noise-free signal (*cf. e.g.* [Gar2013]).

Here, a much faster and easy-to-implement method for the case of a 1-dimensional underlying deterministic signal is proposed. With the help of a rough a-priori knowledge regarding the signal's smoothness, it is possible to obtain certain bounds on the estimation error.

Let  $f \in C^1([a, b])$  be a  $C^1$ -smooth function over an interval  $[a, b]$ . Further let  $N \in \mathbb{N}$ , and  $x_1 < \dots < x_N \in [a, b]$ , and  $Y_1, \dots, Y_N$  i.i.d. random variables, where  $E(Y_n) = 0$  and  $\sigma^2 := E(Y_n^2) < \infty$  and finite 3<sup>rd</sup> and 4<sup>th</sup> central moments  $\mu_3 := E(Y_n^3) < \infty$  and  $\mu_4 := E(Y_n^4) < \infty$ . The noisy data points are given by  $(x_n, y_n)$ , where

$$y_n = f(x_n) + Y_n, \quad n = 1, \dots, N.$$

The basic idea is to find a relation between the sample noise variance of  $y_n - f(x_n)$  and the sum of squared neighbor differences of the  $y_n$ s, which itself is a combined random variable. This

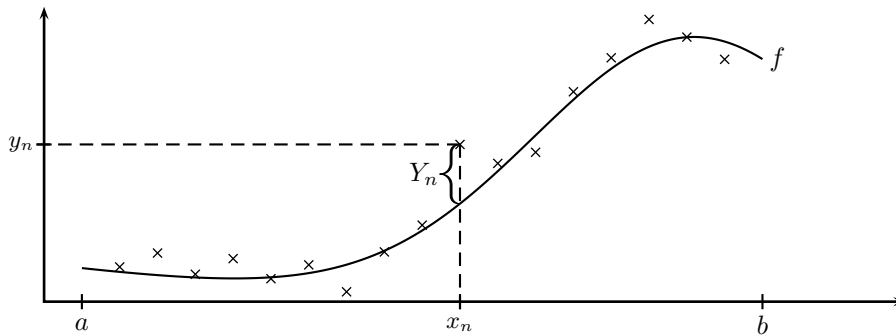


Figure C.1: A smooth deterministic signal  $f$  is sampled with additive i.i.d. noise.

reveals a way to access the noise variance without exactly knowing  $f$ :

$$\begin{aligned}
\sum_{n=1}^{N-1} (y_n - y_{n+1})^2 &= \sum_{n=1}^{N-1} ([y_n - f(x_n)] + [f(x_n) - f(x_{n+1})] + [f(x_{n+1}) - y_{n+1}])^2 \\
&= \sum_{n=1}^{N-1} (y_n - f(x_n))^2 + \sum_{n=1}^{N-1} (f(x_n) - f(x_{n+1}))^2 + \sum_{n=1}^{N-1} (f(x_{n+1}) - y_{n+1})^2 \\
&\quad + 2 \sum_{n=1}^{N-1} (y_n - f(x_n)) (f(x_n) - f(x_{n+1})) \\
&\quad + 2 \sum_{n=1}^{N-1} (y_n - f(x_n)) (f(x_{n+1}) - y_{n+1}) \\
&\quad + 2 \sum_{n=1}^{N-1} (f(x_n) - f(x_{n+1})) (f(x_{n+1}) - y_{n+1}) \\
&= \sum_{n=1}^{N-1} (y_n - f(x_n))^2 + \sum_{n=1}^{N-1} (f(x_n) - f(x_{n+1}))^2 + \sum_{n=1}^{N-1} (f(x_{n+1}) - y_{n+1})^2 \\
&\quad + 2 \sum_{n=1}^{N-1} ([y_n - y_{n+1}] + [f(x_{n+1}) - f(x_n)]) (f(x_n) - f(x_{n+1})) \\
&\quad + 2 \sum_{n=1}^{N-1} (y_n - f(x_n)) (f(x_{n+1}) - y_{n+1}) \\
&= \sum_{n=1}^{N-1} (y_n - f(x_n))^2 + \sum_{n=1}^{N-1} (y_{n+1} - f(x_{n+1}))^2 - \sum_{n=1}^{N-1} (f(x_n) - f(x_{n+1}))^2 \\
&\quad + 2 \sum_{n=1}^{N-1} (y_n - y_{n+1}) (f(x_n) - f(x_{n+1})) \\
&\quad - 2 \sum_{n=1}^{N-1} (y_n - f(x_n)) (y_{n+1} - f(x_{n+1}))
\end{aligned}$$

The non-deterministic terms on the RHS can be treated as new random variables  $Z_1, Z_2, Z_3$ :

$$\begin{aligned}
Z_1 &:= \sum_{n=1}^{N-1} (y_n - f(x_n))^2, \\
Z_2 &:= \sum_{n=1}^{N-1} (y_n - f(x_n)) (y_{n+1} - f(x_{n+1})), \\
Z_3 &:= \sum_{n=1}^{N-1} (y_n - y_{n+1}) (f(x_n) - f(x_{n+1})).
\end{aligned}$$

For  $Z_1$ , one has

$$\begin{aligned}
\mathbb{E}(Z_1) &= \sum_{n=1}^{N-1} \mathbb{E} \left( (y_n - f(x_n))^2 \right) = \sum_{n=1}^{N-1} \mathbb{E}(Y_n^2) = (N-1)\sigma^2, \\
\text{Var}(Z_1) &= \mathbb{E} \left( \left( \sum_{n=1}^{N-1} (y_n - f(x_n))^2 - (N-1)\sigma^2 \right)^2 \right) \\
&= \mathbb{E} \left( \left( \sum_{n=1}^{N-1} (y_n - f(x_n))^2 \right)^2 \right) \\
&\quad - 2(N-1)\sigma^2 \underbrace{\mathbb{E} \left( \sum_{n=1}^{N-1} (y_n - f(x_n))^2 \right)}_{(N-1)\sigma^2} + (N-1)^2\sigma^4 \\
&= \sum_{n'=1}^{N-1} \sum_{n=1}^{N-1} \mathbb{E} \left( (y_n - f(x_n))^2 (y_{n'} - f(x_{n'}))^2 \right) - (N-1)^2\sigma^4 \\
&= 2 \sum_{n'=1}^{N-1} \sum_{n=n'+1}^{N-1} \mathbb{E} \left( (y_n - f(x_n))^2 \right) \mathbb{E} \left( (y_{n'} - f(x_{n'}))^2 \right) \\
&\quad + \sum_{n=1}^{N-1} \mathbb{E} \left( (y_n - f(x_n))^4 \right) - (N-1)^2\sigma^4 \\
&= (N-1)(N-2)\sigma^4 + \sum_{n=1}^{N-1} \mathbb{E} \left( (y_n - f(x_n))^4 \right) - (N-1)^2\sigma^4 \\
&= \sum_{n=1}^{N-1} \underbrace{\mathbb{E} \left( (y_n - f(x_n))^4 \right)}_{4^{\text{th}} \text{ central moment } \mu_4} - (N-1)\sigma^4 = (N-1)(\mu_4 - \sigma^4).
\end{aligned}$$

Having the independence of the  $Y_n$  in mind, the second random variable  $Z_2$  can be evaluated quite simply:

$$\begin{aligned}
\mathbb{E}(Z_2) &= \mathbb{E} \left( \sum_{n=1}^{N-1} (y_n - f(x_n))(y_{n+1} - f(x_{n+1})) \right) = \sum_{n=1}^{N-1} \mathbb{E}(Y_n) \mathbb{E}(Y_{n+1}) = 0, \\
\text{Var}(Z_2) &= \mathbb{E} \left( \left( \sum_{n=1}^{N-1} (y_n - f(x_n))(y_{n+1} - f(x_{n+1})) \right)^2 \right) = \mathbb{E} \left( \sum_{n'=1}^{N-1} \sum_{n=1}^{N-1} Y_n Y_{n+1} Y_{n'} Y_{n'+1} \right) \\
&= \sum_{n=1}^{N-1} \mathbb{E}(Y_n^2) \mathbb{E}(Y_{n+1}^2) = (N-1)\sigma^4.
\end{aligned}$$

The third random variable  $Z_3$  gives

$$\begin{aligned}
\mathbb{E}(Z_3) &= \sum_{n=1}^{N-1} (f(x_n) - f(x_{n+1})) \mathbb{E}((y_n - y_{n+1})) = \sum_{n=1}^{N-1} (f(x_n) - f(x_{n+1}))^2 \\
\text{Var}(Z_3) &= \mathbb{E} \left( \left( \sum_{n=1}^{N-1} (y_n - y_{n+1}) (f(x_n) - f(x_{n+1})) - \sum_{n=1}^{N-1} (f(x_n) - f(x_{n+1}))^2 \right)^2 \right) \\
&= \mathbb{E} \left( \left( \sum_{n=1}^{N-1} (Y_n - Y_{n+1}) (f(x_n) - f(x_{n+1})) \right)^2 \right) \\
&= \sum_{n=1}^{N-1} \sum_{n'=1}^{N-1} \mathbb{E}((Y_n - Y_{n+1})(Y_{n'} - Y_{n'+1})) (f(x_n) - f(x_{n+1}))(f(x_{n'}) - f(x_{n'+1})) \\
&= \sum_{n=1}^{N-1} \mathbb{E}((Y_n - Y_{n+1})^2) (f(x_n) - f(x_{n+1}))^2 \\
&\quad + \sum_{n=1}^{N-2} \mathbb{E}((Y_n - Y_{n+1})(Y_{n+1} - Y_{n+2})) (f(x_n) - f(x_{n+1}))(f(x_{n+1}) - f(x_{n+2})) \\
&\quad + \sum_{n=2}^{N-1} \mathbb{E}((Y_n - Y_{n+1})(Y_{n-1} - Y_n)) (f(x_n) - f(x_{n+1}))(f(x_{n-1}) - f(x_n)) \\
&= \sum_{n=1}^{N-1} (\mathbb{E}(Y_n^2) + \mathbb{E}(Y_{n+1}^2)) (f(x_n) - f(x_{n+1}))^2 \\
&\quad - 2 \sum_{n=1}^{N-2} \mathbb{E}(Y_{n+1}^2) (f(x_n) - f(x_{n+1}))(f(x_{n+1}) - f(x_{n+2})) \\
&= 2\sigma^2 \sum_{n=1}^{N-1} (f(x_n) - f(x_{n+1}))^2 - 2\sigma^2 \sum_{n=1}^{N-2} (f(x_n) - f(x_{n+1}))(f(x_{n+1}) - f(x_{n+2})).
\end{aligned}$$

Defining a summarizing random variable based on the appropriately scaled sum of squared neighbor differences

$$Z := \frac{1}{2(N-1)} \sum_{n=1}^{N-1} (y_n - y_{n+1})^2,$$

and combining the overall information reveals the  $\sigma^2$ -estimation capabilities of  $Z$ :

$$\begin{aligned}
\mathbb{E}(Z) &= \frac{1}{2(N-1)} \left[ 2\mathbb{E}(Z_1) - 2\mathbb{E}(Z_2) + 2\mathbb{E}(Z_3) - \sum_{n=1}^{N-1} (f(x_n) - f(x_{n+1}))^2 \right] \\
&= \sigma^2 + \frac{1}{2(N-1)} \sum_{n=1}^{N-1} (f(x_n) - f(x_{n+1}))^2
\end{aligned}$$

$$\begin{aligned}
\text{Var}(Z) &= \mathbb{E} \left( \left( \frac{1}{2(N-1)} \sum_{n=1}^{N-1} (y_n - y_{n+1})^2 \right. \right. \\
&\quad \left. \left. - \sigma^2 - \frac{1}{2(N-1)} \sum_{n=1}^{N-1} (f(x_n) - f(x_{n+1}))^2 \right)^2 \right), \\
&= \mathbb{E} \left( \left( \frac{1}{2(N-1)} \left[ \sum_{n=1}^{N-1} (y_n - f(x_n))^2 - 2 \sum_{n=1}^{N-1} (f(x_n) - f(x_{n+1}))^2 \right. \right. \right. \\
&\quad \left. \left. + \sum_{n=1}^{N-1} (y_{n+1} - f(x_{n+1}))^2 \right. \right. \\
&\quad \left. \left. + 2 \sum_{n=1}^{N-1} (y_n - y_{n+1})(f(x_n) - f(x_{n+1})) \right. \right. \\
&\quad \left. \left. - 2 \sum_{n=1}^{N-1} (y_n - f(x_n))(y_{n+1} - f(x_{n+1})) \right] - \sigma^2 \right)^2 \right) \\
&= \mathbb{E} \left( \left( \frac{1}{2} \left[ \frac{1}{N-1} \sum_{n=1}^{N-1} (y_n - f(x_n))^2 - \sigma^2 \right] \right. \right. \\
&\quad \left. \left. + \frac{1}{2} \left[ \frac{1}{N-1} \sum_{n=1}^{N-1} (y_{n+1} - f(x_{n+1}))^2 - \sigma^2 \right] \right. \right. \\
&\quad \left. \left. + \frac{1}{N-1} \left[ \sum_{n=1}^{N-1} (y_n - y_{n+1})(f(x_n) - f(x_{n+1})) - \sum_{n=1}^{N-1} (f(x_n) - f(x_{n+1}))^2 \right] \right. \right. \\
&\quad \left. \left. - \frac{1}{N-1} \left[ \sum_{n=1}^{N-1} (y_n - f(x_n))(y_{n+1} - f(x_{n+1})) \right] \right)^2 \right) \\
&= \frac{1}{2} \text{Var} \left( \frac{Z_1}{N-1} \right) + \text{Var} \left( \frac{Z_2}{N-1} \right) + \text{Var} \left( \frac{Z_3}{N-1} \right) \\
&\quad + \frac{1}{2} \mathbb{E} \left( \left[ \frac{1}{N-1} \sum_{n=1}^{N-1} Y_n^2 - \sigma^2 \right] \left[ \frac{1}{N-1} \sum_{n=1}^{N-1} Y_{n+1}^2 - \sigma^2 \right] \right) \\
&\quad + \frac{1}{N-1} \mathbb{E} \left( \left[ \frac{1}{N-1} \sum_{n=1}^{N-1} Y_n^2 - \sigma^2 \right] \left[ \sum_{n=1}^{N-1} (Y_n - Y_{n+1})(f(x_n) - f(x_{n+1})) \right] \right) \\
&\quad - \frac{1}{N-1} \mathbb{E} \left( \left[ \frac{1}{N-1} \sum_{n=1}^{N-1} Y_n^2 - \sigma^2 \right] \left[ \sum_{n=1}^{N-1} Y_n Y_{n+1} \right] \right) \\
&\quad + \frac{1}{N-1} \mathbb{E} \left( \left[ \frac{1}{N-1} \sum_{n=1}^{N-1} Y_{n+1}^2 - \sigma^2 \right] \left[ \sum_{n=1}^{N-1} (Y_n - Y_{n+1})(f(x_n) - f(x_{n+1})) \right] \right) \\
&\quad - \frac{1}{N-1} \mathbb{E} \left( \left[ \frac{1}{N-1} \sum_{n=1}^{N-1} Y_{n+1}^2 - \sigma^2 \right] \left[ \sum_{n=1}^{N-1} Y_n Y_{n+1} \right] \right) \\
&\quad - \frac{2}{(N-1)^2} \mathbb{E} \left( \left[ \sum_{n=1}^{N-1} (Y_n - Y_{n+1})(f(x_n) - f(x_{n+1})) \right] \left[ \sum_{n=1}^{N-1} Y_n Y_{n+1} \right] \right)
\end{aligned}$$

$$\begin{aligned}
&= \frac{1}{2} \text{Var} \left( \frac{Z_1}{N-1} \right) + \text{Var} \left( \frac{Z_2}{N-1} \right) + \text{Var} \left( \frac{Z_3}{N-1} \right) \\
&\quad + \frac{1}{2(N-1)^2} \sum_{n'=1}^{N-1} \sum_{n=1}^{N-1} \text{E} \left( (Y_{n'}^2 - \sigma^2)(Y_{n+1}^2 - \sigma^2) \right) \\
&\quad + \frac{1}{(N-1)^2} \sum_{n'=1}^{N-1} \sum_{n=1}^{N-1} (f(x_n) - f(x_{n+1})) \text{E} \left( (Y_{n'}^2 - \sigma^2)(Y_n - Y_{n+1}) \right) \\
&\quad - \frac{1}{(N-1)^2} \sum_{n'=1}^{N-1} \sum_{n=1}^{N-1} \text{E} \left( (Y_{n'}^2 - \sigma^2)Y_n Y_{n+1} \right) \\
&\quad + \frac{1}{(N-1)^2} \sum_{n'=1}^{N-1} \sum_{n=1}^{N-1} (f(x_n) - f(x_{n+1})) \text{E} \left( (Y_{n'+1}^2 - \sigma^2)(Y_n - Y_{n+1}) \right) \\
&\quad - \frac{1}{(N-1)^2} \sum_{n'=1}^{N-1} \sum_{n=1}^{N-1} \text{E} \left( (Y_{n'+1}^2 - \sigma^2)Y_n Y_{n+1} \right) \\
&\quad - \frac{2}{(N-1)^2} \sum_{n'=1}^{N-1} \sum_{n=1}^{N-1} (f(x_n) - f(x_{n+1})) \text{E} \left( (Y_n - Y_{n+1})Y_{n'} Y_{n'+1} \right) \\
&= \frac{1}{2} \text{Var} \left( \frac{Z_1}{N-1} \right) + \text{Var} \left( \frac{Z_2}{N-1} \right) + \text{Var} \left( \frac{Z_3}{N-1} \right) \\
&\quad + \frac{1}{2(N-1)^2} \sum_{n'=1}^{N-1} \sum_{n=1}^{N-1} [\text{E} (Y_{n'}^2 Y_{n+1}^2) - \sigma^2 \text{E} (Y_{n'}^2) - \sigma^2 \text{E} (Y_{n+1}^2) + \sigma^4] \\
&\quad + \frac{1}{(N-1)^2} \sum_{n=1}^{N-1} (f(x_n) - f(x_{n+1})) \text{E} \left( (Y_n^2 - \sigma^2)Y_n \right) \\
&\quad - \frac{1}{(N-1)^2} \sum_{n=1}^{N-2} (f(x_n) - f(x_{n+1})) \text{E} \left( (Y_{n+1}^2 - \sigma^2)Y_{n+1} \right) \\
&\quad - \frac{1}{(N-1)^2} \sum_{n=1}^{N-1} (f(x_n) - f(x_{n+1})) \text{E} \left( (Y_{n+1}^2 - \sigma^2)Y_{n+1} \right) \\
&\quad + \frac{1}{(N-1)^2} \sum_{n=2}^{N-1} (f(x_n) - f(x_{n+1})) \text{E} \left( (Y_n^2 - \sigma^2)Y_n \right) \\
&= \frac{1}{2} \text{Var} \left( \frac{Z_1}{N-1} \right) + \text{Var} \left( \frac{Z_2}{N-1} \right) + \text{Var} \left( \frac{Z_3}{N-1} \right) \\
&\quad + \frac{1}{2(N-1)^2} \sum_{n=2}^{N-1} (\mu_4 - \sigma^4) \\
&\quad + \frac{1}{(N-1)^2} (f(x_{N-1}) - f(x_N) + f(x_2) - f(x_1)) \mu_3
\end{aligned}$$

$$\begin{aligned}
&= \frac{1}{2} \frac{\mu_4 - \sigma^4}{N-1} + \frac{\sigma^4}{N-1} + \frac{(N-2)(\mu_4 - \sigma^4)}{2(N-1)^2} \\
&\quad + \frac{2\sigma^2}{(N-1)^2} \sum_{n=1}^{N-1} (f(x_n) - f(x_{n+1}))^2 \\
&\quad - \frac{2\sigma^2}{(N-1)^2} \sum_{n=1}^{N-2} (f(x_n) - f(x_{n+1}))(f(x_{n+1}) - f(x_{n+2})) \\
&\quad + \frac{\mu_3}{(N-1)^2} (f(x_{N-1}) - f(x_N) + f(x_2) - f(x_1)) \\
&= \frac{\mu_4}{N-1} - \frac{1}{2} \frac{\mu_4 - \sigma^4}{(N-1)^2} + \frac{2\sigma^2}{(N-1)^2} \sum_{n=1}^{N-1} (f(x_n) - f(x_{n+1}))^2 \\
&\quad - \frac{2\sigma^2}{(N-1)^2} \sum_{n=1}^{N-2} (f(x_n) - f(x_{n+1}))(f(x_{n+1}) - f(x_{n+2})) \\
&\quad + \frac{\mu_3}{(N-1)^2} (f(x_{N-1}) - f(x_N) + f(x_2) - f(x_1)).
\end{aligned}$$

The following theorem summarizes the new estimation method:

**Theorem 5** (Noise Variance Estimation by Squared Neighbor Differences (SND)). *Let  $f$  be a function over an interval  $[a, b]$ . Further let  $N \in \mathbb{N}$ , and  $x_1 < \dots < x_N \in [a, b]$ , and  $Y_1, \dots, Y_N$  i.i.d. random variables, where  $\mathbb{E}(Y_n) = 0$  and  $\sigma^2 := \mathbb{E}(Y_n^2) < \infty$  and finite 3<sup>rd</sup> and 4<sup>th</sup> central moments  $\mu_3 := \mathbb{E}(Y_n^3) < \infty$  and  $\mu_4 := \mathbb{E}(Y_n^4) < \infty$ .  $(x_n, y_n)$  shall denote noisy data points, where*

$$y_n = f(x_n) + Y_n, \quad n = 1, \dots, N.$$

Let  $Z$  denote the scaled sum over squared neighbor differences between the mean-shifted random variables  $y_n$ , namely

$$Z = \frac{1}{2(N-1)} \sum_{n=1}^{N-1} (y_n - y_{n+1})^2.$$

Then, the realization of  $Z$  approximates the variance of  $Y_n$  in the following sense:

(a) The expected value of  $Z$  is given by

$$\mathbb{E}(Z) = \sigma^2 + \frac{1}{2(N-1)} \sum_{n=1}^{N-1} (f(x_n) - f(x_{n+1}))^2.$$

(b) The variance of  $Z$  is given by

$$\begin{aligned}
\text{Var}(Z) &= \frac{\mu_4}{N-1} - \frac{1}{2} \frac{\mu_4 - \sigma^4}{(N-1)^2} + \frac{2\sigma^2}{(N-1)^2} \sum_{n=1}^{N-1} (f(x_n) - f(x_{n+1}))^2 \\
&\quad - \frac{2\sigma^2}{(N-1)^2} \sum_{n=1}^{N-2} (f(x_n) - f(x_{n+1}))(f(x_{n+1}) - f(x_{n+2})) \\
&\quad + \frac{\mu_3}{(N-1)^2} (f(x_{N-1}) - f(x_N) + f(x_2) - f(x_1)).
\end{aligned}$$

(c) In the case of normally distributed  $Y_n$  the variance can be further evaluated:

$$\begin{aligned} \text{Var}(Z) &= \frac{3\sigma^4}{N-1} - \frac{\sigma^4}{(N-1)^2} + \frac{2\sigma^2}{(N-1)^2} \sum_{n=1}^{N-1} (f(x_n) - f(x_{n+1}))^2 \\ &\quad - \frac{2\sigma^2}{(N-1)^2} \sum_{n=1}^{N-2} (f(x_n) - f(x_{n+1}))(f(x_{n+1}) - f(x_{n+2})). \end{aligned}$$

(d) If  $f \in C^1([a, b])$ , upper bounds on the error terms can be found:

$$\frac{1}{N-1} \sum_{n=1}^{N-1} (f(x_n) - f(x_{n+1}))^2 \leq \frac{h^2}{N-1} \sum_{n=1}^{N-1} \max_{[x_n, x_{n+1}]} |f'|^2 \leq h^2 \max_{[a, b]} |f'|^2,$$

and

$$\begin{aligned} \frac{1}{N-2} \left| \sum_{n=1}^{N-2} (f(x_n) - f(x_{n+1}))(f(x_{n+1}) - f(x_{n+2})) \right| &\leq \frac{h^2}{N-2} \sum_{n=1}^{N-2} \max_{[x_n, x_{n+2}]} |f'|^2 \\ &\leq h^2 \max_{[a, b]} |f'|^2, \end{aligned}$$

where  $|x_n - x_{n+1}| \leq h, \forall n \in \{1, \dots, N-1\}$ .

(e) If  $f \in C^1([a, b])$ , the variance of  $Z$  decreases w.r.t. to the number of data points, namely

$$\text{Var}(Z) \rightarrow 0, \quad \text{for } N \rightarrow \infty.$$

Together with Chebychev's inequality (cf. e.g. [Was2004]) this yields convergence of  $Z$  in probability to its expected value.

*Proof.* (a) and (b) have been proved previously.

(c) This directly follows from the central moments for zero-mean normally distributed random variables,  $\mu_3 = 0, \mu_4 = 3\sigma^4$ .

(d) According to the mean value theorem, there exist  $\hat{x}_n \in (x_n, x_{n+1})$ , s.t.

$$\frac{1}{N-1} \sum_{n=1}^{N-1} (f(x_n) - f(x_{n+1}))^2 = \frac{1}{N-1} \sum_{n=1}^{N-1} (x_{n+1} - x_n)^2 f'(\hat{x}_n)^2.$$

The upper bounds follow immediately.

(e) Since  $[a, b] \subset \mathbb{R}$  is compact and  $f \in C^1([a, b])$ , one can find an  $M > 0$ , s.t.  $|f'| < M$  on  $[a, b]$ . With  $h = [a, b]$  it follows from (d)

$$\text{Var}(Z) \leq \frac{\mu_4}{N-1} - \frac{1}{2} \frac{\mu_4 - \sigma^4}{(N-1)^2} + \frac{4\sigma^2(b-a)^2 M^2}{(N-1)} + \frac{2(b-a)M\mu_3}{(N-1)^2} \rightarrow 0, \quad N \rightarrow \infty.$$

□

For evaluation, the proposed SND (Squared Neighbor Differences) approach is compared against

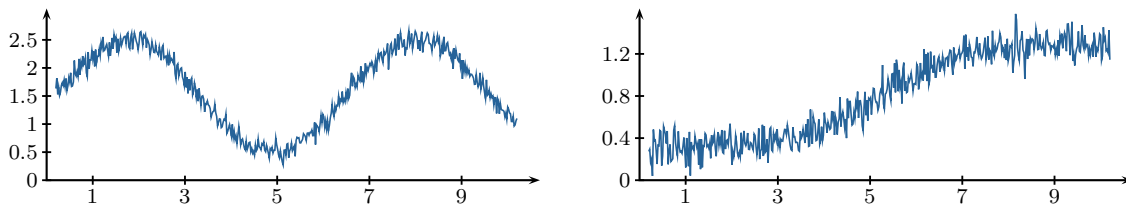


Figure C.2: As input for the algorithm evaluation a sinus curve and a sigmoid curve are disturbed by zero-mean additive Gaussian noise.

$N$	$\sigma^2$	<i>EVAR</i>			<i>SND</i>			<i>perfect</i>		
		comp. time ( $\mu\text{s}$ )	mean error (%)	max error (%)	comp. time ( $\mu\text{s}$ )	mean error (%)	max error (%)	comp. time ( $\mu\text{s}$ )	mean error (%)	max error (%)
10	0.1	1995	4371	5900	2.2	2933	4090	3.6	36.9	239.4
	0.5	2363	160.8	673.8	2.9	119.5	609.7	4.8	37.0	283.8
	1	1978	53.1	391.0	2.1	51.5	393.9	3.4	36.9	252.3
	2	1826	41.2	258.5	2.1	43.9	438.5	3.5	36.3	287.3
100	0.1	1551	21.0	100.0	2.3	27.6	113.4	3.7	11.3	60.6
	0.5	1587	15.8	180.0	2.3	13.8	90.0	3.7	11.2	66.6
	1	1543	21.7	119.4	2.3	13.9	85.6	3.7	11.3	60.5
	2	1571	14.5	97.2	2.3	13.8	77.2	3.9	11.5	58.3
500	0.1	1857	6.9	28.7	3.3	6.2	40.0	5.2	5.1	29.2
	0.5	2165	5.7	26.2	5.0	6.2	36.1	7.0	5.0	27.7
	1	2214	5.5	37.4	4.4	6.2	33.2	7.6	5.1	23.7
	2	1702	5.4	26.4	3.4	6.1	33.1	5.3	5.0	24.8

Table C.1: Comparison of SND (proposed), EVAR ([Gar2013]) and the perfect estimation on the sinus function.

the EVAR algorithm (*cf.* [Gar2013]) and a perfect estimation by ordinary empirical variance estimation assuming the deterministic signal to be known. The deterministic signals  $f$  are chosen to be a sinus curve and a sigmoid function (*cf.* Fig. C.2). Since EVAR relies on Gaussian additive noise and evenly-gridded data, the  $y_n$  are generated according to these requirements. Table C.1 and Table C.2 provide some results of the experiments, taking 10000 tests per configuration into account. While EVAR and SND have similar estimation accuracies and both are even close to the perfect results, the SND computation is more than a factor 500 faster than EVAR and even slightly faster than the perfect estimation (tested in MATLAB [Mat2012]).

The results prove that the proposed SND approach is a considerable alternative to classical noise estimation methods. It is easy to implement, does not restrict to Gaussian noise and is very fast. Drawbacks are the systematical error and the restriction to one dimension. As future work, one can consider introducing a correction term to reduce the bias, and an extension to more than one dimension based on higher-dimensional neighbor differences.

$N$	$\sigma^2$	<i>EVAR</i>			<i>SND</i>			<i>perfect</i>		
		comp. time ( $\mu\text{s}$ )	mean error (%)	max error (%)	comp. time ( $\mu\text{s}$ )	mean error (%)	max error (%)	comp. time ( $\mu\text{s}$ )	mean error (%)	max error (%)
10	0.1	1642	67.7	264.5	2.1	120.1	497.0	3.5	36.6	337.0
	0.5	1590	51.8	288.5	2.0	43.1	363.6	3.4	37.2	282.4
	1	1675	45.7	354.9	2.1	43.9	463.9	3.5	37.2	374.1
	2	1570	42.0	215.1	2.1	43.4	310.6	3.5	37.2	261.3
100	0.1	1620	14.1	88.2	2.2	13.8	81.1	3.7	11.3	63.8
	0.5	1622	13.2	87.9	2.3	13.7	72.7	3.8	11.3	57.9
	1	1669	13.0	98.9	2.4	13.8	75.7	3.9	11.4	63.3
	2	1680	12.3	98.0	2.3	13.8	83.1	3.7	11.1	65.4
500	0.1	1606	5.4	25.1	3.2	6.2	33.4	5.4	5.1	24.0
	0.5	1508	5.3	24.6	3.3	6.2	32.3	5.2	5.1	23.8
	1	1505	5.2	23.5	3.2	6.1	32.4	5.2	5.0	24.1
	2	1558	5.2	23.9	3.3	6.2	31.4	5.3	5.1	23.8

Table C.2: Comparison of SND (proposed), EVAR ([Gar2013]) and the perfect estimation on the sigmoid function.

---

## Appendix D. Proofs from the Analytical Discussion of $\mathcal{F}$

*Proof of Lemma 3 on page 86: Non-Convexity and Non-Coercivity of  $\mathcal{F}$ .*

(a) It is easy to see that for any  $\tilde{L}$  and any  $K \in \mathbb{R}$

$$\mathcal{F}_{c,\tilde{L}}(K) = \sum_{m=1}^M \sum_{n=1}^{N_m} \frac{1}{(\sigma_n^m)^2} (\tilde{L} - L_n^m)^2,$$

since  $\mathcal{L}$  is a convex combination of  $L_{\text{air}}$  and  $L_0$ . Elementary analysis reveals that this term is uniquely minimized in  $\bar{L}$ :

$$\left. \frac{d}{d\tilde{L}} \sum_{m=1}^M \sum_{n=1}^{N_m} \frac{1}{(\sigma_n^m)^2} (\tilde{L} - L_n^m)^2 \right|_{\tilde{L}=\bar{L}} = 2S_1\bar{L} - 2S_L = 2S_1\frac{S_L}{S_1} - 2S_L = 0.$$

Finally, one has

$$\mathcal{F}_c = \sum_{m=1}^M \sum_{n=1}^{N_m} \frac{1}{(\sigma_n^m)^2} (\bar{L} - L_n^m)^2 = \frac{S_L^2}{S_1^2} S_1 - 2\frac{S_L}{S_1} S_L + S_{LL} = S_{LL} - \frac{S_L^2}{S_1}.$$

(b) This directly follows from (a), choosing for instance  $p_n := (K_n, \bar{L}, \dots, \bar{L})$  and  $C := \mathcal{F}_c(0)$ , where  $(K_n)_{n \in \mathbb{N}} \subset \mathbb{R}$  can be chose as an arbitrary sequence that satisfies  $K_n \rightarrow \infty$ , for  $n \rightarrow \infty$ .

(c) Let  $\xi = (1, 0, \dots, 0)^T$ . Let furthermore  $(L_0^1, \dots, L_0^M) \in \mathbb{R}^M$  be an arbitrary set of parameters and  $L_{\text{air}} > \max_{n,m} L_n^m$ . One obviously can find a  $\bar{K} > 0$ , s.t. for any  $K > \bar{K}$

$$\underbrace{2(L_{\text{air}} - L_0^m)e^{-Kd_n^m}}_{\rightarrow 0, \text{ for } K \rightarrow 0} + \underbrace{L_n^m - L_{\text{air}}}_{< 0} < 0.$$

Therefore, for any  $K > \bar{K}$  one has (cf. Lemma 2 on page 84)

$$\begin{aligned} \frac{\partial^2 \mathcal{F}}{\partial K \partial K} &= 2 \sum_{m=1}^M \sum_{n=1}^{N_m} \underbrace{\frac{1}{(\sigma_n^m)^2} (L_{\text{air}} - L_0^m) e^{-Kd_n^m} (d_n^m)^2}_{> 0} \\ &\quad \cdot \underbrace{\left[ 2(L_{\text{air}} - L_0^m) e^{-Kd_n^m} + L_n^m - L_{\text{air}} \right]}_{< 0} < 0. \end{aligned}$$

Hence for  $p = (K, L_{\text{air}}, L_0^1, \dots, L_0^M)$ , where  $K > \bar{K}$ , it holds

$$\xi^T \text{Hess } \mathcal{F}(p) \xi = \frac{\partial^2 \mathcal{F}}{\partial K \partial K}(p) < 0.$$

In particular,  $\mathcal{F}$  is not convex at such a  $p$ .

□

*Proof of Lemma 4 on page 86: Critical Points of  $\mathcal{F}_{f,K}$ .*

**UNIQUE CRITICAL POINT:**  $(L_{\text{air}}, L_0^1, \dots, L_0^M) \in \mathbb{R}^{M+1}$  is (by definition) a critical point of  $\mathcal{F}$  if and only if it solves  $0 = \nabla \mathcal{F}_{f,K} = \nabla_{L_{\text{air}}, L_0^1, \dots, L_0^M} \mathcal{F}$ , which, due to Lemma 2 on page 84, can be written as equation system

$$\begin{aligned} 0 &= 2 \sum_{m=1}^M \sum_{n=1}^{N_m} \frac{1}{(\sigma_n^m)^2} (\mathcal{L} - L_n^m) (1 - e^{-Kd_n^m}), \\ 0 &= 2 \sum_{n=1}^{N_m} \frac{1}{(\sigma_n^m)^2} (\mathcal{L} - L_n^m) e^{-Kd_n^m}, \quad m = 1, \dots, M, \end{aligned}$$

which is equivalent to the system

$$0 = \sum_{m=1}^M \sum_{n=1}^{N_m} \frac{1}{(\sigma_n^m)^2} (\mathcal{L} - L_n^m), \quad 0 = \sum_{n=1}^{N_m} \frac{1}{(\sigma_n^m)^2} (\mathcal{L} - L_n^m) e^{-Kd_n^m}, \quad m = 1, \dots, M.$$

This can be written as linear equation system

$$\begin{pmatrix} S_{\mathcal{L}} \\ S_{\text{Le}}^1 \\ \vdots \\ S_{\text{Le}}^M \end{pmatrix} = \begin{pmatrix} S_{(1-e)} & S_{\text{e}}^1 & \cdots & S_{\text{e}}^M \\ S_{\text{e}(1-e)}^1 & S_{\text{ee}}^1 & & \\ \vdots & & \ddots & \\ S_{\text{e}(1-e)}^M & & & S_{\text{ee}}^M \end{pmatrix} \begin{pmatrix} L_{\text{air}} \\ L_0^1 \\ \vdots \\ L_0^M \end{pmatrix}. \quad (\text{D.1})$$

For any  $m \in \{1, \dots, M\}$ , one has

$$S_{\text{ee}}^m = \sum_{n=1}^{N_m} \frac{1}{(\sigma_n^m)^2} e^{-2Kd_n^m} > 0. \quad (\text{D.2})$$

Since  $d_n^m > 0$  and  $K \neq 0$ , one has

$$S_{(1-e)} = \sum_{m=1}^M \sum_{n=1}^{N_m} \frac{1}{(\sigma_n^m)^2} (1 - e^{-Kd_n^m}) \left\{ \begin{array}{l} > 0, \text{ if } K > 0 \\ < 0, \text{ if } K < 0 \end{array} \right\} \neq 0.$$

Therefore, the rows of the matrix in (D.1) are linearly independent and in turn the system uniquely

solvable. Ignoring the first line, the equation system can be rewritten as

$$\begin{pmatrix} S_{ee}^1 & & \\ & \ddots & \\ & & S_{ee}^M \end{pmatrix} \begin{pmatrix} L_0^1 \\ \vdots \\ L_0^M \end{pmatrix} = \begin{pmatrix} S_{Le}^1 \\ \vdots \\ S_{Le}^M \end{pmatrix} - L_{\text{air}} \begin{pmatrix} S_{e(1-e)}^1 \\ \vdots \\ S_{e(1-e)}^M \end{pmatrix}.$$

Therefore,

$$\forall m \in \{1, \dots, M\} : \quad L_0^m = \frac{S_{Le}^m - L_{\text{air}} S_{e(1-e)}^m}{S_{ee}^m}, \quad (\text{D.3})$$

which can be substituted into the first row of (D.1) to additionally obtain  $L_{\text{air}}$  (in different formulations):

$$\begin{aligned} S_L &= L_{\text{air}} S_{(1-e)} + \sum_{m=1}^M S_e^m L_0^m = L_{\text{air}} S_{(1-e)} + \sum_{m=1}^M S_e^m \frac{S_{Le}^m}{S_{ee}^m} - L_{\text{air}} \sum_{m=1}^M S_e^m \frac{S_{e(1-e)}^m}{S_{ee}^m} \\ \Leftrightarrow L_{\text{air}} &= \frac{S_L - \sum_{m=1}^M \frac{S_e^m S_{Le}^m}{S_{ee}^m}}{S_{(1-e)} - \sum_{m=1}^M \frac{S_e^m S_{e(1-e)}^m}{S_{ee}^m}} \quad \Leftrightarrow \quad L_{\text{air}} = \frac{S_L - \sum_{m=1}^M \frac{S_e^m S_{Le}^m}{S_{ee}^m}}{S_1 - \sum_{m=1}^M \frac{S_e^m S_{e(1-e)}^m}{S_{ee}^m}}. \end{aligned} \quad (\text{D.4})$$

The  $L_0^m$  can be obtained by substituting (D.4) into (D.3):

$$\begin{aligned} L_0^m &= \frac{S_{Le}^m - L_{\text{air}} S_{e(1-e)}^m}{S_{ee}^m} = \frac{S_{Le}^m - \frac{S_L - \sum_{l=1}^M \frac{S_e^l S_{Le}^l}{S_{ee}^l}}{S_1 - \sum_{l=1}^M \frac{S_e^l S_{e(1-e)}^l}{S_{ee}^l}} S_{e(1-e)}^m}{S_{ee}^m} \\ &= \frac{S_{Le}^m \left( S_1 - \sum_{l=1}^M \frac{S_e^l S_{e(1-e)}^l}{S_{ee}^l} \right) - S_{e(1-e)}^m \left( S_L - \sum_{l=1}^M \frac{S_e^l S_{Le}^l}{S_{ee}^l} \right)}{S_1 S_{ee}^m - S_{ee}^m \sum_{l=1}^M \frac{S_e^l S_{e(1-e)}^l}{S_{ee}^l}} \\ &= \frac{S_{Le}^m S_1 - S_{e(1-e)}^m S_L - S_{Le}^m \sum_{l=1}^M \frac{S_e^l S_{e(1-e)}^l}{S_{ee}^l} + S_{e(1-e)}^m \sum_{l=1}^M \frac{S_e^l S_{Le}^l}{S_{ee}^l}}{S_1 S_{ee}^m - S_{ee}^m \sum_{l=1}^M \frac{S_e^l S_{e(1-e)}^l}{S_{ee}^l}} \\ &= \frac{S_{Le}^m S_1 - S_{e(1-e)}^m S_L + \sum_{l=1}^M \frac{S_e^l}{S_{ee}^l} \left[ S_{Le}^l S_{e(1-e)}^m - S_e^l S_{Le}^m \right]}{S_1 S_{ee}^m - S_{ee}^m \sum_{l=1}^M \frac{S_e^l S_{e(1-e)}^l}{S_{ee}^l}}. \end{aligned}$$

*CONVEXITY:* One has (cf. Lemma 2 on page 84)

$$\text{Hess } \mathcal{F}_{f,K} = 2 \begin{pmatrix} S_{(1-e)(1-e)} & S_{e(1-e)}^1 & \cdots & S_{e(1-e)}^M \\ S_{e(1-e)}^1 & S_{ee}^1 & & \\ \vdots & & \ddots & \\ S_{e(1-e)}^M & & & S_{ee}^M \end{pmatrix}.$$

To show the convexity inequality one should have in mind the following estimation:

$$\forall a, b \in \mathbb{R} : \quad a^2 + ab + b^2 = \frac{a^2 + b^2}{2} + \frac{(a+b)^2}{2} \geq \frac{a^2 + b^2}{2}. \quad (\text{D.5})$$

Let now  $\xi = (\xi^1, \dots, \xi^{M+1})^T \in \mathbb{R}^{M+1} \setminus \{0\}$  arbitrary but fixed. From  $K \neq 0$  and (D.5) it follows

$$\begin{aligned}
\xi^T \text{Hess } \mathcal{F}_{f,K} \xi &= 2\xi^1 \xi^1 S_{(1-e)(1-e)} + 2 \sum_{m=1}^M \xi^1 \xi^{m+1} S_{e(1-e)}^m + 2 \sum_{m=1}^M \xi^{m+1} \xi^{m+1} S_{ee}^m \\
&= 2 \sum_{m=1}^M \sum_{n=1}^{N_m} \frac{1}{(\sigma_n^m)^2} \left[ \xi^1 \xi^1 \left(1 - e^{-Kd_n^m}\right)^2 + \xi^{m+1} \xi^{m+1} \left(e^{-Kd_n^m}\right)^2 \right. \\
&\quad \left. + \xi^1 \xi^{m+1} e^{-Kd_n^m} \left(1 - e^{-Kd_n^m}\right) \right] \\
&\geq \sum_{m=1}^M \sum_{n=1}^{N_m} \frac{1}{(\sigma_n^m)^2} \left[ \underbrace{\xi^1 \xi^1 \left(1 - e^{-Kd_n^m}\right)^2}_{>0, \text{ since } Kd_n^m \neq 0} + \xi^{m+1} \xi^{m+1} \underbrace{\left(e^{-Kd_n^m}\right)^2}_{>0} \right] \\
&\geq |\xi|^2 \min_{m \in \{1, \dots, M\}} \min_{n \in \{1, \dots, N_m\}} \frac{1}{(\sigma_n^m)^2} \left\{ \left(1 - e^{-Kd_n^m}\right)^2, \left(e^{-Kd_n^m}\right)^2 \right\} > 0.
\end{aligned}$$

Therefore,  $\mathcal{F}_{f,K}$  is strictly convex and the unique critical point is a minimum.

$K = 0$ : Obviously,  $\mathcal{F}_{f,0}$  is constant in  $L_{\text{air}}$ , since

$$\mathcal{F}_{f,0} = \sum_{m=1}^M \sum_{n=1}^{N_m} \frac{1}{(\sigma_n^m)^2} (L_0^m - L_n^m)^2.$$

The remaining critical point equations in  $L_0^1, \dots, L_0^M$  can once again be written as

$$\begin{pmatrix} S_1^1 & & \\ & \ddots & \\ & & S_1^M \end{pmatrix} \begin{pmatrix} L_0^1 \\ \vdots \\ L_0^M \end{pmatrix} = \begin{pmatrix} S_L^1 \\ \vdots \\ S_L^M \end{pmatrix},$$

which is uniquely solved in  $(\bar{L}^1, \dots, \bar{L}^M)$ , independent of the specific  $L_{\text{air}}$ . Furthermore,  $\mathcal{F}_{f,0}$  is convex (and even strictly convex in  $(L_0^1, \dots, L_0^M)$ ), which implies the unique minimization at the critical line.  $\square$

*Proof of Lemma 5 on page 87: Properties of  $\mathcal{F}_{\min}$ .* The matrix in the linear equation system (D.1), which leads to the definition of  $L_{\text{air},\min}$  and  $L_{0,\min}^m$ , is continuous in  $K$ . Furthermore, Cramer's rule shows that an inverse matrix is a continuous function of the matrix entries. Therefore, on  $\mathbb{R} \setminus \{0\}$  the functions  $L_{\text{air},\min}$  and  $L_{0,\min}^m$  are continuous. So does  $\mathcal{F}_{\min}$  which is a composition of continuous functions now. This partially implies (a). To also show that 0 is a removable discontinuity one has to write out  $\mathcal{F}_{\min}$  in full:

$$\begin{aligned}
\mathcal{F}_{\min} &= \sum_{m=1}^M \sum_{n=1}^{N_m} \frac{1}{(\sigma_n^m)^2} \left( \left(1 - e^{-Kd_n^m}\right) L_{\text{air},\min} + e^{-Kd_n^m} L_{0,\min} - L_n^m \right)^2 \\
&= \sum_{m=1}^M \sum_{n=1}^{N_m} \frac{1}{(\sigma_n^m)^2} \left( \left(1 - e^{-Kd_n^m}\right) L_{\text{air},\min} + e^{-Kd_n^m} \frac{S_{Le}^m - L_{\text{air},\min} S_{e(1-e)}^m}{S_{ee}^m} - L_n^m \right)^2
\end{aligned}$$

$$\begin{aligned}
&= \sum_{m=1}^M \sum_{n=1}^{N_m} \frac{1}{(\sigma_n^m)^2} \left( \left( 1 - e^{-Kd_n^m} - \frac{S_e^m}{S_{ee}^m} e^{-Kd_n^m} \right) L_{\text{air,min}} + e^{-Kd_n^m} \frac{S_{Le}^m}{S_{ee}^m} - L_n^m \right)^2 \\
&= \sum_{m=1}^M \sum_{n=1}^{N_m} \frac{1}{(\sigma_n^m)^2} \left( \left( 1 - \frac{S_e^m}{S_{ee}^m} e^{-Kd_n^m} \right) L_{\text{air,min}} + e^{-Kd_n^m} \frac{S_{Le}^m}{S_{ee}^m} - L_n^m \right)^2 \\
&= L_{\text{air,min}}^2 \sum_{m=1}^M \sum_{n=1}^{N_m} \frac{1}{(\sigma_n^m)^2} \left( 1 - \frac{S_e^m}{S_{ee}^m} e^{-Kd_n^m} \right)^2 \\
&\quad + 2L_{\text{air,min}} \sum_{m=1}^M \sum_{n=1}^{N_m} \frac{1}{(\sigma_n^m)^2} \left( 1 - \frac{S_e^m}{S_{ee}^m} e^{-Kd_n^m} \right) \left( e^{-Kd_n^m} \frac{S_{Le}^m}{S_{ee}^m} - L_n^m \right) \\
&\quad + \sum_{m=1}^M \sum_{n=1}^{N_m} \frac{1}{(\sigma_n^m)^2} \left( e^{-Kd_n^m} \frac{S_{Le}^m}{S_{ee}^m} - L_n^m \right)^2 \\
&= L_{\text{air,min}}^2 \left[ S_1 - 2 \sum_{m=1}^M \frac{S_e^m S_e^m}{S_{ee}^m} + \sum_{m=1}^M \frac{S_e^m S_e^m S_{ee}^m}{S_{ee}^m S_{ee}^m} \right] \\
&\quad + 2L_{\text{air,min}} \left[ \sum_{m=1}^M \frac{S_{Le}^m S_e^m}{S_{ee}^m} - S_L - \sum_{m=1}^M \frac{S_{Le}^m S_e^m S_{ee}^m}{S_{ee}^m S_{ee}^m} + \sum_{m=1}^M \frac{S_{Le}^m S_e^m}{S_{ee}^m} \right] \\
&\quad + \left[ \sum_{m=1}^M \frac{S_{Le}^m S_{Le}^m S_{ee}^m}{S_{ee}^m S_{ee}^m} - 2 \sum_{m=1}^M \frac{S_{Le}^m S_{Le}^m}{S_{ee}^m} + S_{LL} \right] \\
&= L_{\text{air,min}}^2 \left[ S_1 - \sum_{m=1}^M \frac{S_e^m S_e^m}{S_{ee}^m} \right] - 2L_{\text{air,min}} \left[ S_L - \sum_{m=1}^M \frac{S_{Le}^m S_e^m}{S_{ee}^m} \right] + \left[ S_{LL} - \sum_{m=1}^M \frac{S_{Le}^m S_{Le}^m}{S_{ee}^m} \right] \\
&= \left[ S_{LL} - \sum_{m=1}^M \frac{S_{Le}^m S_{Le}^m}{S_{ee}^m} \right] - \frac{\left( S_L - \sum_{m=1}^M \frac{S_e^m S_{Le}^m}{S_{ee}^m} \right)^2}{S_1 - \sum_{m=1}^M \frac{S_e^m S_e^m}{S_{ee}^m}}.
\end{aligned}$$

This not only proves (b) but also allows for a discussion of the discontinuity in 0: In terms of (7.11) and (7.12),  $\mathcal{F}_{\text{min}}$  can be written as

$$\mathcal{F}_{\text{min}} = \left[ S_{LL} - \sum_{m=1}^M \frac{S_{Le}^m S_{Le}^m}{S_{ee}^m} \right] - \frac{(L_{\text{air}}^{\text{num}})^2}{L_{\text{air}}^{\text{denom}}},$$

where  $L_{\text{air}}^{\text{denom}}(0) = 0$  as well as  $L_{\text{air}}^{\text{num}}(0) = 0$ . With the help of Appendix E and constraint (7.13) it can be shown that furthermore

$$L_{\text{air}}^{\text{denom}'}(0) = 0,$$

and

$$L_{\text{air}}^{\text{denom}''}(0) = 2 \sum_{m=1}^M \frac{S_{dd}^m S_1^m - S_d^m S_d^m}{S_1^m} = 2 \left[ S_{dd} - \sum_{m=1}^M \frac{S_d^m S_d^m}{S_1^m} \right]^* > 0.$$

Therefore,  $L_{\text{air}}^{\text{denom}}$  has a double root in 0 and  $(L_{\text{air}}^{\text{num}})^2$  at least a double root in 0, which makes the

discontinuity removable. L'Hôspital's rule even makes it possible to compute  $\mathcal{F}_{\min}(0)$ :

$$\begin{aligned}\mathcal{F}_{\min}(0) &= \left[ S_{LL} - \sum_{m=1}^M \frac{S_L^m S_L^m}{S_1^m} \right] - \frac{[(L_{\text{air}}^{\text{num}})^2]''(0)}{L_{\text{air}}^{\text{denom}''}(0)} \\ &= \left[ S_{LL} - \sum_{m=1}^M \frac{S_L^m S_L^m}{S_1^m} \right] - \frac{\left( S_{Ld} - \sum_{m=1}^M \frac{S_L^m S_d^m}{S_1^m} \right)^2}{S_{dd} - \sum_{m=1}^M \frac{S_d^m S_d^m}{S_1^m}},\end{aligned}$$

where

$$\begin{aligned}[(L_{\text{air}}^{\text{num}})^2]' &= 2L_{\text{air}}^{\text{num}} L_{\text{air}}^{\text{num}'} = 0, \\ [(L_{\text{air}}^{\text{num}})^2]'' &= 2(L_{\text{air}}^{\text{num}'})^2 + 2L_{\text{air}}^{\text{num}} L_{\text{air}}^{\text{num}''}, \\ [(L_{\text{air}}^{\text{num}})^2]''(0) &= 2(L_{\text{air}}^{\text{num}'(0)})^2 + 0(L_{\text{air}}^{\text{num}''(0)}) \\ &= 2 \left( \sum_{m=1}^M \frac{S_{Ld}^m S_1^m - S_L^m S_d^m}{S_1^m} \right)^2 = 2 \left( S_{Ld} - \sum_{m=1}^M \frac{S_L^m S_d^m}{S_1^m} \right)^2.\end{aligned}$$

*PROOF OF \*:* Based on the Cauchy-Schwarz inequality and (7.13) one can see that

$$S_{dd} - \sum_{m=1}^M \frac{S_d^m S_d^m}{S_1^m} > 0,$$

as described in the following: For each  $m \in \{1, \dots, M\}$  one can rewrite

$$S_{dd}^m S_1^m - S_d^m S_d^m = |a_m|^2 |b_m|^2 - (\langle a_m, b_m \rangle)^2,$$

where

$$a_m = \left( \frac{d_n^m}{\sigma_n^m} \right)_{n=1, \dots, N_m}, \quad b_m = \left( \frac{1}{\sigma_n^m} \right)_{n=1, \dots, N_m}.$$

The Cauchy-Schwarz inequality shows that

$$|a_m|^2 |b_m|^2 - (\langle a_m, b_m \rangle)^2 \geq 0,$$

where the equality is achieved if and only if  $a_m$  and  $b_m$  are linearly dependent. Furthermore, one has  $S_1 > 0$ . Therefore, the term of interest is a sum over non-negative terms:

$$S_{dd} - \sum_{m=1}^M \frac{S_d^m S_d^m}{S_1^m} = \sum_{m=1}^M \underbrace{\frac{S_{dd}^m S_1^m - S_d^m S_d^m}{S_1^m}}_{\geq 0} \geq 0. \quad (\text{D.6})$$

Obviously, the sum is 0 if and only if all summands are 0. Due to Cauchy-Schwarz, this is the case if and only if for each  $m$  the vectors  $a_m$  and  $b_m$  are linearly dependent. This is equivalent to

$$\forall m \in \{1, \dots, M\}, \exists \alpha^m \in \mathbb{R} : d_n^m = \sigma_n^m \left[ \frac{d_n^m}{\sigma_n^m} \right] = \sigma_n^m \left[ \alpha^m \frac{1}{\sigma_n^m} \right] = \alpha^m,$$

which is again equivalent to  $\neg(7.13)$ . Therefore,

$$(7.13) \Leftrightarrow S_{dd} - \sum_{m=1}^M \frac{S_d^m S_d^m}{S_1^m} > 0.$$

*REGARDING (c):* This directly follows from Lemma 3(a) on page 86 and the definition of  $\mathcal{F}_{\min}$ , since for any  $K \in \mathbb{R} \setminus \{0\}$

$$\mathcal{F}_{\min}(K) = \min \{ \mathcal{F}(K, x) : x \in \mathbb{R}^{M+1} \} \leq \mathcal{F}(K, \bar{L}, \dots, \bar{L}) = \mathcal{F}_c(K) = S_{LL} - \frac{S_L^2}{S_1}.$$

*REGARDING (d):* Let  $d_{\min}^m := d_{n_{\min}}^m$  and  $d_{\max}^m := d_{n_{\max}}^m$ . Then, one has

$$\begin{aligned} \frac{S_{Le}^m S_{Le}^m}{S_{ee}^m} &= \frac{\sum_{k=1}^{N_m} \sum_{l=1}^{N_m} \frac{L_k^m L_l^m}{(\sigma_k^m)^2 (\sigma_l^m)^2} e^{-K(d_k^m + d_l^m)}}{\sum_{n=1}^{N_m} \frac{1}{(\sigma_n^m)^2} e^{-2K d_n^m}} \\ &= \frac{\sum_{k=1}^{N_m} \sum_{l=1}^{N_m} \frac{L_k^m L_l^m}{(\sigma_k^m)^2 (\sigma_l^m)^2} e^{-K((d_k^m - d_{\min}^m) + (d_l^m - d_{\min}^m))}}{\sum_{n=1}^{N_m} \frac{1}{(\sigma_n^m)^2} e^{-2K(d_n^m - d_{\min}^m)}}, \end{aligned}$$

where  $d_n^m - d_{\min}^m > 0$  for all  $n \neq n_{\min}^m$  and  $d_n^m - d_{\min}^m = 0$  for  $n = n_{\min}^m$ . Therefore, all but one summands of the numerator and the denominator converge to 0, for  $K \rightarrow \infty$ , more precisely

$$\frac{S_{Le}^m S_{Le}^m}{S_{ee}^m} \rightarrow \frac{\frac{L_{\min}^m L_{\min}^m}{(\sigma_{\min}^m)^2 (\sigma_{\min}^m)^2}}{\frac{1}{(\sigma_{\min}^m)^2}} = \frac{(L_{\min}^m)^2}{(\sigma_{\min}^m)^2}, \quad \text{for } K \rightarrow \infty.$$

Analogously one obtains

$$\begin{aligned} \frac{S_{Le}^m S_{Le}^m}{S_{ee}^m} &\rightarrow \frac{(L_{\min}^m)^2}{(\sigma_{\min}^m)^2}, \quad \text{for } K \rightarrow \infty, & \frac{S_{Le}^m S_{Le}^m}{S_{ee}^m} &\rightarrow \frac{(L_{\max}^m)^2}{(\sigma_{\max}^m)^2}, \quad \text{for } K \rightarrow -\infty, \\ \frac{S_{Le}^m S_e^m}{S_{ee}^m} &\rightarrow \frac{L_{\min}^m}{(\sigma_{\min}^m)^2}, \quad \text{for } K \rightarrow \infty, & \frac{S_{Le}^m S_e^m}{S_{ee}^m} &\rightarrow \frac{L_{\max}^m}{(\sigma_{\max}^m)^2}, \quad \text{for } K \rightarrow -\infty, \\ \frac{S_e^m S_e^m}{S_{ee}^m} &\rightarrow \frac{1}{(\sigma_{\min}^m)^2}, \quad \text{for } K \rightarrow \infty, & \frac{S_e^m S_e^m}{S_{ee}^m} &\rightarrow \frac{1}{(\sigma_{\max}^m)^2}, \quad \text{for } K \rightarrow -\infty. \end{aligned}$$

This implies

$$\begin{aligned} \mathcal{F}_{\min}(K) &\rightarrow \left[ S_{LL} - \sum_{m=1}^M \frac{(L_{\min}^m)^2}{(\sigma_{\min}^m)^2} \right] - \frac{\left( S_L - \sum_{m=1}^M \frac{L_{\min}^m}{(\sigma_{\min}^m)^2} \right)^2}{S_1 - \sum_{m=1}^M \frac{1}{(\sigma_{\min}^m)^2}}, \quad \text{for } K \rightarrow \infty, \\ \mathcal{F}_{\min}(K) &\rightarrow \left[ S_{LL} - \sum_{m=1}^M \frac{(L_{\max}^m)^2}{(\sigma_{\max}^m)^2} \right] - \frac{\left( S_L - \sum_{m=1}^M \frac{L_{\max}^m}{(\sigma_{\max}^m)^2} \right)^2}{S_1 - \sum_{m=1}^M \frac{1}{(\sigma_{\max}^m)^2}}, \quad \text{for } K \rightarrow -\infty. \end{aligned}$$

*REGARDING (e):* Obviously,  $\mathcal{F}_{\min}$ 's formulation in (b) and the discussion above allow to apply Theorem 3 on page 171 (cf. Appendix B), hence  $\mathcal{F}_{\min} \in C^\infty(\mathbb{R})$ . From Lemma 4 on page 86 and

the definition (7.10) one obtains, for any  $K \neq 0$ ,

$$\begin{aligned} \frac{\partial \mathcal{F}}{\partial L_{\text{air}}} (K, L_{\text{air},\min}(K), L_{0,\min}^1(K), \dots, L_{0,\min}^M(K)) \\ &= \frac{\partial \mathcal{F}_{f,K}}{\partial L_{\text{air}}} (L_{\text{air},\min}(K), L_{0,\min}^1(K), \dots, L_{0,\min}^M(K)) = 0, \\ \frac{\partial \mathcal{F}}{\partial L_0^m} (K, L_{\text{air},\min}(K), L_{0,\min}^1(K), \dots, L_{0,\min}^M(K)) \\ &= \frac{\partial \mathcal{F}_{f,K}}{\partial L_0^m} (L_{\text{air},\min}(K), L_{0,\min}^1(K), \dots, L_{0,\min}^M(K)) = 0, \quad \forall m \in \{1, \dots, M\}. \end{aligned}$$

Therefore, the definition of  $\mathcal{F}_{\min}$  and the chain rule yield

$$\begin{aligned} \mathcal{F}'_{\min}(K) &= \frac{d}{dK} [\mathcal{F}(K, L_{\text{air},\min}(K), L_0^1(K), \dots, L_0^M(K))] \\ &= \frac{\partial \mathcal{F}}{\partial K} + L'_{\text{air},\min} \underbrace{\frac{\partial \mathcal{F}}{\partial L_{\text{air}}}}_{=0} + \sum_{m=1}^M L_{0,\min}^{m'} \underbrace{\frac{\partial \mathcal{F}}{\partial L_0^m}}_{=0} \\ &= \frac{\partial \mathcal{F}}{\partial K} (K, L_{\text{air},\min}(K), L_0^1(K), \dots, L_0^M(K)). \end{aligned} \tag{D.7}$$

Furthermore,  $\mathcal{F}'_{\min}$  can be computed as

$$\begin{aligned} \mathcal{F}'_{\min} &= \frac{d}{dK} \left[ S_{\text{LL}} - \sum_{m=1}^M \frac{S_{\text{Le}}^m S_{\text{Le}}^m}{S_{\text{ee}}^m} - \frac{(L_{\text{air}}^{\text{num}})^2}{L_{\text{air}}^{\text{denom}}} \right] \\ &= 2 \sum_{m=1}^M \frac{S_{\text{Led}}^m S_{\text{Le}}^m S_{\text{ee}}^m - S_{\text{eed}}^m S_{\text{Le}}^m S_{\text{Le}}^m}{S_{\text{ee}}^m S_{\text{ee}}^m} - \frac{2L_{\text{air}}^{\text{num}} L_{\text{air}}^{\text{num}'} L_{\text{air}}^{\text{denom}} - (L_{\text{air}}^{\text{num}})^2 L_{\text{air}}^{\text{denom}'}}{(L_{\text{air}}^{\text{denom}})^2}. \end{aligned}$$

To evaluate  $\mathcal{F}'_{\min}$  in  $K = 0$ , one once again has to make use of l'Hôpital's rule and Appendix E. Some preparatory computations are required. The derivatives of the denominator are

$$\begin{aligned} \left[ (L_{\text{air}}^{\text{denom}})^2 \right]' &= 2L_{\text{air}}^{\text{denom}} L_{\text{air}}^{\text{denom}'}, \\ \left[ (L_{\text{air}}^{\text{denom}})^2 \right]'' &= 2L_{\text{air}}^{\text{denom}'} L_{\text{air}}^{\text{denom}'} + 2L_{\text{air}}^{\text{denom}} L_{\text{air}}^{\text{denom}''}, \\ \left[ (L_{\text{air}}^{\text{denom}})^2 \right]''' &= 6L_{\text{air}}^{\text{denom}'} L_{\text{air}}^{\text{denom}''} + 2L_{\text{air}}^{\text{denom}} L_{\text{air}}^{\text{denom}'''}, \\ \left[ (L_{\text{air}}^{\text{denom}})^2 \right]'''' &= 6L_{\text{air}}^{\text{denom}''} L_{\text{air}}^{\text{denom}''} + 8L_{\text{air}}^{\text{denom}'} L_{\text{air}}^{\text{denom}'''} + 2L_{\text{air}}^{\text{denom}} L_{\text{air}}^{\text{denom}''''}. \end{aligned}$$

The derivatives of the numerator are

$$\begin{aligned} \left[ 2L_{\text{air}}^{\text{num}} L_{\text{air}}^{\text{num}'} L_{\text{air}}^{\text{denom}} - (L_{\text{air}}^{\text{num}})^2 L_{\text{air}}^{\text{denom}'} \right]' \\ = 2(L_{\text{air}}^{\text{num}'})^2 L_{\text{air}}^{\text{denom}} + 2L_{\text{air}}^{\text{num}} L_{\text{air}}^{\text{num}''} L_{\text{air}}^{\text{denom}} - (L_{\text{air}}^{\text{num}})^2 L_{\text{air}}^{\text{denom}''}, \end{aligned}$$

$$\begin{aligned}
& [2L_{\text{air}}^{\text{num}} L_{\text{air}}^{\text{num}'} L_{\text{air}}^{\text{denom}} - (L_{\text{air}}^{\text{num}})^2 L_{\text{air}}^{\text{denom}'}]'' \\
&= 6L_{\text{air}}^{\text{num}'} L_{\text{air}}^{\text{num}''} L_{\text{air}}^{\text{denom}} + 2(L_{\text{air}}^{\text{num}'})^2 L_{\text{air}}^{\text{denom}'} + 2L_{\text{air}}^{\text{num}} L_{\text{air}}^{\text{num}'''} L_{\text{air}}^{\text{denom}} \\
&\quad + 2L_{\text{air}}^{\text{num}} L_{\text{air}}^{\text{num}''} L_{\text{air}}^{\text{denom}'} - 2L_{\text{air}}^{\text{num}} L_{\text{air}}^{\text{num}'} L_{\text{air}}^{\text{denom}''} - (L_{\text{air}}^{\text{num}})^2 L_{\text{air}}^{\text{denom}'''} , \\
& [2L_{\text{air}}^{\text{num}} L_{\text{air}}^{\text{num}'} L_{\text{air}}^{\text{denom}} - (L_{\text{air}}^{\text{num}})^2 L_{\text{air}}^{\text{denom}'}]''' \\
&= 6(L_{\text{air}}^{\text{num}''})^2 L_{\text{air}}^{\text{denom}} + 8L_{\text{air}}^{\text{num}'} L_{\text{air}}^{\text{num}'''} L_{\text{air}}^{\text{denom}} + 12L_{\text{air}}^{\text{num}'} L_{\text{air}}^{\text{num}''} L_{\text{air}}^{\text{denom}'} \\
&\quad + 2L_{\text{air}}^{\text{num}} L_{\text{air}}^{\text{num}'''} L_{\text{air}}^{\text{denom}} + 4L_{\text{air}}^{\text{num}} L_{\text{air}}^{\text{num}'''} L_{\text{air}}^{\text{denom}'} \\
&\quad - 4L_{\text{air}}^{\text{num}} L_{\text{air}}^{\text{num}'} L_{\text{air}}^{\text{denom}'''} - (L_{\text{air}}^{\text{num}})^2 L_{\text{air}}^{\text{denom}''''} , \\
& [2L_{\text{air}}^{\text{num}} L_{\text{air}}^{\text{num}'} L_{\text{air}}^{\text{denom}} - (L_{\text{air}}^{\text{num}})^2 L_{\text{air}}^{\text{denom}'}]'''' \\
&= 20L_{\text{air}}^{\text{num}''} L_{\text{air}}^{\text{num}'''} L_{\text{air}}^{\text{denom}} + 18(L_{\text{air}}^{\text{num}''})^2 L_{\text{air}}^{\text{denom}'} + 10L_{\text{air}}^{\text{num}'} L_{\text{air}}^{\text{num}'''} L_{\text{air}}^{\text{denom}} \\
&\quad + 12L_{\text{air}}^{\text{num}'} L_{\text{air}}^{\text{num}''} L_{\text{air}}^{\text{denom}''} + 2L_{\text{air}}^{\text{num}} L_{\text{air}}^{\text{num}''''} L_{\text{air}}^{\text{denom}} + 24L_{\text{air}}^{\text{num}'} L_{\text{air}}^{\text{num}'''} L_{\text{air}}^{\text{denom}'} \\
&\quad + 6L_{\text{air}}^{\text{num}} L_{\text{air}}^{\text{num}''''} L_{\text{air}}^{\text{denom}'} + 4L_{\text{air}}^{\text{num}} L_{\text{air}}^{\text{num}'''} L_{\text{air}}^{\text{denom}''} - 4(L_{\text{air}}^{\text{num}'})^2 L_{\text{air}}^{\text{denom}'''} \\
&\quad - 4L_{\text{air}}^{\text{num}} L_{\text{air}}^{\text{num}''} L_{\text{air}}^{\text{denom}'''} - 6L_{\text{air}}^{\text{num}} L_{\text{air}}^{\text{num}'} L_{\text{air}}^{\text{denom}''''} - (L_{\text{air}}^{\text{num}})^2 L_{\text{air}}^{\text{denom}''''} .
\end{aligned}$$

Making use of

$$L_{\text{air}}^{\text{num}}(0) = 0, \quad L_{\text{air}}^{\text{denom}}(0) = 0, \quad L_{\text{air}}^{\text{denom}'}(0) = 0,$$

one obtains

$$\begin{aligned}
& [(L_{\text{air}}^{\text{denom}})^2]'(0) = 0, \quad [(L_{\text{air}}^{\text{denom}})^2]''(0) = 0, \quad [(L_{\text{air}}^{\text{denom}})^2]'''(0) = 0, \\
& [(L_{\text{air}}^{\text{denom}})^2]''''(0) = 6(L_{\text{air}}^{\text{denom}''}(0))^2 = 24 \left( S_{\text{dd}} - \sum_{m=1}^M \frac{S_{\text{d}}^m S_{\text{d}}^m}{S_1^m} \right)^2 >^* 0
\end{aligned}$$

and

$$\begin{aligned}
& [2L_{\text{air}}^{\text{num}} L_{\text{air}}^{\text{num}'} L_{\text{air}}^{\text{denom}} - (L_{\text{air}}^{\text{num}})^2 L_{\text{air}}^{\text{denom}'}]'(0) = 0, \\
& [2L_{\text{air}}^{\text{num}} L_{\text{air}}^{\text{num}'} L_{\text{air}}^{\text{denom}} - (L_{\text{air}}^{\text{num}})^2 L_{\text{air}}^{\text{denom}'}]''(0) = 0, \\
& [2L_{\text{air}}^{\text{num}} L_{\text{air}}^{\text{num}'} L_{\text{air}}^{\text{denom}} - (L_{\text{air}}^{\text{num}})^2 L_{\text{air}}^{\text{denom}'}]'''(0) = 0, \\
& [2L_{\text{air}}^{\text{num}} L_{\text{air}}^{\text{num}'} L_{\text{air}}^{\text{denom}} - (L_{\text{air}}^{\text{num}})^2 L_{\text{air}}^{\text{denom}'}]'''' \\
&= 12L_{\text{air}}^{\text{num}'}(0)L_{\text{air}}^{\text{num}''}(0)L_{\text{air}}^{\text{denom}''}(0) - 4(L_{\text{air}}^{\text{num}'}(0))^2 L_{\text{air}}^{\text{denom}'''}(0).
\end{aligned}$$

Hence,

$$\begin{aligned}
\mathcal{F}'_{\text{min}}(0) &= 2 \sum_{m=1}^M \frac{S_{\text{Ld}}^m S_{\text{L}}^m S_1^m - S_{\text{d}}^m S_{\text{L}}^m S_{\text{L}}^m}{S_1^m S_1^m} \\
&\quad - L_{\text{air}}^{\text{num}'}(0) \frac{6L_{\text{air}}^{\text{num}''}(0)L_{\text{air}}^{\text{denom}''}(0) - 2L_{\text{air}}^{\text{num}'}(0)L_{\text{air}}^{\text{denom}'''}(0)}{3(L_{\text{air}}^{\text{denom}''}(0))^2}.
\end{aligned}$$

The second derivative  $\mathcal{F}''_{\min}$  can be computed analogously as

$$\begin{aligned} \mathcal{F}''_{\min} = 2 \sum_{m=1}^M & \left[ \frac{-S_{\text{Ledd}}^m S_{\text{Le}}^m S_{\text{ee}}^m S_{\text{ee}}^m - S_{\text{Led}}^m S_{\text{Led}}^m S_{\text{ee}}^m S_{\text{ee}}^m + 4S_{\text{Led}}^m S_{\text{Le}}^m S_{\text{eed}}^m S_{\text{ee}}^m}{S_{\text{ee}}^m S_{\text{ee}}^m S_{\text{ee}}^m} \right. \\ & \left. + \frac{2S_{\text{Le}}^m S_{\text{Le}}^m S_{\text{eed}}^m S_{\text{ee}}^m - 4S_{\text{Le}}^m S_{\text{Le}}^m S_{\text{eed}}^m S_{\text{eed}}^m}{S_{\text{ee}}^m S_{\text{ee}}^m S_{\text{ee}}^m} \right] \\ & - \left[ 2 \frac{(L_{\text{air}}^{\text{num}'})^2 (L_{\text{air}}^{\text{denom}})^2 + (L_{\text{air}}^{\text{num}})^2 (L_{\text{air}}^{\text{denom}'})^2 + L_{\text{air}}^{\text{num}} L_{\text{air}}^{\text{num}''} (L_{\text{air}}^{\text{denom}})^2}{(L_{\text{air}}^{\text{denom}})^3} \right. \\ & \left. - \frac{4L_{\text{air}}^{\text{num}} L_{\text{air}}^{\text{num}'} L_{\text{air}}^{\text{denom}} L_{\text{air}}^{\text{denom}'} + (L_{\text{air}}^{\text{num}})^2 L_{\text{air}}^{\text{denom}} L_{\text{air}}^{\text{denom}''}}{(L_{\text{air}}^{\text{denom}})^3} \right]. \end{aligned}$$

To compute  $\mathcal{F}''_{\min}(0)$ , the second term's numerator and denominator have to be derived up to the sixth order. The derivatives of the denominator are

$$\begin{aligned} [(L_{\text{air}}^{\text{denom}})^3]' &= 3 (L_{\text{air}}^{\text{denom}})^2 L_{\text{air}}^{\text{denom}'}, \\ [(L_{\text{air}}^{\text{denom}})^3]'' &= 6L_{\text{air}}^{\text{denom}} (L_{\text{air}}^{\text{denom}'})^2 + 3 (L_{\text{air}}^{\text{denom}})^2 L_{\text{air}}^{\text{denom}''}, \\ [(L_{\text{air}}^{\text{denom}})^3]''' &= 6 (L_{\text{air}}^{\text{denom}'})^3 + 18L_{\text{air}}^{\text{denom}} L_{\text{air}}^{\text{denom}'} L_{\text{air}}^{\text{denom}''} + 3 (L_{\text{air}}^{\text{denom}})^2 L_{\text{air}}^{\text{denom}'''}, \\ [(L_{\text{air}}^{\text{denom}})^3]'''' &= 36 (L_{\text{air}}^{\text{denom}'})^2 L_{\text{air}}^{\text{denom}''} + 18L_{\text{air}}^{\text{denom}} (L_{\text{air}}^{\text{denom}''})^2 \\ & \quad + 24L_{\text{air}}^{\text{denom}} L_{\text{air}}^{\text{denom}'} L_{\text{air}}^{\text{denom}'''} + 3 (L_{\text{air}}^{\text{denom}})^2 L_{\text{air}}^{\text{denom}''''}, \\ [(L_{\text{air}}^{\text{denom}})^3]''''' &= 90L_{\text{air}}^{\text{denom}'} (L_{\text{air}}^{\text{denom}''})^2 + 60 (L_{\text{air}}^{\text{denom}'})^2 L_{\text{air}}^{\text{denom}'''} \\ & \quad + 60L_{\text{air}}^{\text{denom}} L_{\text{air}}^{\text{denom}''} L_{\text{air}}^{\text{denom}'''} + 30L_{\text{air}}^{\text{denom}} L_{\text{air}}^{\text{denom}'} L_{\text{air}}^{\text{denom}''''} \\ & \quad + 3 (L_{\text{air}}^{\text{denom}})^2 L_{\text{air}}^{\text{denom}''''}, \\ [(L_{\text{air}}^{\text{denom}})^3]'''''' &= 90 (L_{\text{air}}^{\text{denom}''})^3 + 360L_{\text{air}}^{\text{denom}'} L_{\text{air}}^{\text{denom}''} L_{\text{air}}^{\text{denom}'''} + 90 (L_{\text{air}}^{\text{denom}'})^2 L_{\text{air}}^{\text{denom}''''} \\ & \quad + 60L_{\text{air}}^{\text{denom}} (L_{\text{air}}^{\text{denom}'''} )^2 + 90L_{\text{air}}^{\text{denom}} L_{\text{air}}^{\text{denom}''} L_{\text{air}}^{\text{denom}''''} \\ & \quad + 36L_{\text{air}}^{\text{denom}} L_{\text{air}}^{\text{denom}'} L_{\text{air}}^{\text{denom}''''} + 3 (L_{\text{air}}^{\text{denom}})^2 L_{\text{air}}^{\text{denom}''''''}, \end{aligned}$$

which at  $K = 0$  leads to

$$\begin{aligned} [(L_{\text{air}}^{\text{denom}})^3]'(0) &= 0, & [(L_{\text{air}}^{\text{denom}})^3]''(0) &= 0, & [(L_{\text{air}}^{\text{denom}})^3]'''(0) &= 0, \\ [(L_{\text{air}}^{\text{denom}})^3]''''(0) &= 0, & [(L_{\text{air}}^{\text{denom}})^3]'''''(0) &= 0, & [(L_{\text{air}}^{\text{denom}})^3]''''''(0) &= 90 (L_{\text{air}}^{\text{denom}''}(0))^3. \end{aligned}$$

The derivatives of the numerator are very complex. Therefore, only the relevant evaluations in  $K = 0$  are given here:

$$\left[ 2 (L_{\text{air}}^{\text{num}'})^2 (L_{\text{air}}^{\text{denom}})^2 + \dots - (L_{\text{air}}^{\text{num}})^2 L_{\text{air}}^{\text{denom}} L_{\text{air}}^{\text{denom}''} \right]'(0) = 0,$$

$$\begin{aligned}
& \left[ 2 (L_{\text{air}}^{\text{num}'})^2 (L_{\text{air}}^{\text{denom}})^2 + \dots - (L_{\text{air}}^{\text{num}})^2 L_{\text{air}}^{\text{denom}} L_{\text{air}}^{\text{denom}''} \right]'' (0) = 0, \\
& \left[ 2 (L_{\text{air}}^{\text{num}'})^2 (L_{\text{air}}^{\text{denom}})^2 + \dots - (L_{\text{air}}^{\text{num}})^2 L_{\text{air}}^{\text{denom}} L_{\text{air}}^{\text{denom}''} \right]''' (0) = 0, \\
& \left[ 2 (L_{\text{air}}^{\text{num}'})^2 (L_{\text{air}}^{\text{denom}})^2 + \dots - (L_{\text{air}}^{\text{num}})^2 L_{\text{air}}^{\text{denom}} L_{\text{air}}^{\text{denom}''} \right]'''' (0) = 0, \\
& \left[ 2 (L_{\text{air}}^{\text{num}'})^2 (L_{\text{air}}^{\text{denom}})^2 + \dots - (L_{\text{air}}^{\text{num}})^2 L_{\text{air}}^{\text{denom}} L_{\text{air}}^{\text{denom}''} \right]''''' (0) = 0, \\
& \left[ 2 (L_{\text{air}}^{\text{num}'})^2 (L_{\text{air}}^{\text{denom}})^2 + \dots - (L_{\text{air}}^{\text{num}})^2 L_{\text{air}}^{\text{denom}} L_{\text{air}}^{\text{denom}''} \right]'''''' (0) \\
& = 90 (L_{\text{air}}^{\text{num}''}(0))^2 (L_{\text{air}}^{\text{denom}''}(0))^2 + 120 L_{\text{air}}^{\text{num}'(0)} L_{\text{air}}^{\text{num}''''(0)} (L_{\text{air}}^{\text{denom}''}(0))^2 \\
& \quad - 120 L_{\text{air}}^{\text{num}'(0)} L_{\text{air}}^{\text{num}''(0)} L_{\text{air}}^{\text{denom}''(0)} L_{\text{air}}^{\text{denom}''''(0)} + 40 (L_{\text{air}}^{\text{num}'(0)})^2 (L_{\text{air}}^{\text{denom}''''(0)})^2 \\
& \quad - 30 (L_{\text{air}}^{\text{num}'(0)})^2 L_{\text{air}}^{\text{denom}''(0)} L_{\text{air}}^{\text{denom}''''(0)}.
\end{aligned}$$

This leads to  $\mathcal{F}_{\min}''(0)$  as claimed.  $\square$

*Proof of Lemma 6 on page 90: Characterization of  $\mathcal{F}$ 's Critical Points.*

REGARDING (a): One has to check both implications:

" $\Rightarrow$ ": Let  $(K, L_{\text{air}}, L_0^1, \dots, L_0^M) \in \mathbb{R}^{M+2}$  be a critical point of  $\mathcal{F}$ . Then,  $\mathcal{F}_{f,K}$  has a critical point in  $(L_{\text{air}}, L_0^1, \dots, L_0^M)$  (due to its definition (7.10)).

CASE  $K \neq 0$ : Due to Lemma 4 on page 86 this requires

$$(L_{\text{air}}, L_0^1, \dots, L_0^M) = (L_{\text{air},\min}(K), L_{0,\min}^1(K), \dots, L_{0,\min}^M(K)).$$

Now, from  $\nabla \mathcal{F} = 0$ , the definition of  $\mathcal{F}_{\min}$  and the chain rule it follows

$$\begin{aligned}
\mathcal{F}'_{\min}(K) &= \frac{d}{dK} [\mathcal{F}(K, L_{\text{air},\min}(K), L_{0,\min}^1(K), \dots, L_{0,\min}^M(K))] \\
&= \underbrace{\frac{\partial \mathcal{F}}{\partial K}}_{=0} + L'_{\text{air},\min} \underbrace{\frac{\partial \mathcal{F}}{\partial L_{\text{air}}}}_{=0} + \sum_{m=1}^M L_{0,\min}^{m'} \underbrace{\frac{\partial \mathcal{F}}{\partial L_0^m}}_{=0} = 0
\end{aligned}$$

CASE  $K = 0$ : From  $\nabla \mathcal{F}_{f,0} = 0$ , and the second part of Lemma 4 on page 86 it follows that  $L_0^m = \bar{L}^m$ .  $\partial \mathcal{F} / \partial K = 0$  and Lemma 2 on page 84 lead to the constraint (7.14):

$$\begin{aligned}
0 &= \frac{\partial \mathcal{F}}{\partial K}(0) = -2L_{\text{air}} S_{\text{Ld}} - 2 \sum_{m=1}^M [L_0^m L_{\text{air}} (-S_{\text{d}}^m) + L_0^m L_0^m S_{\text{d}}^{cm} - L_0^m S_{\text{Ld}}^m] \\
&= -2L_{\text{air}} \left( S_{\text{Ld}} - \sum_{m=1}^M \bar{L}^m S_{\text{d}}^m \right) - 2 \sum_{m=1}^M [\bar{L}^m \bar{L}^m S_{\text{d}}^m - \bar{L}^m S_{\text{Ld}}^m] \\
&= -2L_{\text{air}} \left( S_{\text{Ld}} - \sum_{m=1}^M \frac{S_{\text{L}}^m S_{\text{d}}^m}{S_1^m} \right) + 2 \sum_{m=1}^M \frac{S_{\text{L}}^m}{S_1^m} \left[ S_{\text{Ld}}^m - \frac{S_{\text{L}}^m S_{\text{d}}^m}{S_1^m} \right].
\end{aligned}$$

“ $\Leftarrow$ ”: CASE  $K \neq 0$ : Let

$$\mathcal{F}'_{\min}(K) = 0 \quad \wedge \quad (L_{\text{air}}, L_0^1, \dots, L_0^M) = (L_{\text{air},\min}(K), L_{0,\min}^1(K), \dots, L_{0,\min}^M(K)).$$

Then,  $\nabla \mathcal{F}_{f,K} = 0$  at this point (cf. Lemma 4 on page 86) and  $\partial \mathcal{F} / \partial K = \mathcal{F}'_{\min} = 0$  (cf. Lemma 5(e) on page 88). Hence,  $\nabla \mathcal{F} = 0$ .

CASE  $K = 0$ : This works analogously to the forward implication.

REGARDING (b): One has to check both implications:

“ $\Rightarrow$ ”: Let  $p = (K, L_{\text{air}}, L_0^1, \dots, L_0^M) \in \mathbb{R}^{M+2}$  be a (strict) local minimum of  $\mathcal{F}$ . In particular  $\nabla \mathcal{F}(p) = 0$ .

Due to (a), it remains to show  $d^2 \mathcal{F}_{\min} / (dK)^2 \geq 0$  (strict case:  $> 0$ ). This can be done with the help of Lemma 2(a) on page 90, the chain rule and the equality of mixed partials (Schwarz's theorem):

$$\begin{aligned} \mathcal{F}''_{\min}(K) &= \frac{d^2}{dK dK} [\mathcal{F}(K, L_{\text{air},\min}(K), L_{0,\min}^1(K), \dots, L_{0,\min}^M(K))] \\ &= \frac{d}{dK} \left[ \frac{\partial \mathcal{F}}{\partial K} + L'_{\text{air},\min} \frac{\partial \mathcal{F}}{\partial L_{\text{air}}} + \sum_{m=1}^M L_{0,\min}^{m'} \frac{\partial \mathcal{F}}{\partial L_0^m} \right] \\ &= \frac{\partial^2 \mathcal{F}}{\partial K \partial K} + L'_{\text{air},\min} \frac{\partial^2 \mathcal{F}}{\partial K \partial L_{\text{air}}} + \sum_{m=1}^M L_{0,\min}^{m'} \frac{\partial^2 \mathcal{F}}{\partial K \partial L_0^m} \\ &\quad + \underbrace{L''_{\text{air},\min} \frac{\partial \mathcal{F}}{\partial L_{\text{air}}}}_{=0} + L'_{\text{air},\min} \frac{\partial^2 \mathcal{F}}{\partial K \partial L_{\text{air}}} \\ &\quad + (L'_{\text{air},\min})^2 \frac{\partial \mathcal{F}}{\partial L_{\text{air}} \partial L_{\text{air}}} + L'_{\text{air},\min} \sum_{m=1}^M L_{0,\min}^{m'} \frac{\partial^2 \mathcal{F}}{\partial L_{\text{air}} \partial L_0^m} \\ &\quad + \sum_{m=1}^M L_{0,\min}^{m''} \frac{\partial \mathcal{F}}{\partial L_0^m} + \sum_{m=1}^M L_{0,\min}^{m'} \frac{\partial^2 \mathcal{F}}{\partial K \partial L_0^m} \\ &\quad + L'_{\text{air},\min} \sum_{m=1}^M L_{0,\min}^{m'} \frac{\partial^2 \mathcal{F}}{\partial L_{\text{air}} \partial L_0^m} + \sum_{m=1}^M \sum_{l=1}^M L_{0,\min}^{m'} L_{0,\min}^{l'} \frac{\partial^2 \mathcal{F}}{\partial L_0^m \partial L_0^l} \\ &= \xi_{\min}^T \text{Hess } \mathcal{F}(p) \xi_{\min}, \end{aligned}$$

where

$$\xi_{\min} := (1, L'_{\text{air},\min}, L_{0,\min}^{1'}, \dots, L_{0,\min}^{M'})^T \neq 0.$$

In the case of a local minimum Hess  $\mathcal{F}(p)$  is positive semi-definite, in particular

$$\mathcal{F}''_{\min}(K) = \xi_{\min}^T \text{Hess } \mathcal{F}(p) \xi_{\min} \geq 0;$$

in the case of a strict local minimum it is even positive definite and thus  $\mathcal{F}''_{\min}(K) > 0$ .

“ $\Leftarrow$ ”: Let

$$(L_{\text{air}}, L_0^1, \dots, L_0^M) = (L_{\text{air},\min}(K), L_{0,\min}^1(K), \dots, L_{0,\min}^M(K))$$

and  $K \neq 0$  be a (strict) local minimum of  $\mathcal{F}_{\min}$ , *i.e.*

$$\mathcal{F}'_{\min}(K) = 0, \quad \wedge \quad \mathcal{F}''_{\min}(K) \geq 0 \quad (\text{strict case: } \mathcal{F}''_{\min}(K) > 0).$$

Assume  $p := (K, L_{\text{air}}, L_0^1, \dots, L_0^M) \in \mathbb{R}^{M+2}$  not to be a (strict) local minimum of  $\mathcal{F}$ . In this case, there exist a  $\xi \in \mathbb{R}^{M+2}$  and an  $\varepsilon > 0$  s.t.

$$\forall s \in (0, \varepsilon) : \quad \mathcal{F}(p + s\xi) \leq \mathcal{F}(p) \quad (\text{strict case: } \mathcal{F}(p + s\xi) < \mathcal{F}(p)).$$

Because  $\mathcal{F}_{f,K}$  is strictly convex (*cf.* Lemma 4 on page 86) it has to be  $\xi^1 \neq 0$ . Therefore, one has

$$\forall s \in (0, \min\{\varepsilon, |K|\}) : \quad \mathcal{F}_{\min}(K + s\xi^1) \leq \mathcal{F}(p + s\xi) \stackrel{(<)}{\leq} \mathcal{F}(p) = \mathcal{F}_{\min}(K),$$

which is a contradiction to  $K$  (strictly) locally minimizing  $\mathcal{F}_{\min}$ . Therefore,  $p$  is a (strict) local minimum of  $\mathcal{F}$ .

*REGARDING (c):* Assume  $p = (K, L_{\text{air}}, L_0^1, \dots, L_0^M) \in \mathbb{R}^{M+2}$  is a local maximum of  $\mathcal{F}$ , where  $K \neq 0$ . Then, it is in particular a critical point of  $\mathcal{F}$  and thus, according to (a),

$$(L_{\text{air}}, L_0^1, \dots, L_0^M) = (L_{\text{air},\min}(K), L_{0,\min}^1(K), \dots, L_{0,\min}^M(K)),$$

which is a strict global minimum of  $\mathcal{F}_{f,K}$  (*cf.* Lemma 4 on page 86). Hence, for all  $x \in \mathbb{R}^{M+1} \setminus \{0\}$  one has

$$\mathcal{F}(p) = \mathcal{F}_{f,K}(L_{\text{air}}, L_0^1, \dots, L_0^M) < \mathcal{F}_{f,K}(L_{\text{air}} + x^1, L_0^1 + x^2, \dots, L_0^M + x^{M+1}) = \mathcal{F}(p + (0, x)).$$

This is a contradiction to the local maximality of  $\mathcal{F}$  in  $p$ . □



---

## Appendix E. Derivation of $L_{\text{air,min}}$ 's Numerator and Denominator

In order to implement the parameter estimation method proposed in Sec. 7.4 for tracking-based visibility estimation, the restricted objective function  $\mathcal{F}_{\text{min}}$  has to be computed up to the second derivative. According to Lemma 5 on page 87 this requires the derivation of  $L_{\text{air,min}}$ 's numerator  $L_{\text{air}}^{\text{num}}$  (see (7.11)) and denominator  $L_{\text{air}}^{\text{denom}}$  (see (7.12)) up to the 3<sup>rd</sup> and 4<sup>th</sup> order respectively. This can be done by straightforward calculations. Moreover, all terms have to be evaluated in 0. As it is useful for the implementation, they are provided in the notation of Remark 24 on page 91.

### E.1 Numerator Derivatives

$L_{\text{air}}^{\text{num}}$  and  $L_{\text{air}}^{\text{num}}(0)$  are given by

$$L_{\text{air}}^{\text{num}} = \sum_{m=1}^M \frac{S_{\text{L}}^m S_{\text{ee}}^m - S_{\text{Le}}^m S_{\text{e}}^m}{S_{\text{ee}}^m}, \quad L_{\text{air}}^{\text{num}}(0) = 0.$$

$L_{\text{air}}^{\text{num}'}$  and  $L_{\text{air}}^{\text{num}'}(0)$  are given by

$$L_{\text{air}}^{\text{num}'} = \sum_{m=1}^M \frac{S_{\text{Led}}^m S_{\text{ee}}^m S_{\text{e}}^m - 2S_{\text{Le}}^m S_{\text{eed}}^m S_{\text{e}}^m + S_{\text{Le}}^m S_{\text{ee}}^m S_{\text{ed}}^m}{(S_{\text{ee}}^m)^2},$$

$$L_{\text{air}}^{\text{num}'}(0) = \sum_{m=1}^M \frac{S_{\text{Ld}}^m S_{\text{1}}^m - S_{\text{L}}^m S_{\text{d}}^m}{S_{\text{1}}^m}.$$

$L_{\text{air}}^{\text{num}''}$  and  $L_{\text{air}}^{\text{num}''}(0)$  are given by

$$L_{\text{air}}^{\text{num}''} = \sum_{m=1}^M \frac{-S_{\text{Ledd}}^m S_{\text{ee}}^m S_{\text{ee}}^m S_{\text{e}}^m + 4S_{\text{Led}}^m S_{\text{eed}}^m S_{\text{ee}}^m S_{\text{e}}^m - 2S_{\text{Le}}^m S_{\text{eed}}^m S_{\text{ee}}^m S_{\text{ed}}^m}{(S_{\text{ee}}^m)^3}$$

$$+ \sum_{m=1}^M \frac{4S_{\text{Le}}^m S_{\text{eedd}}^m S_{\text{ee}}^m S_{\text{e}}^m - 8S_{\text{Le}}^m S_{\text{eed}}^m S_{\text{eed}}^m S_{\text{e}}^m + 4S_{\text{Le}}^m S_{\text{eed}}^m S_{\text{ee}}^m S_{\text{ed}}^m - S_{\text{Le}}^m S_{\text{ee}}^m S_{\text{ee}}^m S_{\text{edd}}^m}{(S_{\text{ee}}^m)^3},$$

$$L_{\text{air}}^{\text{num}''}(0) = \sum_{m=1}^M \frac{-S_{\text{Ldd}}^m S_{\text{1}}^m S_{\text{1}}^m + 2S_{\text{Ld}}^m S_{\text{d}}^m S_{\text{1}}^m + 3S_{\text{L}}^m S_{\text{dd}}^m S_{\text{1}}^m - 4S_{\text{L}}^m S_{\text{d}}^m S_{\text{d}}^m}{(S_{\text{1}}^m)^2}.$$

$L_{\text{air}}^{\text{num}''''}$  and  $L_{\text{air}}^{\text{num}''''}(0)$  are given by

$$\begin{aligned}
L_{\text{air}}^{\text{num}''''} &= \sum_{m=1}^M \frac{S_{\text{Ledd}}^m S_{\text{ee}}^m S_{\text{ee}}^m S_{\text{ee}}^m S_e^m - 6S_{\text{Ledd}}^m S_{\text{eed}}^m S_{\text{ee}}^m S_{\text{ee}}^m S_e^m + 3S_{\text{Ledd}}^m S_{\text{ee}}^m S_{\text{ee}}^m S_{\text{ee}}^m S_{\text{ed}}^m}{(S_{\text{ee}}^m)^4} \\
&+ \sum_{m=1}^M \frac{-12S_{\text{Led}}^m S_{\text{eedd}}^m S_{\text{ee}}^m S_{\text{ee}}^m S_e^m + 24S_{\text{Led}}^m S_{\text{eed}}^m S_{\text{eed}}^m S_{\text{ee}}^m S_e^m - 12S_{\text{Led}}^m S_{\text{eed}}^m S_{\text{ee}}^m S_{\text{ee}}^m S_{\text{ed}}^m}{(S_{\text{ee}}^m)^4} \\
&+ \sum_{m=1}^M \frac{3S_{\text{Led}}^m S_{\text{ee}}^m S_{\text{ee}}^m S_{\text{ee}}^m S_{\text{edd}}^m - 8S_{\text{Le}}^m S_{\text{eeddd}}^m S_{\text{ee}}^m S_{\text{ee}}^m S_e^m + 48S_{\text{Le}}^m S_{\text{eedd}}^m S_{\text{eed}}^m S_{\text{ee}}^m S_e^m}{(S_{\text{ee}}^m)^4} \\
&+ \sum_{m=1}^M \frac{-12S_{\text{Le}}^m S_{\text{eedd}}^m S_{\text{ee}}^m S_{\text{ee}}^m S_{\text{ed}}^m + 24S_{\text{Le}}^m S_{\text{eed}}^m S_{\text{eed}}^m S_{\text{ee}}^m S_{\text{ed}}^m - 48S_{\text{Le}}^m S_{\text{eed}}^m S_{\text{eed}}^m S_{\text{ee}}^m S_e^m}{(S_{\text{ee}}^m)^4} \\
&+ \sum_{m=1}^M \frac{-6S_{\text{Le}}^m S_{\text{eed}}^m S_{\text{ee}}^m S_{\text{ee}}^m S_{\text{edd}}^m + S_{\text{Le}}^m S_{\text{ee}}^m S_{\text{ee}}^m S_{\text{ee}}^m S_{\text{edd}}^m}{(S_{\text{ee}}^m)^4}, \\
L_{\text{air}}^{\text{num}''''}(0) &= \sum_{m=1}^M \frac{S_{\text{Lddd}}^m S_1^m S_1^m S_1^m - 3S_{\text{Ldd}}^m S_d^m S_1^m S_1^m - 9S_{\text{Ld}}^m S_{\text{dd}}^m S_1^m S_1^m + 12S_{\text{Ld}}^m S_d^m S_d^m S_1^m}{(S_1^m)^3} \\
&+ \sum_{m=1}^M \frac{-7S_{\text{L}}^m S_{\text{ddd}}^m S_1^m S_1^m + 30S_{\text{L}}^m S_{\text{dd}}^m S_d^m S_1^m - 24S_{\text{L}}^m S_d^m S_d^m S_d^m}{(S_1^m)^3}.
\end{aligned}$$

## E.2 Denominator Derivatives

$L_{\text{air}}^{\text{denom}}$  and  $L_{\text{air}}^{\text{denom}}(0)$  are given by

$$L_{\text{air}}^{\text{denom}} = \sum_{m=1}^M \frac{S_1^m S_{\text{ee}}^m - S_e^m S_e^m}{S_{\text{ee}}^m}, \quad L_{\text{air}}^{\text{denom}}(0) = 0.$$

$L_{\text{air}}^{\text{denom}'}$  and  $L_{\text{air}}^{\text{denom}'}(0)$  are given by

$$L_{\text{air}}^{\text{denom}'} = \sum_{m=1}^M \frac{-2S_{\text{eed}}^m S_e^m S_e^m + 2S_{\text{eed}}^m S_{\text{ed}}^m S_e^m}{(S_{\text{ee}}^m)^2}, \quad L_{\text{air}}^{\text{denom}'}(0) = 0.$$

$L_{\text{air}}^{\text{denom}''}$  and  $L_{\text{air}}^{\text{denom}''}(0)$  are given by

$$\begin{aligned}
L_{\text{air}}^{\text{denom}''} &= \sum_{m=1}^M \frac{4S_{\text{eedd}}^m S_{\text{ee}}^m S_e^m S_e^m - 8S_{\text{eed}}^m S_{\text{eed}}^m S_e^m S_e^m + 8S_{\text{eed}}^m S_{\text{ee}}^m S_{\text{ed}}^m S_e^m}{(S_{\text{ee}}^m)^3} \\
&+ \sum_{m=1}^M \frac{-2S_{\text{ee}}^m S_{\text{ee}}^m S_{\text{edd}}^m S_e^m - 2S_{\text{ee}}^m S_{\text{ee}}^m S_{\text{ed}}^m S_{\text{ed}}^m}{(S_{\text{ee}}^m)^3}, \\
L_{\text{air}}^{\text{denom}''}(0) &= \sum_{m=1}^M \frac{2S_{\text{ddd}}^m S_1^m - 2S_d^m S_d^m}{S_1^m}.
\end{aligned}$$

$L_{\text{air}}^{\text{denom}''''}$  and  $L_{\text{air}}^{\text{denom}''''}(0)$  are given by

$$\begin{aligned}
L_{\text{air}}^{\text{denom}''''} &= \sum_{m=1}^M \frac{-8S_{\text{eedd}}^m S_{\text{ee}}^m S_{\text{ee}}^m S_{\text{ee}}^m S_{\text{e}}^m S_{\text{e}}^m + 48S_{\text{eedd}}^m S_{\text{eed}}^m S_{\text{ee}}^m S_{\text{ee}}^m S_{\text{e}}^m S_{\text{e}}^m - 24S_{\text{eedd}}^m S_{\text{ee}}^m S_{\text{ee}}^m S_{\text{ee}}^m S_{\text{ed}}^m S_{\text{e}}^m}{(S_{\text{ee}}^m)^4} \\
&+ \sum_{m=1}^M \frac{-48S_{\text{eed}}^m S_{\text{eed}}^m S_{\text{eed}}^m S_{\text{e}}^m S_{\text{e}}^m + 48S_{\text{eed}}^m S_{\text{eed}}^m S_{\text{ee}}^m S_{\text{ed}}^m S_{\text{e}}^m S_{\text{e}}^m - 12S_{\text{eed}}^m S_{\text{ee}}^m S_{\text{ee}}^m S_{\text{eed}}^m S_{\text{e}}^m}{(S_{\text{ee}}^m)^4}, \\
&+ \sum_{m=1}^M \frac{-12S_{\text{eed}}^m S_{\text{ee}}^m S_{\text{ee}}^m S_{\text{ed}}^m S_{\text{ed}}^m + 2S_{\text{ee}}^m S_{\text{ee}}^m S_{\text{ee}}^m S_{\text{eedd}}^m S_{\text{e}}^m + 6S_{\text{ee}}^m S_{\text{ee}}^m S_{\text{ee}}^m S_{\text{eed}}^m S_{\text{ed}}^m}{(S_{\text{ee}}^m)^4}, \\
L_{\text{air}}^{\text{denom}''''}(0) &= \sum_{m=1}^M \frac{-6S_{\text{ddd}}^m S_1^m S_1^m + 18S_{\text{dd}}^m S_{\text{d}}^m S_1^m - 12S_{\text{d}}^m S_{\text{d}}^m S_{\text{d}}^m}{(S_1^m)^2}.
\end{aligned}$$

$L_{\text{air}}^{\text{denom}''''''}$  and  $L_{\text{air}}^{\text{denom}''''''}(0)$  are given by

$$\begin{aligned}
L_{\text{air}}^{\text{denom}''''''} &= \sum_{m=1}^M \frac{16S_{\text{eedddd}}^m S_{\text{ee}}^m S_{\text{ee}}^m S_{\text{ee}}^m S_{\text{e}}^m S_{\text{e}}^m - 128S_{\text{eedddd}}^m S_{\text{eed}}^m S_{\text{ee}}^m S_{\text{ee}}^m S_{\text{e}}^m S_{\text{e}}^m}{(S_{\text{ee}}^m)^5} \\
&+ \sum_{m=1}^M \frac{64S_{\text{eedd}}^m S_{\text{ee}}^m S_{\text{ee}}^m S_{\text{ee}}^m S_{\text{ed}}^m S_{\text{e}}^m - 96S_{\text{eedd}}^m S_{\text{eed}}^m S_{\text{ee}}^m S_{\text{ee}}^m S_{\text{e}}^m S_{\text{e}}^m}{(S_{\text{ee}}^m)^5} \\
&+ \sum_{m=1}^M \frac{576S_{\text{eedd}}^m S_{\text{eed}}^m S_{\text{eed}}^m S_{\text{ee}}^m S_{\text{e}}^m S_{\text{e}}^m - 384S_{\text{eedd}}^m S_{\text{eed}}^m S_{\text{ee}}^m S_{\text{ee}}^m S_{\text{ed}}^m S_{\text{e}}^m}{(S_{\text{ee}}^m)^5} \\
&+ \sum_{m=1}^M \frac{48S_{\text{eedd}}^m S_{\text{ee}}^m S_{\text{ee}}^m S_{\text{ee}}^m S_{\text{eed}}^m S_{\text{e}}^m + 48S_{\text{eedd}}^m S_{\text{ee}}^m S_{\text{ee}}^m S_{\text{ee}}^m S_{\text{ed}}^m S_{\text{ed}}^m}{(S_{\text{ee}}^m)^5} \\
&+ \sum_{m=1}^M \frac{384S_{\text{eed}}^m S_{\text{eed}}^m S_{\text{eed}}^m S_{\text{ee}}^m S_{\text{ed}}^m S_{\text{e}}^m - 384S_{\text{eed}}^m S_{\text{eed}}^m S_{\text{eed}}^m S_{\text{ed}}^m S_{\text{e}}^m S_{\text{e}}^m}{(S_{\text{ee}}^m)^5} \\
&+ \sum_{m=1}^M \frac{-96S_{\text{eed}}^m S_{\text{eed}}^m S_{\text{ee}}^m S_{\text{ee}}^m S_{\text{eed}}^m S_{\text{e}}^m - 96S_{\text{eed}}^m S_{\text{eed}}^m S_{\text{ee}}^m S_{\text{ee}}^m S_{\text{ed}}^m S_{\text{ed}}^m}{(S_{\text{ee}}^m)^5} \\
&+ \sum_{m=1}^M \frac{16S_{\text{eed}}^m S_{\text{ee}}^m S_{\text{ee}}^m S_{\text{ee}}^m S_{\text{eedd}}^m S_{\text{e}}^m + 48S_{\text{eed}}^m S_{\text{ee}}^m S_{\text{ee}}^m S_{\text{ee}}^m S_{\text{eed}}^m S_{\text{ed}}^m}{(S_{\text{ee}}^m)^5} \\
&+ \sum_{m=1}^M \frac{-2S_{\text{ee}}^m S_{\text{ee}}^m S_{\text{ee}}^m S_{\text{ee}}^m S_{\text{eedddd}}^m S_{\text{e}}^m - 8S_{\text{ee}}^m S_{\text{ee}}^m S_{\text{ee}}^m S_{\text{ee}}^m S_{\text{eedd}}^m S_{\text{ed}}^m}{(S_{\text{ee}}^m)^5} \\
&+ \sum_{m=1}^M \frac{-6S_{\text{ee}}^m S_{\text{ee}}^m S_{\text{ee}}^m S_{\text{ee}}^m S_{\text{eed}}^m S_{\text{eed}}^m}{(S_{\text{ee}}^m)^5}, \\
L_{\text{air}}^{\text{denom}''''''}(0) &= \sum_{m=1}^M \frac{14S_{\text{dddd}}^m S_1^m S_1^m S_1^m - 56S_{\text{ddd}}^m S_{\text{d}}^m S_1^m S_1^m - 54S_{\text{dd}}^m S_{\text{d}}^m S_1^m S_1^m}{(S_1^m)^3} \\
&+ \sum_{m=1}^M \frac{192S_{\text{dd}}^m S_{\text{d}}^m S_{\text{d}}^m S_1^m - 96S_{\text{d}}^m S_{\text{d}}^m S_{\text{d}}^m S_{\text{d}}^m}{(S_1^m)^3}.
\end{aligned}$$



---

# Bibliography

- [Abr1964] Milton Abramowitz and Irene A. Stegun. “Handbook of Mathematical Functions With Formulas, Graphs, and Mathematical Tables”. 55. 9th printing. Courier Corporation, 1964.
- [Alb2002] Ferran Albajar, Marino Bornatici and Folker Engelmann. “Electron Cyclotron Radiative Transfer in Fusion Plasmas”. In: *Nuclear Fusion* 42.6 (2002), 670–678. DOI: 10.1088/0029-5515/42/6/305.
- [Alv2012] José M. Álvarez, Theo Gevers, Yann LeCun and Antonio M. López. “Road Scene Segmentation from a Single Image”. In: *Computer Vision – ECCV 2012*. Vol. 7578. Lecture Notes in Computer Science. Springer Berlin Heidelberg, 2012, 376–389. DOI: 10.1007/978-3-642-33786-4\_28.
- [ARM2010] ARM. “Specification of Cortex-A9 Floating-Point Unit (1.5 GHz), Revision: r2p2”. 2010.
- [Bab2011] Raouf Babari, Nicolas Hautière, Éric Dumont, Roland Brémond and Nicolas Paparoditis. “A Model-Driven Approach to Estimate Atmospheric Visibility with Ordinary Cameras”. In: *Atmospheric Environment* 45.30 (May 2011), 5316–5324. DOI: 10.1016/j.atmosenv.2011.06.053.
- [Bar2012] Žarko P. Barbarić, Boban P. Bondžulić and Srđjan T. Mitrović. “Passive ranging using image intensity and contrast measurements”. In: *Electronics Letters* 48.18 (Aug. 2012), 1122–1123. DOI: 10.1049/e1.2012.0632.
- [Bec2014] Jan Becker, Maria-Belen Aranda Colas, Stefan Nordbruch and Michael Fausten. “Bosch’s Vision and Roadmap Toward Fully Autonomous Driving”. In: *Road Vehicle Automation*. Ed. by Gereon Meyer and Sven Beiker. Lecture Notes in Mobility. Springer, 2014, 49–59. DOI: 10.1007/978-3-319-05990-7\_5.
- [Ber2004] Ludwig Bergmann and Clemens Schaefer. “Lehrbuch der Experimentalphysik, Band 3, Optik – Wellen- und Teilchenoptik”. Ed. by Heinz Niedrig. 10th ed. Walter de Gruyter, Berlin, 2004.
- [Bey2012] Jürgen Beyerer, Fernando Puente-León and Christian Frese. “Automatische Sichtprüfung: Grundlagen, Methoden und Praxis der Bildgewinnung und Bildauswertung”. Berlin Heidelberg: Springer, 2012. DOI: 10.1007/978-3-642-23966-3.
- [Bic2002] David R. Bickel. “Robust estimators of the mode and skewness of continuous data”. In: *Computational Statistics & Data Analysis* 39.2 (2002), 153–163. DOI: 10.1016/S0167-9473(01)00057-3.
- [Bic2006] David R. Bickel and Rudolf Frühwirth. “On a fast, robust estimator of the mode: Comparisons to other robust estimators with applications”. In: *Computational Statistics & Data Analysis* 50.12 (2006), 3500–3530. DOI: 10.1016/j.csda.2005.07.011.

- [Boh1998] Craig F. Bohren and Donald R. Huffman. “Absorption and Scattering of Light by Small Particles”. Originally published in 1983. Wiley, 1998. DOI: 10.1002/9783527618156.
- [Boo1978] Carl de Boor. “A Practical Guide to Splines”. 1st ed. Vol. 27. Applied Mathematical Science. Springer, 1978.
- [Bou2007] Clément Boussard, Nicolas Hautière and Brigitte d’Andréa-Novel. “Vision guided by vehicle dynamics for onboard estimation of the visibility range”. In: *Intelligent Autonomous Vehicles*. Vol. 6. 1. 2007, 324–329.
- [Bou2008] Clément Boussard, Nicolas Hautière and Brigitte d’Andréa-Novel. “Vehicle Dynamics Estimation for Camera-based Visibility Distance Estimation”. In: *Intelligent Robots and Systems, 2008. IROS 2008. IEEE/RSJ International Conference on*. IEEE. Sept. 2008, 600–605. DOI: 10.1109/IROS.2008.4650756.
- [Bou2010] Clément Boussard, Nicolas Hautière and Brigitte d’Andréa-Novel. “Visibility Distance Estimation based on Structure from Motion”. In: *11th International Conference on Control Automation, Robotics and Vision*. IEEE. Dec. 2010, 1416–1421. DOI: 10.1109/ICARCV.2010.5707416.
- [Bro2009] Sebastián Bronte, Luis Miguel Bergasa and Pablo Fernandez Alcantarilla. “Fog Detection System Based on Computer Vision Techniques”. In: *Proceedings of the 12th International Conference on Intelligent Transportation Systems*. IEEE. Oct. 2009, 1–6. DOI: 10.1109/ITSC.2009.5309842.
- [Bur1974] Burle Industries Incorporated. “Electro-optics Handbook”. Burle Industries Incorporated, Tube Products Division, 1974.
- [Cas2002] George Casella and Roger L. Berger. “Statistical Inference”. 2nd ed. Duxbury Press, California, 2002.
- [Cha1960] Subrahmanyan Chandrasekhar. “Radiative Transfer”. Dover Publications, 1960.
- [Chaz2008] Pierre Charbonnier, Valérie Muzet, Philippe Nicolle, Nicolas Hautière, Jean-Philippe Tarel and Didier Aubert. “Stereovision applied to road scene analysis”. In: *Bulletin des Laboratoires des Ponts et Chaussées* 272 (Oct. 2008). Originally published in French as “La stéréovision appliquée à l’analyse de scènes routières”, 57–73.
- [CIE2012] CIE. “Termlist”. 2012. URL: <http://eilv.cie.co.at/> (visited on 03/15/2013).
- [Cro2003] Paul J. Croft. “Fog. Encyclopedia of Atmospheric Sciences”. 2003.
- [Dai2015] Jian Sheng Dai. “Euler-Rodrigues formula variations, quaternion conjugation and intrinsic connections”. In: *Mechanism and Machine Theory* 92 (2015), 144–152. DOI: 10.1016/j.mechmachtheory.2015.03.004.
- [Das1995] Subhudev Das and Narendra Ahuja. “Performance Analysis of Stereo, Vergence, and Focus as Depth Cues for Active Vision”. In: *Pattern Analysis and Machine Intelligence, IEEE Transactions on* 17.12 (Dec. 1995), 1213–1219. DOI: 10.1109/34.476513.
- [Dav2006] Anthony B. Davis. “Effective Propagation Kernels in Structured Media with Broad Spatial Correlations, Illustration with Large-scale Transport of Solar Photons Through Cloudy Atmospheres”. In: *Computational Methods in Transport*. Vol. 48. Lecture Notes in Computational Science and Engineering. Springer Berlin Heidelberg, 2006, 85–140. DOI: 10.1007/3-540-28125-8\_5.

- [Dei1964] Diran Deirmendjian. “Scattering and Polarization Properties of Water Clouds and Hazes in the Visible and Infrared”. In: *Applied Optics* 3.2 (Feb. 1964), 187–196. DOI: 10.1364/AO.3.000187.
- [Dij1959] Edsger Wybe Dijkstra. “A Note on Two Problems in Connexion with Graphs”. In: *Numerische Mathematik* 1.1 (1959), 269–271. DOI: 10.1007/BF01386390.
- [Dum2004] Éric Dumont and Viola Cavallo. “Extended Photometric Model of Fog Effects on Road Vision”. In: *Transportation Research Record: Journal of the Transportation Research Board* 1862.1 (2004), 77–81. DOI: 10.3141/1862-09.
- [Dum2008] Éric Dumont, Roland Brémond and Nicolas Hautière. “Night-time visibility as a function of headlamp beam pattern and pavement reflection properties”. In: *International Congress VISION*. 2008.
- [Dum2010] Éric Dumont, Nicolas Hautière and Romain Gallen. “A Semi-Analytic Model of Fog Effects on Vision”. In: *Atmospheric Turbulence, Meteorological Modeling and Aerodynamics* (May 2010), 635–670.
- [Eil1996] Paul H. C. Eilers and Brian D. Marx. “Flexible Smoothing with B-Splines and Penalties”. In: *Statistical Science* 11.2 (May 1996), 89–102. DOI: doi:10.1214/ss/1038425655.
- [Eis1979] Murray Eisenberg and Robert Guy. “A Proof of the Hairy Ball Theorem”. In: *The American Mathematical Monthly* 86.7 (1979), 571–574.
- [Eld1961] Ralph G. Eldridge. “A Few Fog Drop-Size Distributions”. In: *Journal of Meteorology* 18.5 (Oct. 1961), 671–676. DOI: 10.1175/1520-0469(1961)018<0671:AFFDSD>2.0.CO;2.
- [Els2011] Jürgen Elstrodt. “Maß- und Integrationstheorie”. 7th ed. Springer Berlin Heidelberg, 2011. DOI: 10.1007/978-3-642-17905-1.
- [Eur2010] European Machine Vision Association. “EMVA Standard 1288, Standard for Characterization of Image Sensors and Cameras”. 2010. URL: <http://www.emva.org>.
- [Fli1999] Alexander Flisch, Joachim Wirth, Robert Zanini, Michael Breitenstein, Adrian Rudin, Florian Wendt, Franz Mnich and Roland Golz. “Industrial Computed Tomography in Reverse Engineering Applications”. In: *Proceedings of Computerized Tomography for Industrial Applications and Image Processing in Radiology*. Mar. 1999, 45–53.
- [Fol2014] Johannes Foltin and Stephan Lenor. “Verfahren und Vorrichtung zum Erkennen eines Wetter-Phänomens”. DE Patent App. DE201,310,210,890. Dec. 2014. URL: <http://www.google.com/patents/DE102013210890A1>.
- [Fre2007] Roland W. Freund and Ronald W. Hoppe. “Stoer/Bulirsch: Numerische Mathematik 1”. 10th ed. Springer, 2007. DOI: 10.1007/978-3-540-45390-1.
- [Gac2010] Christina Gackstatter, Patrick Heinemann, Sven Thomas and Gudrun Klinker. “Stable Road Lane Model Based on Clothoids”. In: *Advanced Microsystems for Automotive Applications*. VDI-Buch. Springer, Feb. 2010, 133–143. DOI: 10.1007/978-3-642-16362-3\_14.
- [Gal2000] Aurel Galántai. “The theory of Newton’s method”. In: *Journal of Computational and Applied Mathematics* 124.1 (2000), 25–44. DOI: 10.1016/S0377-0427(00)00435-0.

- [Gal2009] Romain Gallen, Nicolas Hautière and Éric Dumont. “Static Estimation of the Meteorological Visibility Distance in Night Fog with Imagery”. In: *IAPR Conference on Machine Vision Applications (MVA’09)*. 2009.
- [Gal2010a] Romain Gallen, Nicolas Hautière and Éric Dumont. “Static Estimation of the Meteorological Visibility Distance in Night Fog with Imagery”. In: *Transactions on Information and Systems, IEICE* 93.7 (2010), 1780–1787. DOI: 10.1587/transinf.E93.D.1780.
- [Gal2010b] Romain Gallen, Nicolas Hautière and Sébastien Glaser. “Advisory Speed for Intelligent Speed Adaptation in Adverse Conditions”. In: *Intelligent Vehicles Symposium (IV)*. IEEE. June 2010, 107–114. DOI: 10.1109/IVS.2010.5548035.
- [Gal2011a] Romain Gallen, Aurélien Cord, Nicolas Hautière and Didier Aubert. “Towards Night Fog Detection through use of In-Vehicle Multipurpose Cameras”. In: *Intelligent Vehicles Symposium (IV)*. IEEE. June 2011, 399–404. DOI: 10.1109/IVS.2011.5940486.
- [Gal2011b] Romain Gallen, Éric Dumont and Nicolas Hautière. “A conventional approach to nighttime visibility in adverse weather conditions”. In: *International Symposium on Automotive Lighting (ISAL’11)*. 2011.
- [Gal2011c] Romain Gallen, Nicolas Hautière, Éric Dumont and Michèle Colomb. “Introducing Forward Scattering in Adaptive Rear Lighting Systems”. In: *27th Session of the CIE*. July 2011, 704–713.
- [Gal2013] Romain Gallen, Nicolas Hautière, Aurélien Cord and Sébastien Glaser. “Supporting Drivers in Keeping Safe Speed in Adverse Weather Conditions by Mitigating the Risk Level”. In: *Transactions on Intelligent Transportation Systems, IEEE* 14.4 (Dec. 2013), 1558–1571. DOI: 10.1109/TITS.2013.2262523.
- [Gal2014] Romain Gallen, Aurélien Cord, Nicolas Hautière, Éric Dumont and Didier Aubert. “Nighttime Visibility Analysis and Estimation Method in the Presence of Dense Fog”. In: *Transactions on Intelligent Transportation Systems, IEEE* PP.99 (2014), 1–11. DOI: 10.1109/TITS.2014.2331177.
- [Gal2015] Romain Gallen, Aurélien Cord, Nicolas Hautière, Éric Dumont and Didier Aubert. “Nighttime Visibility Analysis and Estimation Method in the Presence of Dense Fog”. In: *Transactions on Intelligent Transportation Systems, IEEE* 16.1 (Feb. 2015), 310–320. DOI: 10.1109/TITS.2014.2331177.
- [Gar2013] Damien Garcia. “Variance Estimation”. 2013. URL: <http://www.biomecardio.com/matlab/evan.html> (visited on 09/24/2014).
- [Gen2012] Wei Geng, Xiaobo Lu, Li Yang, Wujun Chen and Yang Liu. “Detection Algorithm of Video Image Distance based on Rectangular Pattern”. In: *5th International Congress on Image and Signal Processing*. IEEE. Oct. 2012, 856–860. DOI: 10.1109/CISP.2012.6469874.
- [Ghe2015] Ionut Gheorghe, Weidong Li, Thomas Popham and Keith J. Burnham. “Superpixel based semantic segmentation for assistance in varying terrain driving conditions”. In: *Progress in Systems Engineering*. Vol. 1089. Advances in Intelligent Systems and Computing. Springer International Publishing, 2015, 691–698. DOI: 10.1007/978-3-319-08422-0\_98.

- [Gra1999] Hans Grauert and Hans-Christoph Grunau. “Lineare Algebra und Analytische Geometrie”. Oldenbourg, 1999.
- [Gra2004] Roy Gordon Grainger, Jonathan Lucas, Gareth Eythion Thomas and Graham B. L. Ewen. “Calculation of Mie derivatives”. In: *Applied Optics* 43.28 (2004), 5386–5393. DOI: 10.1364/AO.43.005386.
- [Gra2012] Roy Gordon Grainger. “Some Useful Formulae for Aerosol Size Distributions and Optical Properties”. In: *Lecture Notes, University of Oxford* (2012).
- [Gul2007] Ismail Gultepe et al. “Fog Research: A Review of Past Achievements and Future Perspectives”. In: *Fog and Boundary Layer Clouds: Fog Visibility and Forecasting*. Ed. by Ismail Gultepe. Pageoph Topical Volumes. Birkhäuser Basel, 2007, 1121–1159. DOI: 10.1007/978-3-7643-8419-7\_3.
- [Hal1973] George M. Hale and Marvin R. Querry. “Optical Constants of Water in the 200-nm to 200- $\mu$ m Wavelength Region”. In: *Applied Optics* 12.3 (Mar. 1973), 555–563. DOI: 10.1364/AO.12.000555.
- [Hal1995] Forrest G. Hall, John R. Townshend and Edwin T. Engman. “Status of Remote Sensing Algorithms for Estimation of Land Surface State Parameters”. In: *Remote Sensing of Environment* 51.1 (1995), 138–156. DOI: 10.1016/0034-4257(94)00071-T.
- [Har2000] David Harvey. “Modern Analytical Chemistry”. McGraw-Hill, 2000. DOI: 10.1021/ed077p705.2.
- [Har2004] Richard I. Hartley and Andrew Zisserman. “Multiple View Geometry in Computer Vision”. 2nd ed. Cambridge University Press, 2004.
- [Has1994] Richard C. Haskell, Lars O. Svaasand, Tsong-Tseh Tsay, Ti-Chen Feng, Matthew S. McAdams and Bruce J. Tromberg. “Boundary Conditions for the Diffusion Equation in Radiative Transfer”. In: *Journal of the Optical Society of America. A, Optics and Image Science* 11.10 (Oct. 1994), 2727–2741. DOI: 10.1364/JOSAA.11.002727.
- [Hau2005] Nicolas Hautière, Raphaël Labayrade and Didier Aubert. “Detection of Visibility Conditions Through use of Onboard Cameras”. In: *Intelligent Vehicles Symposium (IV)*. IEEE. June 2005, 193–198. DOI: 10.1109/IVS.2005.1505101.
- [Hau2006a] Nicolas Hautière, Raphaël Labayrade and Didier Aubert. “Estimation of the Visibility Distance by Stereovision: a Generic Approach”. In: *IEICE Transactions on Information and Systems* 89.7 (2006). Presented first at the Conference on Machine Vision Applications, May 16–18, 2005, Japan, 2084–2091. DOI: 10.1093/ietisy/e89-d.7.2084.
- [Hau2006b] Nicolas Hautière, Raphaël Labayrade and Didier Aubert. “Real-Time Disparity Contrast Combination for Onboard Estimation of the Visibility Distance”. In: *Transactions on Intelligent Transportation Systems, IEEE* 7.2 (June 2006), 201–212. DOI: 10.1109/TITS.2006.874682.
- [Hau2006c] Nicolas Hautière, Jean-Philippe Tarel, Jean Lavenant and Didier Aubert. “Automatic Fog Detection and Estimation of Visibility Distance through use of an Onboard Camera”. In: *Machine Vision and Applications* 17.1 (2006), 8–20. DOI: 10.1007/s00138-005-0011-1.
- [Hau2007a] Nicolas Hautière. “Artificial Perception under Adverse Conditions: the Case of the Visibility Range”. In: (2007). Young Researchers Seminar, FERSI FEHRL ECTRI, Brno, Czech Republic.

- [Hau2007b] Nicolas Hautière, Didier Aubert and Éric Dumont. “Mobilized and Mobilizable Visibility Distances for Road Visibility in Fog”. In: *26th session of the CIE, Beijing, China 2* (2007), 92–95.
- [Hau2007c] Nicolas Hautiere, Jean-Philippe Tarel and Didier Aubert. “Towards Fog-Free In-Vehicle Vision Systems through Contrast Restoration”. In: *Computer Vision and Pattern Recognition (CVPR). International Conference on*. IEEE. June 2007, 1–8. DOI: 10.1109/CVPR.2007.383259.
- [Hau2007d] Nicolas Hautière, Jean-Philippe Tarel and Roland Brémont. “Perceptual Hysteresis Thresholding: Towards Driver Visibility Descriptors”. In: *Intelligent Computer Communication and Processing (ICCP), International Conference on*. IEEE. Sept. 2007, 89–96. DOI: 10.1109/ICCP.2007.4352146.
- [Hau2008a] Nicolas Hautière, Didier Aubert, Éric Dumont and Jean-Philippe Tarel. “Experimental Validation of Dedicated Methods to In-Vehicle Estimation of Atmospheric Visibility Distance”. In: *IEEE Transactions on Instrumentation and Measurement* 57.10 (Oct. 2008), 2218–2225. DOI: 10.1109/TIM.2008.922096.
- [Hau2008b] Nicolas Hautière, Raphaël Labayrade, Clément Boussard, Jean-Philippe Tarel and Didier Aubert. “Perception through Scattering Media for Autonomous Vehicles”. In: *Autonomous Robots Research Advances*. Ed. by Weihua Yang. Hauppauge, NY: Nova Science Publishers, Inc., Apr. 2008. Chap. 8, 223–267.
- [Hau2009] Nicolas Hautière, Jean-Philippe Tarel and Didier Aubert. “Free Space Detection for Autonomous Navigation in Daytime Foggy Weather”. In: *IAPR Conference on Machine Vision Applications (MVA’09)*. May 2009, 501–504.
- [Hau2010] Nicolas Hautière, Jean-Philippe Tarel and Didier Aubert. “Mitigation of Visibility Loss for Advanced Camera-Based Driver Assistance”. In: *Intelligent Transportation Systems, IEEE Transactions on* 11.2 (June 2010), 474–484. DOI: 10.1109/TITS.2010.2046165.
- [Hau2011] Nicolas Hautière, Raouf Babari, Éric Dumont, Roland Brémont and Nicolas Paparoditis. “Estimating Meteorological Visibility Using Cameras: A Probabilistic Model-Driven Approach”. In: *Computer Vision – ACCV 2010*. Vol. 6495. Lecture Notes in Computer Science. Springer Berlin Heidelberg, 2011, 243–254. DOI: 10.1007/978-3-642-19282-1\_20.
- [Hau2014] Nicolas Hautière, Jean-Philippe Tarel, Houssam Halmaoui, Roland Brémont and Didier Aubert. “Enhanced Fog Detection and Free-Space Segmentation for Car Navigation”. In: *Machine Vision and Applications* 25.3 (2014). Online published in 2011, 667–679. DOI: 10.1007/s00138-011-0383-3.
- [Hen1941] Louis George Henyey and Jesse Leonard Greenstein. “Diffuse Radiation in the Galaxy”. In: *Astrophysical Journal* 93 (1941), 70–83. DOI: 10.1086/144246.
- [Hul1957] Hendrik Christoffel van de Hulst. “Light Scattering by Small Particles”. Dover Publications, 1957.
- [Ish1978] Akira Ishimaru. “Wave Propagation and Scattering in Random Media”. Vol. 2. Academic Press New York, 1978.
- [Jah2012] Bernd Jähne. “Digitale Bildverarbeitung”. 7th ed. Springer, 2012. DOI: 10.1007/978-3-642-04952-1.

- [Jar2008] Wojciech Jarosz. “Efficient Monte Carlo Methods for Light Transport in Scattering Media”. PhD thesis. University of California, San Diego, 2008.
- [Jiu1974] James E. Jiusto. “Remarks on Visibility in Fog”. In: *Journal of Applied Meteorology* 13.5 (1974), 608–610. DOI: 10.1175/1520-0450(1974)013<0608:ROVIF>2.0.CO;2.
- [Kaj1986] James T. Kajiya. “The Rendering Equation”. In: *Proceedings of the 13th Annual Conference on Computer Graphics and Interactive Techniques*. Vol. 20. SIGGRAPH '86 4. ACM, Aug. 1986, 143–150. DOI: 10.1145/15886.15902.
- [Kam1952] H. J. aufm Kampe and H. K. Weickmann. “Trabert’s Formula and the Determination of the Water Content in Clouds”. In: *Journal of Meteorology* 9.3 (1952), 167–171. DOI: 10.1175/1520-0469(1952)009<0167:TFATDO>2.0.CO;2.
- [Kan2008] Kenichi Kanatani. “Statistical Optimization for Geometric Fitting: Theoretical Accuracy Bound and High Order Error Analysis”. In: *International Journal of Computer Vision* 80.2 (2008), 167–188. DOI: 10.1007/s11263-007-0098-0.
- [Kha2012] M. S. Khan, M. Grabner, S. S. Muhammad, M. S. Awan, E. Leitgeb, V. Kvicera and R. Nebuloni. “Empirical Relations for Optical Attenuation Prediction from Liquid Water Content of Fog”. In: *Radioengineering* 21.3 (2012), 911–916.
- [Klo2008] Brigitte Klose. “Meteorologie: Eine interdisziplinäre Einführung in die Physik der Atmosphäre”. German. Springer, 2008. DOI: 10.1007/978-3-662-43578-6.
- [Kno2012] Ian Knowles and Robert J. Renka. “Methods for Numerical Differentiation of Noisy Data”. In: *Proceedings of the Variational and Topological Methods: Theory, Applications, Numerical Simulations, and Open Problems. Electronic Journal of Differential Equations: Conference 21 (2014)*. June 2012, 235–246.
- [Kos1924] Harald Koschmieder. “Theorie der Horizontalen Sichtweite”. In: *Physik der Freien Atmosphäre* 12 (1924), 33–55. DOI: 10.1007/978-3-663-04661-5\_2.
- [Kos2014] Panagiotis Kosmopoulos, Stelios Kazadzis, Helena A. Flocas, Eleni Marinou, Vassilis Amiridis, Michael Taylor and C. P. Jacovidis. “A 3D aerosol climatology in the atmosphere of Greece by remote sensing & radiative-transfer modeling techniques”. In: *12th International Conference on Meteorology, Climatology & Atmospheric Physics*. Vol. 2. 2014.
- [Kur1951] Daisuke Kuroiwa. “Electron-Microscope Study of Fog Nuclei”. In: *Journal of Meteorology* 8.3 (June 1951), 157–160. DOI: 10.1175/1520-0469(1951)008<0157:EMSOFN>2.0.CO;2.
- [Kwo1998] Taek Mu Kwon. “An Automatic Visibility Measurement System Based on Video Cameras”. In: (Sept. 1998).
- [Lab2002] Raphael Labayrade, Didier Aubert and Jean-Philippe Tarel. “Real Time Obstacle Detection in Stereovision on Non Flat Road Geometry Through “V-Disparity” Representation”. In: *Intelligent Vehicle Symposium (IV)*. Vol. 2. IEEE. 2002, 646–651. DOI: 10.1109/IVS.2002.1188024.
- [Lag2008] Andrea Lagorio, Enrico Grosso and Massimo Tistarelli. “Automatic Detection of Adverse Weather Conditions in Traffic Scenes”. In: *Advanced Video and Signal Based Surveillance, 2008. AVSS '08. IEEE Fifth International Conference on*. IEEE. Sept. 2008, 273–279. DOI: 10.1109/AVSS.2008.50.

- [Len2013] Stephan Lenor, Bernd Jähne, Stefan Weber and Ulrich Stopper. “An Improved Fog Model for Estimating the Meteorological Visibility from a Road Surface Luminance Curve”. In: *Pattern Recognition*. Vol. 8142. Lecture Notes in Computer Science. 35th GCPR 2013, Saarbrücken. Springer Berlin Heidelberg, Sept. 2013, 184–193. DOI: 10.1007/978-3-642-40602-7\_19.
- [Len2014] Stephan Lenor, Johannes Martini, Bernd Jähne, Ulrich Stopper, Stefan Weber and Florian Ohr. “Tracking-Based Visibility Estimation”. In: *Pattern Recognition*. Lecture Notes in Computer Science. 36th GCPR 2014, Münster. Springer International Publishing, Sept. 2014, 365–376. DOI: 10.1007/978-3-319-11752-2\_29.
- [Len2015] S. Lenor. “Verfahren und Vorrichtung zur bildbasierten Sichtweitschätzung”. DE Patent App. DE201,410,208,271. Nov. 2015. URL: <http://www.google.com/patents/DE102014208271A1>.
- [Li2014] Yunlong Li, Peter Hoogeboom and Herman W.J. Russchenberg. “Radar Observations and Modeling of Fog At 35 GHz”. In: *Antennas and Propagation (EuCAP), 8th European Conference on*. IEEE. Apr. 2014, 1053–1057. DOI: 10.1109/EuCAP.2014.6901948.
- [Liu1994] Pingyu Liu. “A new phase function approximating to Mie scattering for radiative transport equations”. In: *Physics in Medicine and Biology* 39.6 (1994), 1025–1036. DOI: 10.1088/0031-9155/39/6/008.
- [Liu2014] Chunxue Liu, Xiaobo Lu, Saiping Ji and Wei Geng. “A Fog Level Detection Method Based on Image HSV Color Histogram”. In: *Progress in Informatics and Computing (PIC), International Conference on*. IEEE. May 2014, 373–377. DOI: 10.1109/PIC.2014.6972360.
- [Mad2004] Kaj Madsen, Hans Bruun Nielsen and Ole Tingleff. “Methods for Non-Linear Least Squares Problems”. 2nd ed. Lecture Notes, IMM. Technical University of Denmark, Apr. 2004.
- [Mae2000] Roy De Maesschalck, Delphine Jouan-Rimbaud and Désiré Luc Massart. “The Mahalanobis distance”. In: *Chemometrics and Intelligent Laboratory Systems* 50.1 (2000), 1–18. DOI: 10.1016/S0169-7439(99)00047-7.
- [Mar1963] Donald W. Marquardt. “An Algorithm for Least-Squares Estimation of Nonlinear Parameters”. In: *Journal of the Society for Industrial and Applied Mathematics* 11.2 (1963), 431–441. DOI: 10.1137/0111030.
- [Mar2010] John Markoff. “Google Cars Drive Themselves, in Traffic”. In: *New York Times* (Oct. 10, 2010), A1.
- [Mar2013] Johannes Martini. “Tracking-basierte Nebelerkennung und Sichtweitschätzung für mobile Mono-Kamerasysteme bei Tag”. German. Supported by Robert Bosch GmbH, Stephan Lenor. Diplomarbeit. Karlsruher Institut für Technologie, Aug. 31, 2013.
- [Mat2002] Christian Mätzler. “MATLAB Functions for Mie Scattering and Absorption”. In: *Research Report at Institut für Angewandte Physik, Bern* 8 (June 2002).
- [Mat2012] The MathWorks Inc. “MATLAB version 8.0.0.783 (R2012b)”. Natick, Massachusetts, 2012.

- [Met2007] Samy Metari and François Deschenes. “A New Convolution Kernel for Atmospheric Point Spread Function Applied to Computer Vision”. In: *Computer Vision (ICCV), IEEE 11th, International Conference on*. IEEE. Oct. 2007, 1–8. DOI: 10.1109/ICCV.2007.4408899.
- [Mid1952] William Edgar Knowles Middleton. “Vision Through the Atmosphere”. University of Toronto Press, 1952. DOI: 10.1002/qj.49708134734.
- [Mid2009] Paul A. Midgley and Rafal E. Dunin-Borkowski. “Electron tomography and holography in materials science”. In: *Nature Materials* 8.4 (Apr. 2009), 271–280. DOI: 10.1038/nmat2406.
- [Mie1908] Gustav Mie. “Beiträge zur Optik trüber Medien, speziell kolloidaler Metallösungen”. In: *Annalen der Physik* 330.3 (1908), 377–445. DOI: 10.1002/andp.19083300302.
- [Mih1984] Dimitri Mihalas and Barbara Weibel Mihalas. “Foundations of Radiation Hydrodynamics”. Oxford University Press, 1984.
- [Min2010] An Ming-wei, Guo Zong-liang, Li Jibin and Zhou Tao. “Visibility Detection Based on Traffic Camera Imagery”. In: *Information Sciences and Interaction Sciences (ICIS), 2010 3rd International Conference on*. IEEE. June 2010, 411–414. DOI: 10.1109/ICICIS.2010.5534795.
- [Mis2002a] Michael I. Mishchenko. “Vector radiative transfer equation for arbitrarily shaped and arbitrarily oriented particles: a microphysical derivation from statistical electromagnetics”. In: *Applied Optics* 41.33 (2002), 7114–7134. DOI: 10.1364/AO.41.007114.
- [Mis2002b] Michael I. Mishchenko, Larry D. Travis and Andrew A. Lacis. “Scattering, Absorption, and Emission of Light by Small Particles”. Cambridge University Press, 2002.
- [Mor2006] Kenji Mori, Terutoshi Kato, Tomokazu Takahashi, Ichiro Ide, Hiroshi Murase, Takayuki Miyahara and Yukimasa Tamatsu. “Visibility Estimation in Foggy Conditions by In-vehicle Camera and Radar”. In: *Innovative Computing, Information and Control, 2006. ICICIC’06. First International Conference on*. Vol. 2. IEEE. 2006, 548–551. DOI: 10.1109/ICICIC.2006.373.
- [Mor2007] Kenji Mori, Tomokazu Takahashi, Ichiro Ide, Hiroshi Murase, Takayuki Miyahara and Yukimasa Tamatsu. “Recognition of foggy conditions by in-vehicle camera and millimeter wave radar”. In: *Intelligent Vehicles Symposium (IV)*. IEEE. June 2007, 87–92. DOI: 10.1109/IVS.2007.4290096.
- [Mun1988] Walter H. Munk and Peter F. Worcester. “Ocean Acoustic Tomography”. In: *Oceanography* 1 (1 1988), 8–10. DOI: 10.1088/1742-6596/118/1/012002.
- [Nag2011] Richard Kent Nagle, Edward B. Saff and Arthur David Snider. “Fundamentals of Differential Equations”. 8th ed. Pearson, 2011.
- [Neb2005] Roberto Nebuloni. “Empirical relationships between extinction coefficient and visibility in fog”. In: *Applied Optics* 44.18 (June 2005), 3795–3804. DOI: 10.1364/AO.44.003795.
- [Neg2013] Mihai Negru and Sergiu Nedevschi. “Image Based Fog Detection and Visibility Estimation for Driving Assistance Systems”. In: *Intelligent Computer Communication and Processing (ICCP), International Conference on*. IEEE. Sept. 2013, 163–168. DOI: 10.1109/ICCP.2013.6646102.

- [Neg2014] Mihai Negru and Sergiu Nedevschi. “Assisting Navigation in Homogenous Fog”. In: *Computer Vision Theory and Applications (VISAPP), 9th International Conference on*. 2014, 619–626. DOI: 10.5220/0004740006190626.
- [Nol1987] Guust Nolet. “Seismic Tomography: With Applications in Global Seismology and Exploration Geophysics”. 1st ed. Vol. 5. *Modern Approaches in Geophysics*. Springer, 1987. DOI: 10.1007/978-94-009-3899-1.
- [Oku2014] Ryosuke Okuda, Yuki Kajiwaru and Kazuaki Terashima. “A Survey of Technical Trend of ADAS and Autonomous Driving”. In: *VLSI Technology, Systems and Application (VLSI-TSA), Proceedings of Technical Program – 2014 International Symposium on*. IEEE. Apr. 2014, 1–4. DOI: 10.1109/VLSI-TSA.2014.6839646.
- [Org2008] World Meteorological Organization. ““Guide to Meteorological Instruments and Methods of Observation (CIMO guide)””. 7th ed. 2008.
- [Pav2012] Mario Pavlić, Heidrun Belzner, Gerhard Rigoll and Slobodan Ilić. “Image based fog detection in vehicles”. In: *Intelligent Vehicles Symposium (IV)*. IEEE. June 2012, 1132–1137. DOI: 10.1109/IVS.2012.6232256.
- [Pav2013] Mario Pavlić, Gerhard Rigoll and Slobodan Ilić. “Classification of Images in Fog and Fog-Free Scenes for Use in Vehicles”. In: *Intelligent Vehicles Symposium (IV)*. IEEE. June 2013, 481–486. DOI: 10.1109/IVS.2013.6629514.
- [Pel1990] Eli Peli. “Contrast in complex images”. In: *Journal of the Optical Society of America A* 7.10 (Oct. 1990), 2032–2040. DOI: 10.1364/JOSAA.7.002032.
- [Per2001] Annamaneni Peraiah. “An Introduction to Radiative Transfer: Methods and applications in astrophysics”. Cambridge University Press, 2001.
- [Pom1997] Dean Pomerleau. “Visibility Estimation from a Moving Vehicle using the RALPH Vision System”. In: *Proceedings of the Conference on Intelligent Transportation System*. IEEE. Nov. 1997, 906–911. DOI: 10.1109/ITSC.1997.660594.
- [Qiu2008] Lin Qiu and Wilfrid A. Nixon. “Effects of Adverse Weather on Traffic Crashes: Systematic Review and Meta-Analysis”. In: *Transportation Research Record: Journal of the Transportation Research Board* 2055 (2008), 139–146. DOI: 10.3141/2055-16.
- [Ros2008] Martin Roser and Frank Moosmann. “Classification of Weather Situations on Single Color Images”. In: *Intelligent Vehicles Symposium (IV)*. IEEE. June 2008, 798–803. DOI: 10.1109/IVS.2008.4621205.
- [Ryb1979] George B. Rybicki and Alan Paige Lightman. “Radiative Processes in Astrophysics”. Wiley, 1979. DOI: 10.1002/9783527618170.
- [Sax2008] Ashutosh Saxena, Sung H. Chung and Andrew Y. Ng. “3-D Depth Reconstruction from a Single Still Image”. In: *International Journal of Computer Vision* 76.1 (2008), 53–69. DOI: 10.1007/s11263-007-0071-y.
- [Shaz003] Eugene A. Sharkov. “Passive Microwave Remote Sensing of the Earth: Physical Foundations”. Springer Praxis Books / Geophysical Sciences. Springer, 2003.
- [Shiz006] Richard C. Shirkey and David H. Tofsted. “High Resolution Electro-Optical Aerosol Phase Function Database PFNDAT2006”. Tech. rep. DTIC Document, Aug. 2006.

- [Sit2011] Hu Sitao, Dai Chuchu, Wang Xuemei and Zhu Jing. “Influence Mechanism of Mass Fog on Highway Traffic Safety”. In: *Transportation, Mechanical, and Electrical Engineering (TMEE), International Conference on*. IEEE. Dec. 2011, 791–794. DOI: 10.1109/TMEE.2011.6199321.
- [Siv1996] Michael Sivak. “The information that drivers use: is it indeed 90 % visual?” In: *Perception* 25.9 (1996), 1081–1089. DOI: 10.1068/p251081.
- [Son2012] Hongjun Song, Yangzhou Chen and Yuanyuan Gao. “Homogenous Fog Condition Recognition based on Traffic Scene”. In: *Proceedings of the International Conference on Modelling, Identification and Control*. IEEE. June 2012, 612–617.
- [Str1941] Julius Adams Stratton. “Electromagnetic Theory”. Vol. 33. McGraw-Hill, 1941.
- [Su2014] Hao Su, Qixing Huang, Niloy J. Mitra, Yangyan Li and Leonidas Guibas. “Estimating Image Depth Using Shape Collections”. In: *Transactions on Graphics* 33.4 (July 2014). DOI: 10.1145/2601097.2601159.
- [Tai2008] Frédéric Taillade, Etienne Belin and Éric Dumont. “An analytical model for backscattered luminance in fog: comparisons with Monte Carlo computations and experimental results”. In: *Measurement Science and Technology* 19.5 (2008), 055302. DOI: 10.1088/0957-0233/19/5/055302.
- [Tar2005] Albert Tarantola. “Inverse Pproblem Theory and Methods for Model Parameter Estimation”. Society for Industrial and Applied Mathematics, 2005. DOI: 10.1137/1.9780898717921.
- [Tar2010] Jean-Philippe Tarel, Nicolas Hautière, Aurélien Cord, Dominique Gruyer and Housam Halmaoui. “Improved Visibility of Road Scene Images under Heterogeneous Fog”. In: *Intelligent Vehicles Symposium (IV)*. IEEE. June 2010, 478–485. DOI: 10.1109/IVS.2010.5548128.
- [Tom1976] Claudio Tomasi and Francesco Tampieri. “Features of the proportionality coefficient in the relationship between visibility and liquid water content in haze and fog”. In: *Atmosphere* 14.2 (1976), 61–76. DOI: 10.1080/00046973.1976.9648403.
- [Tra1901] Wilhelm Trabert. “Die Extinktion des Lichtes in einem trüben Medium (Sehweite in Wolken)”. German. In: *Meteorologische Zeitschrift, Wien* 18 (1901), 518–524.
- [Tra2015] U.S. Department of Transportation. “Road Weather Management Program – How Do Weather Events Impact Roads?” Last modified on April 9, 2015. 2015. URL: [http://www.ops.fhwa.dot.gov/weather/q1\\_roadimpact.htm](http://www.ops.fhwa.dot.gov/weather/q1_roadimpact.htm) (visited on 10/10/2015).
- [VDI1983] VDI-Kommission Reinhaltung der Luft. “VDI 3786 part 6: Meteorological Measurements of Air Pollution, Turbidity of Ground-Level Atmosphere, Standard Visibility”. 1983.
- [Vis1987] Raymond Viskanta and M. P. Mengüç. “Radiation Heat Transfer in Combustion Systems”. In: *Progress in Energy and Combustion Science* 13.2 (1987), 97–160. DOI: 10.1016/0360-1285(87)90008-6.
- [Wal2002] Wolfgang Walter. “Analysis 2”. 5th ed. Springer, 2002. DOI: 10.1007/978-3-642-55922-8.
- [Wal2004] Wolfgang Walter. “Analysis 1”. 7th ed. Springer, 2004. DOI: 10.1007/3-540-35078-0.

- [Was2004] Larry Wasserman. "All of Statistics: A Concise Course in Statistical Inference". Springer, 2004. DOI: 10.1007/978-0-387-21736-9.
- [Web2002] Andrew G. Webb. "Introduction to Biomedical Imaging". IEEE Press Series on Biomedical Engineering. Wiley, 2002.
- [Web2014] Stefan Weber, Stephan Lenor and Ulrich Stopper. "Verfahren und Vorrichtung zum Bestimmen einer Sichtweite bei Nebel am Tag". DE Patent App. DE201,310,204,597. Sept. 2014. URL: <http://www.google.com/patents/DE102013204597A1>.
- [Web2015] Stefan Weber, Stephan Lenor, Ulrich Stopper and Johannes Martini. "Verfahren und Vorrichtung zur Tracking-basierten Sichtweitenschätzung". DE Patent App. DE201,410,208,272. Nov. 2015. URL: <http://www.google.com/patents/DE102014208272A1>.
- [Wed2006] Andreas Wedel, Uwe Franke, Jens Klappstein, Thomas Brox and Daniel Cremers. "Realtime Depth Estimation and Obstacle Detection from Monocular Video". In: *Pattern Recognition*. Vol. 4174. Lecture Notes in Computer Science. Springer, 2006, 475-484. DOI: 10.1007/11861898\_48.
- [Wer2007] Dirk Werner. "Funktionalanalysis". 6th ed. Springer Berlin Heidelberg, 2007.
- [Wil1928] Hurd Curtis Willett. "Fog and Haze, Their Causes, Distribution, and Forecasting". In: *Monthly Weather Review* 56.11 (Nov. 1928), 435-468. DOI: 10.1175/1520-0493(1928)56<435:FAHTCD>2.0.CO;2.
- [Wis1980] Warren J. Wiscombe. "Improved Mie scattering algorithms". In: *Applied Optics* 19.9 (May 1980), 1505-1509. DOI: 10.1364/AO.19.001505.
- [Zhaz009] Chen Zhao-zheng, Li Jia and Chen Qi-mei. "Real-Time Video Detection of Road Visibility Conditions". In: *Computer Science and Information Engineering, 2009 WRI World Congress on*. Vol. 5. IEEE. Mar. 2009, 472-476. DOI: 10.1109/CSIE.2009.169.
- [Zhaz012] Junming Zhao, Jianyu Tan and Linhua Liu. "On the derivation of vector radiative transfer equation for polarized radiative transport in graded index media". In: *Journal of Quantitative Spectroscopy and Radiative Transfer* 113.3 (2012), 239-250. DOI: 10.1016/j.jqsrt.2011.11.002.
- [Zie2014] Julius Ziegler et al. "Making Bertha Drive—An Autonomous Journey on a Historic Route". In: *Intelligent Transportation Systems Magazine, IEEE* 6.2 (2014), 8-20. DOI: 10.1109/MITS.2014.2306552.

---

# Index

- L*, *see* luminance, *see* radiance
- $L_{\text{air}}$ , *see* air light parameter
- $S^n$ , *see* sphere
- $L_v$ , *see* luminance
- $L_e$ , *see* radiance
- $v_i$ -fit, 126
- 3D reconstruction, 71, 76
  
- absorption, 13, 25, 27, 33, 38, 39, 157
- absorption coefficient, 32, 38
- absorption efficiency, 28, 32
- absorption index, 27
- ACC, *see* adaptive cruise control
- accidents, 5
- accuracy, 48, 98, 109, 138, 161
- adaptive cruise control, 4
- ADAS, *see* advanced driver assistance systems
- advanced driver assistance systems, 3, 5, 68, 76
- advantages, 161
- advection fog, 23
- adverse weather, 4
- advFastMLE, 92, 96, 102, 112
- AEB, *see* autonomous emergency braking
- air light, 48, 121, 122, 160
- air light parameter, 48–50, 75, 84, 86, 91, 92, 100, 123, 126, 130, 132, 154, 159
- albedo, 137
- ambient light, *see* air light
- analytical discussion, 83, 95
- applications, 19
- asymmetry parameter, 30, 33, 34, 125, 126, 137, 139, 142
- asymptote, 88, 95
- atmospheric aerosol, 5, 15, 23
- atmospheric parameters, 125
- attenuation, 6, 16, 20, 63
- autonomous driving, 3, 162
- autonomous emergency braking, 4
  
- backscattered veil, 67
- backscattering, 18, 67, 162
- backward scattering, 30
- Banach space, 166
- basic splines, 135
- beam of radiation, 38
- Beer-Lambert law, 16, 38
- bisection, 94
- blindness detection, 162
- boundary, 166
- boundary condition, 40, 44
- boundary directions, 40
- boundary distance function, 45
- boundary function, 40
- boundary problem, *see* radiative boundary problem
- brightness, 15, 26, 75
- bundle adjustment, 77, 107, 109
  
- camera, 4, 25, 68
  - driver assistance, 9, 61, 63
  - embedded, 19
  - front, 4, 6, 9, 68
  - multi-purpose, 19, 68
  - stationary, 67
  - surround-view, 4
  - traffic surveillance, 20, 67, 68
- camera characteristics, 70
- camera image, 71
- camera noise model, 72
- camera parameters, 121
- CAN, *see* Controller Area Network
- Cauchy-Schwarz inequality, 102, 169
- chain rule, 169
- classical formulation, 41, 44, 45
- classification, 66
- closure, 166
- CMOS, 68, 71
- coercive, 86, 167
- color, 20, 68

- combined approaches, 161
- compact, 166
- complex numbers, 164
- computational effort, 112, 147
- computer vision, 20, 71, 76, 116
- condensation, 23
- condensation nuclei, 23
- conservation of energy, 38
- continuous uniform distribution, 165
- contrast, 6, 15, 63, 162
- contrast restoration, 20
- Controller Area Network, 77
- convergence, 50, 93, 112, 130
- convex, 86, 87, 101, 166, 168
  - quasi-, 93, 97, 168
  - strictly, 168
  - strictly quasi-, 168
- convexity, 189
- Cramer's rule, 169
- crash rate, 5
- critical point, 86, 87, 90, 167, 188, 197
- cross product, 165
- curvature, 77, 107, 169
- curve, 168
  
- dark signal, 72
- dark signal non-uniformity, 72
- data acquisition, 71, 76, 116, 152
- data quality, 77, 100, 135, 161
- definite
  - negative, 164
  - negative semi-, 164
  - positive, 164
  - positive semi-, 164
- denominator, 87, 202
- depth, *see* distance
- derivatives, 84, 135, 171, 201, 202
- dew point, 23
- diameter, 166
- diffusion, 162
- digital gray value, 71
- digital number, 71
- dipped beam, 19
- directional boundary, 40
- disadvantages, 161
- discontinuity, 191
- distance, 61, 64, 70, 76, 77, 152
- distance-luminance pairs, 152
  
- DN, *see* digital number
- domain, 166
- driver assistance system, *see* advanced driver
  - assistance systems
- driving dynamics, 4
- drop-size distribution, 13, 16, 19, 24, 32, 35, 142
- droplets, 13, 23
- Duntley's law, 16
  
- edge weights, 118, 164
- edges, 117, 164
- effective cross section, 28
- electromagnetic field, 25
- electromagnetic radiation, 25, 26
- electromagnetic spectrum, 20
- electronic stability control, 3, 77, 107, 109
- emission, 25, 39
- emission source term, 38
- environment, 3, 21
- equilibrium, 39
- ESC, *see* electronic stability control
- estimation error, 177
- Euclidean norm, 165
- Euclidean scalar product, 165
- existence, 50, 95, 173
- experiments, 65, 106, 138, 147, 153, 160
- explicit solution, 173
- exposure time, 72
- extinction coefficient, 6, 13, 16, 17, 32, 38, 61, 65,
  - 69, 75, 79, 115, 137, 138, 159
- extinction efficiency, 28, 32
  
- fastMLE, 92, 102, 112
- feasibility, 99, 109, 147
- field of view, 4, 68
- first-order linear ODE, 43, 173
- fish-eye, 4
- fixed point, 48, 51
- flat-world assumption, 55, 64, 123, 152, 160
- floating-point unit, 112
- focal length, 65, 124
- fog, 5, 9, 13, 23, 38, 69, 157
- fog detection, 5
- fog droplets, 5, 13, 26
- fog lamps
  - front, 19
  - rear, 19
- fogged-up windshield, 64

- forward problem, 47  
 forward scattering, 30  
 forward scattering parameter, *see* asymmetry parameter  
 FPU, *see* floating-point unit  
 frame rate, 68  
 free-space detection, 20  
 frequency, 25, 66, 71  
 Fubini's theorem, 169  
 Fubini-Tonelli theorem, 169  
  
 Gauß-Newton algorithm, 83, 112  
 general radiative transfer equation, 38  
 geometric fitting, 82  
 geometrical cross section, 28  
 geometry, 124  
 glare, 4, 17, 64, 66, 162  
 gradient, 167  
 gradient descent, 82, 112  
 graph, 117, 164  
 ground truth, 109  
  
 halos, 66, 162  
 haze, 23, 161  
 headlamps, *see* headlights  
 headlights, 4, 18, 19, 66  
 hemisphere, 41, 165  
 Henyey-Greenstein phase function, 34, 125, 137, 142, 157  
 Hess matrix, 168  
 high beam, 66  
 high dynamic range, 68, 70  
 higher-order models, 10, 49, 61, 115, 141, 158  
 highway assistant, 3  
 homogeneous atmosphere, 39, 48, 69, 157  
 horizontal line, 65  
 horizontal vision, 49, 79, 121, 153, 159  
 humidity, 23  
  
 ice crystals, 23, 27  
 ice fog, 24  
 image acquisition, 71  
 image intensity, 70, 73  
 image plane, 42  
 image sensor, *see* imager  
 imager, 71, 161  
 imaginary unit, 164  
 infimum, 166  
  
 inflection point, 65, 115, 121, 125, 126, 135, 138, 141, 159  
 infrared, 4, 17  
 initial value problem, 43, 173  
 injury rate, 5  
 integers, 163  
 integral formulation, 10, 42, 45, 56  
 Internet of Things, 21  
 intrinsic luminance, 44, 48, 76, 120, 122  
 inverse matrix, 190  
 inverse problem, 48, 61, 70, 75, 79, 158  
 inversion sampling, 137  
 irradiance, 26, 73  
  
 Jacobian matrix, 83, 168  
  
 Koschmieder's model, 49, 61, 65, 75, 79, 83, 100, 109, 115, 120, 153, 158  
 Koschmieder's model for horizontal vision, *see* Koschmieder's model  
 Kronecker delta, 165  
  
 l'Hôpital's rule, 171  
 Lambertian surface, 69, 76  
 lane departure warning, 4  
 lane keeping support, 4  
 laser scanner, 4  
 least-square problem, 80  
 Lebesgue Measurable, 167  
 Lebesgue's dominated convergence theorem, 169  
 Leibniz's integral rule, 169  
 Levenberg-Marquardt algorithm, 83, 112  
 lidar, 4, 77  
 light, 13, 19, 25, 42  
 light control, 4, 19  
 light transport, 10, 13, 38, 48, 157  
 light transport models, *see* radiative transfer model  
 likelihood function, 80  
 likelihood objective function, 83, 158  
 line of sight, 6, 42, 44, 121, 122  
 linearity, 50, 70, 86, 161  
 linearity of integration, 169  
 liquid water content, 36, 142  
 log-normal drop-size distribution, 24, 35, 142, 157  
 look-up tables, 128, 141, 160  
 low beam, 66

- luminance, 13, 15, 26, 61, 70, 73, 76, 77, 152  
 luminance model, 130  
 LWC, *see* liquid water content
- Mahalanobis distance, 82  
 mathematical positive orientation, 78  
 MATLAB, 70  
 maximum likelihood problem, 79  
 maximum norm, 54  
 Maxwell's equations, 25, 26, 38  
 measure and integration theory, 169  
 measuring devices, 13, 18, 61  
 measuring principle, 70  
 meteorological visibility, 6, 9, 13, 15–17, 19, 61, 64, 69, 109, 121, 157  
 Michelson contrast, 17, 67  
 Mie expansion coefficients, 28  
 Mie scattering, *see* Mie theory  
 Mie theory, 13, 27, 142, 157  
 minimization, 82, 87, 91, 99, 104, 112  
 mist, *see* haze  
 model fit, 76, 79, 126, 153  
 model-based algorithms, 10, 61, 158  
 monochromatic, 39  
 monotonicity, 50, 97, 118  
 Monte Carlo, 67, 75, 108, 137  
 MPC, *see* multi-purpose camera  
 multi-purpose camera, 19, 68
- natural numbers, 163  
 nephelometer, 18  
 Newton's method, 82, 91, 92, 112  
 Newton-Cotes rule, *see* Simpson's rule  
 night-view, 4  
 nighttime, 18, 66, 162  
 nodes, 117, 164  
 noise, 71, 177  
 noise estimation, 177  
 noise level, 72, 97  
 noise variance, 72, 118, 177  
 non-coercive, 86, 187  
 non-convex, 86, 187  
 non-homogeneous fog, 17, 69, 162  
 non-linear least square, 83  
 norm, 166  
 normal distribution, 79, 165  
 normalization, 30, 34, 133, 146  
 nowcasting, 21
- numerator, 87, 201  
 numerical instabilities, 93  
 numerical integration, *see* quadrature
- object detection, 20  
 object tracks, 75, 76, 95, 104, 158  
 objective function, 79, 80, 101, 118, 136, 153  
 observations, 70  
 open ball, 165  
 open questions, 95, 159  
 optimization algorithm, 82  
 ordinary differential equation, 42, 173
- parameter estimation, 48, 61, 70, 79, 81, 91, 99, 101, 112, 121, 125, 126, 133, 135, 153, 201  
 parking assist system, 3  
 partial road surface luminance curve, 151, 160  
 particle properties, 13  
 penalization term, 101, 135  
 perfect scattering, 13, 39  
 phase function, 28, 32, 34, 38, 57, 122, 125, 133, 142  
 phase matrix, 38  
 photo response non-uniformity, 72  
 photoelectric effect, 71  
 photometry, 25  
 photon, 25, 71, 137  
 pitch angle, 121, 124, 148  
 pixel, 42, 71  
 Planck constant, 25, 72  
 plane-parallel atmosphere, 13, 48, 55  
 plane-parallel radiative boundary problem, 56, 61, 130  
 plane-parallel radiative transfer equation, 56  
 pointwise convergence, 50  
 Poisson distribution, 72  
 polarization, 4, 25, 38  
 principal point, 124  
 product rule, 169  
 pRSLC, *see* partial road surface luminance curve
- quadrature, 127, 132, 146  
 quantization noise, 72  
 quantum efficiency, 71  
 quantum mechanics, 25
- radar, 4, 20, 65, 77  
 radiance, 13, 25, 73

- radiation fog, 23
- radiative boundary problem, 10, 13, 37, 41, 45, 47, 130
- radiative transfer equation, 13, 37, 39, 41, 42
- radiative transfer model, 10, 13, 48, 76, 122, 158
- radiative transfer problem, 13, 115
- radiative transfer theory, 10, 37, 70, 121, 130, 158
- radiometric calibration, 73
- radiometry, 25
- radius of curvature, 77, 169
- range of convergence, 83, 91, 94, 112
- rate of convergence, 51
- rational numbers, 163
- Rayleigh scattering, 30
- real numbers, 163
- real-time, 9, 117, 153, 158
- reflection, 25
- refraction, 25
- refractive index, 27
- regularization term, 99
- relative error, 169
- removable discontinuity, 88, 190
- residuum, 81
- resolution, 68, 135
- Ricatti-Bessel functions, 28
- road plane, 108, 121, 160
- road sign recognition, 4, 76
- road surface luminance curve, 10, 61, 64, 68, 109, 115, 116, 120, 146, 151, 159
- Rodrigues' rotation formula, 169, 173
- rotation, 41, 124, 173
- RSLC, *see* road surface luminance curve
- RSLC model, 10, 61, 65, 120, 122, 125, 130, 137, 146, 160
- RTE, *see* radiative transfer equation
- RTT, *see* radiative transfer theory
  
- sample covariance, 177
- sample mean, 177
- scattering, 6, 13, 18, 25, 27, 38, 108, 137, 157
- scattering atmospheres, 39
- scattering coefficient, 32, 38
- scattering efficiency, 28, 32
- scattering phase function, *see* phase function
- scatterometer, 18
- Schwarz's theorem, 169
- segmentation, 71, 77, 116, 152, 158
- self-glare, 162
- sensor data fusion, 4, 20, 162
- shortest path, 118
- shot noise, 72
- sight impairments, 5, 23, 162
- signal, 72, 97, 135, 177
- signal-to-noise ratio, 97, 135, 136
- simplicity, 97
- Simpson's rule, 127, 132, 169
- simulation framework, 112
- size parameter, 27, 30
- smooth boundary, 41
- smoothing, 77, 135, 148
- SND, *see* squared neighbor differences
- special orthogonal group, 164
- spectral irradiance, *see* irradiance
- spectral luminous efficacy, 25, 70, 73
- spectral radiance, *see* radiance
- speed
  - adaption, 19
  - warning, 19
- speed of light, 25, 38, 72
- sphere, 24, 39, 41, 57, 165, 173
- splines, 135, 177
- squared neighbor differences, 118, 177, 183
- stabilized estimation, 100, 154, 159
- standard deviation, 98, 153
- stationary, 21, 39, 67, 158
- stereo vision, 4, 76
- stokes vector, 38
- stopping criterion, 82, 92
- structure from motion, 76, 109
- sublimation, 24
- sum notation, 83, 91
- sum-of-squares objective function, 80, 83
- superpixel, 76
- supersaturation, 23
- supremum, 166
- surface integral, 39
- synthetic tracks, 109
- system gain, 72
- system parameters, 125, 140
  
- temporal noise, 72
- time-independent RTE, 38
- tracking, 20, 71, 75, 76, 159
- tracking-based approach, 61, 109, 158
- traffic jam assistant, 3
- traffic safety, 5

traffic surveillance, 67  
transmissometer, 18  
travel angle, 78  
travel distance, 78  
two-dimensional uncertainties, 81

ultrasonic sensor, 3, 20, 77  
uncertainty, 79, 81, 153, 159  
uniform boundedness, 44, 47, 50, 88, 93  
uniform convergence, 51  
uniform distribution, 137  
uniqueness, 87, 97, 173, 188  
unit sphere, *see* sphere

vanishing point, 65, 148  
vehicle bus, 77  
vehicle parameters, 3  
vehicle trajectory, 77  
vertices, *see* nodes  
visibility, 15, 23, 63, 69, 157  
visibility assessment, 9, 63, 157  
visibility estimation, 5, 9, 13, 36, 42, 61, 75, 104,  
115, 120, 135, 152, 153, 158  
visibility lidar, 18  
visible spectrum, 25  
visual contrast, 6, 15, 17  
visual perception, 25  
visual perception threshold, 13, 16, 63  
volume scattering, 32

wave properties, 13, 25  
wavelength, 17, 27  
wavelength independence, 13, 30, 33, 36  
Weber contrast, *see* visual contrast  
well-definedness, 50, 87